

Aus dem Institut für Physikalische Chemie der  
Universität Freiburg (Schweiz)

**ELECTRON-MOLECULE COLLISIONS:  
A NOVEL INSTRUMENT FOR MEASURING  
INELASTIC DIFFERENTIAL CROSS SECTIONS  
AT 180° ANGLE  
AND  
APPLICATIONS**

INAUGURAL - DISSERTATION

zur Erlangung der Würde eines *Doctor rerum naturalium*  
der Mathematisch-naturwissenschaftlichen Fakultät  
der Universität Freiburg in der Schweiz

vorgelegt von

**KNUT ROGER ASMIS**  
aus Rüderswil (BE)

Diss. Nr. 1142

Peter Gaffuri Repro-Atelier Zytglogge, Bern  
1996

Von der Mathematisch-naturwissenschaftlichen Fakultät der  
Universität Freiburg in der Schweiz angenommen, auf Antrag der  
Herren Professoren Dr. M. Allan und Dr. E. Haselbach.

Freiburg, den 24. Oktober 1996

Der Dekan:  
Prof. Dr. J.-P. Berrut

*To my parents*

The present work was realized under the supervision of Prof. Dr. Michael Allan, who conceived of and initiated this project and to whom I am indebted for his invaluable guidance during the past four years. I thank him for generously sharing with me his profound knowledge of basic physical chemistry and his technical expertise.

I thank Prof. E. Haselbach for having given me the possibility to pursue my Ph.D. thesis at the Institute of Physical Chemistry and for his continuous support and encouragement. I am especially grateful for the freedom granted me to pursue the scientific goals of my particular interest.

## Table of Contents

TABLE OF CONTENTS .....	i
ABBREVIATIONS .....	iv
SYMBOLS.....	v
1. INTRODUCTION.....	1
1.1. Scope of the Present Work .....	1
1.2. Basic Phenomena in Electron-Molecule Collisions .....	2
1.2.1. Definition of Scattering Cross Sections.....	2
1.2.2. Resonances in Electron-Molecule Collisions .....	3
1.2.3. Nonresonant Electronic Excitation .....	4
1.3. Electron Impact Experiments .....	6
1.3.1. Electron Transmission Spectroscopy .....	7
1.3.2. Energy-Loss Spectroscopy.....	7
1.3.3. Dependence of the Differential Cross Section on Electron Energy and Scattering Angle .....	8
1.3.4. Dissociative Attachment Spectroscopy.....	8
1.4. Electron Impact Spectroscopy: Historical Overview and Present Applications.....	9
2. INSTRUMENTS .....	10
2.1. Electron Energy Filters .....	10
2.1.1. Trochoidal Filter .....	10
2.1.2. Cylindrical Filter .....	10
2.1.3. Hemispherical Filter .....	11
2.2. Trochoidal Electron Spectrometer.....	11
2.2.1. Sensitivity in Function of $E_{in}$ and $E_r$ .....	12
2.2.2. Energy Scale Calibration .....	13
2.3. Dissociative Attachment Spectrometer .....	14
2.4. Photoelectron Spectrometer.....	14
3. COMPUTATIONAL METHODS .....	16
3.1. The CASSCF/CASPT2 Method.....	16
3.2. The INDO/S method.....	18
3.2.1. Excitation Energies of Bound States .....	19
3.2.2. Resonances.....	19
3.2.3. Concept of the Parent State.....	20
3.2.4. Definition of the Decay Factor.....	21
3.3. Method of Scaled Virtual Orbital Energies .....	23

*“Nicht der Besitz der Wahrheit, sondern das erfolgreiche Ringen um sie  
macht das Glück des Forschers aus.”*

Gotthold Ephraim Lessing



4. DEVELOPMENT OF AN INSTRUMENT FOR INELASTIC DIFFERENTIAL CROSS SECTION MEASUREMENTS AT 0° AND 180° .....	25
4.1. Introduction.....	25
4.2. Historical Perspective .....	26
4.3. Principle of Operation.....	27
4.4. Development.....	29
4.5. Experimental Setup.....	31
4.6. Calibration.....	32
4.7. Performance .....	34
5. RESULTS .....	36
5.1. Electron Impact Excitation of Helium: Measurement of Absolute Differential Cross Sections at 0° and 180° for Near-Threshold Excitation and Ionization.....	36
5.1.1. Introductory Remarks.....	36
5.1.2. Near-Threshold Ionization .....	37
5.1.3. Article.....	39
5.2. Measurement of Absolute Differential Cross Sections at 0° and 180° for the Excitation of the Lowest Triplet State in Ethylene .....	56
5.2.1. Introduction .....	56
5.2.2. Results and Discussion.....	56
5.3. Electron Energy-Loss Spectroscopy and Theoretical Study of Triplet and Singlet Excited States of Fulvene.....	64
5.3.1. Introductory Remarks.....	64
5.3.2. Article (Submitted for Publication).....	65
5.4. Selective Decay of 2p-1h Shape Resonances in 1,3- Butadiene .....	86
5.4.1. Introduction .....	86
5.4.2. Results .....	87
5.4.3. Discussion .....	96
5.4.4. Summary and Conclusions.....	103
5.5. 2p-1h Shape Resonances in Cyclic Conjugated Dienes.....	105
5.5.1. Introduction .....	105
5.5.2. Results .....	105
5.5.3. Discussion .....	126
5.5.4. Conclusions .....	134
5.6. Dissociative Attachment Study of Ozone .....	136
5.6.1. Introductory Remarks.....	136
5.6.2. Publications .....	136
5.7. Resolution Enhancement of the Photoelectron Spectrometer.....	165
5.7.1. Introductory Remarks.....	165
5.7.2. Publication.....	167

5.8. INDO/S Study of 2,2-Dimethylisoidene and all-trans-1,3,5,7-Octatetraen.....	176
5.8.1. Introductory Remarks .....	176
5.8.2. Publication .....	176
6. SUMMARY .....	185
7. APPENDIX.....	187
7.1. True-Spin States for the Three-Electron Systems .....	187
7.2. Characteristics of the ZINDO Output.....	190
REFERENCES.....	193
ACKNOWLEDGEMENTS .....	197
CURRICULUM VITAE.....	198

**Abbreviations**

AE	electron attachment energy
CAS	complete active space
CI	configuration interaction
AO	atomic orbital
CIS	configuration interaction singles
CNDO	complete neglect of differential overlap
CSF	configuration state function
DA	dissociative attachment
DCS	differential cross section
$\Delta E$	energy-loss
EEL	electron energy-loss
$E_{in}$	incident electron energy
$E_r$	residual electron energy
ET	energy transmission
HF	Hartree-Fock
HOMO	highest occupied MO
INDO	intermediate neglect of differential overlap
INDO/S	INDO parametrized for spectroscopy
IP	ionization potential
LUMO	lowest unoccupied MO
MC	multi-configurational
MO	molecular orbital
PE	photoelectron
PT2	second-order perturbation theory
SCF	self-consistent field
ZDO	zero differential overlap
ZINDO	Zerner INDO

**Symbols**

$\Phi$	configuration state function
$\Omega$	solid angle
$\Psi$	spectroscopic state (many-electron wave function)
$\chi$	atomic orbital
$\delta$	Kronecker delta
$\epsilon$	orbital energy
$\phi$	azimuthal scattering angle
$\varphi$	molecular space orbital
$\lambda$	molecular spin orbital
$\pi$	symmetry label
$\theta$	polar scattering angle
$\rho$	Larmor radius
$\sigma$	cross section (or symmetry label)
$\omega$	weight of the CASSCF function

# 1. INTRODUCTION

## 1.1. Scope of the Present Work

The present thesis reviews the work related to electron-molecule collisions, which I carried out towards my Ph.D. degree at the Physical Chemistry Institute of the University in Fribourg during the years 1993-1996. This work comprised the following activities:

- (a) The construction and development of an instrument to study a particular aspect of electron-molecule collisions, namely the measurement of electrons scattered inelastically from gaseous molecules into an angle of  $180^\circ$ .
- (b) The application of this novel tool and the other available instruments, in particular the trochoidal electron spectrometer, the dissociative attachment spectrometer and the photoelectron spectrometer to current topics of chemical interest.
- (c) The exploitation of the available computational infrastructure to carry out quantum mechanical electronic structure calculations, aiding the interpretation of the collected experimental data.
- (d) The improvement of the performance of the trochoidal electron spectrometer as well as the photoelectron spectrometer.

The most noteworthy achievement was the construction of the instrument mentioned in point (a). To the best of my knowledge it enabled the first measurement of inelastic differential cross sections (DCSs) at  $180^\circ$  in the gas phase. Preliminary results were presented at the *International Symposium on Electron- and Photon-Molecule Collisions and Swarms* in Berkeley (Asmis and Allan 1995). Very recently another research group has started to develop an alternative method for measuring  $180^\circ$  DCSs (Zubek *et al.* 1996).

Previous experimental studies were limited to observable scattering angles of typically up to  $140^\circ$  (see for example Allan 1992), due to mechanical constraints in the particular experimental technique. With the new instrument we can measure the ratio of the  $0^\circ$  and  $180^\circ$  inelastic DCS. The combination of the  $0^\circ/180^\circ$  DCS ratio with the absolute  $0^\circ$  DCS, measured for example with the electrostatic electron spectrometer available in Fribourg, then yields the absolute  $180^\circ$  DCS. Absolute values for DCSs are of importance, especially with respect to testing the quality of predictions based on modern scattering theory.

## 1.2. Basic Phenomena in Electron-Molecule Collisions

A general electron-molecule scattering process is shown Figure 1-1. An incident electron with a kinetic energy  $E_{in}$  and initial impact parameter  $b$  is scattered on a gaseous target molecule  $M$  into a direction  $\theta$  with a residual energy  $E_r$ . During the scattering process the incident electron may lose energy to the excitation of the target. The excitation may be translational, rotational, vibrational and electronic. If the excitation is more than only translational then we speak of *inelastic* scattering, otherwise of *elastic* scattering.

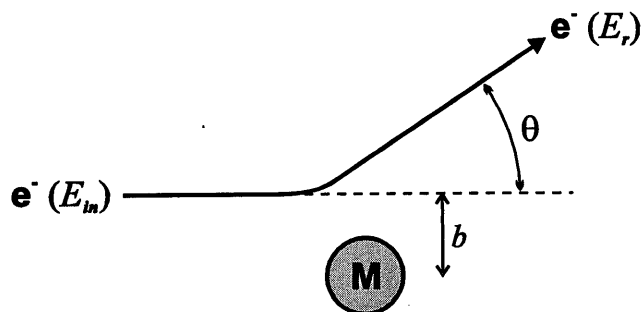


Figure 1-1

Schematic diagram of a general electron scattering process.

The transferred energy amount is termed the *electron energy-loss*  $\Delta E$  and is given by the difference of the incident and residual electron kinetic energy.

$$\Delta E = E_{in} - E_r \quad (1-1)$$

$\Delta E$  is related to the energy levels of the target molecule. For polyatomic molecules translational excitation can generally be neglected, due to the large mass differences of the collision partners. Thus we can write  $\Delta E$  as the sum of the electronic, vibrational and rotational excitation energies:

$$\Delta E = \Delta E_{el} + \Delta E_{vib} + \Delta E_{rot} \quad (1-2)$$

### 1.2.1. Definition of Scattering Cross Sections

The time-independent probability for the occurrence of a particular collision process is termed its *cross section*  $\sigma$  (Trajmar and Cartwright 1984). It is a function of the spherical angles of scattering (the polar angle  $\theta$  and the azimuthal angle  $\phi$ ), the incident electron energy  $E_{in}$ , as well as the electronic structure of the target molecule.

The customary *differential cross section* defines the probability of exciting the target (with fixed orientation) to a discrete final state  $n$ , with the electron scattered into a small solid angle  $\Omega$  in the direction  $(\theta, \phi)$ .

$$\frac{d\sigma_n(\theta, \phi, E_{in})}{d\Omega} \quad (1-3)$$

In most scattering experiments the target molecules are randomly oriented. Furthermore, the measuring apparatus has a finite energy and angular resolution. Thus we average over these properties and obtain the *measured* differential cross section (DCS).

$$DCS_n(\theta, E_{in}) = \left( \frac{d\sigma_n(\theta, E_{in})}{d\Omega} \right) \quad (1-4)$$

The measured DCS is independent of the azimuthal scattering angle  $\phi$  and has the dimension of area per unit solid angle. Integration of the DCS over all polar angles  $\theta$  yields the *integral cross section*  $\sigma_n$ .

$$\sigma_n(E_{in}) = 2\pi \int_0^\pi DCS_n(\theta, E_{in}) \sin\theta d\theta \quad (1-5)$$

The summation of the integral cross sections for all energetically accessible processes renders the *total electron scattering cross section*  $\sigma_T$ .

$$\sigma_T(E_{in}) = \sum_n \sigma_n(E_{in}) \quad (1-6)$$

In many experiments the gas density in the collision region and the absolute sensitivity of the instrument are not known exactly and only *relative* cross sections are obtained. The more elaborate experiments determine *absolute* cross sections.

### 1.2.2. Resonances in Electron-Molecule Collisions

In electron scattering *resonance* is defined as the temporary formation of a compound state between the incident electron and the target molecule with a lifetime appreciably longer than the electron passage time (Takayanagi 1984). Often the temporary anion itself is also called a resonance and the scattering mechanism involving the resonance is termed *resonant* scattering. Resonances manifest themselves as variations in the various cross sections at specific impact energies.

Resonances are formed at incident energies where the electron wave function has a large amplitude within the target and the electron can access, classically speaking, a quasistationary orbit in the field of the target molecule.

The quasistationary nature of the resonance is maintained by either of the following mechanisms until autodetachment occurs:

- (a) The electron is trapped by a potential barrier in the effective potential, formed by the combination of static, polarization, exchange and centrifugal interactions. The existence of the resonance is due to the shape of the effective potential and we speak of *shape resonances*.
- (b) The electron is trapped by an electronic excitation, which it induces. Such resonances are termed *Feshbach resonances*.

Shape resonances are generally pictured as electron capture in an empty valence orbital of the neutral molecule. If the electron capture is accompanied by electronic excitation, we speak of *two-particle-one-hole* (2p-1h) or *core-excited* shape resonances, otherwise of *one-particle* (1p) or *simple* shape resonances. The lifetime of a shape resonance is given by the probability of the electron to tunnel through the potential barrier and is often of the same order of magnitude as a vibrational period. The nuclei can thus start to relax on the anion potential surface, causing vibrational excitation of the target molecule after the resonance has eventually decayed into the neutral molecule through autodetachment. Which vibrations (and which electrons) have been excited is informative of the nature of the resonance involved.

In Feshbach resonances the excitation energy of the corresponding neutral excited state is bigger than the incident electron energy. The energy difference is termed the *Feshbach decrement* and is generally of the order of 0.5 eV (Robin 1985). The decay requires a change of electronic state. Consequently, Feshbach resonances are often characterized by longer lifetimes than shape resonances and pronounced vibrational structure. Feshbach resonances often involve Rydberg orbitals.

### 1.2.3. Nonresonant Electronic Excitation

Electronic excitation, in particular excitation of spin-forbidden transitions, is often dominated by resonant mechanisms up to about 5 eV above threshold. *Nonresonant* scattering is of importance especially at higher  $E_i$  and will be discussed here briefly (see for example McDaniel 1989 for a more detailed discussion).

If the electric field experienced by the molecule (mean radius  $r$ ) is approximately uniform over its spatial extent, as is the case for large impact parameters  $b$  ( $b \gg r$ , see Figure 1-1 for the definition of  $b$ ), the electric field most strongly interacts with the transition electric dipole moment of the molecule. Under these conditions *dipole-allowed* transitions will predominantly be excited. The large impact parameter produces only little deflection for high-energy electrons and thus the cross sections for optically allowed transition are generally peaked in the forward direction.

For smaller impact parameters ( $b > r$ ) the molecule will experience a nonuniform electric field. The nonuniform field components can interact with higher electric moments of the molecule, leading to the possibility of exciting *dipole-forbidden* transitions. Because large scattering angles occur only when there is a strong interaction between the electron and molecule, which in turn requires a small impact parameter  $b$ , dipole-forbidden transitions are enhanced relative to dipole-allowed transitions at larger scattering angles.

In collisions where the impact parameter is even smaller ( $b \leq r$ ) the electron essentially makes a direct impact with the target molecule, resulting in the possibility for electron exchange to take place. In classical terms, the incident electron attaches to the molecule, kicking out one of the electrons of the target. If the exchanged electrons are in different spin states, *spin-forbidden* transitions can be induced. Due to the small impact parameter electron exchange processes show no forward peaking.

The outcome of an electron-molecule collision is strongly dependent on the incident electron energy. Electron exchange processes are most probable when the incident energy approaches the kinetic energy of the target electron (around 10 eV). For the discussion of spin-allowed transitions it is useful to introduce the concepts of the *momentum transfer*  $K$  and the *apparent generalized oscillator strength*  $F_n$  (see for example Hall and Read 1984).  $K$  is the magnitude of the linear momentum exchanged between the electron and the molecule and can be expressed in terms of the Bohr radius  $a_0$ , the Rydberg constant  $R$ , the scattering angle  $\theta$ , the incident electron energy  $E_{in}$  and the energy-loss  $\Delta E$ .

$$(Ka_0)^2 = \frac{1}{R} \left[ (2E_{in} - \Delta E) - 2\sqrt{E_{in}(E_{in} - \Delta E)} \cos \theta \right] \quad (1-7)$$

The apparent generalized oscillator strength  $F_n$  is a convenient expression for the electron impact transition intensity to the state  $n$  as a function of the momentum transfer  $K$  and can be calculated from the experimental differential cross section  $DCS_n$ .

$$F_n(K) = \frac{\kappa_0}{2\kappa_n} K^2 \Delta E DCS_n(K) \quad (1-8)$$

$\kappa_0$  and  $\kappa_n$  are the magnitudes of the electron momentum before and after scattering.  $F_n$  may be expressed, within certain approximations, in powers of  $K$  (Hudson *et al.* 1982):

$$F_n(K) = 2\Delta E \left[ \mu_1^2 + (\mu_2^2 - 2\mu_1\mu_3)K^2 + (\mu_3^2 - 2\mu_2\mu_4 + 2\mu_1\mu_5)K^4 + \dots \right], \quad (1-9)$$

where  $\mu_1$  is the transition dipole moment,  $\mu_2$  the transition quadrupole moment,  $\mu_3$  the transition octupole moment, etc..

From eq. 1-7 we see that in the limit of high incident energy and small scattering angle  $K$  approaches zero and vice versa a decrease in electron energy and an increase in scattering angle increases  $K$ . Thus on the basis of eq. 1-9 the dipole selection rules become active at high incident energies and small scattering angles, while at small incident energies and large scattering angles dipole-forbidden but higher-pole-allowed transitions will be enhanced.

### 1.3. Electron Impact Experiments

The different types of experiments used to study electron-molecule collisions will be described briefly in this chapter. Detailed information on the instruments used in the present work is given in Chapters 2 and 4.

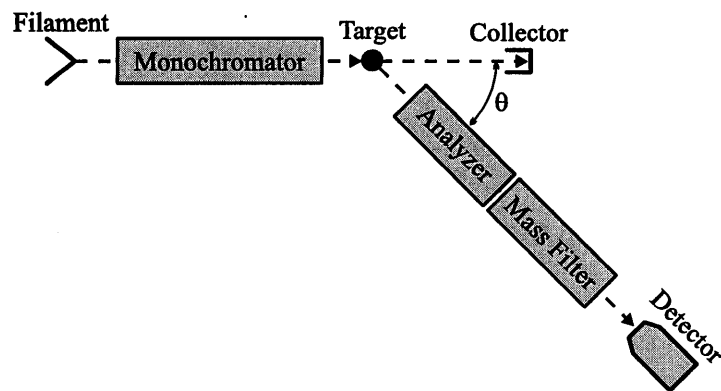


Figure 1-2

Schematic diagram of a generalized electron impact spectrometer.

All electron impact experiments have a similar instrumental arrangement (Figure 1-2). The electrons are taken from a hot filament and fed into the monochromator, where they are dispersed with respect to their forward kinetic energy. They pass the monochromator with a low and fixed energy. A nearly monoenergetic beam exits the monochromator, is accelerated to the desired incident energy and enters the target region, where it can interact with the target molecules. Electrons scattered into a particular angle  $\theta$  are decelerated to an energy suitable for the operation of the analyzer. The energy selected electrons exiting the analyzer are counted. In dissociative attachment spectroscopy the stable fragment anions are extracted from the target chamber, energy and mass analyzed and counted.

#### 1.3.1. Electron Transmission Spectroscopy

In the *electron transmission* (ET) experiment the transmitted electron current is measured at the collector as a function of incident electron energy. Given the gas density  $N$ , the injected electron current  $I_0$  and the cell length  $L$ , the current transmitted to the collector  $I$  is given by

$$I = I_0 e^{-NQL} \quad (1-10)$$

$Q$  is ideally the total scattering cross section. Real transmission spectrometers deviate from this picture, as discussed in detail by Jordan and Burrow (1987).

Since the nonresonant part of the total scattering cross section generally varies only weakly with incident energy, ET spectroscopy is used for the detection of resonances. These can cause larger variations in the transmitted current. To improve the visibility of variations in an ET spectrum, usually the derivative of the transmitted current  $dI/dE_{in}$  is plotted against  $E_{in}$ . In particular 1p shape and Feshbach resonances are detected. 1p shape resonances generally cause the larger change in the total scattering cross section, while Feshbach resonances are characterized by narrower structures.

#### 1.3.2. Energy-Loss Spectroscopy

In the *energy-loss* (EL) experiment electrons scattered into a fixed direction are counted as a function of the electron energy-loss  $\Delta E$ . Either the incident or the residual energy is kept fix. The constant residual energy mode is preferably used when working at near-threshold incident energies, as is the case in the present work. In this mode each state is excited at the same energy above its threshold excitation energy.

The peak locations in an EL spectrum correspond to the energy levels of the target. The intensities are related to the excitation cross sections. Compared to optical spectroscopic methods, selection rules governing the excitation processes are much less restrictive. The following rules of thumb can be deduced from the arguments given in the Section 1.2.3:

- Spin-forbidden transitions are enhanced at low residual energies ( $< 5$  eV) and large scattering angles.
- Dipole-forbidden, spin-allowed transitions are best observed at intermediate residual energies (1-10 eV) and large scattering angles.
- Dipole- and spin-allowed transitions are almost exclusively observed at high residual energies ( $> 20$  eV) and small scattering angles. In the limit of zero momentum transfer the EL spectrum resembles the corresponding optical absorption spectrum.

### 1.3.3. Dependence of the Differential Cross Section on Electron Energy and Scattering Angle

The spectrum attained, when measuring the dependence of the differential cross section on the incident electron energy is termed the *excitation function*. In this case the intensity of a feature observed in the EL spectrum is monitored as a function of  $E_{in}$ . This is achieved by varying the incident and residual energy in such a fashion, that the energy-loss is kept constant. In the angular dependence experiment the differential cross section is measured as a function of the scattering angle, keeping the incident and residual energy fixed.

Both type of spectra contain information on the scattering mechanisms involved in the excitation process and therefore help in their identification and classification. If resonant scattering is involved, important information about the energy and the lifetime of the resonance can be extracted, due to the more or less strong variation in the excitation function at the resonance energy. The most important decay channels are:

- 1p shape resonances decay preferentially into the (vibrationally excited) electronic ground state of the neutral target.
- 2p-1h shape resonances decay predominantly into electronically, especially triplet, excited states of the neutral target.
- Resonances can fragment, producing a neutral and a negatively charged species (dissociative attachment).

### 1.3.4. Dissociative Attachment Spectroscopy

In the *dissociative attachment* (DA) experiment the yield of stable fragment anions is monitored as a function of incident electron energy. Three mechanisms are responsible for the generation of stable anions in electron scattering processes:

- Dissociative attachment*: Resonances can fragment, producing a neutral and a negatively charged species.
- Electron attachment*: If the molecule possesses a positive electron affinity then metastable anions can be formed, generally at low incident energies.
- Ion pair formation*: At higher incident energies (>10 eV) ion pair production can also occur.

Further information on the excited states of the anion can be gained by the measurement of the fragment ion kinetic energy. First the analyzer is set to high transmission and the mass spectrum for a fixed incident electron and ion kinetic energy is measured. Then the incident electron energy and ion mass are kept fix and the ion yield is measured as a function of ion kinetic energy.

## 1.4. Electron Impact Spectroscopy: Historical Overview and Present Applications

The beginning of electron impact spectroscopy is generally traced back to the historical electron energy-loss experiment of Franck and Hertz (1914). In the 1930's electron-atom and electron-molecule collision cross sections were measured for the first time. The discovery of resonances in electron-molecule and shortly thereafter in electron-atom collisions together with the development of high-resolution spectrometers in the 1960's and 1970's revitalized the interest in electron collision research (Schulz 1973).

In the early 1970's the first applications to topics of chemical interest appeared. Kuppermann *et al.* (1979) pioneered the use of electron energy-loss spectroscopy to study spin- and dipole-forbidden transitions in organic compounds. Burrow and Jordan (1987) initiated the study of resonances of organic compounds by electron transmission spectroscopy with the aim to assess electron affinities.

Today the applications of electron impact experiments to chemistry are of diverse nature. Promising approaches are pursued both in the application of electron impact techniques to molecules adsorbed on surfaces and molecules imbedded in low temperature matrices (Swiderek *et al.* 1994, Antic *et al.* 1994, Azria *et al.* 1994 and Meinke *et al.* 1994).

Pursuing research in the field of electron-molecule collisions is of fundamental scientific importance and simultaneously of current interest for the understanding of the numerous technological and environmental systems where electron collisions take place. Examples are atmospheric and interstellar chemistry as well as various discharge devices, including commercial ozonizers, plasma etching and plasma assisted chemical vapor deposition reactors, electrical discharge lamps and excimer lasers.

## 2. INSTRUMENTS

In this chapter a general description of the instruments used in this work is given. A detailed description of the instruments can be found in Allan (1989), Bulliard (1994), Dressler (1985) and Schafer (1992). The development and construction of the novel instrument, which measures electrons scattered inelastically into 180°, is described in Chapter 4.

### 2.1. Electron Energy Filters

To study electron scattering we need to employ electron energy filters. These filters are used to generate a beam of nearly monoenergetic electrons of variable energy (monochromator) and to energy analyze the scattered electrons or stable ion fragments (analyzer). Many filters can be operated as analyzers as well as monochromators. The goal is to optimize the two mutually exclusive requirements of high resolution and high transmission.

#### 2.1.1. Trochoidal Filter

In a *trochoidal filter* electrons are dispersed with respect to their forward velocities  $v_z$  by the combination of an axial magnetic field  $\vec{B}$  and perpendicular electrostatic field  $\vec{E}$ . Under these conditions the electrons describe a trochoidal (cycloidal) motion, characterized by a constant velocity  $v_x$  in the direction perpendicular to the magnetic and electric fields.

$$v_x = \frac{|\vec{E} \times \vec{B}|}{|\vec{B}|^2} \quad (2-1)$$

Only those electrons which reach the exit aperture, displaced by some distance  $d_x$  with respect to the entrance aperture, are transmitted. A beam emerging from a trochoidal monochromator has a typical full-width at half-maximum of 30 to 50 meV with beam currents in the  $10^{-9}$  to  $10^{-8}$  Ampere range.

A trochoidal monochromator was first realized by Stamatovic and Schulz (1968, 1970). Subsequently, this type of filter has been used as a monochromator preferentially in electron transmission and electron attachment studies, as well as monochromator and analyzer in electron energy-loss experiments (for a summary see Illenberger and Momigny 1992).

#### 2.1.2. Cylindrical Filter

In a *cylindrical filter* electrons travel in the field between two concentric cylindrical segments. The electric field strength  $E(R)$  between the two segments with curvature radii of  $R_{\text{inner}}$  and  $R_{\text{outer}}$  is given by:

$$E(R) = \frac{\Delta V}{R \cdot \ln\left(\frac{R_{\text{outer}}}{R_{\text{inner}}}\right)} \quad (2-2)$$

The potential difference  $\Delta V$  of the cylindrical segments required for a circular motion of a particle of charge  $q$  depends linearly on its kinetic energy  $E_{\text{kin}}$  and is independent of the radius of the circular motion.

$$\Delta V = \frac{2E_{\text{kin}}}{q} \cdot \ln\left(\frac{R_{\text{outer}}}{R_{\text{inner}}}\right) \quad (2-3)$$

It has been shown by Hughes and Rojansky (1929) that at 127°17' the analyzer focuses a diverging beam entering through the entrance slit onto the exit slit.

#### 2.1.3. Hemispherical Filter

In the *hemispherical filter* electrons travel in the electric field between two concentric spheres with radius  $R_{\text{inner}}$  and  $R_{\text{outer}}$ .

$$E(R) = \frac{\Delta V \cdot R_{\text{inner}} \cdot R_{\text{outer}}}{(R_{\text{outer}} - R_{\text{inner}}) \cdot R^2} \quad (2-4)$$

In this case the requirement for circular motion leads to a dependency of the electric potential difference  $\Delta V$  on  $R_0$ , the radius of a plane of constant potential.

$$\Delta V = \frac{2E_{\text{kin}}}{q} \cdot \frac{(R_{\text{outer}} - R_{\text{inner}})}{R_{\text{inner}} \cdot R_{\text{outer}}} \cdot R_0 \quad (2-5)$$

Purcell (1938) has shown that for 180° this configuration focuses conically diverging electrons entering the entrance aperture onto the exit aperture.

## 2.2. Trochoidal Electron Spectrometer

The *trochoidal electron spectrometer* (Figure 2-1) uses three trochoidal electron energy filters, one in the monochromator and two in the analyzer. The electrons are collimated by an axial magnetic field  $\vec{B}$ . Free electrons with an energy distribution of approximately 0.5 eV are produced by emission from an electrically heated iridium-thorium filament. They are extracted into the trochoidal monochromator. A nearly monoenergetic beam of electrons emerges from the monochromator and enters the collision chamber, which is filled with the target gas. Forward and inelastically backward scattered electrons enter the analyzer together with the main beam. The first analyzer filter is operated at low resolution, separating the scattered electrons from the unscattered main beam,



while the second analyzer is operated at higher resolution. A continuous dynode multiplier (channeltron) is used to count the electrons exiting the analyzer.

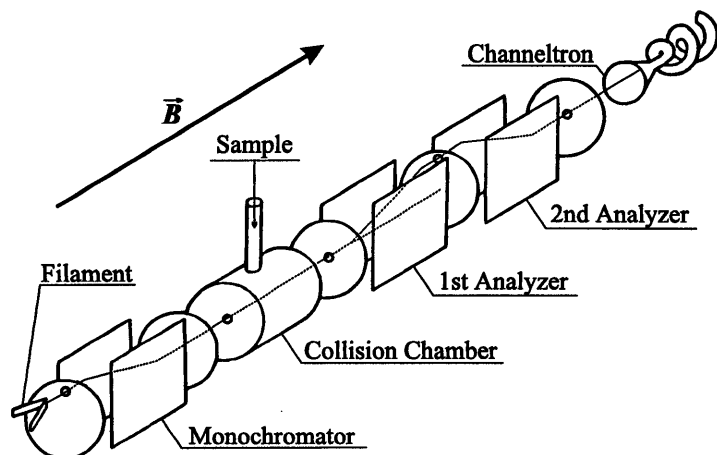


Figure 2-1

Schematic diagram of the trochoidal electron spectrometer (Allan 1989).

The instrument can record three types of spectra: EL and ET spectra, as well as excitation functions. In the ET experiment the analyzer is converted to an electron collector, by short-circuiting all its parts and setting them to a potential of +40V.

In the course of this Ph.D. study the analog control circuitry was replaced by a digital control circuitry, similar to that already installed in the electrostatic electron spectrometer (Allan 1992), dissociative attachment spectrometer (Bulliard 1994) and photoelectron spectrometer (present work). Much time was invested in the upgrade of the acquisition/control program with the aim to make the program more user-friendly and create a single, instrument-independent version. Both the control circuitry and the acquisition/control program are described in the manual of the trochoidal spectrometer (Asmis 1996).

### 2.2.1. Sensitivity in Function of $E_{in}$ and $E_r$

The transmission of the monochromator is not a function of  $E_{in}$ , therefore the sensitivity of the instrument remains constant, when constant  $E_r$  spectra are recorded. On the other hand, the transmission of the analyzer is a function of  $E_r$ , due to the dependence of the acceptance angle of the analyzer on  $E_r$ . In a first approximation the acceptance angle is inversely proportional to the scattered electron energy (Allan 1989). This results in a good angular resolution at high residual energies, while the acceptance half-angle approaches  $90^\circ$  at threshold.

In order to verify this transmission dependency, the distribution of electrons from near-threshold ionization of helium is measured, which was assumed to be uniform. In Chapter 5.1 it will be shown, that the assumption of uniformity in the forward and the backward direction is false. This calibration method is nonetheless applicable to the trochoidal instrument, because it measures a superposition of forward and backward scattered electrons and the summation of forward and backward scattered electrons does yield a uniform distribution, when the collection efficiency for the detection of backward and forward scattered electrons is equal.

### 2.2.2. Energy Scale Calibration

In general  $N_2$  is used as a calibration gas. The residual energy scale is calibrated on the feature peaking at 0.07 eV, seen in the constant incident energy spectrum (corrected for transmission) for an incident energy of 10.00 eV. The signal is due to electrons autodetaching from metastable  $N^*$ , formed by dissociative electron attachment to  $N_2$ . The incident energy scale is calibrated on the peak at an energy-loss of 7.772, seen in the constant  $E_r$  spectrum of  $N_2$  at a residual energy of 30 meV. It is due to the excitation into the  $B^3\Pi_g$  ( $v = 2$ ) state. The incident energy scale can also be calibrated, though with lower accuracy, on the energy transmission feature of  $N_2$  at an incident energy of 1.93 eV ( $^2\Pi$  shape resonance).

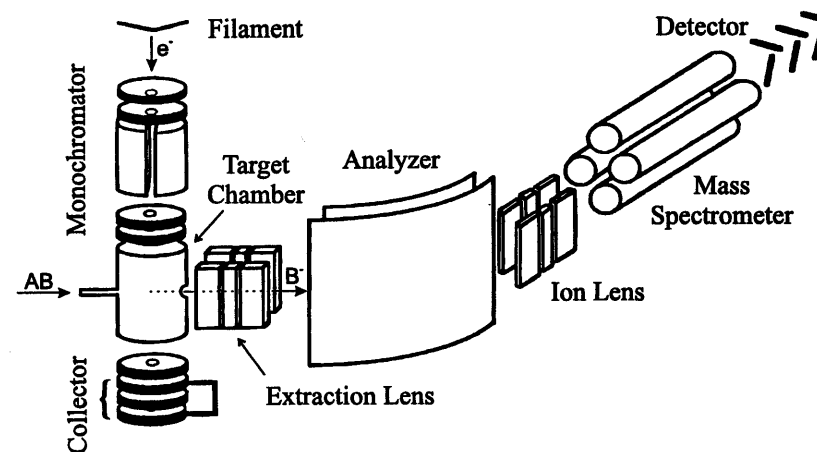


Figure 2-2

Schematic diagram of the dissociative attachment spectrometer (Bulliard 1994).

### 2.3. Dissociative Attachment Spectrometer

Electrons emitted by the hot filament are energy selected in the trochoidal monochromator (Figure 2-2). The nearly monoenergetic beam of electrons interacts with a static gas (AB) in the target chamber. The unscattered beam plus forward and inelastically backward scattered electrons are monitored at the collector. The negative ions formed are extracted perpendicularly to the electron beam by an extraction lens. A 90° cylindrical ion filter energy analyzes the ion beam, which is then focused with the help of a lens arrangement at the mass spectrometer entry. Horizontal and vertical deflectors (not shown) optimally direct the accelerated ions into the mass spectrometer. Mass analyzed ions are detected by a channeltron.

### 2.4. Photoelectron Spectrometer

The modified Turner type (Turner 1968) photoelectron spectrometer (Perkin Elmer model PS16) used in this work is schematically depicted in Figure 2-3.

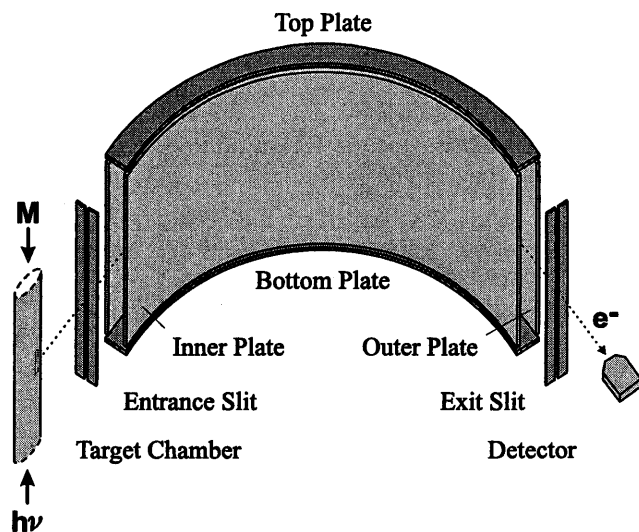


Figure 2-3  
Schematic diagram of the photoelectron spectrometer.

Photons of 21.22 eV energy, emitted by a helium discharge lamp, can ionize the gaseous targets. The photoelectrons, exiting the ionization chamber through a small slit, pass the entrance slit and enter the cylindrical analyzer. The electron

beam is focused in the horizontal (inner and outer plate) and vertical plane (top and bottom plate). Energy selected electrons leave the analyzer *via* the exit slit and are detected by a channeltron.

The resolution of the analyzer is inversely proportional to the pass energy of the photoelectrons in the analyzer. In the normal mode of operation the pass energy is varied during a scan and the photoelectrons pass the analyzer with the original kinetic energy acquired during photoionization. For the chemically interesting ionization energy region the energy resolution is deteriorated, due to the relatively high kinetic energy of around 10 eV. In the retardation mode of operation (Dressler *et al.* 1983) the potential of the entrance slit (preretardation device) is varied and the analyzer is adjusted to the desired low pass energy (1-4 eV), resulting in a constant and high resolution for all energies in the photoelectron spectrum.

### 3. COMPUTATIONAL METHODS

Throughout the course of my Ph.D. study I employed electronic structure calculations in order to help in the interpretation of the experimental data. The methods encompassed the determination of equilibrium geometries, ionization potentials and excitation energies, as well as the characterization of resonances. For the theoretical background on electronic structure theory the reader is referred to the textbooks of Kutzelnigg (1975), Lowe (1978), Szabo and Ostlund (1989) and Yarkony (1995).

Electronic structure calculations on bound states are generally based on the *Rayleigh-Ritz variation principle*. On the other hand, the treatment of resonances is not straightforward by means of a variational calculation, because temporary anions lie in the continuum of the neutral species plus free electron. Consequently, the unfilled orbitals are prone to collapse onto continuum solutions, if flexible basis sets are used. In order to overcome this restriction several types of stabilization methods have been proposed. (Juang and Chao 1994, Chen and Gallup 1990, and references therein).

The most rigorous theoretical treatments of collision cross sections are formulated in terms of scattering theory (Collins and Schneider 1988, Gianturco and Jain 1986, Lane 1980, and references therein). However, accurate potentials for electron-molecule interaction are available for only a few small molecules. In addition, scattering approaches do not exploit our chemical intuition about orbital charge distributions and their implications for the structural and spectroscopic properties of anions. From a computational viewpoint, quantum mechanical scattering calculations are considerably more difficult and demanding than modified bound-state variational approaches.

#### 3.1. The CASSCF/CASPT2 Method

The *ab initio* CASSCF/CASPT2 approach discussed in this section is more difficult to apply than the semi-empirical INDO/S method described in Section 3.2 and definitely can not be used in form of a "black-box". However, it is by far the more accurate method for the calculation of excitation energies, reproducing the (lower) excited valence as well as Rydberg states usually with an accuracy of 0.2 eV or better (Roos *et al.* 1994).

The *complete-active-space self-consistent field* (CASSCF) method (see for example Roos 1987) is one of the most widely used multi-configurational (MC) SCF methods today. In MCSCF methods the molecular wave function  $\Psi$  is written as a linear combination of configuration state functions (CSFs, see the Appendix for the relationship between electron configurations, Slater determinants and CSFs)  $\Phi_i$ :

$$\Psi = \sum_i a_i \Phi_i . \quad (3-1)$$

The MCSCF wave function is then optimized by varying not only the expansion coefficients  $a_i$  (like in a configuration interaction calculation) but also the expansion coefficients  $c_{jr}$  that relate the MOs  $\varphi_j$  to the basis functions  $\chi_r$ .

$$\varphi_j = \sum_r c_{jr} \chi_r \quad (3-2)$$

In CASSCF calculations one divides the MO space into *inactive*, *active* and *external* orbitals. The inactive and active orbitals are occupied in the MCSCF wave function, while the external, *i.e.* virtual, orbitals span the rest of the orbital space. The inactive orbitals are kept doubly occupied in all CSFs. The electrons not in the inactive orbitals are called *active* electrons and form together with the active orbitals the *active space*. The CASSCF wave function is then written as a linear combination of all those CSFs that can be formed by distributing the active electrons among the active orbitals in all possible ways and that have the same spin and symmetry eigenvalues as the state to be treated. The size of the complete CI expansion  $N_{\text{CAS}}$  as a function of  $n$  active orbitals,  $N$  active electrons and a total spin  $S$  is given by the Weyl formula,

$$N_{\text{CAS}} = \frac{2S+1}{n+1} \binom{n+1}{N/2-S} \binom{n+1}{N/2+S+1} . \quad (3-3)$$

Obviously  $N_{\text{CAS}}$  increases rapidly as a function of the number of active orbitals  $n$  and the current computational limit is normally reached for  $n$  around 12-15 orbitals, except for cases with only a few active electrons or holes.

The choice of active orbitals for the CASSCF wave function is the crucial step in the calculation. The active orbitals must encompass all orbitals which have an occupation number appreciably different from zero or two in any of the electronic states of a given symmetry, which is to be included in the calculation. Thus the number of active orbitals will depend on the energy range to be covered by the calculation. It is possible to use a different set of active orbitals for states of different symmetry. Apart from describing the excitation process, the active orbitals must cover the near-degeneracy effects. For example, the active space should include all valence  $\pi$ -orbitals in conjugated systems if possible.

CASSCF results will not by themselves yield very accurate excitation energies. Dynamical correlation effects are often different for different excited states, and if they are not accounted for, errors as large as 1 to 2 eV can easily occur. CASPT2 (Andersson and Roos 1994) makes use of *second order perturbation theory* (PT2) and computes the first order wave function and the second order energy in the full space of CSFs generated by the MO basis. Thus

the contributions from inactive electron pairs to the correlation energy are computed. A good measure of the reliability of the CASPT2 result is given by the weight  $\omega$  of the CASSCF reference function in the zero plus first order wave function. An approximate estimate for  $\omega$  is obtained from the formula:

$$\omega = (1 + \alpha)^{-N/2} \quad (3-4)$$

where  $N$  is the number of electrons and  $\alpha$  is a constant in the range 0.01-0.02. If  $\omega$  comes out considerably smaller than the above estimate then the calculation has to be reconsidered, because second order perturbation theory is only a valid approximation in cases where the perturbation is small.

No theory has been developed to perform calculations on transition moments at the same level of accuracy as is used for the energies. Thus the transition densities and the corresponding oscillator strengths are computed with the CAS state interaction (CASSI) method (Malmqvist and Roos 1989) using the CASSCF wave function and the CASPT2 energies.

### 3.2. The INDO/S method

The *INDO/S* method was the method of choice for the calculation of excitation energies at the beginning of my Ph.D. study. It is a semi-empirical method and is simple to use. INDO/S like most other semi-empirical methods makes use of minimal basis sets (basis restricted to AO's that are occupied in the separated-atom limit ground state) and thus cannot treat Rydberg states and the configuration mixing between valence and Rydberg configurations appropriately. While results of INDO/S calculations are in general not more exact than  $\pm 1$  eV for the lowest excited valence states, it is computationally less demanding and can thus be applied to larger polyatomic molecules than *ab initio* methods of comparable accuracy.

The *intermediate neglect of differential overlap* (INDO) method was proposed by Pople *et al.* (1967) and is an improvement on *the complete neglect of differential overlap* (CNDO) method (Pople and Segal 1965). Both methods treat only the valence electrons explicitly. They are self-consistent-field methods that iteratively solve the Roothaan equations (Roothaan 1951) using different approximations for the integrals.

The CNDO method uses the *zero differential overlap* (ZDO, eq. 3-5) approximation for all pairs of *atomic orbitals* (AOs). The differential overlap  $dS$  between two AOs  $\chi_r$  and  $\chi_s$  is the product of these functions in the differential volume element  $dv$ .

$$dS = \chi_r(1)\chi_s(1)dv = 0, \quad \text{for } r \neq s \quad (3-5)$$

Note that the statement  $\chi_r$  and  $\chi_s$  for  $r \neq s$  have ZDO is much stronger than the statement that they are orthogonal. The attractive feature of the ZDO approximation is that it causes many electron-repulsion integrals, in particular all non-Coulomb integrals, to vanish:

$$(rs|tu) = \delta_{rs}\delta_{tu}(rr|tt) \quad \text{with } \delta_{ab} = \begin{cases} 0 & \text{for } a \neq b \\ 1 & \text{for } a = b \end{cases} \quad (3-6)$$

The quantity  $\delta_{ab}$  is called the Kronecker delta function, a convenient shorthand. The electron repulsion integrals of the type  $(rr|tt)$  are treated as empirical parameters, rather than being evaluated theoretically. In the INDO method fewer two-electron integrals are neglected, in particular the differential overlap between AOs on the same atom is not neglected in one-center electron-repulsion integrals, but is still neglected in two-center electron-repulsion integrals.

#### 3.2.1. Excitation Energies of Bound States

Versions of INDO parametrized to predict electronic spectra are called INDO/S. The ground state of a closed-shell molecule is generally well represented by a single-determinant wave function, but one typically requires *configuration interaction* (CI) for the appropriate representation of excited states. The present study makes use of the INDO/S method implemented in the ZINDO package (Bacon and Zerner 1979, Edwards and Zerner 1987).

The INDO/S parameters of ZINDO were optimized for CI calculations including only single excitations. Different parameters exist for singlet and triplet excited states. The INDO/S calculations were, if not otherwise noted, performed at the INDO/1 optimized geometry.

#### 3.2.2. Resonances

Many previous attempts by modified bound-state variational methods to characterize resonances of polyatomic molecules have been restricted to description of 1p shape resonances. With respect to 2p-1h resonances I attempted several approaches, in particular stabilization calculations of the type proposed by Nestmann and Peyerimhoff (1985), where the eigenvalues and eigenfunctions are determined as a function of a scaling parameter.

Resonance states can be viewed as arising from coupling between the discrete states and the continuum. In a diabatic picture stabilization calculations give rise to both localized bound-state-like anion and discretized continuum solutions. The energies of the diabatic bound-state-like anion are relatively insensitive to variation of the scaling parameter, while the energies of the discretized continuum solutions vary much more rapidly with the relevant scaling parameter.

All of the attempts failed in the application to 2p-1h resonances, in part because these states lie higher in energy than 1p resonances, in a region where many bound-state-like as well as discretized continuum solutions lie, making the interpretation of the dependency between the scaling parameter and a single bound-state-like solution complicated.

Finally the simplest variant of a stabilization calculation was used. Semiempirical INDO/S calculations were performed on the anion states of interest. The use of a minimal basis, inherent to standard semi-empirical methods, ensured that the additional electron stayed close to the molecule, thus neglecting any noticeable coupling with the continuum. At the same time the diffuseness of anionic states and dynamical correlation effects are ignored and the resulting description of the resonance is deteriorated. Although the results can be at most of qualitative nature, I still expect to qualitatively correctly reproduce the essential physics of the problem, in particular the observed branching ratios for the decay of the resonances into the various states of the neutral.

### 3.2.3. Concept of the Parent State

Useful in the characterization of the electronic structure of resonances is the concept of the parent (electronic) state (see for example Hall and Read 1984, and Allan 1989). The parent state of a resonance is that state of the neutral, which is obtained by formal removal of the captured electron, *i.e.* the parent state of a 1p resonance is the electronic ground state (of the neutral) and that of a 2p-1h resonance an electronically excited state. It is often found that the decay of a resonance into its parent state is the preferred decay channel, if it is energetically accessible.

An example for the advantages and also disadvantages of this concept is the interpretation of the two  $\pi^*$  resonances observed in ethylene (Allan 1994). The 1p  $\pi^*$  resonance, formed by electron capture in the  $\pi^*$  orbital, decays preferably into the (vibrationally excited) electronic ground state of neutral and to a lesser degree into the  $\pi \rightarrow \pi^*$  excited triplet state. The 2p-1h  $\pi^*$  resonance, described by a singly occupied  $\pi$  orbital and a doubly occupied  $\pi^*$  orbital, predominantly decays into the  $\pi \rightarrow \pi^*$  excited triplet state. Thus both resonances decay preferably into their parent state. In contrast, the formation of the triplet state (slightly above threshold) by the 1p  $\pi^*$  resonance cannot be understood in the frame of this concept. Also note that the parent state concept in this form is only applicable to systems, where the states or resonances of interest can be described appropriately by a single electron configuration, as is the case for ethylene.

For the further discussion of resonances it will prove useful to extend the original concept of the parent state in two ways. (i) The definition of the parent state will not be restricted to the removal of the *captured* electron, but any electron. This extension allows for the rationalization of the formation of the  $\pi$

$\rightarrow \pi^*$  excited triplet state by the 1p  $\pi^*$  resonance in ethylene. This triplet state is now also a parent state of the 1p  $\pi^*$  resonance, generated by the removal of an electron from the doubly occupied  $\pi$  orbital, and thus a possible "candidate" for a preferred decay channel. (ii) A measure for the "percentage of parentage", called the *decay factor*  $d$ , is introduced to treat systems, where configuration interaction (CI) is important, *e.g.* butadiene and the cyclic dienes discussed in Sections 5.4 and 5.5. The decay factor  $d$  is defined in the following section. It is used in combination with energy and lifetime considerations to explain qualitatively the observed branching ratios in the decay of resonances.

### 3.2.4. Definition of the Decay Factor

The decay factor  $d$  is determined on the basis of a comparison of the CI wave functions. CI calculations are performed for the neutral and anion states of interest. The CI wave functions have the following form:

$$\Psi_i^{\text{neutral}} = \sum_j a_{ij}^{\text{neutral}} \Phi_j^{\text{neutral}} \quad \Psi_q^{\text{anion}} = \sum_r a_{qr}^{\text{anion}} \Phi_r^{\text{anion}} \quad (3-7)$$

Here  $\Phi$  represents an element, *i.e.* configuration state function (CSF), of the orthonormal CI space and is either a single Slater determinant or a linear combination of Slater determinants. The  $a$ 's refer to the CI coefficients.

Now we define the *decay operator*  $\mathbf{D}$ . It has the effect of removing an electron from  $\Phi^{\text{anion}}$  and generating all possible corresponding  $\Phi^{\text{neutral}}$ :

$$\mathbf{D}\Phi_r^{\text{anion}} = \sum_k b_{rk}^{\text{decay}} \Phi_k^{\text{neutral}} \quad (3-8)$$

Here the index  $k$  runs over all possible  $\Phi_k^{\text{neutral}}$ , with

$$b_{rk}^{\text{decay}} = 1 \quad (3-9)$$

if  $\Phi_k^{\text{neutral}}$  can be generated from  $\Phi_r^{\text{anion}}$  and

$$b_{rk}^{\text{decay}} = 0 \quad (3-10)$$

if not. The possible results of the application of  $\mathbf{D}$  are summarized in Table 3-1. Two general cases are considered. In the case of a single unpaired electron three Slater determinants of the neutral can be generated. The third is not an eigenfunction of the  $\mathbf{S}^2$  operator, but appears both in the triplet and singlet expression, and thus both states are generated. In the case of three unpaired electrons the expression can always be transformed in such a way, that of the two CI coefficients one is associated with the triplet and the other with the singlet state of interest (see Appendix).

**Table 3-1**  
Generation table for the decay operator  $D$ .

${}^2\Phi_{ab}^{\text{anion}}$	${}^2\Phi_{ab}^{\text{anion-1}}$	$D({}^2\Phi_{ab}^{\text{anion}})$
$ \lambda_a \bar{\lambda}_a \lambda_b $	$ \lambda_a \bar{\lambda}_a   \lambda_a \lambda_b   \bar{\lambda}_a \lambda_b $	${}^1\Phi_{aa}^{\text{neutral}}$ ${}^3\Phi_{ab}^{\text{neutral}}$ ${}^1\Phi_{ab}^{\text{neutral}}$
${}^2\Phi_{abc}^{\text{anion}}$	${}^2\Phi_{abc}^{\text{anion-1}}$	$D({}^2\Phi_{abc}^{\text{anion}})$
$2 \lambda_a \lambda_b \bar{\lambda}_c  -  \lambda_a \bar{\lambda}_b \lambda_c  -  \bar{\lambda}_a \lambda_b \lambda_c $	$2 \lambda_a \lambda_b  - ( \lambda_a \bar{\lambda}_b  +  \bar{\lambda}_a \lambda_b )$	${}^3\Phi_{ab}^{\text{neutral}}$
$ \lambda_a \bar{\lambda}_b \lambda_c  -  \bar{\lambda}_a \lambda_b \lambda_c $	$ \lambda_a \bar{\lambda}_b  -  \bar{\lambda}_a \lambda_b $	${}^1\Phi_{ab}^{\text{neutral}}$
$2 \lambda_a \bar{\lambda}_b \lambda_c  -  \lambda_a \lambda_b \bar{\lambda}_c  -  \bar{\lambda}_a \lambda_b \lambda_c $	$2 \lambda_a \lambda_c  - ( \lambda_a \bar{\lambda}_c  +  \bar{\lambda}_a \lambda_c )$	${}^3\Phi_{ac}^{\text{neutral}}$
$ \lambda_a \lambda_b \bar{\lambda}_c  -  \bar{\lambda}_a \lambda_b \lambda_c $	$ \lambda_a \bar{\lambda}_c  -  \bar{\lambda}_a \lambda_c $	${}^1\Phi_{ac}^{\text{neutral}}$
$2 \bar{\lambda}_a \lambda_b \lambda_c  -  \lambda_a \lambda_b \bar{\lambda}_c  -  \lambda_a \bar{\lambda}_b \lambda_c $	$2 \lambda_b \lambda_c  - ( \lambda_b \bar{\lambda}_c  +  \bar{\lambda}_b \lambda_c )$	${}^3\Phi_{bc}^{\text{neutral}}$
$ \lambda_a \lambda_b \bar{\lambda}_c  -  \lambda_a \bar{\lambda}_b \lambda_c $	$ \lambda_b \bar{\lambda}_c  -  \bar{\lambda}_b \lambda_c $	${}^1\Phi_{bc}^{\text{neutral}}$

If a different set of MOs is used for the CI calculation on the neutral and the anion, then it is assumed that these MO sets are similar enough, such that  $D$  can assign unequivocally each orbital of the anion ( $\lambda$ ) to the corresponding orbital of the neutral ( $\lambda'$ ).

$$D[\Phi_r^{\text{anion}}(\lambda)] = \sum_k [b_{rk}^{\text{decay}} \Phi_k^{\text{neutral}}(\lambda')] \quad (3-11)$$

The decay factor  $d_{iq}$  between the  $q^{\text{th}}$  state of the anion and the  $i^{\text{th}}$  state of the neutral is then defined as follows:

$$d_{iq} = \langle \Psi_i^{\text{neutral}} | D | \Psi_q^{\text{anion}} \rangle \quad (3-12)$$

$$= \left\langle \sum_j a_{ij}^{\text{neutral}} \Phi_j^{\text{neutral}} \middle| D \middle| \sum_r a_{qr}^{\text{anion}} \Phi_r^{\text{anion}} \right\rangle \quad (3-13)$$

$$= \sum_j \sum_r a_{ij}^{\text{neutral}} a_{qr}^{\text{anion}} \langle \Phi_j^{\text{neutral}} | D | \Phi_r^{\text{anion}} \rangle \quad (3-14)$$

$$= \sum_j \sum_r a_{ij}^{\text{neutral}} a_{qr}^{\text{anion}} \left\langle \Phi_j^{\text{neutral}} \middle| \sum_k b_{rk}^{\text{decay}} \Phi_k^{\text{neutral}} \right\rangle \quad (3-15)$$

$$= \sum_j \sum_r \sum_k a_{ij}^{\text{neutral}} a_{qr}^{\text{anion}} b_{rk}^{\text{decay}} \langle \Phi_j^{\text{neutral}} | \Phi_k^{\text{neutral}} \rangle \quad (3-16)$$

$$= \sum_j \sum_r \sum_k a_{ij}^{\text{neutral}} a_{qr}^{\text{anion}} b_{rk}^{\text{decay}} \delta_{jk} \quad (3-17)$$

$$= \sum_k \sum_r a_{ik}^{\text{neutral}} a_{qr}^{\text{anion}} b_{rk}^{\text{decay}} \quad (3-18)$$

Thus  $d_{iq}$  is determined by forming the double sum over those products of the CI coefficients  $a_{ik}^{\text{neutral}}$  and  $a_{qr}^{\text{anion}}$  for which  $b_{rk}^{\text{decay}} = 1$ , i.e. those CSFs of the neutral which can be generated from the CSFs of the anion wave function by the removal of a single electron.  $d_{iq}$  can take values between 0 and 1. The higher the value of the decay factor  $d_{iq}$ , the higher is the parent state character of the neutral state  $i$  with respect to the anion state  $q$ . In combination with a favorable resonance lifetime and energy a high parent state character is assumed to indicate a preferred decay channel.

Practically, INDO/S calculations are performed on the neutral and anionic states of interest. The neutral states of interest in our cases are adequately, in the ability of the INDO/S method, described by CI calculation including all single excitation. The characterization of 2p-1h resonances requires at least the inclusion of double excitations. From the optimized wave functions decay factors  $d_{iq}$  are determined using eq. 3-18.

### 3.3. Method of Scaled Virtual Orbital Energies

Chen and Gallup (1990) have proposed the following parametrization of a linear scaling equation for the determination of *electron attachment energies* (AEs) from virtual orbital energies  $\epsilon_{\text{HF}}$  obtained from a HF-SCF calculation on the neutral species, employing a 6-31G basis set (at the HF/6-31G optimized geometry):

$$\text{AE} = \frac{\epsilon_{\text{HF}} - 2.33 \text{ eV}}{1.31} \quad (3-19)$$

Equation 3-19 is based on an extension of Koopmans' theorem (Koopmans 1934), which states that the canonical orbital energy  $\epsilon_{\text{HF}}$  of an occupied orbital multiplied by -1 is a good approximation for the appropriate *ionization potential* IP.

$$IP = -\epsilon_{HF} \quad (3-20)$$

Koopmans' theorem has been extended to treat anions, by relating the canonical orbital energy of an unoccupied orbital with the appropriate attachment energy.

$$AE = \epsilon_{HF} \quad (3-21)$$

Two points make the application of Koopmans' theorem to the determination of AEs problematic: (i) Flexible basis sets are required in order to model the longer range intramolecular interactions found in diffuse negative ion states. However, it is well known that, as the basis set is expanded, virtual orbital energies tend to collapse toward zero, so that the virtual orbital ultimately describes an unbound electron in the (orthogonalized discrete) continuum. As a result scaling methods are limited to medium-sized basis sets, e.g. of 6-31G quality. (ii) Two approximations are inherent in Koopmans' theorem, the neglect of electron reorganization and of electron correlation. These effects tend to cancel in the prediction of IPs while they are believed to operate in the same direction in the calculation of AEs. Thus AEs calculated from eq. 3-21 are in general too large and scaling parameters are introduced to overcome this discrepancy.

The HF-SCF calculations were performed with the GAUSSIAN 94 program package (Frisch *et al.* 1995). Schematic diagrams of the optimized orbitals were drawn with the program MOPLOT (Schmelzer and Haselbach 1971).

## 4. DEVELOPMENT OF AN INSTRUMENT FOR INELASTIC DIFFERENTIAL CROSS SECTION MEASUREMENTS AT 0° AND 180°

### 4.1. Introduction

The knowledge of electron-atom and electron-molecule collision cross sections is necessary for the understanding of any system, in which such collisions are of importance, e.g. plasmas as they occur in discharge devices, the atmosphere or interstellar space. Many of the ionic species present in plasmas are short-lived and thus not available in quantities, which are required (at present) for the experimental determination of the cross sections of interest. In order to model such systems adequately it is thus necessary to be able to rely on theory.

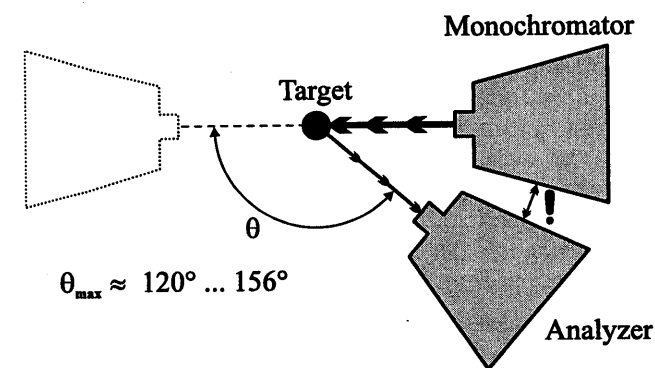


**Figure 4-1**  
Schematic diagram of electrostatic electron spectrometers which are most commonly used for DCS measurements. Mechanical constraints on the analyzer position restrict the measurement of DCS to scattering angles up to  $\theta_{max}$ .

Absolute differential cross section (DCS) measurements are generally performed with an electrostatic electron spectrometer. Although the performance of these electron spectrometers has been improved considerably in the last years, it was not possible until recently, to measure electrons scattered (inelastically on gaseous targets) into large scattering angles. This was due to mechanical constraints inherent to electrostatic electron spectrometers, in which the finite size of the monochromator restricts the movement of the analyzer

(Figure 4-1). The largest attainable angle was between 120° and 156° (136° for the instrument in Fribourg).

In order to determine integral cross sections or to test calculated cross sections predicted by theory in the full scattering angle range it was thus necessary to extrapolate to 180°. It is for example shown in Chapter 5.1 and 5.2 that the angular dependence of DCS can change considerably at high scattering angles and consequently standard extrapolation schemes can introduce a significant error. Furthermore the expenditure of scattering calculations is not independent of the scattering angle and often the higher scattering angles are computationally more demanding and consequently more susceptible to inaccuracies.

In order to overcome these shortcomings an instrument was constructed, which can measure DCSs at 180° and 0° and DCSs ratios for 0° and 180°. Absolute DCSs at 180° can thus be determined in combination with the electrostatic electron spectrometer available in Fribourg (Allan 1995). The development, construction and performance of the novel instrument are described in the following sections of this chapter.

## 4.2. Historical Perspective

The first successful attempt to measure *elastic* 180° DCS in the gas phase was accomplished by Burrow and Sanche (1972). They employed a modified trochoidal electron spectrometer. This technique cannot, however, be readily extended to measure inelastic cross sections. Herzl *et al.* (1981) introduced a technique to study elastic backscattering from surfaces. Cloutier and Sanche (1989) improved the experiment of Burrow and Sanche in order to study inelastic backscattering from surfaces. Their instrument was limited to the study of backscattered electrons from surfaces and energy losses of up to 1 eV.

The results of preliminary experiments with a pulsed incident beam by Allan (1989) demonstrated that the trochoidal electron spectrometer in Fribourg collects efficiently both inelastically forward and backward scattered electrons (Figure 4-2). The determination of DCSs was not possible at the time, due to insufficient separation in arrival times of the forward and backward scattered electrons and limitation to very low residual energies. The current instrument is an enhancement of the old version, including an additional device, which delays the arrival of the backward scattered electrons with respect to the forward scattered ones.

At the time when the results were first presented by us (Asmis and Allan 1995) it was to the best of our knowledge the first measurement of inelastic DCS at 180° in the gas phase. Just recently a different approach has been presented using a novel scheme of electron deflection by a magnetic field in an

instrument equipped with hemispherical analyzers (Zubek *et al.* 1996, Read and Channing 1996).

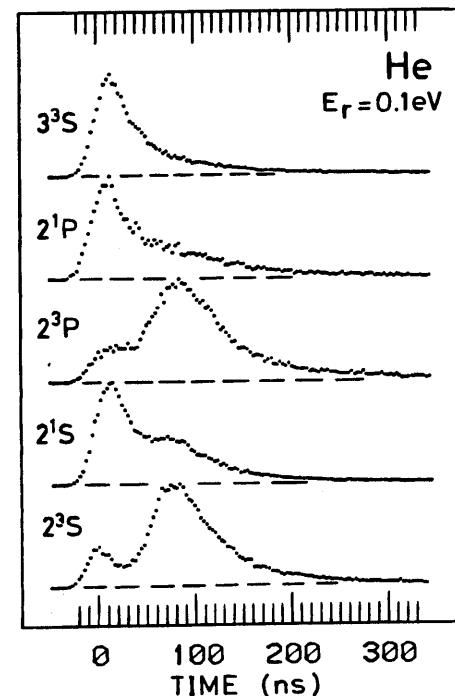


Figure 4-2

Spectra of arrival times of inelastically scattered electrons ( $E_r = 0.1$  eV) after exciting the four lowest excited states in helium (Allan 1989). The first group are the forward scattered electrons. The delayed group are the backward scattered electrons, which have been reflected at the monochromator entrance. The spectra show a mean separation in arrival time of forward from backward scattered electrons of ca. 70 ns.

## 4.3. Principle of Operation

Electrons scattered into 0° and 180° are separated experimentally using the difference in their arrival time at the detector, given by the longer flight path of the backward scattered electrons (Figure 4-3). To this end the incident beam is pulsed, using the electrode M2 as a beam chopper, and scattered electrons are detected as a function of their arrival time with standard delayed coincidence techniques.



The large scatter in the arrival times, depending on whether the electrons are scattered in the beginning or towards the end of the collision chamber, causes the arrival time distributions to overlap (Figure 4-2). Clean separation of the forward from the backward scattered electrons is achieved by introducing a delay line, whose potential is chosen such that the backward scattered electrons traverse it very slowly, *e.g.* 100 meV, postponing their arrival in the detector.

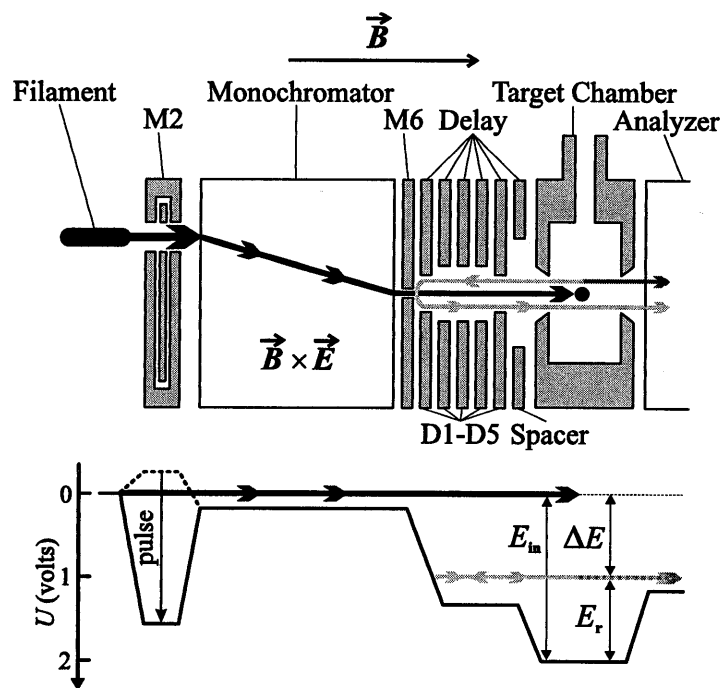


Figure 4-3

Schematic diagram of the magnetically focused trochoidal electron spectrometer (top) and potential diagram (bottom). The nearly monoenergetic electrons emerging from the monochromator are accelerated (decelerated) to the desired incident energy  $E_{in}$  at which they enter the target chamber. Electrons scattered into  $0^\circ$  exit the target chamber with a residual energy  $E_r$ , are decelerated (accelerated) and enter the analyzer at a low and fixed energy suitable for the operation of the analyzer. Electrons scattered into  $180^\circ$  exit the target chamber in the opposite direction. Due to the energy  $\Delta E$  lost during the scattering process, their energy is insufficient to reenter the monochromator and thus they are reflected by the potential barrier at the monochromator exit, reenter the target chamber and finally enter the analyzer just as the forward scattered electrons did. (Not all electrodes of the instrument are shown.)

#### 4.4. Development

The instrument without delay line was characterized by a separation in arrival times of 70 ns for electrons with an energy of 100 meV, about 60 ns too short for clean separation of the electrons scattered into opposite directions. The following considerations influenced the first design of the delay:

- The shortest possible delay line length should be chosen in order to minimize problems due to the alignment of the magnetic field and its non-uniform character especially towards the ends of the instrument.
- Assuming a pass energy of 100 meV for the delay line and considering only the flight path inside the delay line, a delay line length of 12 mm would result in the desired mean arrival time separation of 130 ns.
- The aperture diameter of the delay line electrodes should be large enough to avoid scattering of the electron beam on the electrode edges and small enough to exclusively define the electric potential in the area of the electron beam inside the delay line.
- Efficient pumping of the delay line should be guaranteed.

On the basis of these considerations a delay line was constructed, consisting of five 1 mm thick circular molybdenum plates (Table 4-1), kept in alignment by precision metal balls. This device was introduced between the monochromator exit plate M6 and the target chamber spacer plate (Figure 4-3).

Table 4-1  
Electrode aperture diameters (see Figure 4-3)

electrodes	aperture diameter (mm)
delay line end plates D1 & D5	1.0
delay line inner plates D2 - D4	4.0
monochromator exit M6	0.6
spacer	8.5

First attempts to measure with this device were promising. The desired separation was achieved, but severe "focusing" and background problems were encountered at high incident energies. As electron trajectory simulations showed (Figure 4-4), these were probably the result of the electron lens properties of the region where the electrons are accelerated.

In the original setup (Figure 4-4a) the electrons were accelerated in-between the monochromator exit electrode M6 and the neighboring delay line end plate electrode D1. Due to the severe inhomogeneity of the electric field in this area the beam may be dispersed, causing an increase of the Larmor radius

of the trochoidal electron motion. Electrons spiraling with a Larmor radius larger than the plate's aperture can collide with the plate, resulting in a strong dependence of the electron signal as a function of the delay line pass energy and a background.

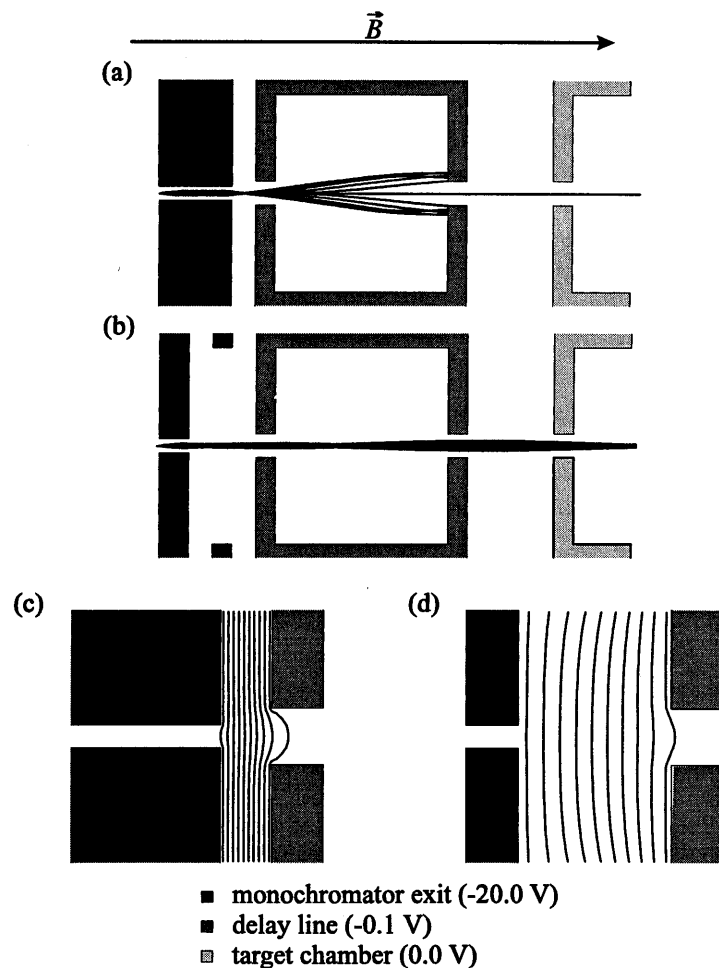


Figure 4-4

Results of a trajectory (a,b) and potential energy(c,d) simulation for first (a,c) and final (b,d) design of the delay line. The magnetic field is 5 Gauss. The electrons were launched at angles of +8, 0 and -8° at 4 evenly spaced points, located in the monochromator exit on the axis of symmetry. The potential energy contour plots show a magnified portion of the monochromator exit / delay line area. The lines represent equipotential surfaces from -19V to -1V with a spacing of 2V.

In the final design (Figure 4-4b) the acceleration region was lengthened by exchanging the first two plates of the delay line (D1 and D2). D2 was electrically isolated from the delay line and short-circuited with the monochromator exit plate M6. Based on the results of the simulation, this arrangement affects the Larmor radius much less. Inspecting the equipotential line diagram (Figure 4-4c,d), we can see that this is due to the higher homogeneity of the electric field in the acceleration region. The final design did no longer cause the problems described in the preceding paragraph.

### 4.5. Experimental Setup

A negative potential sufficient to prevent any electrons from passing the electrode is applied to the inner electrode of M2 (Figure 4-3). The incident beam is then pulsed with 24 ns pulse width and 2 MHz repetition frequency. The arrival times are measured with a time-to-amplitude converter (TAC, range: 400 ns). The TAC is triggered by the detector signal and stopped by the output pulse of the wave generator, which is delay by 750 ns relative to the trigger. The TAC output signal is fed into a discriminator and counted in one of the 511 channels of a multi-channel analyzer (MCA) operated in pulse-height analysis mode. Two modes of operation are possible:

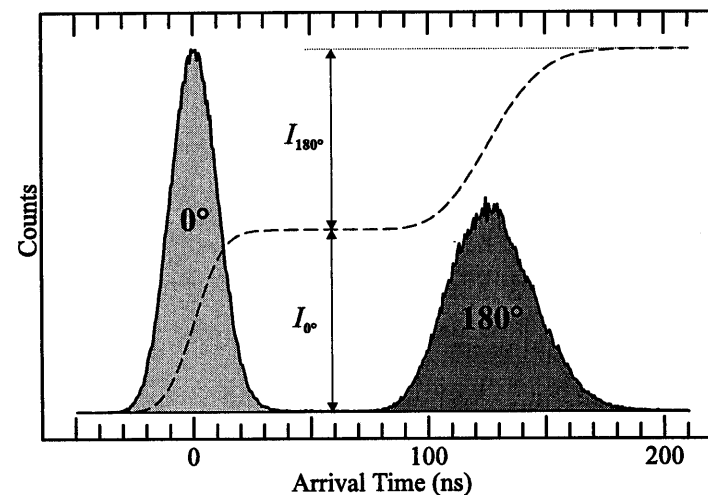


Figure 4-5

Representative arrival time distribution spectrum. The backward scattered electrons (dark gray area) arrive at the detector on average 130 ns later than the forward scattered electrons (light gray area). The right band is wider than the left one, because of the spread of residual energies.

- (a) *discriminator mode*: The discriminator is set to a desired pulse-height range and all electrons arriving in the selected time range are counted. Usually either forward or backward scattered electrons are selected and the relative DCS at 0° or 180° is measured in function of the electron energy.
- (b) *arrival time distribution mode*: The incident and residual energy are kept fix and the electrons are counted as a function of their arrival time in the detector. The quotient of the integrals  $I$  over the arrival time will be called the DCS ratio (see Figure 4-5).

$$\text{DCS ratio} = \frac{I_{180^\circ}}{I_{0^\circ}} \quad (4-1)$$

## 4.6. Calibration

The efficiencies with which the instrument detects electrons scattered in the forward and backward directions are not necessarily equal, but depend strongly on the alignment of the magnetic field. To correct for this, a collection efficiency ratio will be defined.

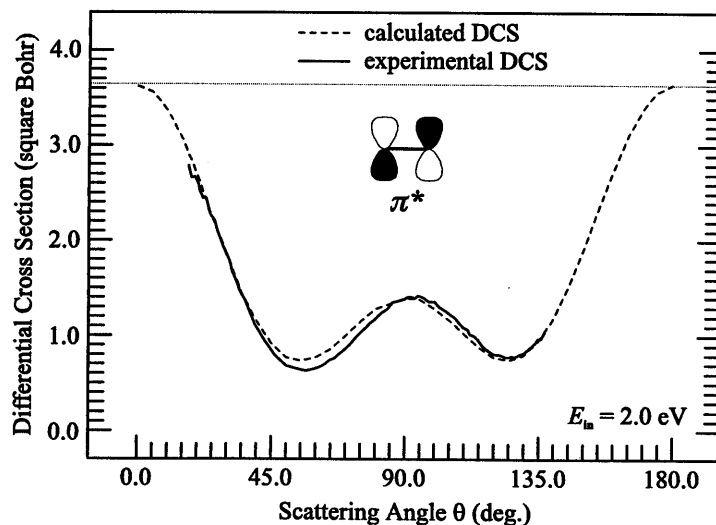


**Figure 4-6**  
Dependence of the absolute DCS of the  $X^1\Sigma_g^+$  ( $v=1 \leftarrow v=0$ ) transition in  $N_2$  on the scattering angle at an incident energy of 2.0 eV. Experimental data (Allan 1994b), as well as *ab initio* calculations (Morrison 1994) demonstrate the symmetric angular behavior of the DCS (within experimental error) and validate the assumption of unity DCS ratio.

A scattering process, whose probabilities to scatter electrons in the forward and backward direction are equal, yields a DCS ratio of unity. We shall call the reciprocal of the measured DCS ratio for this process, which will deviate from unity, the *collection efficiency ratio*. All the following DCS ratio measurements can then be corrected, by multiplication with the collection efficiency ratio. It will be shown that by careful adjustment of the instrument a collection efficiency ratio of close to unity can be achieved (see Figure 4-7). This is desirable, because a collection efficiency ratio far from unity indicates in general severe “focusing” problems.

Resonant excitation of molecular nitrogen represents a suitable process for this calibration (Figure 4-6). The efficient vibrational excitation of  $N_2$  by electron impact in the 2 eV region is dominated by the  $^2\Pi_g$  shape resonance, which can be pictured as the temporary capture of the incident electron into the lowest unoccupied orbital. Since no other mechanism contributes considerably to this process, the angular distribution may be safely assumed to be given by a simple  $d_\pi$  wave (lowest partial wave in the  $\pi_g$  symmetry) and be symmetric around 90° (see for example Grimm-Bosbach *et al.* 1995).

With the first version of the instrument the calibration procedure consisted of measuring the 0° and 180° excitation functions of a vibrational excitation process. The average collection efficiency ratio was then determined by integrating the two spectra and calculating the quotient of the integrals. This was a rather time consuming procedure, but necessary, because of the “focusing” problem. After the redesign of the delay line, “focusing” was much less of a problem and a simpler procedure was adopted, based on single point measurements.

The procedure consists of measuring arrival time distributions for the excitation of  $N_2$  into five different vibrationally excited states at incident energies, where the DCS reaches a maximum (Table 4-2). The collection efficiency ratio was then determined by averaging over the measured DCS ratios. This procedure was repeated before and after the acquisition of a spectrum.

**Table 4-2**  
calibration values

$v$	$\Delta E$ (eV)	$E_{in}$ (eV)
3	0.86	1.28
4	1.13	1.06
5	1.41	0.97
6	1.68	0.77
7	1.95	0.65

## 4.7. Performance

The excitation functions shown in Figure 4-7 demonstrate the good performance of the new instrument. The spectra were corrected for the transmission of the analyzer. The instrumental settings were optimized for a collection efficiency ratio close to unity, so that it was unnecessary to correct the spectra for the collection efficiencies.

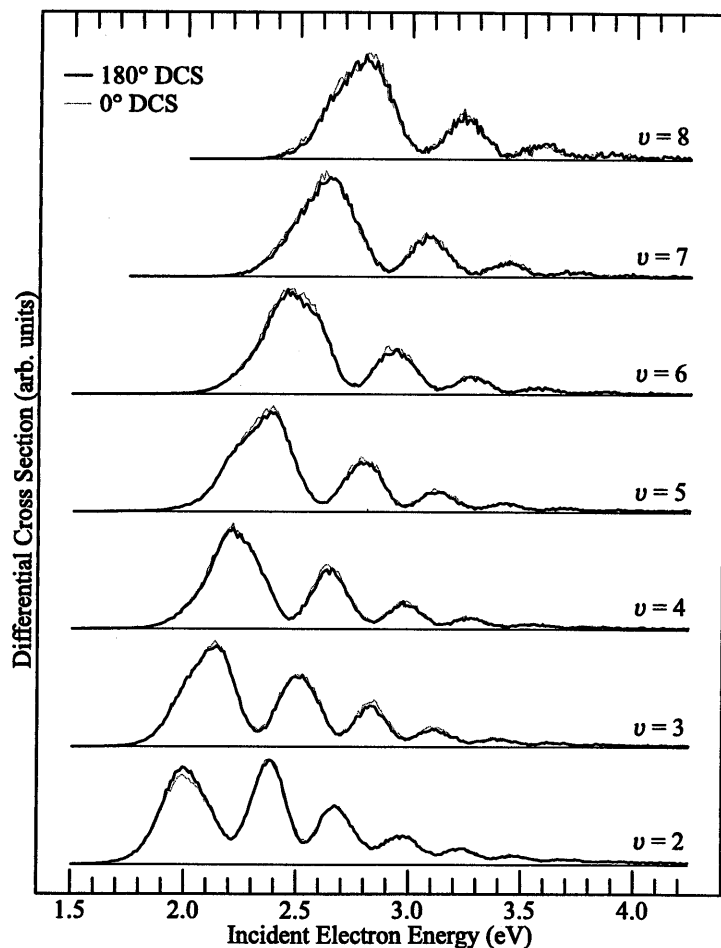


**Figure 4-7**

Vibrational differential cross sections for 0° (broken line) and 180° (solid line) in  $N_2$ , plotted against the same vertical scale for each pair of spectra.

The good overlap of the spectra for forward and backward scattered electrons demonstrates that the collection efficiencies do not vary with electron energy, *i.e.* the absence of any noticeable feature due to focusing. Furthermore all of the spectra displayed were measured in one day, which proves that the instrument is characterized by high signal intensity and good signal to noise ratio.

As for the angular resolution of the instrument and the uncertainty of the measured 180°/0° DCS ratios, the reader is referred to Section 5.1, in which a detailed analysis of these features can be found.

## 5. RESULTS

### 5.1. Electron Impact Excitation of Helium: Measurement of Absolute Differential Cross Sections at $0^\circ$ and $180^\circ$ for Near-Threshold Excitation and Ionization

#### 5.1.1. Introductory Remarks

Numerous theoretical and computational studies have been performed on electron-helium collisions. Because scattering calculations on small atoms are less demanding than on molecules, some of the theoretical data which exists for helium scattering cross sections is among the most accurate available. Consequently, the electron-helium collision system is often used as a testing ground for new methods and theories.

In the course of this project we studied the DCSs of near-threshold excitation and ionization in helium. The results on near-threshold ionization are summarized in section 5.1.2. They are of considerable consequence both theoretically, the problem of two (highly correlated) departing electrons being one of the fundamental problems in atomic physics of current interest, and practically, for the determination of the instrumental response. Generally, this determination has been based on the assumption that the energy distribution of secondary electrons generated by electron impact ionization is uniform slightly above the ionization threshold. Our results indicate that this assumption does not hold for very large and very small scattering angles, *i.e.*  $180^\circ$  and  $0^\circ$ .

In section 5.1.3 an article (submitted for publication) is presented, which describes our recent study on the measurement of absolute differential cross sections (DCSs) for the excitation of the  $n = 2$  states of helium by electron impact spectroscopy. It differs in particular from all previous experimental studies in that it presents for the first time absolute  $180^\circ$  DCSs of these excitation processes. I contributed the  $0^\circ/180^\circ$  DCS ratios as well as the  $0^\circ$  and  $180^\circ$  excitation functions, both measured with the novel instrument developed in the course of the Ph.D. study (see Chapter 4).

The calculation of DCSs at very high and, to a lesser extent, very small scattering angles is in general computationally more demanding than the calculation of DCSs at intermediate scattering angles. Thus our data is of special importance for the testing of modern scattering theories.

#### 5.1.2. Near-Threshold Ionization

The procedure of Pichou *et al.* (1976) is generally used to determine the instrumental response for inelastic scattering as a function of electron energy and scattering angle. It is based on the assumption that the near-threshold ionization continuum of helium provides a standard in the form of a uniform distribution of secondary electrons.

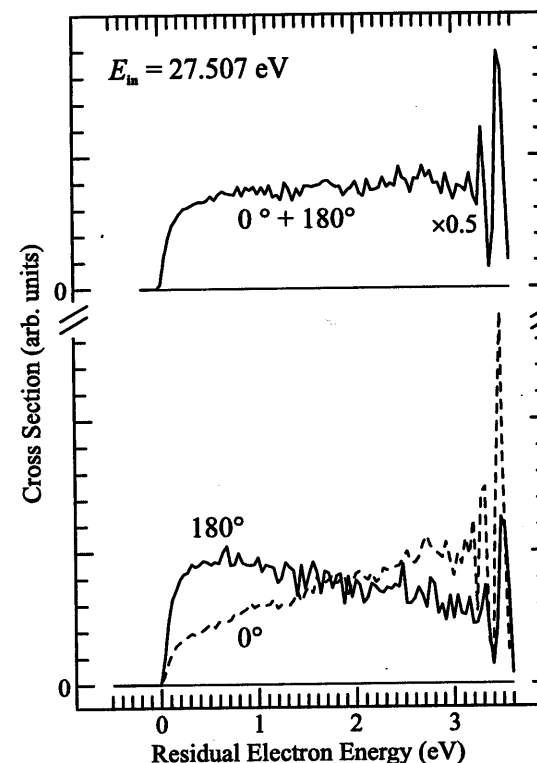
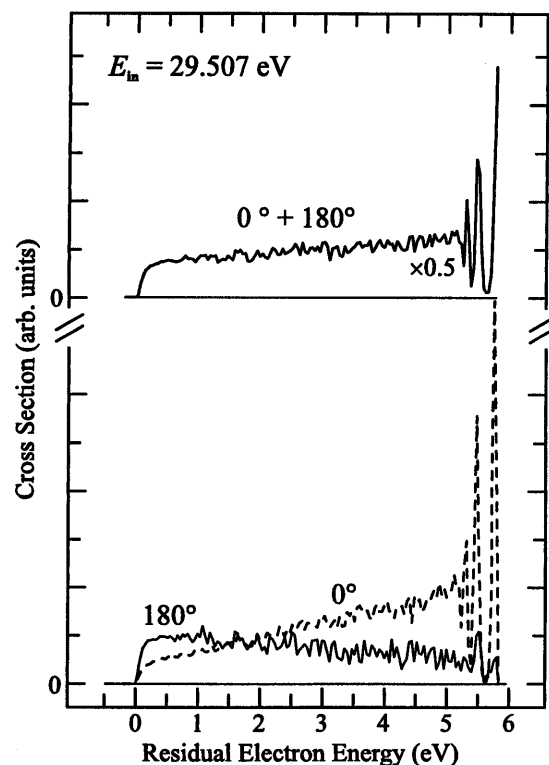


Figure 5.1-1  
EEL spectra of helium measured at a constant incident energy of 27.507 eV and scattering angles of  $0^\circ$  and  $180^\circ$  (bottom). The sum of the  $0^\circ$  and  $180^\circ$  spectra is also shown (top).

EEL spectra measured at  $E_{in} = 27.507$  and  $29.507$  eV (*i.e.* 3 and 5 eV above ionization threshold) and at scattering angles of  $0^\circ$  and  $180^\circ$  are shown in Figures 5.1-1 and 5.1-2. The spectra were corrected for the transmission of the analyzer, assuming it to behave ideally, that is its response falls off as  $1/E_r$ . The  $180^\circ$  spectra reach a maximum slightly above  $E_r = 0$  eV and then drop off in a nearly linear fashion up to the ionization threshold, while the signal in the  $0^\circ$

spectra is weaker slightly above  $E_r = 0$  eV and then increases nearly linearly. The summation of both spectra yields a distribution which is more uniform, especially at 3 eV above the ionization threshold.

Consequently, the procedure of Pichou *et al.* does not provide a suitable standard for the determination of the instrumental response at small and large scattering angles, because the ionization continuum of helium is no longer uniform at these angles. It can still be applied to the trochoidal instrument when measuring in the normal mode of operation, as long as it is ensured that the collection efficiency ratio is close to unity.



**Figure 5.1-2**  
EEL spectra of helium measured at a constant incident energy of 29.507 eV and scattering angles of  $0^\circ$  and  $180^\circ$  (bottom). The sum of the  $0^\circ$  and  $180^\circ$  spectra is also shown (top).

### 5.1.3. Article

#### Measurement of Absolute Differential Cross Sections for the Excitation of the $n = 2$ States of Helium at $0^\circ$ and $180^\circ$

Knut R. Asmis and Michael Allan

Institut de Chimie Physique, Université de Fribourg, Pérolles, CH-1700 Fribourg, Switzerland

#### Abstract.

A novel scheme for the measurement of inelastic differential cross sections (DCS) at  $180^\circ$  is presented. It uses a magnetically focused electron impact spectrometer where the backward scattered electrons are reflected into the forward direction by a potential barrier, and enter the energy analyzer. Pulsed incident beam and time-of-flight detection are used to differentiate the backward and forward scattered electrons. The instrument yields the ratio of the forward and backward DCS. This data is then combined with the results from an instrument using electrostatic hemispherical analyzers to yield absolute DCSs as a function of scattering angle from  $0^\circ$  to  $136^\circ$  plus one more data point, the DCS at  $180^\circ$ . Absolute DCS is also obtained as a function of incident energy at  $0^\circ$  and at  $180^\circ$ . The technique is applied to measure the DCSs for the excitation of the four  $n = 2$  states of helium as a function of scattering angle at 22, 25, and 29.5 eV, and as a function of energy from threshold to 28 eV at  $0^\circ$  and  $180^\circ$ . The data is compared with recent theoretical results.

#### Introduction

A number of applications, for example the modeling of technological, atmospheric, and interstellar plasmas, require the knowledge of electron-atom and electron-molecule collision cross sections. Helium has become an important testing ground for the development of both experimental and theoretical techniques for the determination of electron collision cross sections. Both experiment and theory have a long history, but critical improvements have been achieved very recently. The theoretical side of the problem at low and intermediate energies (from threshold to about 80 eV) has recently received considerable attention and substantial progress has been achieved, the key developments and representative publications being the R-matrix theory calculations with 29 discrete states (RM29) by Fon (1994a,b), the close-coupling calculations (CCC) of Fursa and Bray (1995) and the R-matrix calculations with pseudostates (RMPS) of Bartschat *et al.* (1996). There is a substantial amount of experimental data to compare the theory with, and only a

short list is given here. A comprehensive table of existing experimental work was given by Trajmar *et al.* (1992). It begins with the pioneering work of Ehrhard *et al.* (1968), Hall *et al.* (1973), and Pichou *et al.* (1976). More recent measurements concerned with the angular dependence of the DCSs at low energies and relevant to the present work were presented by Brunger *et al.* (1990), Trajmar *et al.* (1992) and Cartwright *et al.* (1992). A very recent measurement was published by Röder *et al.* (1996). The present work is devoted to the improvement of the experimental techniques, in particular we present a novel technique using a magnetically collimated spectrometer with an 'electron-mirror' which extends the scattering angle range to include  $0^\circ$  and  $180^\circ$ . Large scattering angles are in general not accessible to instruments using electrostatic hemispherical energy analyzers, the largest attainable angle being between  $120^\circ$  and  $156^\circ$  ( $136^\circ$  for the instrument in Fribourg). Small scattering angles are attainable mechanically by these instruments, but measurements at very small angles are difficult because the main beam enters the analyzer where it often causes large stray electron background. The high stray electron rejection of our electrostatic instrument permits measurement of absolute inelastic DCSs at  $0^\circ$ . Combining this value with the ratio of the DCSs at  $0^\circ$  and  $180^\circ$  measured by the electron mirror instrument yields absolute DCSs at  $180^\circ$ . The two instruments together thus provide absolute DCSs from  $0^\circ$  to  $136^\circ$  continuously, plus one more point at  $180^\circ$ . When the electron-mirror technique was first presented (Asmis and Allan 1995) it was to the best of our knowledge the first measurement of inelastic differential cross section (DCS) at  $180^\circ$  in the gas phase. (A technique to study elastically backscattered electrons has been devised by Burrow and Sanche, 1972, a technique to measure electrons inelastically backscattered from surfaces by Cloutier and Sanche, 1989) An alternative technique using a novel scheme of electron beam deflection by magnetic field in an instrument equipped with hemispherical analyzers has been very recently presented by Zubek *et al.* (1996) and by Read and Channing (1996).

A study of the DCSs as a function of electron energy in the near-threshold region using the present hemispherical analyzer spectrometer has already been published (Allan 1992) The present contribution concentrates on the angular dependence of the DCSs at low energies, from threshold to 30 eV. The cross sections in dependence on electron energy at  $0^\circ$  and  $180^\circ$  are also given.

### Instruments

**The electron-mirror spectrometer.** The trochoidal electron spectrometer, utilizing an axial magnetic field to collimate the electrons and the trochoidal analyzers (Stamatovic and Schulz 1968, 1970) to reduce the spread of the electron energies, has been shown to detect both forward and backward inelastically scattered electrons (Allan 1989). The latter are reflected into the

forward direction by a potential barrier which they encounter after leaving the target chamber, as shown schematically in Figure 1. The instrument could thus be called an 'electron mirror' spectrometer. (The electrons scattered elastically into  $180^\circ$  are not reflected because their energy is higher than the potential barrier, and re-enter the monochromator. They have been collected and used by Burrow and Sanche (1972) to measure the *elastic* cross sections at  $180^\circ$ . The reflected electrons re-enter the target chamber, traverse it, at a sufficiently low pressure, without a significant chance of a second collision and enter the analyzer together with the forward scattered electrons.

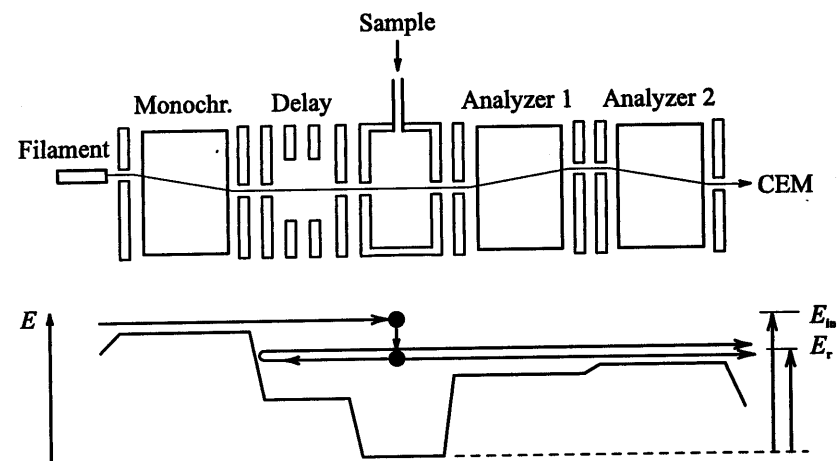


Figure 1

Schematic diagram of the electron mirror spectrometer and the potentials applied to the individual electrodes. (The arrows showing the forward scattered and the reflected electrons are shown slightly vertically offset for clarity but they both have the same energy  $E_r$ .)

This property of the magnetically collimated spectrometer is used in the present work to develop a novel scheme for the measurement of inelastic DCSs at  $180^\circ$ . The instrument is shown schematically in Figure 1. The forward and backward scattered electrons are distinguished using a pulsed electron beam and a time-of-flight detection scheme. Both forward and backward scattered electrons have a given range of arrival times, primarily because of the finite length of the target chamber, along which the collisions take place, causing an overlap of the arrival times (Allan 1989). An 'electron delay line' has therefore been developed (Asmis 1996), delaying the backward scattered electrons before they re-enter the target chamber. The delay line consists of a short (1 cm) path which the electrons have to traverse with a constant and low ( $\approx 0.1$  eV) energy.

The backward scattered electrons travel a relatively long distance and the alignment of the magnetic field is critical to achieve equal collection efficiency for the  $0^\circ$  and  $180^\circ$  electrons. The alignment is tested on the vibrational excitation in  $N_2$  in the 2-4 eV energy range, as shown in Figure 2. The inelastic scattering in  $N_2$  in this energy range is dominated by the  $^2\Pi_g$  resonance (Schulz 1973). The angular distribution is therefore symmetrical around  $90^\circ$  and the DCS has the same magnitude at  $0^\circ$  and  $180^\circ$  (see for example Grimm-Bosbach *et al.* 1996), making this process suitable to test the collection efficiency in the  $0^\circ$  and the  $180^\circ$  directions. A properly adjusted instrument yields equal signal (areas under the peaks in Figure 2) for the forward and the backward electrons.

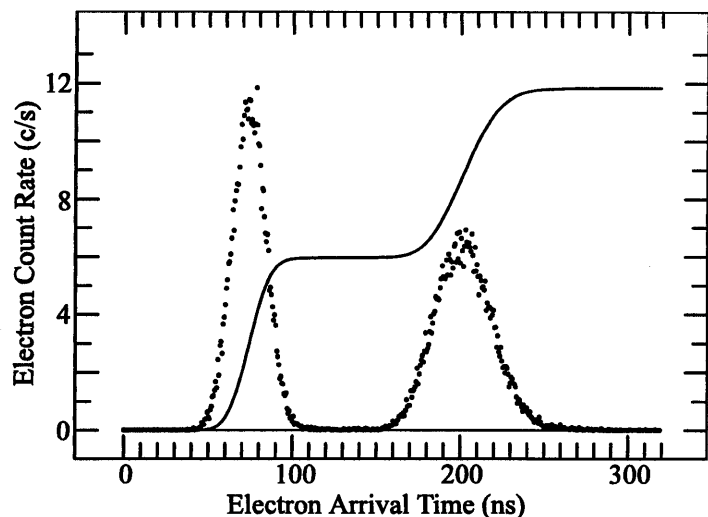


Figure 2

*Illustration of the pulsed mode of operation of the trochoidal electron spectrometer. The figure shows the yield of electrons having excited the  $v = 5$  level of  $N_2$  at an incident energy of 2.4 eV as a function of their arrival time at the detector. The first band corresponds to the forward scattered electrons, the second to the backward scattered electrons. The integral, shown by a solid line, indicates that the areas under both bands are equal, that is an equal collection efficiency for electrons scattered into  $0^\circ$  and into  $180^\circ$ . (The origin of the time scale is arbitrary.)*

The instrument can be used to measure the ratio of differential cross sections at  $0^\circ$  and  $180^\circ$  at a given incident energy and a given energy-loss, by recording the time histogram of the electron arrival times as shown in Figure 2. The ratio of the forward and backward cross sections is equal to the ratio of the areas under the two bands. The instrument can further measure the dependence of the  $0^\circ$  or  $180^\circ$  DCS as a function of incident electron energy by defining

discriminator levels passing only pulses within a window corresponding to either forward or backward scattered electrons. The spectra, where the electron energy is varied, were corrected for the variation of the analyzer response, which was assumed to be inversely proportional to the residual energy  $E_r$ . The supplementary empirical linear correction described by Allan (1989) was not applied in the present work.

A central question is that of angular resolution. An electron scattered with the energy  $E$  into an angle  $\theta$  in the present instrument with an axial magnetic field moves on a spiral whose Larmor radius  $\rho$  (in mm) is connected to the scattering angle by

$$\rho = \frac{33.7}{B} \sqrt{E_t} = 0.513 \sqrt{E_t} = 0.513 \sqrt{E} \sin \theta. \quad (1)$$

The magnetic field  $B$  was 65 Gauss in the present experiment. The electron energy  $E$  and the energy  $E_t = E \times \sin^2 \theta$  associated with the transversal motion are given in electronvolts. Electrons spiraling with large radii  $\rho$  are eliminated by the smallest (resolution-defining) apertures of the analyzer with radii  $R_A = 0.2$  mm (the two apertures just before and just after the second pair of the 'D-plates', see Allan 1989, for a detailed description of the analyzer). The angular resolution of the instrument is given by the range of the Larmor radii  $\rho$  which will pass the analyzer.

The largest radius which will pass the analyzer is thus  $\rho = 0.2$  mm, yielding  $E_t = 0.15$  eV and the largest acceptance angle (for  $E = 4$  eV as an example) of  $\theta_{\max} = 11^\circ$ . A closer consideration reveals, however, that not all electrons with a given spiraling radius  $\rho$  will pass the analyzer and the fraction  $P$  which will pass is a function of  $\rho$ . We now take this dependence into account and attempt to derive a realistic estimate of the analyzer collection efficiency as a function of  $\theta$  using the assumptions illustrated in Figure 3a). The incident beam is assumed to have a uniform density within a radius defined by the smallest apertures within the monochromator, with a radius of 0.23 mm. Collisions take place with uniform rate within the cross section of the incident beam along the length of the collision chamber, each collision being characterized by a distance  $R$  from the instrumental axis, a spiraling radius  $\rho$  which is a function of the scattering angle  $\theta$  and an azimuthal angle of scattering  $\phi$ . Whether a given electron will pass the analyzer is a function of  $R$ ,  $\rho$ , and  $\phi$ . For small  $R$  and  $\rho$  electrons with any  $\phi$  will pass, for larger  $R$  and  $\rho$  only a fraction of electrons, with  $\phi$  within a given range, will pass. We assume that all electrons for which the projection of the spiraling path along the instrumental axis crosses the edge of the aperture will be stopped, this assumption being justified by the low potential at which the apertures are generally operated, resulting in low forward momentum within the aperture and thus "closely wound" spiraling path. Note that the apertures are 1 mm thick, the opening with  $R_A = 0.2$  mm is a 'tunnel', it is longer than it is thick.



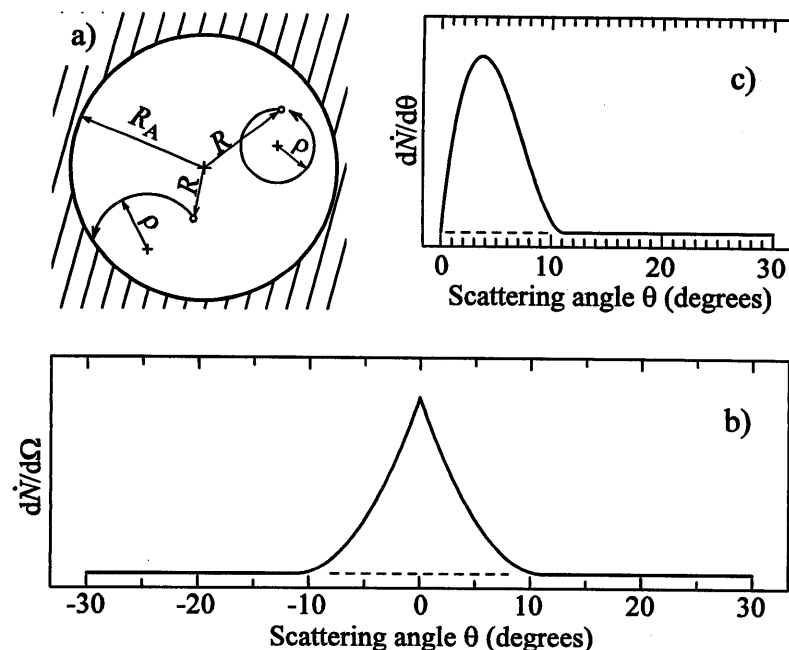


Figure 3

a) Examples of two electron trajectories projected in the axial direction onto the resolution-defining aperture of the analyzer with the radius  $R_A$ . The electron whose trajectory is drawn on the right passes, the electron with the trajectory shown on the left is stopped by the aperture. b) Angular response function of the instrument in any given scattering plane. c) Angular response function integrated over the azimuthal angle  $\phi$ .  $\dot{N} = dN/dt$  is the rate of detected electrons.

We evaluated trigonometrically the fraction of electrons which will pass, as a function of  $R$  for each  $\rho$  (and thus each  $\theta$ ), and then integrated numerically over all  $R < R_A$  (taking into account that the number of points with a given  $R$  increases proportionally with  $R$ ) to obtain the probability that an electron scattered with a given spiraling radius  $\rho$  (and thus a given scattering angle  $\theta$ ) will pass the analyzer. An example of the resulting curve, for  $E = 4$  eV, is shown in Figure 3b). The curve peaks at  $0^\circ$  because electrons scattered with  $\theta = 0^\circ$  will have  $\rho = 0$  and electrons scattered anywhere within the beam cross section will pass the analyzer. The curve in Figure 3b) decreases rapidly with increasing  $\theta$  and with the concurrently increasing  $\rho$ , because many electrons spiraling with larger  $\rho$  will not pass the aperture as illustrated in Figure 3a). The probability for an electron to pass is very small near the limiting value  $\theta_{\max}$  because very restrictive conditions must be fulfilled for it to pass: It has  $\rho = R_A$  and has to be scattered at the very edge of the beam, and with  $\phi$  such as to make the projection of the path exactly tangential to the edge of the aperture. The

width at half height of the angular response curve is thus much smaller than the limiting value  $\theta_{\max}$ . Similarly the width at half height of the energy response curve is much less than the limiting value  $E_t = 0.15$  eV, in qualitative agreement with the observed overall resolution (given not only by the resolution with respect to  $E_t$ , but also by finite resolution with respect to the axial energy  $E_a$ , and other factors) of the instrument, which is typically 45-50 meV and 25 meV in the best case (Allan 1989). In fact, the good value of the observed resolution appears to indicate that the real angular response curve is narrower than shown in Figure 3c). This could be the result of the electron beam intensity not being entirely uniform as assumed above, but decreasing towards the edge.

Finally, to obtain the response of the instrument with respect to the DCS( $\theta$ ) we have to multiply with the solid angle  $d\Omega/d\theta = 2\pi\sin\theta$ , with the result shown in Figure 3c). For 4 eV scattered electrons the observed forward signal is thus most sensitive to DCS at about  $4^\circ$ , the observed backward signal to DCS at about  $176^\circ$ . (Note that the hemispherical analyzer instrument suffers from the same problem when set to  $0^\circ$ , except that its angular resolution at low energies is better.)

The angular response curves shown in Figure 3 become narrower with increasing scattered electron energy as  $1/\sqrt{E}$ . The above consideration assumes that angular distribution of the electrons in the incident beam is very narrow, this assumption being justified by the incident electron energies being substantially higher than the scattered electron energy in the present experiments.

The signal is generally sufficiently strong to attain statistical uncertainty below 5%. The major source of uncertainty stems from the possibility of unequal collection efficiencies at  $0^\circ$  and  $180^\circ$ . The collection efficiencies were tested using the  $N_2$ -signal with each He measurement and the performance of the instrument, once properly adjusted, has been found to be quite stable. Based on the observed signal stability we put the uncertainty of the measured  $0^\circ/180^\circ$  DCS ratio at  $\pm 10\%$ .

**The hemispherical analyzer spectrometer.** This instrument has been described previously by Allan (1992, 1995). It is an essentially standard electrostatic spectrometer using hemispherical deflectors for electron energy selection. The analyzer can be rotated from  $-3^\circ$  to  $135^\circ$  with respect to the incident beam. The angular dependence spectra are measured by repetitively scanning the analyzer position with a stepping motor. Absolute cross sections are determined by normalizing the present data to the value of  $4.0 \times 10^{-19}$  cm<sup>2</sup>/sr for the  $2^3S$  state at 22 eV and  $90^\circ$ , obtained earlier with the same instrument (Allan 1992) by comparison with elastic signal and normalizing to the calculated elastic cross section of Nesbet (1979). The stray electron rejection of this instrument is sufficiently high to permit the measurement of inelastic cross sections even at  $0^\circ$ . This value is then used to normalize the data from the electron mirror spectrometer, yielding absolute data at  $180^\circ$ .

The central and critical part of the measurement is the determination of the instrumental response (or sensitivity) as a function of the incident and residual energies and of scattering angle. Determination of the response as a function of electron energies has been discussed in connection with the present instrument by Allan (1992), determination of the angular response by Allan (1995) and only a brief discussion will be given here. Examples of the response curves as a function of energy was given by Allan (1992), as a function of scattering angle by Allan *et al.* (1996).

Determination of the instrumental response for elastic scattering does not pose problems, the helium elastic signal is measured as a function of either the electron energy or the scattering angle and then digitally divided point-by-point by the calculated elastic DCS of Nesbet (1979) to yield the response curve. Determination of the instrumental response for inelastic scattering is more difficult, in particular when the residual, or both the incident ( $E_{in}$ ) and the residual ( $E_r$ ) energies are low (below about 3 eV), because there are no generally accepted standards. High quality calculations of the inelastic cross sections in helium promise to provide a suitable standard in the future, but they have not (yet) been used as a standard in the present work.

To determine the response function for inelastic scattering as a function of electron energies we used the procedure of Pichou *et al.* (1976). The sensitivity of the analyzer  $SA_{\theta}(E_r)$  as a function of the residual energy  $E_r$  is calibrated up to  $E_r = 3-5$  eV on the near threshold ionization continuum of helium, which provides a standard in the form of a uniform distribution of secondary electrons. The analyzer is assumed to behave ideally above 3-5 eV, that is its response falls off as  $1/E_r$ . An indication that it is really the case, that is that the analyzer is properly tuned, is obtained from elastic scattering. When the incident energy  $E_{in}$  is high (above about 6 eV, that is always in the present work), providing a constant profile of the incident beam as  $E_{in}$  is varied, it suffices to divide the observed spectrum point-by-point by  $SA_{\theta}(E_r)$  to correct it for the variation of the instrumental response. An additional difficulty arrives in determining the response function  $SA_{\theta}(E_r)$  at scattering angles close to  $0^\circ$  or  $180^\circ$ . Results from the electron-mirror spectrometer indicate that the ionization continuum of helium is no longer uniform at these angles and thus does not provide a suitable standard at small and large scattering angles (Asmis and Allan 1996), necessitating additional assumptions at scattering angles far from  $90^\circ$ .

To correct the angular distribution spectra, we first determine the angular response functions on elastic scattering for a series of electron energies. The elastic signal can be recorded down to about  $5^\circ$ , the response functions are extrapolated visually to  $0^\circ$  using results of numerical simulations of the interaction volume as a guide. The resulting response curve is given by the variation of the overlap of the incident electron beam, the analyzer acceptance cone, and the effusive molecular beam with  $\theta$ . The present instrument uses a

monochromator exit aperture with a diameter of 0.25 mm, a  $0.2 \times 0.8$  mm rectangular analyzer entrance slit, and the measurement are made 2-3 mm above an effusive nozzle with 0.25 mm diameter. The incident electron beam and analyzer acceptance cone are thus narrower than the gas beam and the experimentally determined response curves as a function of the scattering angle behave approximately as  $1/\sin\theta$  at intermediate  $\theta$ . The finite size of the molecular beam causes a 'cut-off' at scattering angles below about  $10^\circ$ . The  $1/\sin\theta$  - like behavior is sustained, for a well tuned instrument down to energies of about 1 eV. At lower energies the incident beam and the analyzer acceptance cones become more diffuse because of uncontrolled contact potential variations ('patches') on the surface of the electron optics elements. The experimental sensitivity curves as a function of  $\theta$  become flatter, approaching the limit of wide electron beams with response function independent of scattering angle. In order to determine the response function as a function of scattering angle for inelastic scattering, we limit the work to energies where the beam profiles remain reasonably narrow, that is energies high enough for the experimental response functions for elastic scattering to preserve the  $1/\sin\theta$  - like shape and where the shape varies only slowly with energy. Angular distribution of inelastic signal recorded at  $E_{in}$  and  $E_r$  is then corrected using an average of the angular sensitivity curves determined on elastic helium signal at  $E = E_{in}$  and  $E = E_r$ . This procedure is only approximate, but the error can not be large when the two response curves of which the average is taken are similar in shape.

Finally the analyzer response curve  $SA_{\theta}(E_r)$  as a function of the residual energy was required in the present work at  $\theta = 0^\circ$ , where the calibration on the helium ionization continuum is not applicable. We therefore used the curve determined at  $90^\circ$ , modified slightly to make it consistent with the angular response curves described in the preceding paragraph.

The error of the absolute values is dominated by the uncertainties in determining the instrumental response function and by their drift in time due to drift of contact potentials with varying surface condition. The contribution of statistical uncertainty is generally small. The errors of the present measurement thus can not be determined precisely because of the difficulty to quantify the effects of drifts of the contact potentials. Based on our experience with the size of the drifts we place the error bar at  $\pm 35\%$ , with a confidence of about 95% (two standard deviations). The errors are energy and angle dependent, but in view of the approximate nature of their determination, it does not appear meaningful to express this dependence explicitly. The error is larger at low residual energies and near  $0^\circ$ .

## Results and Discussion

We measured the DCSs for the excitation of the  $n = 2$  states of helium as a function of scattering angle at 22, 25, and 29.6 eV. We confine ourselves to presenting the results graphically, but will send the digitized results

electronically to interested readers. The results for the  $2^3S$  state are shown and compared with the theoretical results of Fon *et al.* (1994a), Fursa & Bray (1995) (The results of Fursa & Bray, 1995, are a private communication of I. Fursa) and of Bartschat *et al.* (1996) in Figure 4. The comparison should be made while bearing in mind that the present experimental data consists of two sets: the shape and the absolute value of the DCSs in the range  $0^\circ$ - $180^\circ$ , from the hemispherical analyzer instrument, with an uncertainty of  $\pm 35\%$ , and the ratios of  $180^\circ$  and  $0^\circ$  DCSs from the magnetically collimated instrument, with an uncertainty of  $\pm 10\%$ .

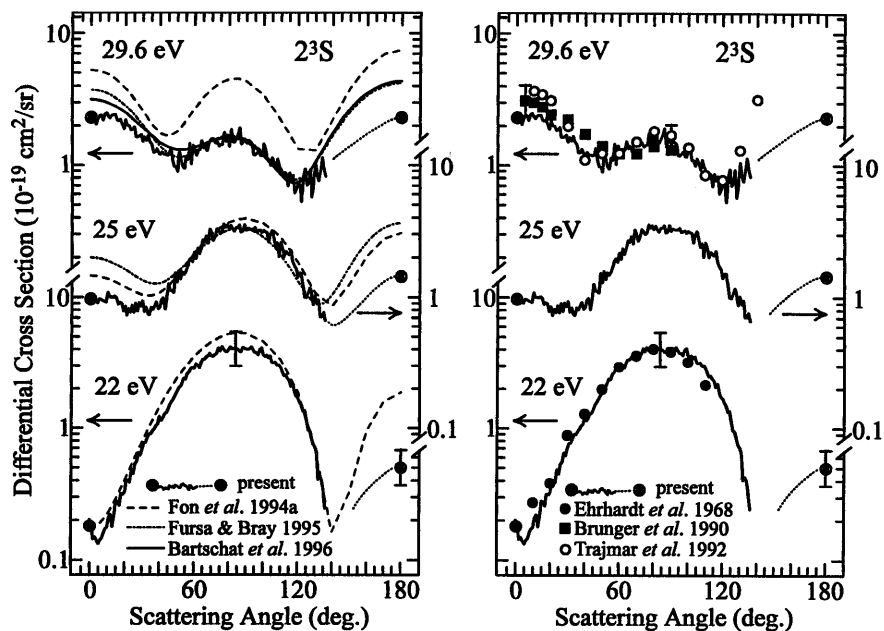


Figure 4

Differential cross sections for the excitation of the  $2^3S$  state of helium. The present results (heavy line: data from the hemispherical analyzer instrument; filled circles at  $0^\circ$  and  $180^\circ$ : results from the electron-mirror instrument, with visual interpolations indicated by thin dotted lines) are compared with calculations on the left, with earlier measurements on the right side of the figure. The results of Fursa & Bray and of Bartschat *et al.* are at 30 eV. The curves are vertically offset and horizontal arrows point to appropriate DCS scale for each electron energy. Representative error bars are indicated (two standard deviations for the present work and the work of Brunger *et al.*)

The data from the hemispherical analyzer instrument agrees generally very well with the three theories for the  $2^3S$  state, except that the RM29 result is larger at 29.6 eV. The experimental results are further somewhat smaller than

theory of Fursa and Bray and of Bartschat *et al.* in the  $0^\circ$ - $10^\circ$  range. The difference is less than the experimental uncertainty, and could be due to the uncertainty of the scheme of determining the instrumental response at very low angles. The ratios of  $180^\circ$  and  $0^\circ$  DCSs are in an agreement with all three theories at 25 and 29.6 eV which is even better than the agreement of the absolute values as can be found out by shifting the corresponding data (encircled points) up by the same amounts in the Figure 4 to normalize it to theory at  $0^\circ$ . At the lowest energy, 22 eV, the 29 states R-matrix theory (RM29) results of Fon *et al.* (1994a) agree very well with the present experiment in the  $0^\circ$ - $136^\circ$  range. Some disagreement is found, however, at  $180^\circ$ . The right side of Figure 4 compares the present results with the experimental results of Brunger (1990), Ehrhardt *et al.* (1968), and of Trajmar *et al.* (1992). The differences generally do not exceed the combined error limits, but there are some differences in the shape of the curves at 29.6 eV (resp. 30 eV), the present shape agreeing better with the recent theory.

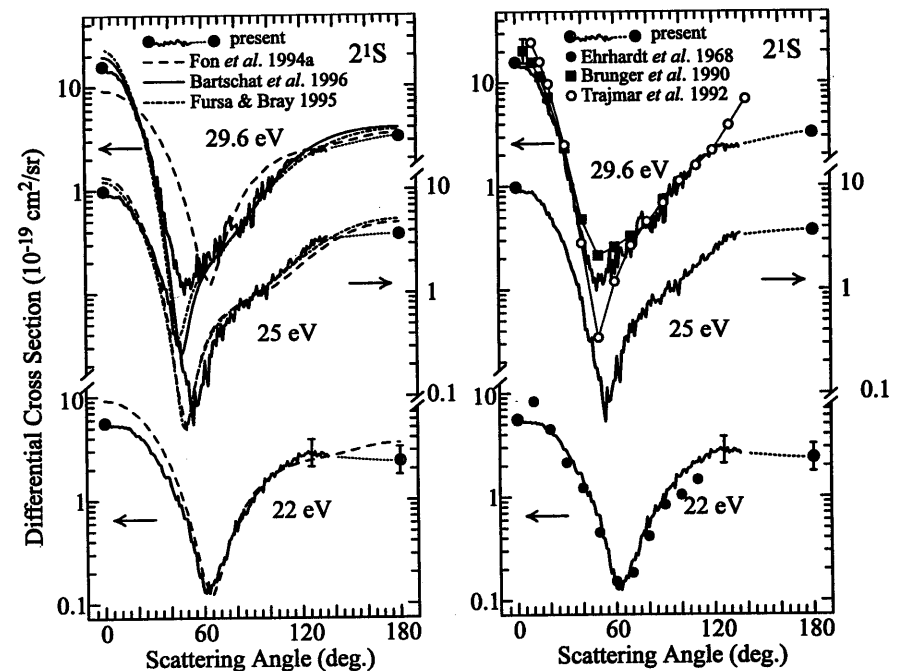


Figure 5

Differential cross sections for the excitation of the  $2^1S$  state of helium. Symbols as in Figure 4.

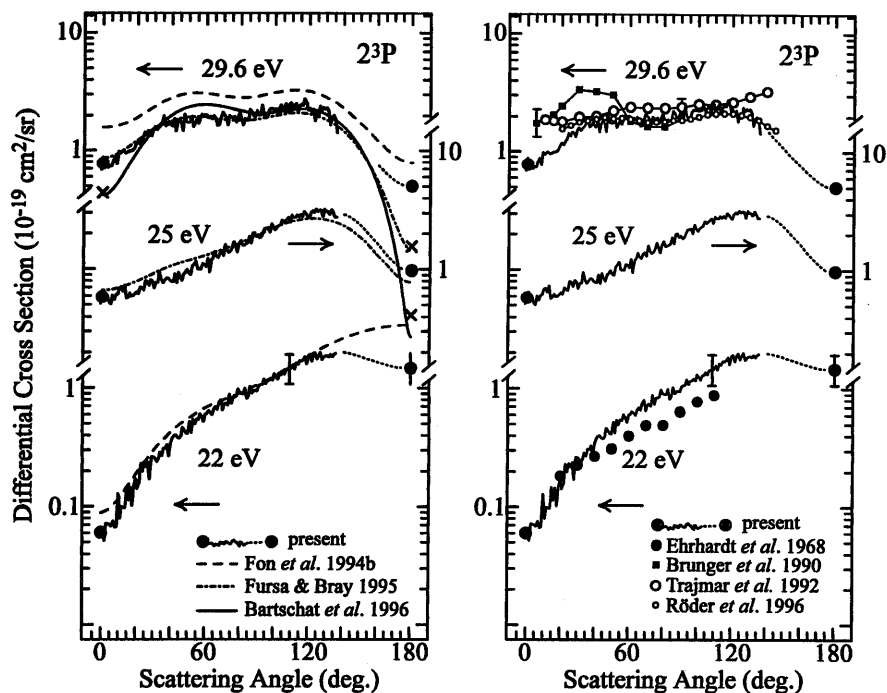


Figure 6

Differential cross sections for the excitation of the  $2^3P$  state of helium. Symbols as in Figure 4. Crosses indicate the DCS of Bartschat *et al.* (1996) at 30 eV, convoluted with the present angular response function (see Figure 3).

Figure 5-7 present the angular distribution results for the remaining  $n = 2$  states and conclusions are generally similar to those made about the  $2^3S$  state above. The present results agree very well with the RMPS results of Fursa & Bray (1995) and of Bartschat *et al.* (1996) for the  $2^3P$  state at intermediate scattering angles, but the RMPS results, and to a lesser degree the CCC(69) results, are substantially smaller at  $180^\circ$ . This discrepancy is partly due to the final angular distribution of the instrument, because the cross section drops very rapidly toward  $180^\circ$  and the signal is increased by the fact that the instrumental response (integrated over azimuthal angles) probes the DCS in the range  $173^\circ$ - $180^\circ$ , peaking at  $177.5^\circ$ . We therefore convoluted the theoretical results with the angular response function of the present experiment, that is the curve shown in Figure 3, except narrower because of the higher scattered electron energy. The convoluted results, indicated by crosses in Figure 6, are still significantly below the experiment.

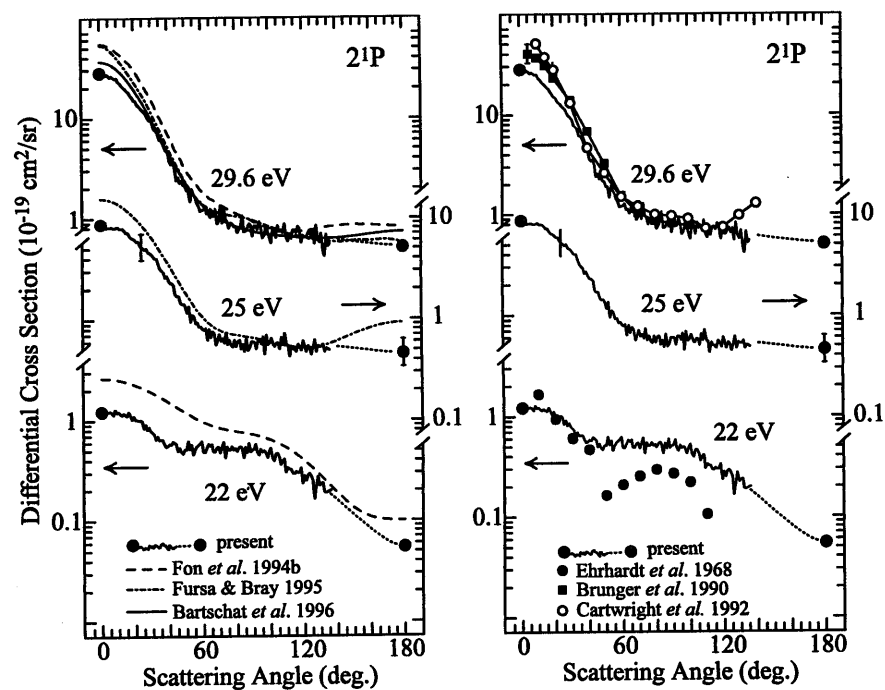


Figure 7

Differential cross sections for the excitation of the  $2^1P$  state of helium. Symbols as in Figure 4.

After finalizing the present measurements we learned of the recent results of Röder *et al.* (1996) which are compared with the present results on the right side of Figure 6. The agreement of the shapes of the curves is excellent, confirming the conclusion of Röder *et al.* that the results of the recent advanced theory are fully confirmed by experiment. The agreement is even more satisfying because the two experiments differ substantially in the scattering geometry: the present experiment requires a substantial correction of the raw data (Sec. 2.2), whereas the instrumental response in the experiment of Röder *et al.* was independent of scattering angle and no correction was required.

The present data agrees very well with the theories for the  $2^1P$  state, the agreement with the ratios of the  $180^\circ$  and  $0^\circ$  DCS being even better than the agreement with the absolute values, similarly as for the  $2^3S$  state. As already pointed out, the present DCSs may be too low by about 30% in the  $0^\circ$ - $10^\circ$  range.

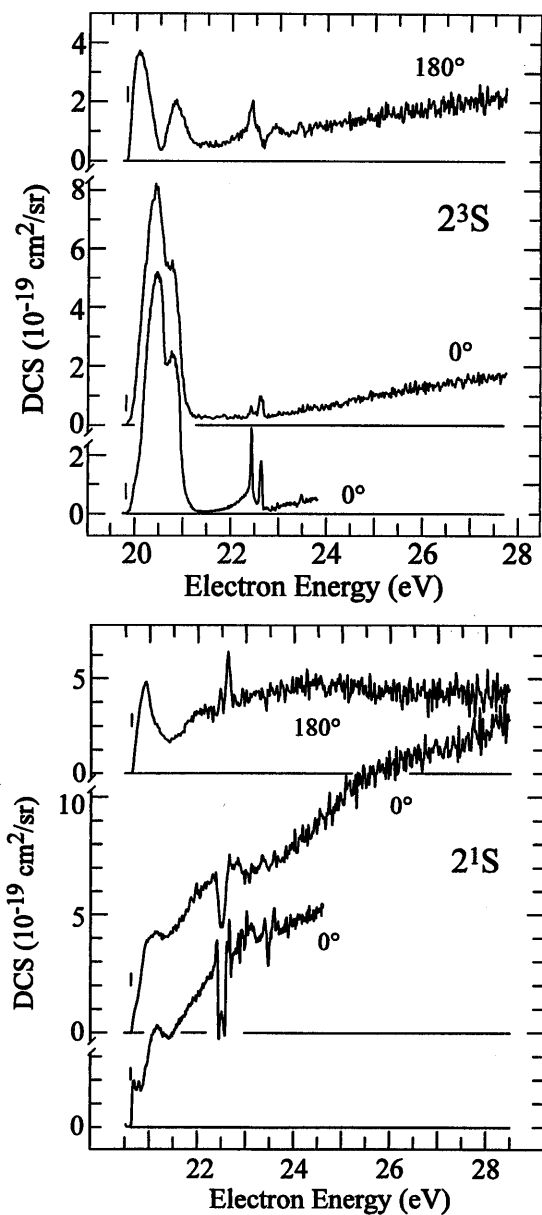


Figure 8

DCS for exiting the  $2^3S$  (top) and  $2^1S$  (bottom) state in helium at  $0^\circ$  and  $180^\circ$ . The lowest curve in each graph has been recorded with the hemispherical analyzer instrument, the top two curves in each graph with the electron mirror instrument.

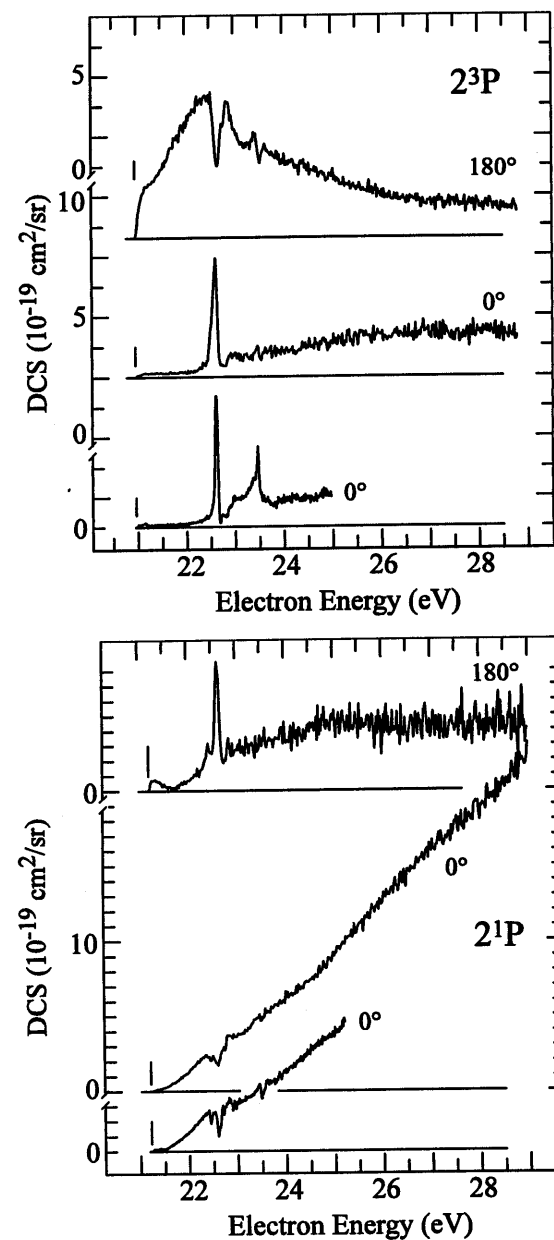


Figure 9

DCS for exiting the  $2^3P$  (top) and  $2^1P$  (bottom) states in helium at  $0^\circ$  and  $180^\circ$ . (See caption of Figure 8 for explanations.)

The DCS for the excitation of the  $n = 2$  states of helium were further measured as a function of incident energy at  $0^\circ$  and  $180^\circ$ . Sample results are shown in Figure 8 and 9. The DCS at  $0^\circ$  can be measured both with the electron mirror spectrometer and with the hemispherical analyzer spectrometer, providing a test of mutual consistency of the instrumental response correction procedure. The agreement of the  $0^\circ$  spectra from the two instruments can be considered as very satisfactory when the higher energy and angular resolutions of the hemispherical analyzer instrument are taken into account in the comparison.

### Conclusions

The RM29 results of Fon *et al.* (1994a,b) are generally in excellent agreement with the present experimental results at 22 and 25 eV, but are expectedly somewhat higher at energies substantially above the ionization energy, *i.e.* at 30 eV. At 30 eV the RMPS and the CCC theory results agree very well with the present results, confirming the conclusion made very recently by Röder *et al.* (1996). Discrepancies between experiment and theory are found in some cases at the extreme angles of  $0^\circ$  and  $180^\circ$ . These discrepancies persist even when the finite angular resolution of the present experiment is taken into account. Discrepancies exceeding the error limits are found only for the triplet states, theory and experiment agree well for the singlet states even at  $0^\circ$  and  $180^\circ$ . The theoretical predictions lie sometimes above, sometimes below the present experimental values at  $180^\circ$ , making it appear improbable that the discrepancies are due to an unexpected systematic error of the novel electron-mirror experiment.

### Acknowledgments

We wish to express our sincere appreciation to Professor E. Haselbach for his continuing support and encouragement in the present work. The spectrometers could not have been constructed without the exceptional enthusiasm and ingenuity of E. Brosi of the mechanical laboratory and P.-H. Chassot of the electronical laboratory. We thank to E. T. Hudson for sending us the results of Bartschat *et al.* (1996) in digital form. This work is part of project 2028-040398.94/1 of the Swiss National Science Foundation.

### References

- Allan M 1989 *J. Electr. Spectr.* **48** 219
- 1992 *J. Phys. B: At. Mol. Opt. Phys.* **25** 1559-75
- 1995 *J. Phys. B: At. Mol. Opt. Phys.* **28** 5163-5175
- Allan M, Asmis K R, Popovic D B, Stepanovic M, Mason N J and Davies J A 1996a *J. Phys. B: At. Mol. Opt. Phys.* **29** (submitted for publication)
- Allan M, Mason N J and Davies J A 1996b *J. Phys. B: At. Mol. Opt. Phys.* **29** (submitted for publication)
- Asmis K R 1996 Ph. D. thesis, unpublished
- Asmis K R and Allan M 1995 contributions to the International Symposium on Electron- and Photon-Molecule Collisions and Swarms, Berkeley, July 1995.
- Asmis K R and Allan M 1996 in preparation
- Bartschat K, Hudson E T, Scott M P, Burke P G and Burke V M 1996 *J. Phys. B: At. Mol. Opt. Phys.* **29** (in press)
- Brunger M J, McCarthy I E, Ratnavelu K, Teubner P J O, Weigold A M, Zhou Y and Allen L J 1990 *J. Phys. B: At. Mol. Opt. Phys.* **23** 1325
- Burrow P D and Sanche L 1972 *Phys. Rev. Lett.* **28** 333
- Cartwright D C, Csanak G, Trajmar S and Register D F 1992 *Phys. Rev. A* **45** 1602
- Ehrhard H, Langhans L and Linder F 1968 *Zeitschr. Phys.* **214** 179
- Fon W C, Lim K P, Ratnavelu K and Sawey P M J 1994a *J. Phys. B: At. Mol. Opt. Phys.* **27** 1561
- Fon W C, Lim K P and Berrington K A 1994b *J. Phys. B: At. Mol. Opt. Phys.* **27** L591
- Fursa D and Bray I 1995 *Phys. Rev. A* **52** 1279
- Grimm-Bosbach T, Thümmel H T, Nesbet R K and Peyerimhoff S D 1996 *J. Phys. B: At. Mol. Opt. Phys.* **29** L105
- Hall R I, Joyez G, Mazeau J, Reinhardt J and Schermann C 1973 *J. Physique* **34** 827
- Nesbet R K 1979 *Phys. Rev. A* **20** 58
- Pichou F, Huetz A, Joyez G, Landau M and Mazeau J 1976 *J. Phys. B: At. Mol. Phys.* **9** 933
- Read F H and Channing J M 1996 *Rev. Sci. Instrum.* **67** 2372
- Röder J, Ehrhardt H, Bray I and Fursa D 1996 *J. Phys. B: At. Mol. Opt. Phys.* **29** L421
- Schulz G J 1973 *Rev. Mod. Phys.* **45** 423
- Stamatovic A and Schulz G J 1968 *Rev. Sci. Instr.* **39** 1752
- 1970 *Rev. Sci. Instr.* **41** 423
- Trajmar S, Register D F, Cartwright D C and Csanak G 1992 *J. Phys. B: At. Mol. Opt. Phys.* **25** 4889
- Zubek M, Gulley N, King G C and Read F 1996 *J. Phys. B: At. Mol. Opt. Phys.* **29** L239

## 5.2. Measurement of Absolute Differential Cross Sections at 0° and 180° for the Excitation of the Lowest Triplet State in Ethylene

### 5.2.1. Introduction

Ethylene was the first molecule studied with the novel instrument. It is a suitable test case for several reasons. (i) Ethylene is the prototype of unsaturated organic molecules. Its chromophore, responsible for resonance phenomena at low energies, is a C=C double bond with  $\pi$  and  $\pi^*$  orbitals. (ii) The lowest singlet-triplet transition (see Figure 5.2-1), which can be pictured as the promotion of an electron from the doubly occupied  $\pi$  orbital into the unoccupied  $\pi^*$  orbital, lies energetically well below all other electronic excitation processes, thus avoiding problems with overlapping bands. (iii) Recent experimental and theoretical results are available concerning the dependence of this excitation process on incident electron energy and scattering angle. Allan (1994) has measured the absolute DCSs at low energies and for scattering angles from 3° to 135°. McKoy and Winstead (1993) and Rescigno and Schneider (1992) have performed *ab initio* scattering calculations. Interestingly, both predict this transition to be strongly backward peaked at higher incident electron energy.

### 5.2.2. Results and Discussion

The procedure for determining absolute 180° DCSs has been described in detail in Chapter 4. This study concentrates on the excitation of the  $1^3B_{1u}$  state. The measurements were performed at an energy-loss of 4.18 eV, close to the vertical excitation energy. Background spectra were recorded at an energy-loss of 3.00 eV, in a region where no signal attributable to ethylene is expected (see Figure 5.2-1). First the instrument was tuned such that the collection efficiency ratio (for backward versus forward scattered electrons) is close to unity. Then the collection efficiency ratio of the instrument was determined on the resonant vibrational excitation of N<sub>2</sub>, after which the arrival time distributions were measured. In general the collection efficiency ratio was determined after each arrival time distribution spectrum and the average value is taken for the calibration. Multiplication of the DCS ratio with the absolute 0° DCS (Allan 1996) then yielded the absolute 180° DCS. Finally the 0° and 180° excitation function were measured and scaled to best fit the absolute values determined in the previous step.

Arrival time distributions measured at  $\Delta E = 4.18$  eV and incident energies of 4.38, 5.68, 7.18, 10.18 and 14.18 eV are shown in Figure 5.2-2. Background signal was subtracted when necessary. The origin of the arrival time is arbitrary. The integral of the electron count over the arrival time is also

shown. Each spectrum shows two bands, one due to the (earlier) arrival of the forward scattered electrons, the other due to the (later) arrival of the electrons scattered in the backward direction.

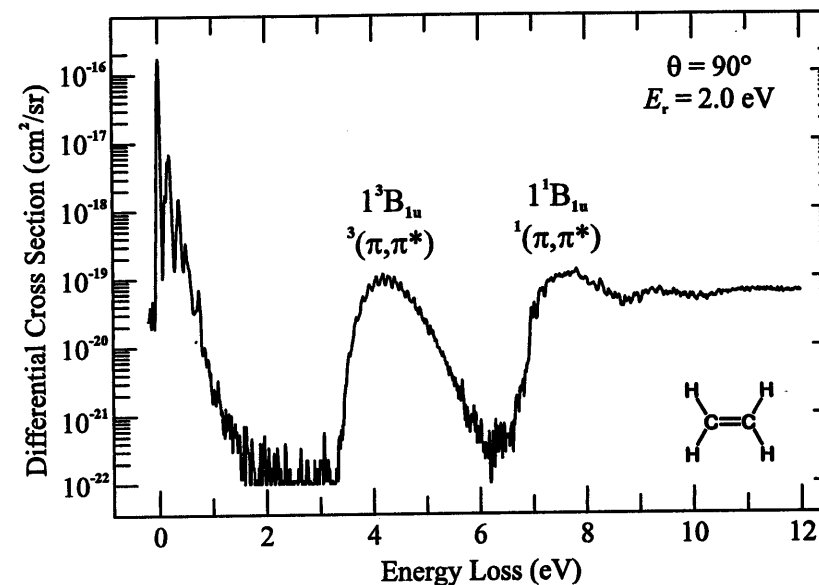


Figure 5.2-1

Global energy-loss spectrum of ethylene, recorded at 90° with a constant residual energy of 2.0 eV (Allan 1994). The lowest triplet state  $1^3B_{1u}$  lies well below all other electronic excitation processes.

Table 5.2-1

180°/0° DCS ratios for the excitation of the  $1^3B_{1u}$  state, determined on the basis of the arrival time distributions shown in Figure 5.2-2. The not corrected and corrected DCS ratios as well as the collection efficiency ratios  $C$  are listed.

$\Delta E$ (eV)	$E_{in}$ (eV)	$C$	180°/0° DCS ratio	
			not corrected	corrected
4.18	4.38	1.038	0.54	0.56
"	5.68	0.963	0.28	0.27
"	7.18	0.963	1.89	1.81
"	10.18	0.973	5.31	5.17
"	14.18	0.963	5.27	5.08

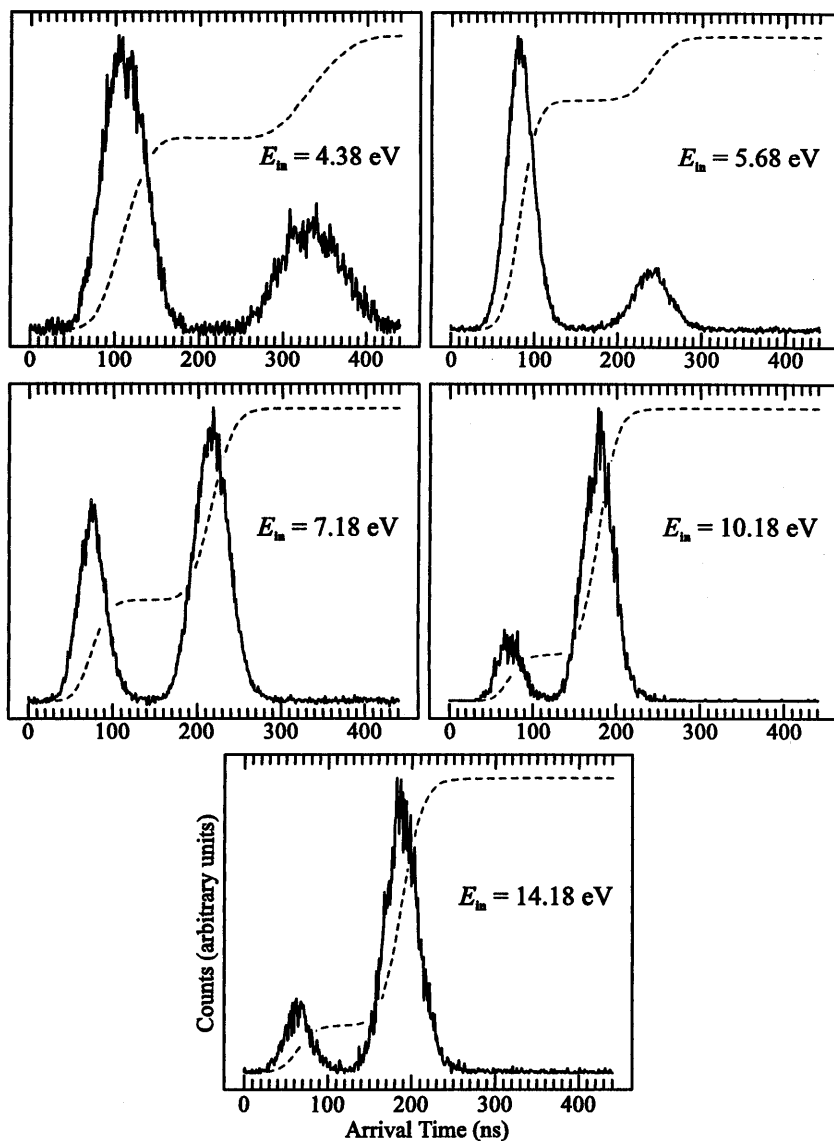


Figure 5.2-2

Arrival time distributions measured at an energy-loss of 4.18 eV, close to the vertical excitation energy of the  $1^3B_{1u}$  state, as a function of incident electron energy: (a) 4.38, (b) 5.68, (c) 7.18, (d) 10.18 and 14.18 eV. The broken line indicates the integral of the counted electrons over the arrival time.

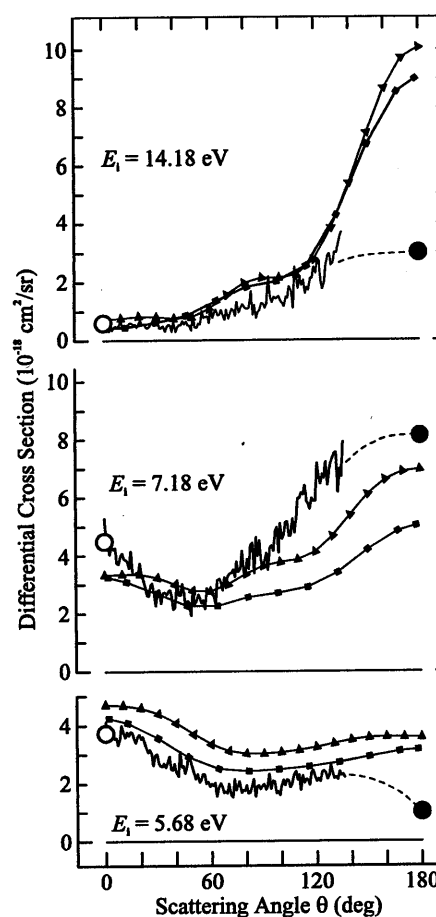


Figure 5.2-3

DCS for the excitation of the triplet band as a function of scattering angle. The lines without symbols represent the experimental cross sections measured with the electrostatic instrument (Allan 1996). The large black dots represent the absolute DCS determined in the present study, by multiplying the measured DCS ratio with the absolute value at 0° (large white dots, taken from Allan 1996). The DCS between 136° and 180° is visually interpolated (broken line). Squares connected by straight lines represent the results of the calculation of Rescigno and Schneider (1992), at 6.0, 7.0 and 15.0 eV, triangles connected by straight lines the results of the calculation of McKoy and Winstead (1993), at 5.5, 7.5 and 14.5 eV. All theoretical values were multiplied by a constant factor of 0.45 to permit a better comparison of the form of the DCSs.

The separation of the bands decreases with higher incident energy, but is still sufficient to avoid overlap. The bands are wider at smaller incident and thus smaller residual energy, because of the spread in residual energies and the increasing analyzer acceptance angle with decreasing residual energy. The “180°” band is wider than the “0°” band due again to the spread in residual energies. All of these observations are not substance specific, but of general nature.

The DCS ratios determined on the basis of the depicted arrival time distributions are listed in Table 5.2-1. The small variations in the collection efficiency ratios  $C$  (within 1% of the ideal ratio of 50% to 50% for electrons scattered into 0° and 180°) underline the good performance of the instrument.



We estimate the uncertainty of the determined DCS ratios, mainly due to the drift of the electrode potentials, to be less than 10%.

The combination of the DCS ratio with the absolute 0° DCS, measured with the electrostatic instrument, yields the absolute 180° DCS. Complications were encountered in the measurement of 0° DCSs with the electrostatic instrument at 14.18 eV, where the cross section is very small, resulting in a larger uncertainty for this value. Furthermore, the present results indicate, that the angular resolution of the electrostatic instrument is somewhat higher than that of the trochoidal instruments (see Section 5.1 for a discussion of the angular resolution of the trochoidal instrument). Consequently, the 0° values used for the determination of the absolute 180° DCSs (large white dots in Figure 5.2-3) were averaged over the DCSs measured at scattering angles ranging from 0° to 3°.

The present results are compared to the experimental results of Allan (1996) and the theoretical results of Rescigno and Schneider (1992, complex Kohn method) and McKoy and Winstead (1993, Schwinger multichannel method) in Figure 5.2-3. Both calculations overestimate the absolute magnitude of the DCS by at least a factor of two. Therefore, all calculated curves have been scaled by a factor 0.45 to permit a better comparison of the form of the DCSs. In a qualitative sense, the calculated results reproduce well the main features in the spectrum showing the dependence of the cross section on the scattering angle, especially the transition from forward peaked scattering process at low incident energy to a strongly backward peaked scattering process at higher incident energy.

The absolute DCSs as a function of incident electron energy are shown for various scattering angles in Figure 5.2-4. The excitation functions shown at the bottom of Figure 5.2-4 were measured with the trochoidal instrument. The spectra were corrected for the transmission of the analyzer, assuming a response function proportional to  $1/E_r$ , and normalized to the absolute single point data. The top five spectra in Figure 5.2-4 were measured with the electrostatic instrument (Allan 1996). The signal in the 0° excitation functions increases strongly above threshold and peaks at 6.3 eV, after which it decreases. A shoulder is revealed on the low-energy side of the band centered about 1.5 eV above threshold. In the 180° excitation function the low energy shoulder is more pronounced and the band maximum has moved to 7.3 eV. Furthermore, the signal drop-off at higher incident energies is less steep at 180° degrees, resulting in a pronounced backward peaking of the DCS in the incident energy range above 7 eV.

The 90° spectrum published earlier (Allan 1994) is intermediate between the present 0° and 180° spectra. The band peaking at 7.0 eV was attributed to the  $^2(\pi, \pi^{*2})$  2p-1h shape resonance and the low-energy shoulder to the high-energy tail of  $^2(\pi^*)$  1p shape resonance. We extend this assignment to the corresponding features in the 0° and 180° excitation functions. The present data

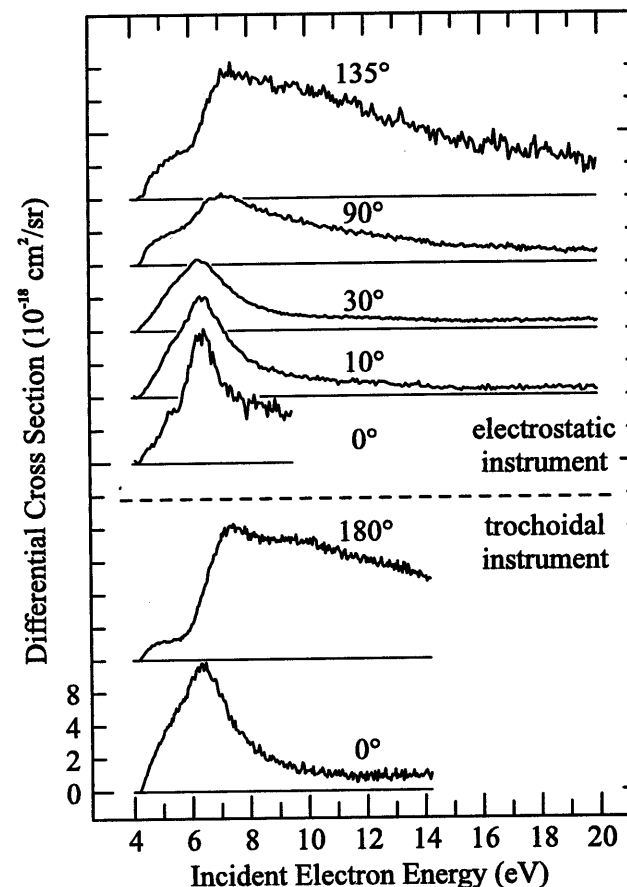


Figure 5.2-4

Absolute DCSs as a function of incident electron energy measured close to the vertical excitation energy of the  $1^3B_{1u}$  state ( $\Delta E = 4.18$  eV). The top five spectra were measured with the electrostatic instrument, the bottom two with the trochoidal instrument.

thus reveals that the excitation of the  $1^3B_{1u}$  state via the  $^2(\pi^*)$  1p shape resonance shows no pronounced angular dependency (at 0°, 90° and 180°). The  $^2(\pi, \pi^{*2})$  2p-1h shape resonance has a stronger influence on the angular distributions. With increasing scattering angle the band observed in the DCS is moved to higher incident energy. Note, that the absolute magnitude of the DCS at the bands maximum in the 0 and 180° excitation functions is similar. The increase in the DCS above 8 eV, when going from 0° over 90° to 180°, indicates a third scattering mechanism, which shows strong backward peaking.

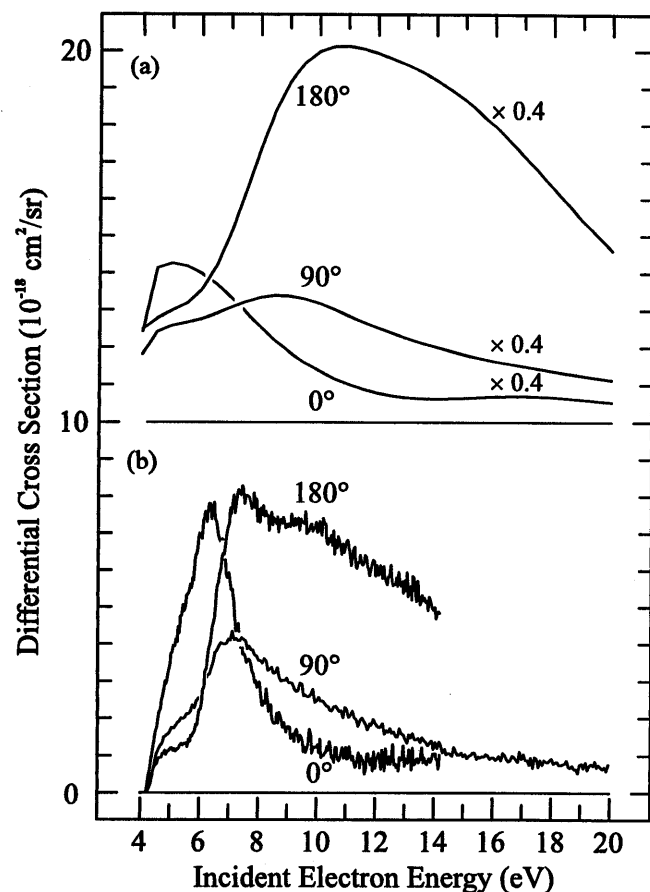


Figure 5.2-5

Comparison of the calculated excitation functions (McKoy and Winstead 1993) to the experimental excitation functions determined at 0°, 90° and 180°. The 0° and 180° excitation functions were recorded with the trochoidal instrument, the 90° excitation function with the electrostatic instrument (Allan 1994).

Both 0° excitation functions, measured with the two different instruments, show a band peaking at 6.3 eV. The band in the spectrum recorded with the electrostatic instrument is not as broad and the signal drop off is less steep. In the excitation function measured at 10° both the band width and the slope of the signal drop off are similar to that measured in the 0° spectrum, recorded with the trochoidal instrument. We assume that both, the lower angular resolution of the trochoidal instrument in comparison to the electrostatic instrument and the higher uncertainty associated with the measurement of 0° DCSs with the electrostatic instrument are responsible for this behavior.

In Figure 5.2-5 the experimental excitation functions are compared to the calculated excitation functions of McKoy and Winstead (1993). As already mentioned, the calculations predict an absolute value by more than a factor of two too high. The qualitative features are reproduced satisfactorily. The main band in both the calculated and experimental spectra moves to higher incident energy with increasing scattering angle and gains in width. Both the magnitude of the shift and the increase in width are over estimated by the theory. The DCS at 180° is predicted to be the largest, in agreement with our observations. There is a subtle final point: a broad, weak shoulder can be discerned in the theoretical spectrum at about 16 eV. Interestingly, a shoulder is observed, at 10 eV, also in the experimental spectra at high scattering angles.

### 5.3. Electron Energy-Loss Spectroscopy and Theoretical Study of Triplet and Singlet Excited States of Fulvene

#### 5.3.1. Introductory Remarks

The article presented in the following section is the result of a combined experimental and theoretical study of the lowest excited states of fulvene and 6,6'-dimethylfulvene. The project was initiated several years ago by the measurement of the EEL spectra of 6,6'-dimethylfulvene (Schafer 1992), which remained unpublished, in part due to complications encountered in the interpretation of the spectra. During the course of this thesis computational models became available, in particular the CASSCF/CASPT2 method, which were superior to previous available models with respect to the accuracy of the predicted excitation energies. The goal was to interpret the EEL spectra on the basis of CASSCF/CASPT2 calculations.

It was soon realized that it would be advantageous to include fulvene, the parent compound of 6,6'-dimethylfulvene, in this study. Surprisingly, no experimental information on the low-lying triplet states of this valence-isomer of benzene was available, probably due to the complications encountered in its synthesis resulting in small yields. After several attempts J.-L. Roulin from our institute was able to synthesize about 100 mg of 96% pure fulvene. Note that with this minimal amount of substance it was possible not just to measure several survey EEL spectra, but also to apply the novel technique for measuring electrons scattered into 180°. This turned out to be of importance, because only on the basis of the 180° spectra was it possible to directly (and more exactly) determine the energies of the two lowest triplet states.

The following article nicely shows the advantages of the novel instrument. (i) Besides being able to determine absolute 180° DCSs of excitation processes in atoms and molecules (see Chapters 5.1 and 5.2) in order to understand better the fundamental principles of electron-atom and electron-molecule collisions, 180° degree spectra are also very useful in the detection of triplet states, relevant for photochemistry. (ii) Although it is now possible *in principal* to detect electrons scattered into large angles, *i.e.* larger than 160°, by modified electrostatic electron spectrometers, their significantly higher (about one order of magnitude) substance consumption leaves the current instrument unrivaled in cases where only material in the order of 100 mg are readily available.

In the course of this study M. Fülcher (University of Lund, Sweden), among others co-programmer of the MOLCAS suite of programs, has kindly agreed to become involved in the present theoretical study. In particular, I had

performed CASSCF/CASPT2 calculations only on the valence excited states and was interested in the inclusions of Rydberg states in the treatment. These kind of calculations require some prior experience and he readily offered his help and performed extensive calculations with adequate basis sets in order to treat Rydberg states. Problems with these calculations were then encountered and could not be solved in the available time period, after which we chose to go on with the publication and postpone the Rydberg state study.

#### 5.3.2. Article (Submitted for Publication)

### Electron-Energy-Loss Spectroscopy and Theoretical Study of Triplet and Singlet Excited States of Fulvene

Knut R. Asmis, Michael Allan, Olivier Schafer

Institut de Chimie Physique, Université de Fribourg, Pérolles, CH-1700 Fribourg, Switzerland

Markus Fülcher

Department of Theoretical Chemistry, Chemical Centre, P.O.B. 124, S-221 00 Lund, Sweden

#### Abstract.

Triplet and singlet excited states of fulvene and 6,6'-dimethylfulvene were studied in the gas phase by electron-energy-loss spectroscopy. Two valence triplet states were observed for each compound, with vertical transition energies of 2.35 eV and 3.10 eV for fulvene and 2.35 eV and 3.00 eV for 6,6'-dimethylfulvene. The states are assigned as  $^3B_2$  and  $^3A_1$ . The  $^1B_2$  and  $^1A_1$  valence singlet states and two Rydberg bands, known from photoabsorption spectroscopy, were also observed. To support the assignments multi-configurational second-order perturbation calculations (CASSCF/CASPT2) were performed. The calculated energies of the first two valence triplet and singlet transitions are within 0.19 eV of the experiment.

#### Introduction

Fulvene was first synthesized at the beginning of this century.<sup>1</sup> The fact that it is a non-alternant cross conjugated cyclic hydrocarbon and at the same time a valence isomer of benzene motivated particular interest in its electronic structure. The specific conjugation pattern of fulvene results in unusual and

interesting properties of its excited states and is manifested in various types of spectra.

Singlet excited states of fulvene were studied by photoabsorption spectroscopy,<sup>2,4</sup> which revealed four electronic transitions in the region from 550 to 168 nm. The lowest, with absorption maximum at 360 nm (3.44 eV), lies in the visible. It is responsible for the yellow color of fulvene and is assigned as a valence  $^1B_2$  transition. It is weak ( $f < 0.01$ ) and is generally reported to be structureless. Weak sharp vibrational structure was observed, however, in the gas phase absorption with very long path length and in the crystal absorption spectra of Domaille *et al.*,<sup>3</sup> with an origin at  $19685\text{ cm}^{-1}$  (2.44 eV). The vibrational structure has several unusual properties: (i) it shows blue shaded sequences, indicating an excited state potential 'stiffer' than the ground state, with respect to a vibration proposed to be  $b_1$  ring out-of-plane bend, and (ii) it is shifted towards the blue in the crystal spectra. The second band lies in the ultraviolet with a maximum at 235 nm (5.28 eV), has vibrational structure and is assigned as a valence  $^1A_1$  transition. Two transitions with sharp vibrational structure are further observed  $\lambda_{0,0} = 202\text{ nm}$  (6.14 eV) and  $\lambda_{0,0} = 178\text{ nm}$  (6.97 eV). They were shown to be Rydberg by matrix isolation and high-pressure perturbation spectra,<sup>4</sup> but ambiguity exists about their assignment.

Less information is available on the triplet states. The lowest excited triplet state of 6,6'-dimethylfulvene (a more stable derivate of fulvene, hereafter referred to as dimethylfulvene) was recently observed in the electron energy-loss (EEL) spectrum in the condensed phase, with the sample deposited at low temperature on a thin film of argon.<sup>5</sup> Preliminary gas phase EEL spectra of dimethylfulvene were recorded in our laboratory but remained unpublished.<sup>6</sup>

The electronic structure of fulvene has been the subject of various semi-empirical and *ab initio* studies which have been reviewed elsewhere.<sup>5,7</sup> There are only few studies of triplet and Rydberg states. Dreyer and Klessinger<sup>7</sup> recently presented semiempirical and *ab initio* calculations of excitation energies and excited state geometries including triplet states. They predicted two low lying triplet states,  $^3B_2$  at 2.45 eV and  $^3A_1$  at 3.04 eV. The higher of these states is calculated to be strongly stabilized by torsion around the exocyclic double bond. Energies of singlet excited valence and Rydberg states were calculated by Galasso.<sup>8</sup>

In the present contribution we present a combined experimental and theoretical study of the triplet and the singlet excited states of both the parent compound fulvene and of dimethylfulvene in the gas phase.

The experimental study employs a magnetically focused electron impact spectrometer to record EEL spectra in the gas phase. This instrument measures, in its standard continuous mode of operation, the sum of electrons scattered into  $0^\circ$  and  $180^\circ$  and is capable to detect dipole allowed transitions at higher residual energies as well as dipole- or spin-forbidden transitions at low residual

energies. To further enhance the visibility of triplet states in cases of overlapping transitions, we recorded selected spectra at a scattering angle of  $180^\circ$  alone, using a newly developed 'electron mirror' device.<sup>9</sup>

In the theoretical part we calculated the excitation energies of both fulvene and dimethylfulvene using the complete-active-space self-consistent field and multi-reference second-order perturbation method (CASSCF/CASPT2)<sup>10-13</sup>.

## Experimental Section

The trochoidal electron spectrometer used in this work has been described in detail previously.<sup>14</sup> It focuses the electron beam by an axial magnetic field and uses trochoidal monochromators<sup>15</sup> both to prepare a quasimonoenergetic incident electron beam and to analyze the energies of the scattered electrons. This spectrometer can be operated in a continuous and a pulsed mode. In both modes of operation electrons scattered into  $180^\circ$  are reflected by a potential barrier, reenter the target chamber and ultimately also reach the analyzer. In the standard continuous mode of operation a superposition of electrons scattered into  $0^\circ$  and  $180^\circ$  is consequently measured. We have recently developed a pulsed mode of operation, where electrons scattered into  $0^\circ$  and  $180^\circ$  are separated using the difference in their arrival time at the detector. The details of this new technique will be described elsewhere.<sup>9,16</sup> The pulsed mode of operation is used here in some cases to enhance the visibility of the triplet states by recording spectra where only electrons scattered into  $180^\circ$  were detected. The resolution was *ca.* 50 meV and the energy scale is accurate to within 30 meV.

Fulvene was prepared by the technique of Jones and Kent<sup>17</sup> involving the gas-phase thermal rearrangement of hexa-1,5-diyne and purified by preparative gas-chromatography. The 96% pure fulvene was stored at 200 K. Hexa-1,5-diyne was obtained from Aldrich Chemical. Dimethylfulvene was purchased from Aldrich Chemical at a stated purity of 98%. The purity of the samples was checked by gas chromatography coupled with mass spectrometry (GC-MS). The samples were degassed by repeated freeze-thaw cycles under vacuum and measured at room temperature, where they showed no signs of decomposition.

## Computational Methods

The structure and atom numbering of fulvene and dimethylfulvene are given in Figure 1. The ground state geometries of fulvene and dimethylfulvene were optimized using the density functional theory (DFT) B3LYP<sup>18,19</sup> method in combination with a triple- $\zeta$  plus double polarization (TZ2P)<sup>20</sup> basis set. During optimization, the molecules were forced to preserve  $C_{2v}$  symmetry, this assumption being justified by earlier experimental<sup>21,22</sup> and theoretical<sup>5,7,23</sup> studies.

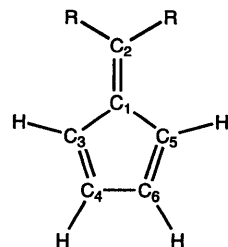


Figure 1

Atom numbering in fulvene ( $R=H$ ) and dimethylfulvene ( $R=CH_3$ ).

To calculate the electronic spectra we used atomic natural orbital (ANO) type basis sets<sup>24</sup> of triple zeta quality for the first row atoms (C/4s3p2d, H/3s1p). The CASSCF/CASPT2 method<sup>10-13</sup> was used for all excited state calculations. This method is a two step procedure to calculate state energies corrected through second-order in perturbation theory with a CASSCF wave function constituting the reference function. In general, the active space is chosen such as to include all strongly correlating orbitals, *i.e.* orbitals with occupation numbers appreciably different from two or zero. Thereby all static correlation and near-degeneracy effects are included in the CASSCF reference function, and consequently there will be no large terms in the perturbation expansion. The dipole transition moments are computed using the CAS State Interaction (CASSI) method.<sup>25</sup> Energy differences corrected by CASPT2 are used in the oscillator strength formula.

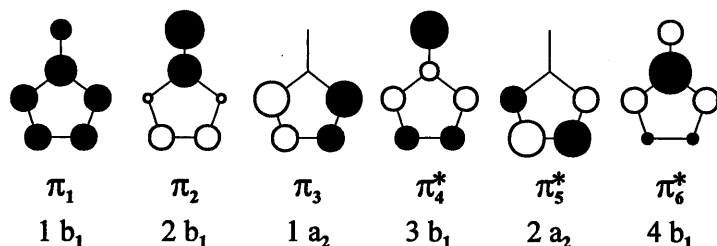


Figure 2

Numbering and symmetry specification of the valence  $\pi$ -orbitals of fulvene. The  $\pi$ -orbitals of dimethylfulvene centered on the fulvene moiety are qualitatively similar and therefore the same numbering is used. The pseudo  $\pi$ -orbitals of dimethylfulvene (C-H bonding and antibonding orbitals) are labeled  $\pi_{CH}$  and  $\pi_{CH}^*$ .

The strongly correlating orbitals in fulvene are the six valence  $\pi$ -orbitals (Figure 2), of which the three lowest in energy ( $\pi_1$ - $\pi_3$ ) are doubly occupied in the ground state SCF wave function. Therefore the minimal active space for

fulvene comprised six  $\pi$ -orbitals (four of  $b_1$  and two of  $a_2$  symmetry) with six active electrons. Due to the appearance of intruder states<sup>26</sup>, the active space was enlarged by four orbitals (two of  $b_1$  and two of  $a_2$  symmetry). The basic CASSCF wave functions were thus constructed by distributing the six  $\pi$ -electrons in all permissible ways among ten  $\pi$ -orbitals.

In comparison to fulvene dimethylfulvene possesses additional pseudo  $\pi$ -orbitals (C-H bonding and antibonding orbitals). At first all ten  $\pi$ -electrons and the corresponding ten  $\pi$ -orbitals were kept active. It was soon realized that the two lowest (pseudo)  $\pi$ -orbitals remained almost doubly occupied and they were therefore moved to the inactive space. To avoid problems caused by intruder states two orbitals (one of  $b_1$  and one of  $a_2$  symmetry) were added to the active space. This resulted in six active electrons distributed among ten active orbitals (six of  $b_1$  and four of  $a_2$  symmetry).

The calculations have been performed with the MOLCAS-3 program package<sup>27</sup> on IBM RS/6000 workstations except for the DFT geometry optimizations which used the GAUSSIAN 94 program package<sup>28</sup>.

Table 1

Experimental vertical (unless otherwise noted) excitation energies ( $\Delta E_{exp}$ ) for the excited states of fulvene. Values in parentheses state oscillator strengths *f*.

state	$\Delta E_{exp}$ (eV)			
	photoabsorption			EEL
	solution <sup>a</sup>	vapor <sup>b</sup>	matrix <sup>c</sup>	vapor <sup>d</sup>
T <sub>1</sub>				2.35
T <sub>2</sub>				3.10
S <sub>1</sub>	3.42 (.008)	3.44 (.0042)	3.44	3.34
S <sub>2</sub>	5.12 (.34)	5.28	5.30	5.27
Rydberg		6.14 <sup>e</sup>		6.16 <sup>e</sup>
Rydberg				6.75
Rydberg		6.97 <sup>e</sup>		7.15 <sup>f</sup>

<sup>a</sup>References 29 and 30. <sup>b</sup>References 2 and 3. <sup>c</sup>Reference 4. <sup>d</sup>Present work. <sup>e</sup>0-0 excitation energy. <sup>f</sup>0-0 excitation energy is 6.99 eV.

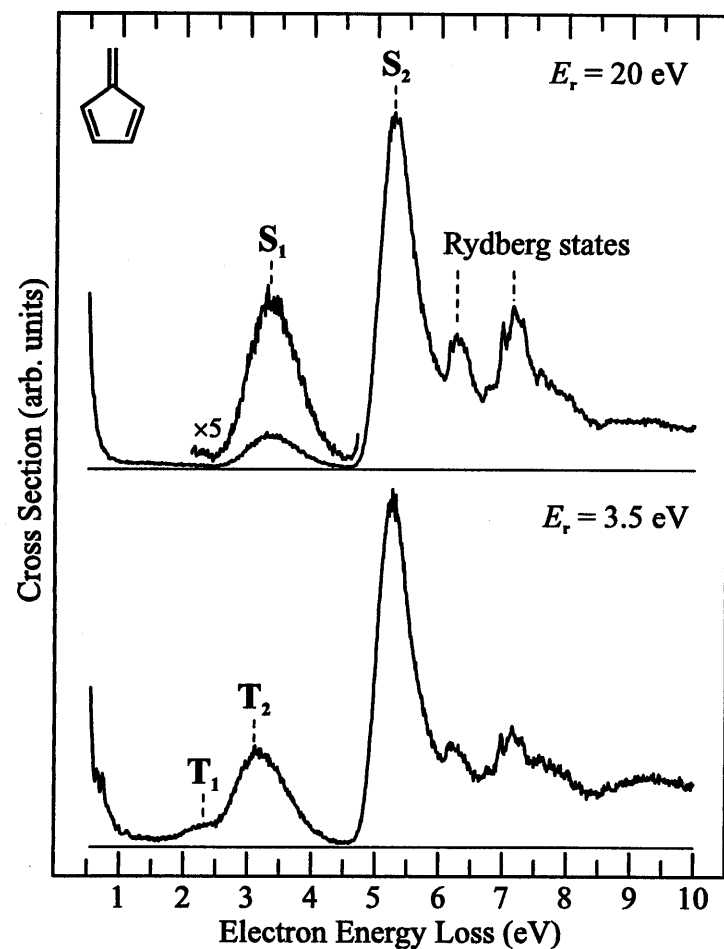


Figure 3

Global energy-loss spectra of fulvene, recorded with a constant residual energy of 20 eV and 3.5 eV. Singlet-triplet excitations are enhanced at low residual energies.

### EEL Spectra of Fulvene

**Valence States.** Representative EEL spectra of fulvene are shown in Figure 3. The top spectrum, recorded at a high residual energy of 20 eV when optically allowed transitions predominate, is in accord with the photoabsorption measurements. The transition energies are summarized in Table 1. The two bands at 3.34 and 5.27 eV are due to the valence singlet-singlet transitions  $S_1$  and  $S_2$ . The bands above 6.0 eV with partly resolved vibrationally structure are due to Rydberg states.

The spectrum recorded at the lower residual energy of 3.5 eV shows the excitation of both the triplet and the singlet states, and the bands which are new with respect to the  $E_r = 20$  eV spectrum may thus be assigned to triplet states. (The signal below 1.5 eV is due to excitation of high vibrational levels of the electronic ground state and will not be further discussed.) The shoulder at 2.35 eV is due to the lowest triplet state  $T_1$ . The maximum of the next band moved to lower energy by 0.18 eV in comparison with the  $E_r = 20$  eV spectrum, indicating the presence of the second triplet state  $T_2$ , partially overlapping with the  $S_1$  state.

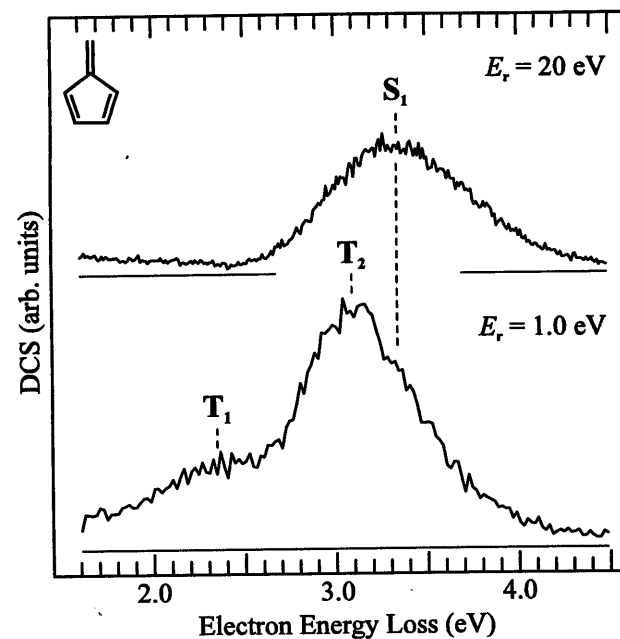


Figure 4

Energy-loss spectra of fulvene recorded in the range of the lowest singlet and triplet transitions at a constant residual energy of 1.0 and 20 eV. The  $E_r = 1.0$  eV spectrum was recorded at a scattering angle of  $180^\circ$ , using the pulsed mode of operation.

Angular distributions of scattered electrons are characteristic of the nature of the electronic states excited. Optically allowed transitions are characterized by a forward peaked behavior, while spin-forbidden transitions show a more isotropic or even backward peaked angular behavior, resulting in a relative enhancement of triplet signal at high scattering angles. We therefore used the capability of our spectrometer to record exclusively the backward signal in the pulsed mode of operation to enhance the triplet transition in the

region of overlap. The result is shown in the bottom part of Figure 4. The shoulder with an onset at 1.8 eV and a vertical transition energy of  $2.35 \pm 0.10$  eV is attributed to the lowest triplet excited state  $T_1$ . The subsequent band peaks at 3.10 eV, significantly below the peak of the  $S_1$  band at 3.34 eV in the  $E_r = 20$  eV spectrum, confirming the presence of the  $T_2$  state. The determination of the vertical transition energy of the  $T_2$  state is complicated by the overlap with the  $S_1$  band, it could lie up to 0.2 eV below the maximum of the band. We put it at  $3.10 \pm 0.2$  eV.

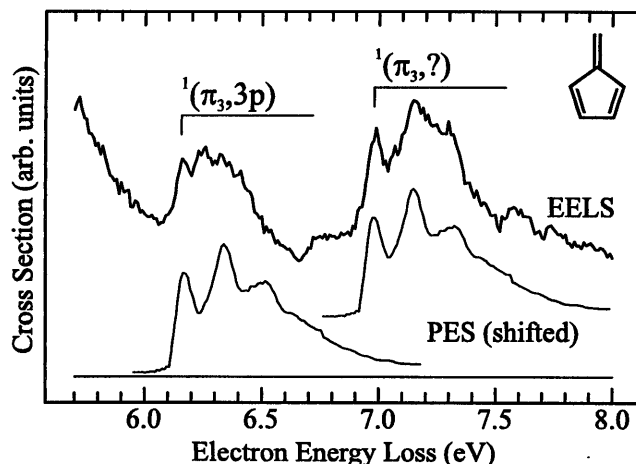


Figure 5

Electron-energy-loss spectra of fulvene recorded with a constant residual energy of 20 eV compared with the profile of the first ionization band in the photoelectron (PE) spectrum. The adiabatic ionization energy is 8.36 eV.<sup>31</sup> PE band is shown shifted by -2.20 and -1.38 eV.

**Rydberg States.** The similarity of the band envelope of the bands at 6.26 eV and 7.15 eV with the band envelope of the lowest UV-photoelectron band<sup>31</sup>, illustrated in Figure 5 suggests that these bands are due to Rydberg states associated with the lowest ionization energy. The two bands are well known from the photoabsorption spectra, but there is no generally accepted assignment. Originally these two bands were attributed by Harman *et al.*<sup>4</sup> to excited 3s-type Rydberg states of  $^1B_1$  symmetry, denoted as  $^1(\pi_2,3s)$  and  $^1(\pi_2,4s)$ . (see Scheme 1 for the numbering of the  $\pi$ -orbitals) Robin<sup>32</sup> proposed the assignment  $(\pi_3,3p)$  and  $(\pi_3,4p)$ . This assignment of the first Rydberg band is now relatively undisputed and results in a quantum defect of  $\delta = 0.51$ , conform with a 3p assignment. It also agrees with the calculated energies of Galasso<sup>8</sup> (6.43 eV for  $3p_x$ , 6.59 eV for  $3p_y$ , both having about the same oscillator strength). It may be of interest to note that the highest occupied molecular orbital (HOMO) of

fulvene  $\pi_3$  is predominantly localized on the cis-butadiene-like substructure, and is reminiscent of the HOMO of cyclopentadiene ( $IE_1 = 8.58$  eV)<sup>33</sup>. And in fact, the EEL spectra of cyclopentadiene<sup>9,34</sup> show a feature at 6.3 eV, which has been assigned to two 3p-Rydberg type transitions<sup>34,35</sup>. Galasso<sup>8</sup> pointed out, that the assignment of the second Rydberg band to  $(\pi_3,4p)$  results in a quantum defect of  $\delta = 0.86$ , too large for a p-type orbital. An alternative assignment is  $^1(\pi_3,3d)$ . It is in agreement with the calculated transition energy<sup>8</sup> (7.22 eV for  $3d_{xy}$ , which carries the largest oscillator strength of all the 3d orbitals), but in disagreement with the calculated oscillator strengths<sup>8</sup> (3d is calculated weaker than 4p). The assignment of the 7.15 eV band thus remains uncertain. Note that no band of similar intensity is observed in the appropriate energy region of the EEL spectra of cyclopentadiene. Finally, a shoulder is observed in our spectra at 6.75 eV, the right energy for an assignment as  $^1(\pi_2,3s)$ , calculated to be at 6.95 eV and to have a substantial oscillator strength.<sup>8</sup>

Table 2  
Experimental vertical excitation energies ( $\Delta E_{exp}$ ) for the excited states of dimethylfulvene.

state	$\Delta E_{exp}$ (eV)		
	photoabsorption	EEL	
	solution <sup>a</sup>	thin film <sup>b</sup>	vapor <sup>c</sup>
$T_1$		2.3	2.35
$T_2$			3.00
$S_1$	3.45	3.35	3.35
$S_2$	4.74	4.9	4.74
Rydberg			5.89 <sup>d</sup>
Rydberg			6.51
Rydberg			6.95

<sup>a</sup>Reference 36. <sup>b</sup>Reference 5. <sup>c</sup>Present work. <sup>d</sup>Further peaks at 5.76 (0-0) and 6.02 eV.

### EEL Spectra of Dimethylfulvene

**Valence states.** Representative EEL spectra are shown in Figure 6, the transition energies are summarized in Table 2. The general features of the spectra are very similar to those of fulvene. The first two bands in the spectrum with  $E_r = 20$  eV, with maxima at 3.35 and 4.74 eV, are attributed to the two lowest valence singlet-singlet transitions  $S_1$  and  $S_2$ , known already from optical measurements in solution (3.45 and 4.68 eV)<sup>36</sup> and from EEL spectra of condensed dimethylfulvene (3.35 and 4.9 eV)<sup>5</sup>. In comparison to the fulvene

spectrum, the  $S_2$  band has gained considerably in intensity especially with respect to the two Rydberg bands at 5.88 and 6.95 eV.

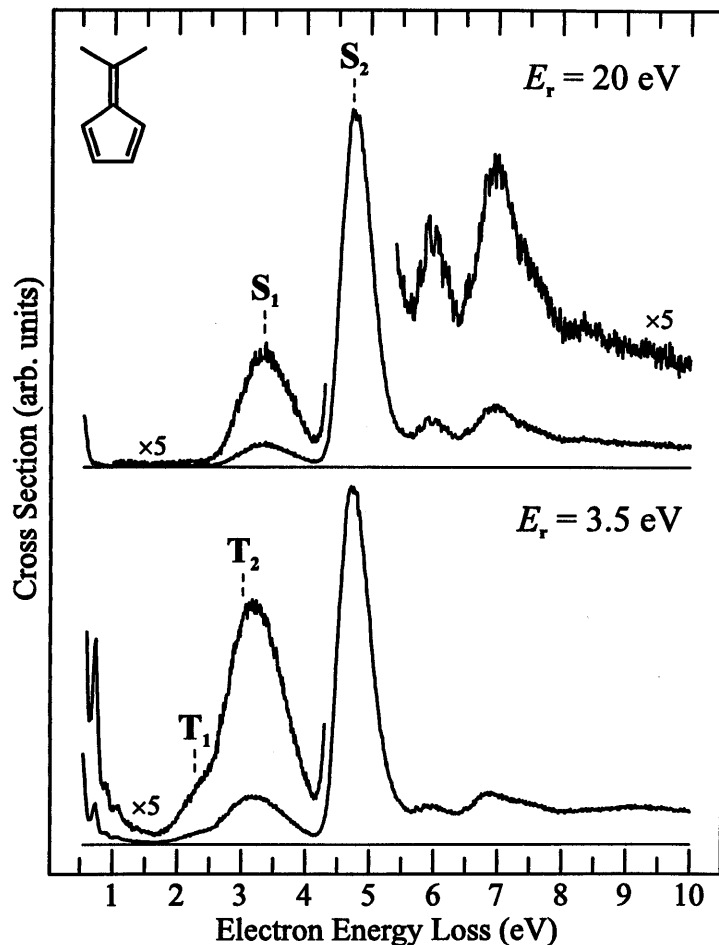


Figure 6

Survey electron energy-loss spectra of dimethylfulvene.

The shoulder at 2.35 eV in the spectrum with  $E_r = 3.5$  eV is assigned to the  $T_1$  state. A shift of the maximum of the subsequent band by 0.15 eV to lower energies in the  $E_r = 3.5$  eV spectrum indicates the presence of the  $T_2$  state. An attempt to resolve the overlapping  $T_2$  and  $S_1$  bands has been made using spectra (Figure 7) where electrons scattered into the forward and the backward directions are separated. The spectra show the presence of the  $T_2$  and  $S_1$  bands

very clearly and the best enhancement of the  $T_2$  band over the  $S_1$  band is attained at  $180^\circ$  and a residual energy of 1 eV, placing  $T_2$  at 3.00 eV.

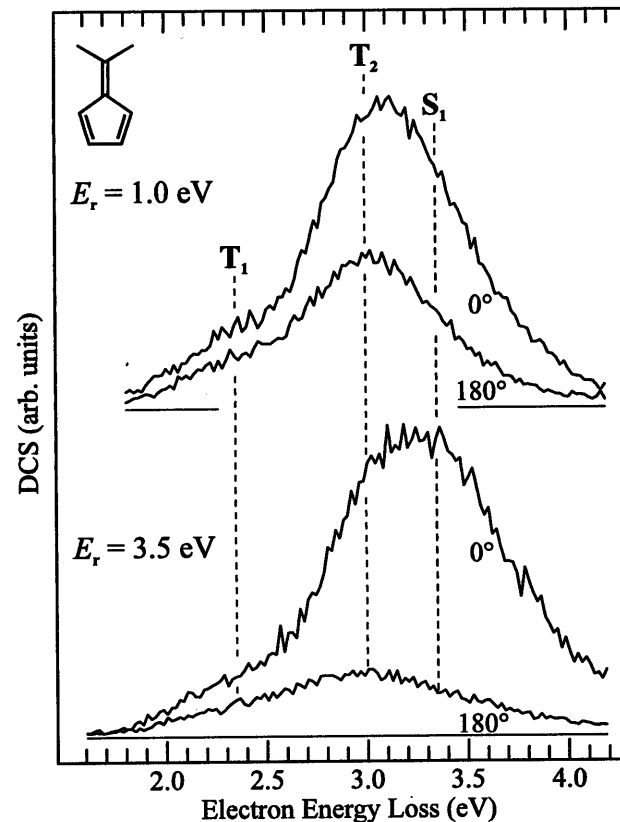


Figure 7

Electron energy-loss spectra of dimethylfulvene in the range of the lowest singlet and triplet transitions, recorded at constant residual energies of 1.0 and 3.5 eV. The spectra were recorded at  $0^\circ$  and  $180^\circ$ , using the pulsed mode of operation. The most complete suppression of the  $S_1$  state, and thus the best visibility of the  $T_2$  state is achieved at  $180^\circ$  and  $E_r = 1.0$  eV.

**Rydberg states.** The similarity of the band profile of the 5.88 eV energy-loss band with the profile of the first photoelectron band (Figure 8) identifies it as Rydberg converging to the first IE (8.08 eV, vertical)<sup>37</sup>. The quantum defect of  $\delta = 0.48$  indicates a  $^1(\pi_{3,3}p)$  assignment. The vibrational structure is surprisingly clear in view of the fact that two overlapping allowed transitions



( $p_x$ , and  $p_y$ ) are expected. The Rydberg assignment of this band is confirmed by its absence in the condensed phase EEL spectra of Swiderek *et al.*<sup>5</sup> (Figure 9).

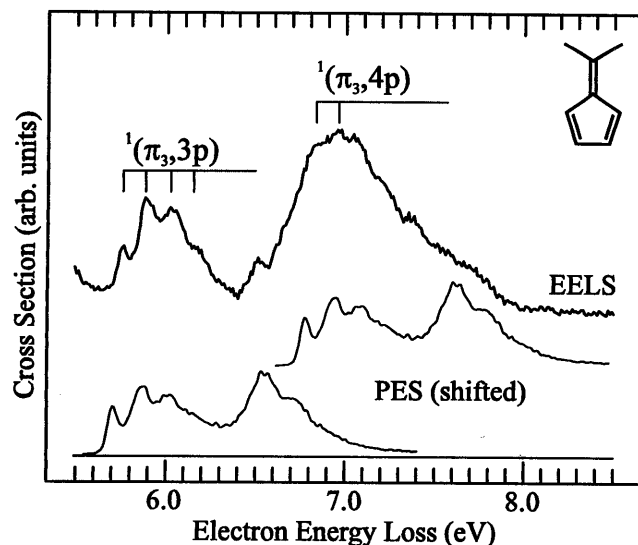


Figure 8

Electron-energy-loss spectra of dimethylfulvene recorded with a constant residual energy of 20 eV compared with the profile of the first two ionization bands in the photoelectron (PE) spectrum. (The adiabatic ionization energies are 7.89 and 8.72.)<sup>6</sup> PE bands are shown shifted by -2.19 and -1.12 eV.

The vibrational structure of the more intense band peaking at 6.95 eV is much less pronounced, a fact which can be explained by several overlapping Rydberg transitions, although a contribution from a valence transition can not be excluded. Problems encountered while attempting to assign this band are similar to those already discussed for fulvene. The possible assignments include  $1(\pi_3,4p)$  and  $1(\pi_3,3d)$ , an unambiguous assignment not being possible at this stage. Finally the peak at 6.51 eV could be assigned as  $1(\pi_2,3p)$  or  $1(\pi_3,3d)$ .

### Calculations

**Geometries.** The calculated bond distances and angles of fulvene and dimethylfulvene are given in Table 3 and compared to a selection of earlier theoretical<sup>5,23</sup> and experimental<sup>21,22</sup> structure determinations. A detailed discussion of the previous theoretical studies on the geometry of fulvene can be found in the paper of Dreyer *et al.*<sup>7</sup>. For fulvene the B3LYP results agree well with the experimental values. The comparison in Table 3 shows that the B3LYP results are of similar quality as the MP2-geometry, but they were attained at a

fraction of the computational cost. For dimethylfulvene the differences between calculation and experiment are larger but still reasonable. Both AM1 and B3LYP predict the  $C_1-C_2$  and  $C_3-C_4$  bonds to be longer than in fulvene, while the experiment determines them to be shorter. Noticeable deviations between theory and experiment are also found for the C-C-H angles.

Table 3

Optimized and experimental ground state geometries (in Å and degrees) and total energies  $E$  (in a.u.) for fulvene and dimethylfulvene ( $C_{2v}$ -symmetry assumed). See Figure 1 for atom numbering.

	fulvene			dimethylfulvene			
	AM1 <sup>a</sup>	MP2 <sup>b</sup> (6-31G*)	B3LYP <sup>c</sup> (TZ2P)	exp. <sup>d</sup>	AM1 <sup>a</sup>	B3LYP <sup>c</sup> (TZ2P)	exp. <sup>e</sup>
$C_1C_2$	1.332	1.348	1.350	1.349	1.346	1.366	1.347
$C_1C_3$	1.483	1.466	1.479	1.470	1.482	1.478	1.476
$C_3C_4$	1.363	1.358	1.361	1.355	1.365	1.365	1.340
$C_4C_6$	1.476	1.468	1.480	1.476	1.472	1.469	1.462
$C_2C_7$	-	-	-	-	1.484	1.511	1.510
$C_3C_1C_5$	105.2	106.6	106.3	106.6	104.8	105.6	106
$C_1C_3C_4$	108.6	107.7	107.8	107.7	108.8	108.3	108
$C_3C_4C_6$	108.8	109.2	109.0	109.0	108.8	108.9	109.0
$C_1C_2R$		122.0	122.0	122.0		122.9	122.0
$C_1C_3H(3)$		123.4	124.5	124.7		125.6	123
$C_3C_4H(4)$		127.3	126.5	126.4		126.2	120
$E$		-231.3983	-232.1682			-310.7804	

<sup>a</sup>Reference 5. <sup>b</sup>Reference 23. <sup>c</sup>Present work. <sup>d</sup>Reference 22. <sup>e</sup>Reference 21.

**Transition Energies.** This study concentrates on the low-lying valence excited singlet and triplet states and does not attempt to treat the Rydberg states correctly. The calculated transition energies of fulvene and dimethylfulvene are given in Table 4 and Table 5. The present results are compared to previous *ab initio* calculations in Table 6. The weight  $\omega$  of the CASSCF reference function in the first-order perturbed wave function is an indication of a balanced treatment of electron correlation and the values of  $\omega$  were therefore included in Tables 4 and 5. They should ideally be the same for the ground and all excited electronic states under consideration. The present values of  $\omega$  for valence excited states are satisfactory, although they are generally somewhat smaller than for the ground state, reflecting the larger importance of dynamic electron correlation effects. Tables 4 and 5 also indicate the wave functions in terms of molecular orbitals (MOs). Although the MOs are not identical for states of

different spin or symmetry in a CASSCF calculation, a qualitative comparison of the contributing configurations is still useful and legitimate, since the nodal properties of the MOs are preserved.

Table 4

Calculated excitation energies  $\Delta E$  (in eV) and wave functions of the  $\pi \rightarrow \pi^*$  excited states of fulvene. Ground state energies (in a.u.) are -230.808485 (CASSCF) and -231.576083 (CASPT2).

state	$\Delta E$		$f^a$	$\omega^b$	wave function <sup>c</sup>
	CASSCF	CASPT2			
singlet states <sup>d</sup>					
$1^1A_1$	0.00	0.00		.79	86% $\pi_1^2 \pi_2^2 \pi_3^2$
$1^1B_2$	4.07	3.29	.005	.77	72% $\pi_3 \rightarrow \pi_4^*$ 13% $\pi_2 \pi_3 \rightarrow \pi_4^{*2}$
$2^1A_1$	5.94	5.30	.060	.75	20% $\pi_2 \rightarrow \pi_4^*$ 17% $\pi_3^2 \rightarrow \pi_4^{*2}$ 13% $\pi_1 \rightarrow \pi_4^*$ 12% $\pi_3 \rightarrow \pi_5^*$
$3^1A_1$	6.78	5.75	.248	.76	52% $\pi_2 \rightarrow \pi_4^*$ 14% $\pi_1 \rightarrow \pi_4^*$ 10% $\pi_3^2 \rightarrow \pi_4^{*2}$
$2^1B_2$	7.77	6.46	.020	.73	52% $\pi_2 \pi_3 \rightarrow \pi_4^{*2}$ 18% $\pi_3 \rightarrow \pi_4^*$
$3^1B_2$	7.16	6.88	.150	.76	87% $\pi_3 \rightarrow \pi_6^*$
triplet states <sup>d</sup>					
$1^3B_2$	2.51	2.27		.78	86% $\pi_3 \rightarrow \pi_4^*$
$1^3A_1$	3.09	2.97		.78	84% $\pi_2 \rightarrow \pi_4^*$
$2^3A_1$	5.27	5.06		.77	44% $\pi_3 \rightarrow \pi_5^*$ 28% $\pi_1 \rightarrow \pi_4^*$
$2^3B_2$	6.15	5.65		.74	40% $\pi_3 \rightarrow \pi_6^*$ 36% $\pi_2 \pi_3 \rightarrow \pi_4^{*2}$

<sup>a</sup>Oscillator strength in a.u.. <sup>b</sup>The weight of the CASSCF reference function in the first-order wave function. <sup>c</sup>Excitations, which contribute more than 10% to the CASSCF wave function are listed. <sup>d</sup>For each symmetry/spin group the lowest  $n$  states were included in the state-average CASSCF calculation:  $n = 3$  ( $1^1A_1$ ), 3 ( $1^1B_2$ ), 2 ( $3^1A_1$ ) and 2 ( $3^1B_2$ ).

Table 5

Calculated excitation energies  $\Delta E$  (in eV) and wave functions of the  $\pi \rightarrow \pi^*$  excited states of dimethylfulvene. Ground state energies (in a.u.) are -308.908494 (CASSCF) and -309.994187 (CASPT2).

state	$\Delta E$		$f^a$	$\omega^b$	wave function <sup>c</sup>
	CASSCF	CASPT2			
singlet states <sup>d</sup>					
$1^1A_1$	0.00	0.00		.73	86% $\pi_1^2 \pi_2^2 \pi_3^2$
$1^1B_2$	4.22	3.29	.006	.71	78% $\pi_3 \rightarrow \pi_4^*$ 10% $\pi_2 \pi_3 \rightarrow \pi_4^{*2}$
$2^1A_1$	5.80	4.93	.134	.69	36% $\pi_2 \rightarrow \pi_4^*$ 13% $\pi_3 \rightarrow \pi_5^*$ 11% $\pi_3^2 \rightarrow \pi_4^{*2}$
$3^1A_1$	6.61	5.40	.243	.69	37% $\pi_2 \rightarrow \pi_4^*$ 21% $\pi_1 \rightarrow \pi_4^*$ 13% $\pi_2^2 \rightarrow \pi_4^{*2}$ 10% $\pi_3^2 \rightarrow \pi_4^{*2}$
$2^1B_2$	6.60	6.52	.046	.72	87% $\pi_3 \rightarrow \pi_{CH}^*$
$3^1B_2$	7.33	7.22	.081	.71	85% $\pi_3 \rightarrow \pi_{CH}^*$
triplet states <sup>d</sup>					
$1^3B_2$	2.41	2.34		.72	87% $\pi_3 \rightarrow \pi_4^*$
$1^3A_1$	2.94	2.93		.72	88% $\pi_2 \rightarrow \pi_4^*$

<sup>a</sup>Oscillator strength in a.u.. <sup>b</sup>The weight of the CASSCF reference function in the first-order wave function. <sup>c</sup>Excitations, which contribute more than 10% to the CASSCF wave function are listed. <sup>d</sup>For each symmetry/spin group the lowest  $n$  states were included in the state-average CASSCF calculation.  $n = 3$  ( $1^1A_1$ ), 3 ( $1^1B_2$ ), 1 ( $3^1A_1$ ) and 1 ( $3^1B_2$ ).

**Singlet states.** In fulvene the lowest valence excited singlet state ( $1^1B_2$ ) is calculated at 3.29 eV, in excellent agreement with the experimental value of 3.34 eV. It corresponds to the  $\pi_3 \rightarrow \pi_4^*$  (HOMO  $\rightarrow$  LUMO) excitation and is predicted to be the weakest ( $f = 0.005$ ) of the five dipole-allowed transitions, in agreement with its low intensity in the spectrum. Two singlet excited states ( $2^1A_1$  and  $3^1A_1$ ) are calculated in the 5-6 eV range where the most intense singlet band is observed. They are a mixture of singly- and doubly-excited configurations. The assignment of the intense singlet band at 5.27 eV (labeled  $S_2$  in the spectrum of Figure 3) thus remains somewhat ambiguous at this stage. The assignment to  $2^1A_1$  results in a good agreement in terms of transition

energy, but a discrepancy in terms of intensity (Table 6). The observed large intensity and large calculated oscillator strength make an assignment to  $3^1A_1$  more preferable, but the discrepancy of calculated and observed transition energies (Table 6) is much larger than customary for the CASPT2 model. This problem could possibly be solved by inclusion of Rydberg states in the calculation. Finally the relatively strong transition to the  $3^1B_2$  state ( $f = .150$ ) is calculated at 6.88 eV, which is likely to be hidden underneath the Rydberg transitions in the crowded spectral region around 7 eV.

Table 6

Excitation energies (in eV) and oscillator strengths (in a.u., in parentheses) for the low-lying excited states of fulvene and dimethylfulvene.

state	CIPSI <sup>a</sup>	RPA <sup>b</sup>	CAS <sup>c</sup>	CAS <sup>d</sup>	CASPT2 <sup>e</sup>	exp. <sup>e</sup>
fulvene						
1 $^3B_2$ (T <sub>1</sub> )	2.76		2.62	2.45	2.27	2.35
1 $^3A_1$ (T <sub>2</sub> )	3.44		3.26	3.04	2.97	3.10
1 $^1B_2$ (S <sub>1</sub> )	3.82 (.006)	4.15 (.023)	4.24	3.72	3.29 (.005)	3.34
2 $^1A_1$ (S <sub>2</sub> ) <sup>f</sup>	5.82 (.09)	5.82 (.721)	6.15	5.89	5.30 (.060)	5.27
3 $^1A_1$ (?) <sup>f</sup>			7.48	6.93	5.75 (.248)	
dimethylfulvene						
1 $^3B_2$ (T <sub>1</sub> )					2.34	2.35
1 $^3A_1$ (T <sub>2</sub> )					2.93	3.00
1 $^1B_2$ (S <sub>1</sub> )					3.29 (.006)	3.35
2 $^1A_1$ (S <sub>2</sub> ) <sup>f</sup>					4.93 (.134)	4.74
3 $^1A_1$ (?) <sup>f</sup>					5.40 (.243)	

<sup>a</sup>Reference 38. <sup>b</sup>Reference 8. <sup>c</sup>Reference 5. <sup>d</sup>Reference 7. <sup>e</sup>Present work. <sup>f</sup>Assignment uncertain.

The situation in dimethylfulvene is very similar to that in fulvene. Note that now both the  $2^1A_1$  and the  $3^1A_1$  states are calculated somewhat higher in energy than the observed intense singlet band, indicating that the present calculation neglecting the Rydberg states provides only approximate description of the higher-lying singlet states.

Note that the calculation correctly reproduces the fact that the  $1^1B_2$  state is at essentially the same energy in dimethylfulvene and in fulvene. In contrast, the energies of both  $^1A_1$  states are calculated to red-shift upon methyl-substitution by 0.37 and 0.35 eV, respectively. This red shift compares

favorably with the 0.53 eV shift of the observed  $S_2$  band. Note also that the calculated oscillator strength of the  $1^1A_1 \rightarrow 2^1A_1$  transition has increased upon methyl-substitution, possibly a consequence of the larger contribution by the  $\pi_2 \rightarrow \pi_4^*$  configuration to the  $2^1A_1$  wave function.

**Triplet states.** The agreement of the experimental and calculated transition energies for the lowest two triplet states is excellent both in fulvene and in dimethylfulvene. The calculation also reproduces correctly the somewhat unexpected fact that both triplet transitions do not shift noticeably upon methyl-substitution. The calculation indicates that the doubly-excited configurations contribute less to the triplet state wave functions than to the singlet state wave functions.

## Discussion and Conclusions

The calculated excitation energies for the three lowest excited states of both fulvene and dimethylfulvene agree with experiment to within 0.13 eV, which is about equal to the uncertainty of localizing the maximum of the broad experimental bands, thus confirming that CASPT2 is a very precise method for calculating excitation energies. The agreement is less satisfactory for the second, intense singlet band. For both compounds, the calculation predicts two excited states,  $2^1A_1$  and  $3^1A_1$ , both with substantial oscillator strength (Table 6), whereas only one band (labeled  $S_2$  in Figs. 3 and 6) is observed in the spectra. The present calculation thus does not entirely account for the observations, it either strongly exaggerates the oscillator strength of the  $3^1A_1$  transition, or it predicts both the  $2^1A_1$  and  $3^1A_1$  states too high in energy (by different amounts) and the  $S_2$  band is an overlap of both transitions. The same problem has already been encountered by Swiderek *et al.*<sup>5</sup> in their CAS calculations, but does not appear in the RPA calculations of Galasso<sup>8</sup>. At the present time it does not appear possible to identify the cause of the discrepancy between experiment and the results of our calculations. We confine ourselves to noting that it may be necessary to include the Rydberg orbitals more extensively in the calculation to obtain the energies of the higher-lying singlet states with better precision, and that it may further be necessary to optimize the MOs separately for each excited state in order to obtain accurate oscillator strengths.<sup>39</sup>

Comparison of the spectra of fulvene and dimethylfulvene reveals that three of the valence bands,  $T_1$ ,  $T_2$ , and  $S_1$ , experience no shift upon methylation (within the  $\pm 0.1$  eV uncertainty of localizing the maxima of the broad bands), whereas  $S_2$  shifts substantially, by 0.53 eV toward lower energy. The behavior of the singlet bands has already been discussed and qualitatively explained by Straub *et al.*<sup>30</sup>. The lack of shift of the two triplet states, although correctly reproduced by the CASPT2 calculations, is interesting and somewhat surprising when orbital energy differences alone are regarded. Tables 4 and 5 show that the electron is promoted from the  $\pi_3$  and  $\pi_2$  orbitals in the  $T_1$  and  $T_2$  states, respectively, and that both transitions have the same final orbital  $\pi_4^*$ . The

ionization energies from the  $\pi_2$  and  $\pi_3$  orbitals experience substantially different shifts, 0.79 and 0.47 eV, upon methyl substitution, however.<sup>37</sup>

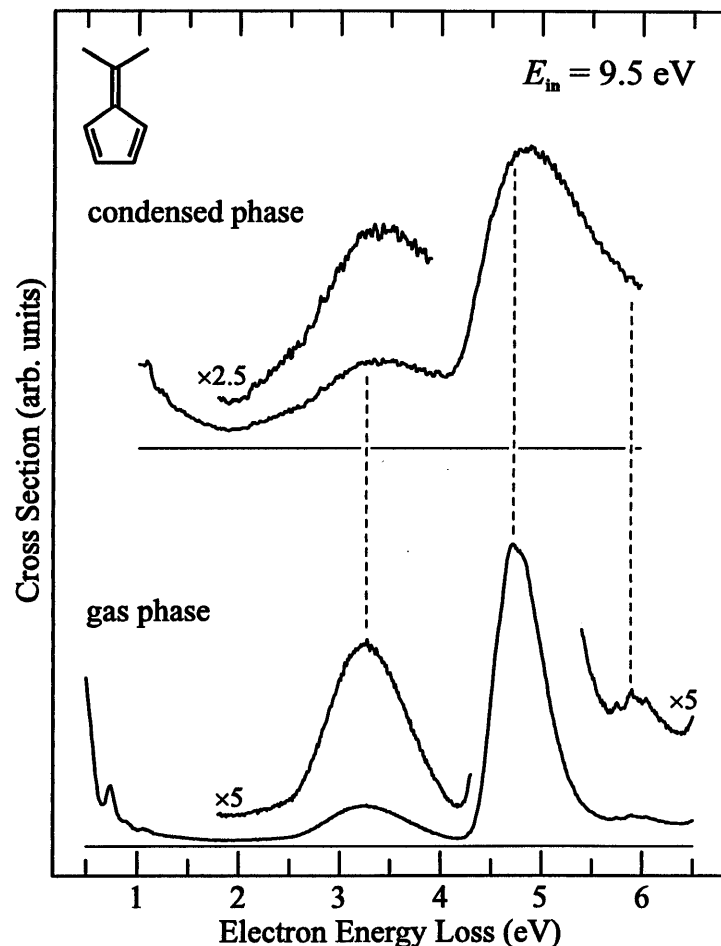


**Figure 9**

Comparison of the present gas phase EEL spectra of dimethylfulvene with the EEL spectra obtained for less than a monolayer of dimethylfulvene deposited on frozen argon by Swiderek *et al.*<sup>5</sup> Both spectra were recorded with a constant incident energy of 9.5 eV.

Very interesting is the comparison of the present gas phase spectrum with the frozen thin film spectrum of Swiderek *et al.*<sup>5</sup> shown for dimethylfulvene in Figure 9. The spectra are very similar in their general aspect, but differ in a

number of interesting details. Perhaps the most interesting is the consistently larger width of the individual electronic bands in the thin film spectrum. This observation has already been made with the matrix spectra of benzene<sup>40</sup> and the thin film spectra of butadiene,<sup>41</sup> and can be expected to occur generally. The increased width of the  $^1E_{1u}$  state of benzene has been ascribed to a drastic reduction of its lifetime due to autoionization.<sup>40</sup> We note that the increased width of in particular the low-lying triplet bands could also be due to an increase of the Franck-Condon width caused by the excitation of molecule-matrix vibrations in the thin-film spectrum, induced by the increased size and thus larger fulvene-matrix equilibrium distance in the electronically excited state.

The Rydberg band at 5.7-6.0 eV is expectedly absent in the thin film spectrum. The fact that the  $T_1$  band is relatively weaker in the present spectrum at an incident energy of 9.5 eV could be caused by the different scattering angles employed in the two experiments and is thus not further significant until more detailed measurements of angular distributions are made. The present results indicate that a comparison of gas phase and frozen thin film spectra for a wider range of compounds could yield interesting information on host-substrate interactions and help to identify Rydberg character of electronic transitions in the future.

#### Acknowledgement

We wish to express our sincere appreciation to Professor E. Haselbach for his continuing support and encouragement in the present work. The spectrometer could not have been constructed without the exceptional enthusiasm and ingenuity of E. Brosi of the mechanical laboratory and P.-H. Chassot of the electronics laboratory. We thank Professor M. Neuenschwander for a sample of dimethylfulvene and J.-L. Roulin for his efforts in the synthesis and purification of fulvene. This work is part of project 2028-040398.94/1 of the Swiss National Science Foundation.

#### References and Notes

- (1) Thiele, J. *Ber. dt. chem. Ges.* **1900**, *33*, 666.
- (2) Brown, R. D.; Domaille, P. J.; Kent, J. E. *Aust. J. Chem.* **1970**, *23*, 1707.
- (3) Domaille, P. J.; Kent, J. E.; O'Dwyer, M. F. *Chem. Phys.* **1974**, *6*, 66.
- (4) Harman, P. J.; Kent, J. E.; O'Dwyer, M. F.; Smith, M. H. *Aust. J. Chem.* **1979**, *32*, 2579.
- (5) Swiderek, P.; Michaud, M.; Sanche L. *J. Chem. Phys.* **1995**, *103*, 8424.
- (6) Schafer, O., Ph. D. Thesis, University of Fribourg, Switzerland, 1992.
- (7) Dreyer, J.; Klessinger, M. *J. Chem. Phys.* **1994**, *101*, 10655.
- (8) Galasso, V. *Chem. Phys.* **1993**, *171*, 171.

- (9) Asmis, K. R., Ph. D. Thesis, University of Fribourg, Switzerland, in preparation.
- (10) Roos, B. O.; Andersson, K. *Chem. Phys. Letters* **1995**, *245*, 215.
- (11) Roos, B. O. in *Advances in Chemical Physics; Ab Initio Methods in Quantum Chemistry - II*, Lawley, K. P., Ed., chapter 69, p 399. John Wiley & Sons Ltd., Chichester, England, 1987.
- (12) Andersson, K.; Malmqvist, P.-A.; Roos, B. O.; Sadlej, A. J.; Wolinski, K. *J. Phys. Chem.* **1990**, *94*, 5483.
- (13) Andersson, K.; Malmqvist, P.-A.; Roos, B. O. *J. Chem. Phys.* **1992**, *96*, 1218.
- (14) Allan, M. *J. Electron Spectrosc. Relat. Phenom.* **1989**, *48*, 219.
- (15) Stamatovic, A.; Schulz, G. *J. Rev. Sci. Instrum.* **1970**, *41*, 423.
- (16) Allan, M.; Asmis, K. R., unpublished results.
- (17) Kent, J. E.; Jones, A. J. *Aust. J. Chem.* **1970**, *23*, 1059.
- (18) Becke, A. D. *Phys. Rev. A* **1988**, *38*, 3098.
- (19) Lee, C.; Yang, W.; Parr, R. G. *Phys. Rev. B* **1988**, *37*, 785.
- (20) (a) Huzinaga, S. *J. Chem. Phys.* **1965**, *42*, 1293. (b) Dunning, T. H. *J. Chem. Phys.* **1971**, *55*, 716. (c) We used the standard Huzinaga and Dunning triple- $\zeta$  basis set of contracted Gaussian functions augmented with three sets of Cartesian d-like polarization functions in a 2,1 contraction on the carbons ( $\alpha_d(\text{C}) = 1.375, 0.407, 0.340$ ) and three sets of p-type polarization functions in a 2,1 contraction on the hydrogens ( $\alpha_p(\text{H}) = 1.220, 0.284, 0.260$ ).
- (21) Chiang, J. F.; Bauer H. S. *J. Am. Chem. Soc.* **1970**, *92*, 261.
- (22) Baron, P. A.; Brown, R. D.; Burden, F. R.; Domaille, P. J.; Kent, J. E. *J. Mol. Spectrosc.* **1972**, *43*, 401.
- (23) Replogle, E. S.; Trucks, G. W.; Staley, S. W. *J. Phys. Chem.* **1991**, *95*, 6908.
- (24) Widmark, P.-O.; Malmqvist, P.-Å.; Roos, B. O. *Theor. Chim. Acta* **1990**, *77*, 291.
- (25) Malmqvist, P.-Å.; Roos, B. O. *Chem. Phys. Letters* **1989**, *155*, 189.
- (26) Roos, B. O.; Fülischer, M.; Malmqvist, P.-Å.; Merchán, M.; Serrano-Andrés, L. *Quantum Mechanical Electronic Structure Calculations with Chemical Accuracy*, Langhoff, S. R., Ed., p 357. Kluwer Academic Publishers, Dordrecht, The Netherlands, 1995.
- (27) Andersson, K.; Fülischer, M. P.; Karlström, G.; Lindh, R.; Malmqvist, P.-Å.; Olsen, J.; Roos, B. O.; Sadlej, A. J.; Blomberg, M. R. A.; Siegbahn, P. E. M.; Kellö, V.; Noga, J.; Urban, M.; Widmark, P.-O. MOLCAS Version 3. Dept. of Theor. Chem., Chem. Center, Univ. of Lund, P.O.B. 124, S-22100 Lund, Sweden, Lund, 1994.
- (28) Frisch, M. J.; Trucks, G. W.; Schlegel, H. B.; Gill, P. M. W.; Johnson, B. G.; Robb, M. A.; Cheeseman, J. R.; Keith, T. A.; Petersson, G. A.; Montgomery, J. A.; Raghavachari, K.; Al-Laham, M. A.; Zakrzewski, V. G.; Ortiz, J. V.; Foresman, J. B.; Cioslowski, J.; Stefanov, B. B.; Nanayakkara, A.; Challacombe, M.; Peng, C. Y.; Ayala, P. Y.; Chen, W.; Wong, M. W.; Andres, J. L.; Replogle, E. S.; Gomperts, R.; Martin, R. L.; Fox, D. J.; Binkley, J. S.; Defrees, D. J.; Baker, J.; Stewart, J. P.; Head-Gordon, M.; Gonzalez, C.; Pople, J. A. Gaussian 94 (Revision B.3); Gaussian, Inc.: Pittsburgh, PA, 1995.

- (29) Thiec, J.; Wiemann, J. *Bull. Soc. Chim. France* **1956**, *23*, 177.
- (30) Straub, P. A.; Meuche, D.; Heilbronner, E. *Helv. Chim. Acta* **1965**, *49*, 517.
- (31) Heilbronner, E.; Gleiter, R.; Hopf, H.; Hornung, V.; de Meijere, A. *Helv. Chim. Acta* **1971**, *54*, 783.
- (32) Robin, M. B. *Higher excited states of polyatomic molecules*, Vol. 3, Academic Press, New York, **1985**.
- (33) Derrick, P. J.; Åsbrink, L.; Edqvist, O.; Jonsson, B. Ö.; Lindholm, E. *Int. J. Mass Spectrom. Ion Physics* **1971**, *6*, 203.
- (34) Frueholz, R. P.; Flicker, W. M.; Mosher, O. A.; Kuppermann, A. *J. Chem. Phys.* **1979**, *70*, 2003.
- (35) Serrano-Andrés, L.; Merchán, M.; Nebot-Gil, I.; Roos, B. O.; Fülischer, M. *J. Am. Chem. Soc.* **1993**, *115*, 6184.
- (36) Meuche, D. *Helv. Chem. Acta* **1966**, *49*, 145.
- (37) Brogli, F.; Clark, P. A.; Heilbronner, E.; Neuenschwander M. *Angew. Chem.* **1973**, *85*, 414.
- (38) Rancurel, P.; Huron, B.; Praud, L.; Malrieu, J. P.; Bertier, G. *J. Mol. Spectrosc.* **1976**, *60*, 259.
- (39) Roos, B. O. in *Lecture Notes in Quantum Chemistry*, Roos, B. O., Ed., p 237, Springer Verlag Berlin Heidelberg, 1992.
- (40) Sanche, L.; Michaud M. *Chem. Phys. Lett.* **1981**, *80*, 184.
- (41) Swiderek, P.; Michaud, M.; Sanche L. *J. Chem. Phys.* **1993**, *98*, 8397.

## 5.4. Selective Decay of 2p-1h Shape Resonances in 1,3- Butadiene

### 5.4.1. Introduction

The current project was aimed at the study of two-particle-one-hole (2p-1h) shape resonances in 1,3-butadiene. It was stimulated by the results of recent experimental (Allan 1994) and computational (McKoy and Winstead 1993) studies on the electron impact excitation of the lowest triplet state  ${}^3B_{1u}$  of ethylene. They found that at low incident energy the excitation of this  $\pi \rightarrow \pi^*$  transition is predominantly resonant. Allan assigned the broad band observed in the  ${}^3B_{1u}$  excitation function to the  ${}^2(\pi, \pi^{*2}) {}^2B_{3u}$  2p-1h resonance, with a hole in the  $\pi$  orbital and double occupancy of the  $\pi^*$  orbital.

A deeper insight into the mechanism of resonant excitation of triplet states may be expected to be gained by this study, because butadiene has two low-lying triplet states and the additional  $\pi$  and  $\pi^*$  MO's should give rise to more 2p-1h resonances. In particular, butadiene permits the study a new dimension of the problem not present in ethylene, the selectivity of the decay of the various resonances into these two triplet states.

EEL and ET spectra as well as excitation functions are presented. The observed 2p-1h resonances are assigned on the basis of semiempirical configuration interaction (CI) calculations on the butadiene anion. This approach neglects the coupling of the anionic states to the continuum, *i.e.* pretends that they are bound by the small size of the basis set, not permitting the electron to escape. We attempt this simple approach expecting that it will qualitatively correctly reproduce the essential physics of the problem, in particular the observed branching ratios for the decay of the resonances into the various states of the neutral.

#### Overview of Previous Studies

The ET spectrum of ethylene shows one resonance, assigned to a one-particle (1p) shape resonance, associated with electron capture into the  $\pi^*$  orbital (Bardsley and Mandl 1968). Confirming the expectations based on  $\pi$  MO theory the ET spectrum of butadiene reveals two resonances, one lying below and the other above the ethylene 1p shape resonance (Jordan and Burrow 1987, and references therein). They have been assigned as  $1^2A_u$  and  $1^2B_g$ , corresponding to the capture of an electron into the  $\pi_{AS}^*$  and  $\pi_{AA}^*$  orbital (Figure 5.4-1) respectively.

Previous studies of butadiene by Abouaf and Benoit (1990) and Falcetta and Jordan (1991) indicate that vibrational excitation is predominantly resonant at lower residual energies. Both, spectra of vibrational excitation cross sections as a function of scattering angle and incident electron energy, demonstrate the

predominant activation of the  $\nu_4$  C=C stretch mode along with other  $a_g$  and  $a_u$  modes by the  $1^2A_u$  resonance (Abouaf and Benoit 1990), as predicted by the selection rules (Wong and Schulz 1975, Gallup 1986). The vibrational modes are only very weakly excited by the  $1^2B_g$  resonance. This indicates that the target geometry is not distorted appreciably during the lifetime of the resonance and thus the  $1^2B_g$  resonance is believed to be very short-lived.

Falcetta and Jordan (1991) have studied the dependence of both the higher vibrational and triplet excitation processes on incident electron energy. They concluded that the  $1^2A_u$  and  $1^2B_g$  resonance lie energetically too low to be detected in the excitation functions of the triplet states, but are observed in the vibrational excitation functions. Features in the excitation functions of the triplet states were assigned to 2p-1h resonances on the basis of semiempirical CI calculations on the cation in combination with the pairing theorem for alternant hydrocarbons (Salem 1966).

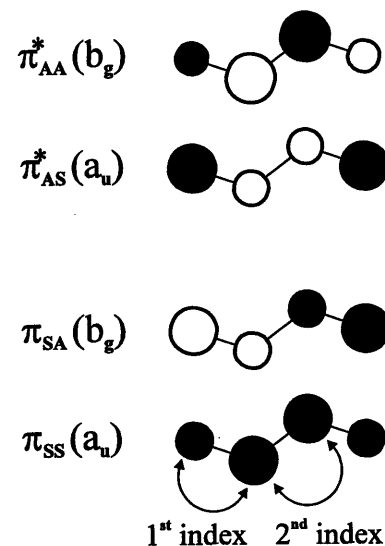


**Figure 5.4-1**  
Labeling and symmetry of the valence  $\pi$ -orbitals in butadiene. The indices S (symmetric) and A (antisymmetric) indicate the nodal properties of the wave function. In contrast to definition introduced by Hoffmann (1971) the indices are not related to any symmetry elements. In our case this nomenclature might seem controversial, but has nonetheless the advantage that the similarities in the nodal properties of the MOs of butadiene and the cycloienes, discussed in the next chapter, are emphasized.

### 5.4.2. Results

#### Electron Energy-Loss Spectra

In agreement with the previously measured low energy EEL spectra of butadiene (Kuppermann *et al.* 1979) our survey EEL spectra (Figure 5.4-2) show two valence triplet states,  $1^3B_u$  and  $1^3A_g$ . They lie at 3.2 and 4.9 eV, well below the first optically allowed transition into the  $1^1B_u$  singlet state at 5.91 eV. The transition into the  $2^1A_g$  state is dipole-forbidden and not observed.

The energy-loss region above 6 eV has been described in detail previously (Reddish *et al.* 1986, and references therein). The various series of sharp peaks are attributed to Rydberg excitations. It is of interest to note that the peak at 6.16 eV ( $E_r = 0.03$  and 0.25 eV) has not been observed in this clarity before and will be discussed in more detail in Section 5.4.3.

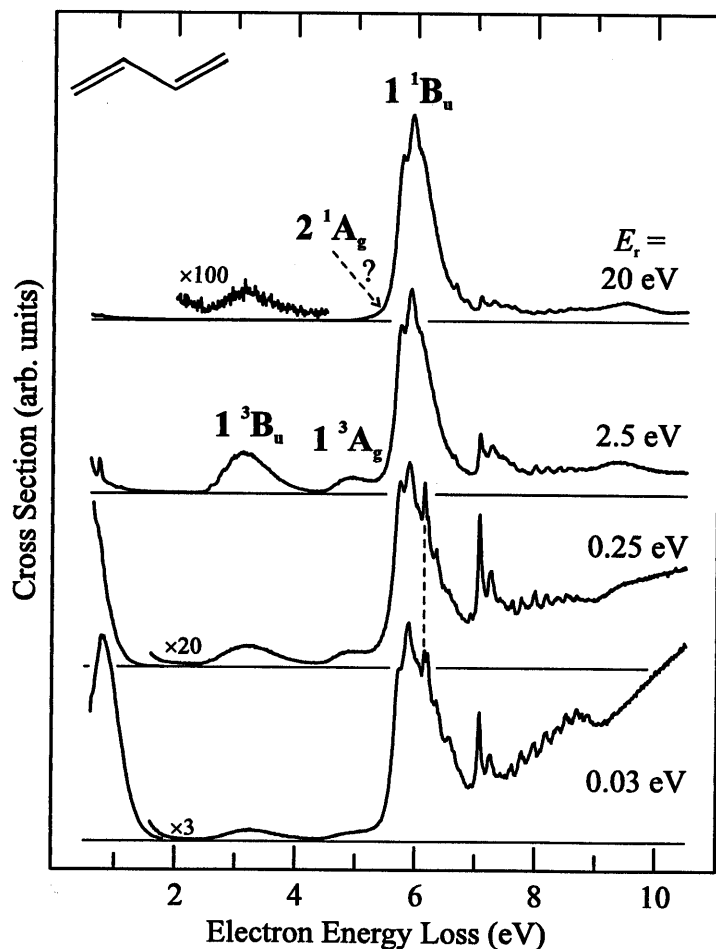


Figure 5.4-2

Survey EEL-spectra of butadiene at residual energies of 0.03, 0.25, 2.5 and 20 eV. The transitions into the lowest two triplet states are strongly enhanced at medium residual energies, while resonant vibrational excitation dominates at low residual energies.

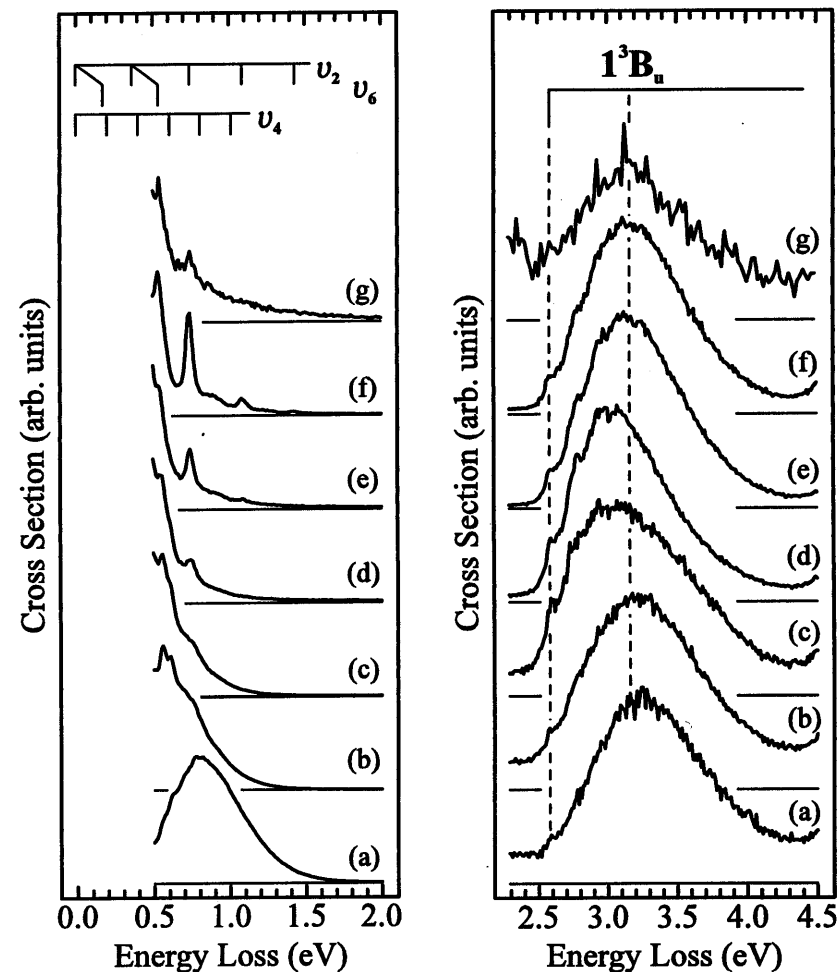


Figure 5.4-3

EEL-spectrum of butadiene recorded with  $E_r = 0.03$  (a), 0.25 (b), 0.50 (c), 1.0 (d), 2.5 (e), 5.0 (f) and 20.0 eV (g) in the energy-loss region of pure vibrational excitation (left) and of the lowest triplet transition (right).

Vibrational energy-loss spectra are shown in Figure 5.4-3 (left). A nearly unstructured band peaking at 0.8 eV is observed with  $E_r = 0.03$  eV. The band moves to lower energy-loss with increasing  $E_r$ , revealing the *unspecific* nature of the resonant vibrational excitation by the  $1^2A_u$  resonance. Unspecific resonant vibrational excitation has been observed in all polyatomic molecules

studied so far (see for example Allan 1989). Activation of the C=C stretch mode ( $\nu_4$ ) is slightly enhanced for  $E_r \leq 2.5$  eV, in accord with the  $\pi^*$  nature of the  $1^2A_u$  resonance. Enhancement of specific vibrational modes due to decay of the  $1^2B_g$  shape resonance, expected to be formed at incident energies around 2.8 eV, is not observed.

Structured spectra are observed for  $E_r \geq 2.5$  eV and are due to *specific* vibrational excitation. The  $\nu_2$  CH-stretch and  $\nu_6$  CH-bend mode are predominantly excited. CH excitation is found in all hydrocarbons and is usually ascribed to broad  $\sigma^*$  resonances (see for example Allan 1989).

Two observations with respect to the lowest triplet band (Figure 5.4-3, right) are of interest to note and will be discussed in more detail in Section 5.4.3. (i) The position of the  $1^3B_u$  band maximum varies with residual energy. With increasing residual energy the bands maximum is moved from 3.24 eV ( $E_r = 0.03$  eV) down to 3.00 eV ( $E_r = 1.0$  eV) and up to 3.16 eV ( $E_r = 20$  eV). (ii) Vibrational structure is observed in the first triplet band at medium residual energies. Starting at 2.59 eV a series of three peaks, spaced by  $0.195$  eV ( $1570 \pm 100$   $\text{cm}^{-1}$ ), is observed onto the otherwise structureless band (Figure 5.4-4), interpreted as an activation of a double bond stretch mode. The peak at 2.59 eV is ascribed to the 0-0 transition.

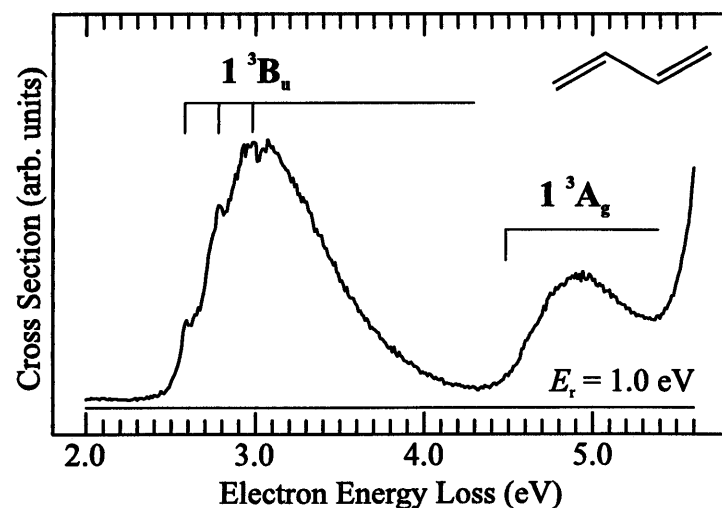


Figure 5.4-4

EEL spectrum recorded at a residual energy of 1.0 eV in the energy-loss region of the two lowest triplet transitions. The  $1^3B_u$  band shows vibrational structure with a spacing of 0.195 eV. The feature at 2.59 eV is assigned to the 0-0 transition.

### ET Spectrum and Excitation Functions

The excitation functions measured at energy-losses of 0.73, 1.08 and 1.42 eV are compared to the ET spectrum in Figure 5.4-5. The excitation energies correspond to the  $n = 2, 3$  and 4 levels of the C-H stretch mode. Note that a background of unresolved vibrations also contributes to the signal.

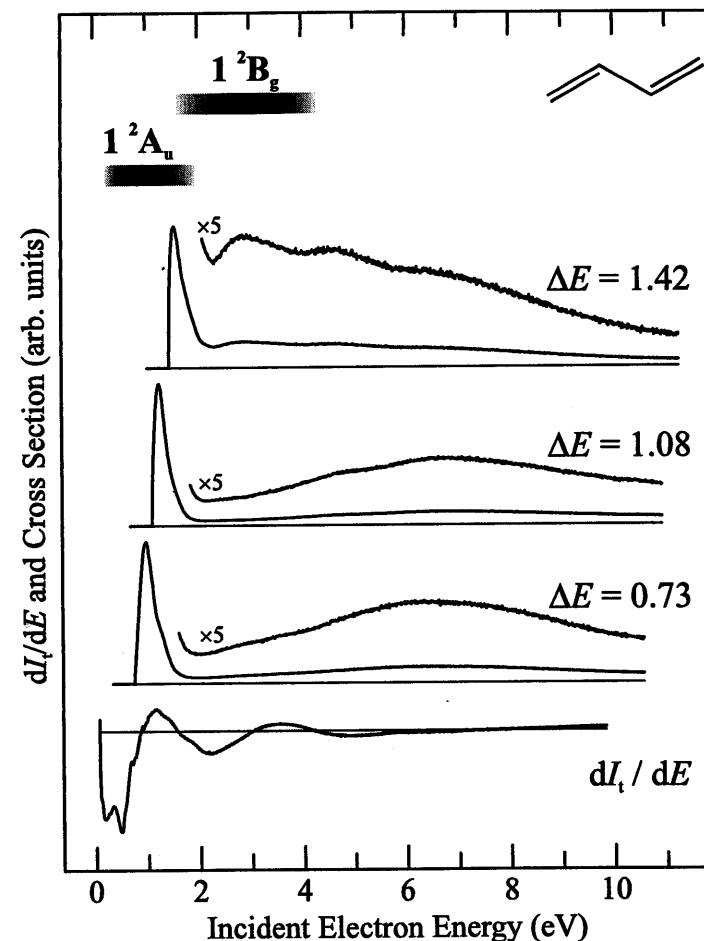


Figure 5.4-5

Comparison of vibrational excitation functions (top three) and the electron transmission spectrum (bottom) of butadiene. The center and width of the lowest two resonances are estimated and indicated by the shaded bars.



The ET spectrum reveals two resonances at 0.80 and 2.87 eV, in accord with the previously determined values of 0.62 and 2.82 (Jordan and Burrow 1987). Their assignment to the 1p shape resonances  $1^2A_u$  and  $1^2B_g$  is straight forward.

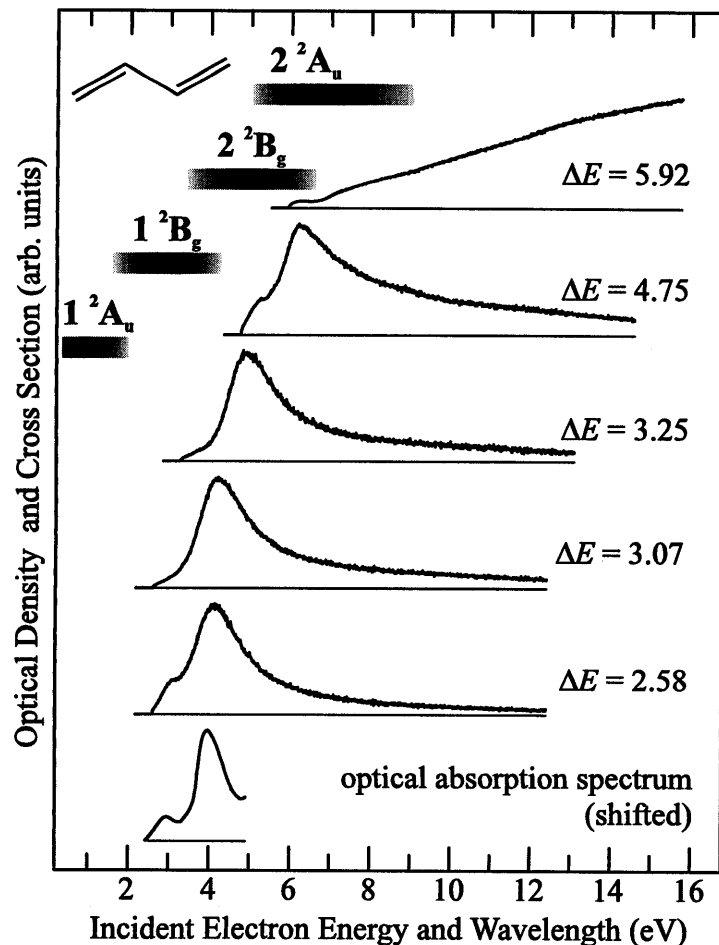


Figure 5.4-6

Excitation functions of the  $1^3B_u$  ( $\Delta E = 2.58, 3.07$  and  $3.25$  eV),  $1^3A_g$  ( $\Delta E = 4.75$  eV) and  $1^1B_u$  ( $\Delta E = 5.92$  eV) excited states of butadiene. The optical absorption spectrum of the radical anion has been shifted by 0.80 eV. The center and width of the lowest four resonances are estimated and indicated by the shaded bars.

All excitation functions show a similar structure: an intense, rather narrow and slightly structured feature slightly above threshold, followed at higher energy by much weaker and broader overlapping bands. Comparison with the ET spectrum reveals the intense feature to be due to the  $1^2A_u$  resonance. Its position is moved with increasing energy-loss to higher incident energies: 0.98 ( $\Delta E = 0.73$  eV), 1.24 ( $\Delta E = 1.08$  eV) and 1.54 eV ( $\Delta E = 1.42$  eV).

The second shape resonance ( $1^2B_g$ ) does not cause substantial signal enhancement in the excitation functions, although it is clearly visible in the ET spectrum. The weak maximum at 2.9 eV in the  $\Delta E = 1.42$  eV spectrum could be attributed to this resonance. The broad feature above 3 eV seems to be the result of at least three very broad overlapping bands centered at 4.7, 6.1 and 7.3 eV. Earlier works on other polyatomic molecules (Allan 1989) have attributed similar features to  $\sigma^*$  resonances.

In Figure 5.4-6 the excitation functions of the lowest electronic excitations are compared to the optical absorption spectrum of the radical anion measured in a glass (Shida and Hamill 1966). Since the absorption spectrum is measured relative to the ground state anion, this spectrum has been shifted by 0.80 eV, the center of the lowest resonance in the ET spectrum.

The optical absorption spectrum of the radical anion shows two peaks at 2.95 and 3.97 eV, assigned to the  $1^2A_u \rightarrow 1^2B_g$  and  $1^2A_u \rightarrow 2^2B_g$  transitions. The excitation functions of the lowest triplet state ( $1^3B_u$ ), measured at three different energy-losses of 2.58, 3.07 and 3.25 eV, are similar in form. The  $\Delta E = 2.58$  eV spectrum (0-0 transition) is the most similar, with an intense band at 4.12 and a pronounced shoulder at 3.11 eV. In agreement with the optical data, these two features are assigned to the  $1^2B_g$  and  $2^2B_g$  resonances. The signal decreases monotonically towards higher incident energy.

With increasing energy-loss the  $2^2B_g$  band moves to higher incident energies and the  $1^2B_g$  shoulder loses in relative intensity. The maximum of the  $2^2B_g$  band is shifted to 4.69 eV ( $\Delta E = 3.07$ ) and finally 4.91 eV ( $\Delta E = 3.25$  eV). The shift is close to linear with a slope less than unity, such that the bands maximum appears at decreasing residual energy with increasing energy-loss.

The excitation function of the second triplet state  $1^3A_g$  ( $\Delta E = 4.75$  eV) is similarly structured. The main band lies at 6.17 eV. A pronounced low energy shoulder is observed and the drop off of the signal intensity towards higher incident energy is less steep.

At least two interpretations of the  $\Delta E = 4.75$  eV spectrum are possible. (i) The shoulder at 5.26 eV is assigned to the  $2^2B_g$  resonance and the main band is attributed to a higher lying resonance ( $2^2A_u$ ). The absence of this band in the  $1^3B_u$  excitation functions means, that the  $2^2A_u$  resonance would selectively decay into the  $1^3A_g$  state and not into the  $1^3B_u$  state. Similarly, the  $2^2B_g$

resonance preferably decays into the  $1^3B_u$  state, causing only a weaker signal enhancement in the excitation function of the  $1^3A_g$  state.

(ii) The main band is due to the  $2^2B_g$  resonance, shifted even higher in incident energy. Assuming a linear dependence between the position of the bands maximum and  $\Delta E$  extrapolation to  $\Delta E = 4.75$  eV would predict the band to lie around 6.3 eV. This value is close to the observed one of 6.17 eV. Note that the shift of bands described previously, for example in the excitation functions of vibrational modes or of the  $1^3B_u$  state, always involved the same starting and final electronic state of the decay process. Here the bands shift is assumed to continue linearly when probing a different final electronic state.

The excitation function of the lowest optically allowed transition into the  $1^1B_u$  state has been added in order to demonstrate the very different behavior of dipole- and spin-allowed transitions. The spectrum is only weakly structured and the intensity increases monotonically with incident energy. This is characteristic for optically-allowed transitions, which are excited via a direct (non-resonant) scattering mechanism.

### Calculations

The energies of the 1p shape resonances can be predicted by applying Koopmans' theorem in combination with linear scaling parameters (Chen and Gallup, 1990). For the 6-31G basis set this results in resonance energies of 0.85 ( $1^2A_u$ ) and 3.56 eV ( $1^2B_g$ ), in reasonable agreement with experiment. This is not surprising, since butadiene was included in the determination of the scaling parameters. The drawback of this method is that it cannot make predictions on the energy of 2p-1h resonances, since it always assumes the core of the resonance to be that of the neutral ground state. A configuration interaction approach is therefore necessary for a description of 2p-1h resonances.

Thus INDO/S CI calculations were carried out. The INDO/S method and the problems, which arise when trying to calculate resonance energies, have been discussed in Chapter 3. All calculations were performed at the INDO/1 optimized geometry of butadiene. For the anionic states all single and double excitations within the  $\pi$ -manifold were considered. The optimized HF/SCF orbitals of neutral butadiene were used. Energies of the anionic states are calculated relative to the ground state anion and were converted to energies relative to the neutral ground state by adding the experimentally determined ground state energy of the anion (0.80 eV, from the ET spectrum). For the excited triplet states all singly excited configurations were included in the CI calculation. The triplet parametrisation was used.

The results for the butadiene anion are summarized in Table 5.4-1. Mixing between 1p and 2p-1h configurations is predicted to be small. The lowest two states of the anion are both of 1p type and calculated to be separated by 1.52 eV. The next three states correspond to 2p-1h resonances.

In order to gain insight into the probable decay channels of these resonances, INDO/S CI-calculations were performed for the neutral states of interest (Table 5.4-2). The lowest two valence triplet states are calculated at 2.31 and 3.78 eV, both about 1 eV lower than the experimental value. An error of 1 eV is common for the INDO/S method and is due to the semiempirical nature of this method.

Table 5.4-1

Calculated INDO/S energies  $E_{\text{calc}}$  (in eV) and wave functions for the lowest doublet states of the butadiene anion.  $E_0$  is the experimentally determined energy of the ground state anion relative to the neutral ground state. All configurations contributing more than 20% ( $a^2 > .20$ ) to the CI-wave function are listed.

state	$E_{\text{calc}}$	$E_0 + E_{\text{calc}}$	$a^2$	$\pi_{\text{SS}}$	$\pi_{\text{SA}}$	$\pi_{\text{AS}}^*$	$\pi_{\text{AA}}^*$
$1^2A_u$	0.00	0.80	0.94	$\uparrow\downarrow$	$\uparrow\downarrow$	$\uparrow$	
$1^2B_g$	1.52	2.32	0.81	$\uparrow\downarrow$	$\uparrow\downarrow$		$\uparrow$
$2^2B_g$	3.55	4.35	0.68	$\uparrow\downarrow$	$\uparrow$	$\uparrow\downarrow$	
$2^2A_u$	5.07	5.87	0.42	$\uparrow\downarrow$	$\uparrow$	$\downarrow$	$\uparrow$
				$\uparrow\downarrow$	$\uparrow$	$\uparrow$	$\downarrow$
$2^2A_u$	5.07	5.87	0.42	$\uparrow\downarrow$	$\downarrow$	$\uparrow$	$\uparrow$
				$\uparrow$	$\uparrow\downarrow$	$\uparrow\downarrow$	
$3^2A_u$	6.50	7.30	0.69	$\uparrow\downarrow$	$\uparrow$	$\downarrow$	$\uparrow$
				$\uparrow\downarrow$	$\uparrow$	$\uparrow$	$\downarrow$
				$\uparrow\downarrow$	$\downarrow$	$\uparrow$	$\uparrow$

Table 5.4-2

Calculated INDO/S energies  $E_{\text{calc}}$  (in eV) and wave functions for the neutral ground and lowest excited triplet states of butadiene.

state	$E_{\text{calc}}$	$a^2$	$\pi_{\text{SS}}$	$\pi_{\text{SA}}$	$\pi_{\text{AS}}^*$	$\pi_{\text{AA}}^*$
$1^1A_g$	0.00	1.00	$\uparrow\downarrow$	$\uparrow\downarrow$		
$1^3B_u$	2.31	0.87	$\uparrow\downarrow$	$\uparrow$	$\uparrow$	
		0.13	$\uparrow$	$\uparrow\downarrow$		$\uparrow$
$1^3A_g$	3.78	0.63	$\uparrow\downarrow$	$\uparrow$		$\uparrow$
		0.37	$\uparrow$	$\uparrow\downarrow$	$\uparrow$	

Based on the optimized wave functions decay factors  $d$  ( $1.0 \geq d \geq 0.0$ ) were determined, as described in Chapter 3. The decay factor  $d$  is a measure for the "percentage of parentage" and is used together with considerations on the resonance lifetime and energy to estimate the tendency of an anionic state to decay into a neutral state via a one-electron process. A high decay factor  $d$  indicates a favorable decay channel, as long as this decay channel is not closed due to energetic reasons, *i.e.* the final state of the decay process lies much higher in energy than the departure state. Decay factors were determined between the five lowest anionic states and the three lowest states of the neutral (Table 5.4-3).

Table 5.4-3

Calculated INDO/S decay factors  $d$  determined between the five lowest anionic states and the three lowest states of the neutral. Higher decay factors ( $d \geq 0.20$ ) are highlighted.

$d$	$1^2A_u$	$1^2B_g$	$2^2B_g$	$2^2A_u$	$3^2A_u$
$1^1A_g$	<b>0.94</b>	<b>0.81</b>	0.10	0.01	0.01
$1^3B_u$	<b>0.82</b>	0.19	<b>0.62</b>	0.10	<b>0.59</b>
$1^3A_g$	<b>0.36</b>	<b>0.54</b>	0.12	<b>0.23</b>	<b>0.24</b>

The 1p resonances,  $1^2A_u$  and  $1^2B_g$ , are predicted to predominantly decay into the neutral ground state. The  $1^2B_g$  resonance further has a smaller chance ( $d = 0.19$ ) to decay into the lowest triplet state, which is predicted to lie 0.01 eV below the  $1^2B_g$  resonance. All other decay channels for the 1p shape resonances can be considered "closed" due to energetic reasons.

The 2p-1h resonances are all calculated above the three neutral states of interest, thus all decay channels considered are open, energetically speaking. Decay into the neutral ground state is predicted to be unfavorable. Note the selectivity for the decay into either one or the other triplet state. The decay of the  $2^2B_g$  resonance into the  $1^3B_u$  state is predicted to be five times more favorable than into the  $1^3A_g$  state. In contrast, the  $2^2A_u$  resonance favors the  $1^3A_g$  state by more than a factor of 2. With respect to the same final state, excitation of the lowest triplet state should occur selectively through the  $2^2B_g$  resonance (ratio 6 : 1), while excitation of the second triplet state should involve predominantly the  $2^2A_u$  resonance (ratio 1 : 2).

### 5.4.3. Discussion

#### Excited States of the Neutral

The results of the EEL spectra with respect to the electronically excited states are compared to the results of previous studies in Table 5.4-4. The

agreement between the different experimental studies is within experimental error. The position of the  $2^1A_g$  state is still object of debate. Recent results from resonance Raman spectroscopic studies (Chadwick *et al.* 1991 and Strahan *et al.* 1993) locate this dipole-forbidden transition around 0.25 eV below the dipole-allowed transition into the  $1^1B_u$  state.

The EEL spectra of Reddish *et al.* (1986) reveal a weak feature at 6.165 eV, which was assigned to a vibrationally excited level of the  $1^1B_u$  state. Doering (1979) assigned the same feature to a undefined singlet-triplet transition, upon which Robin (1985) note that this would be compatible with a transition to  $^3(\pi_{SA}, 3s)$ . The intensity behavior and the sharpness of this peak in our spectra (Figure 5.4-2) leads us to assign the 6.16 eV feature to the  $^3(\pi_{SA}, 3s)$  Rydberg state. The corresponding dipole-forbidden singlet Rydberg state is known to lie at 6.21 eV (also seen in the  $E_r = 0.03$  eV spectrum), resulting in a characteristically small singlet-triplet splitting of 0.05 eV.

Table 5.4-4

Comparison of the vertical and adiabatic (in brackets) excitation energies (in eV) between the current and previous studies.

state	current		previous		
	gas	gas <sup>a</sup>	gas <sup>b</sup>	gas <sup>c</sup>	solid <sup>d</sup>
valence excited states					
$1^3B_u$	3.24 (2.59)	3.22	3.2	3.2	3.50 (2.585)
$1^3A_g$	4.92	4.91	4.95	4.9 (4.65)	5.11 (4.63)
$1^1B_u$	5.91 (5.75)		5.92 (5.74)	5.93 (5.735)	5.82 (5.43)
new assignments					
$^3(\pi_2, 3s)$	6.16				

<sup>a</sup>Mosher *et al.* (1973), <sup>b</sup>Doering (1979), <sup>c</sup>Reddish *et al.* (1986), <sup>d</sup>Swiderek *et al.* (1993).

Interesting is the comparison of the present gas phase spectra with the frozen thin film spectra of Swiderek *et al.* (1993) shown in Figure 5.4-7. The structure in the first triplet band, observed for the first time in the gas phase, is also found in the solid phase spectra. Note, that the onset of both triplet bands occur at similar energies. This confirms the general observation that the

energies of valence excited triplet states are not shifted by a considerable amount upon change of phase (Swiderek *et al.* 1991, and references therein).

Perhaps the most interesting difference in the two spectra depicted in Figure 5.4-7 is the consistently larger width of the individual electronic bands in the thin film spectrum and is explained by the effect of phonon excitations in the film. Observation of broadening of valence states in the solid is not new and is believed to be of general occurrence. This phenomenon is described in more detail in Section 5.3.

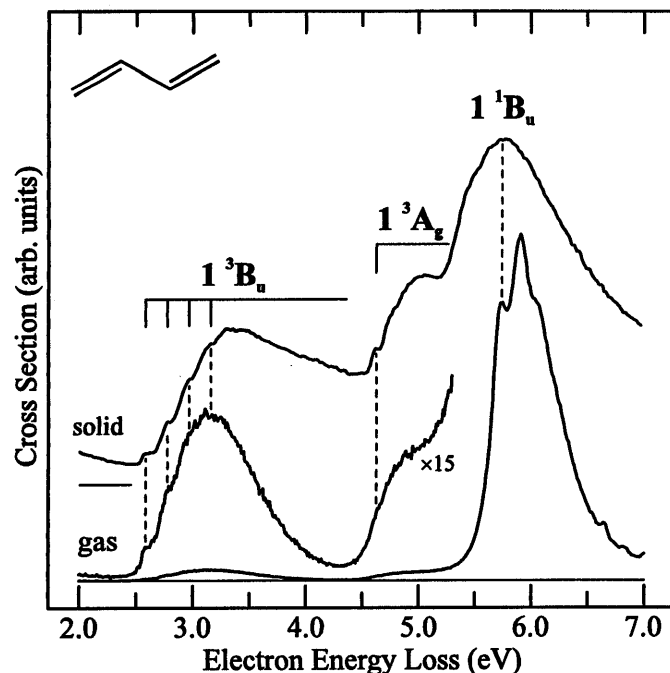


Figure 5.4-7

EEL spectrum ( $E_r = 5.0$  eV) from the current study (gas) is compared to an EEL spectrum of butadiene deposited on a thin film of solid argon (solid), measured at 15 K and a constant primary energy of 9.5 eV (Swiderek *et al.* 1993).

#### Determination of Resonance Energies

In order to assign the observed resonances it is important to qualitatively understand, why the bands associated with the same resonance are found at different incident energies, when measuring at different  $\Delta E$ 's. Further a convention has to be introduced, stating which incident energy shall be associated with the resonance energy.

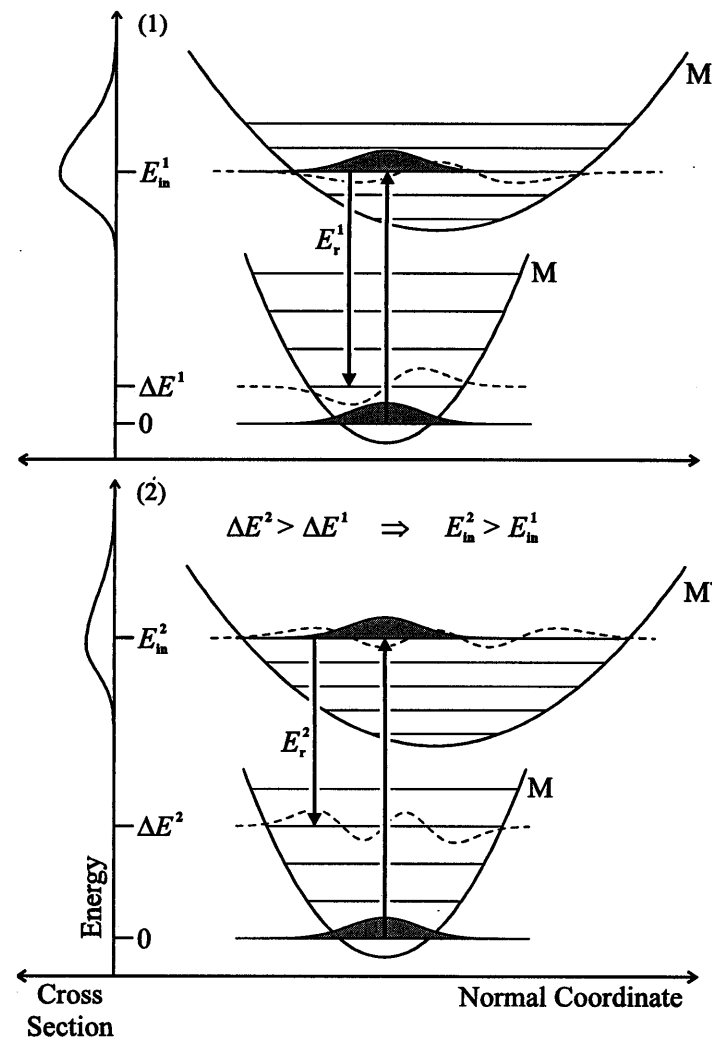


Figure 5.4-8

Potential-well diagrams illustrating resonant vibrational excitation. Depending on which vibrational level is probed, the band observed in the respective excitation function changes in position, intensity and form.

As an example, resonant vibrational excitation is illustrated in Figure 5.4-8. Resonant excitation can be idealized as a two step process. We assume the validity of the Frank-Condon principle, treat the resonance as a quasi-bound

state and depict electron capture and electron ejection by vertical arrows between the vibrational levels of the neutral molecule  $M$  and a bound state of the anion  $M^-$ . Note, that as a result of electron capture in an anti-bonding orbital the potential well of the anion state is wider and shifted to larger values of a schematic normal coordinate. For butadiene the normal coordinate would be related to the C=C bond length.

On electron capture the nuclear wave function of  $M$  in its vibrational ground state (shaded gray) is projected onto a vibrational level of  $M^-$ . There the nuclear wave function relaxes and approaches the form of the respective eigenfunction, this process being generally not completed, because of a short resonance lifetime. The higher the excited level, the bigger the tendency of the molecule to be found close to one of the sides of the potential well, from which then electron ejection is most probable to take place.

The probability of this process and thus the intensity and position of the band observed in the excitation function depend on the overlap of the nuclear wave functions involved. When probing increasingly higher vibrational levels of  $M$ , that is going from case (1) to case (2) in Figure 5.4-8, the higher vibrational levels of  $M^-$  show a more favorable overlap with the respective wave function of the vibrational excited state of the neutral. As a result the band is shifted to higher incident energies. Its overall intensity will in general decrease, due to the worse overlap of the wave functions in the first step.

The determination of resonance energies on the basis of excitation functions is somewhat arbitrary. In order to lift this arbitrariness, we use the following conventions. (i) In the case of electronically excited states, resonance energies are determined from the excitation function measured at, or closest to, the vertical excitation energy. (ii) In the case of pure vibrational excitation that excitation function is used, which is measured at the smallest  $\Delta E$ . This value is in general closest to the one determined from the ET spectrum. Since the trochoidal spectrometer is limited to measure excitation functions for  $\Delta E \geq 0.5$  eV, the resonances observed in the vibrational excitation functions often lie already slightly above the value determined from ET spectroscopy.

In some cases the determination of the vertical excitation energy is not straight forward. In the case of the  $1^3B_u$  band of butadiene, the position of the bands maximum changes with  $E_i$  in the previously described manner. The excitation functions of the  $1^3B_u$  state reveals that with increasing incident energy first the  $1^2B_g$  resonance is responsible for the excitation, then the  $2^2B_g$  resonance and at higher incident energies direct scattering is the most probable.

The dependence of the position of the band maximum on the scattering mechanism is illustrated in Figure 5.4-9. Similar assumptions are made as in the discussion of Figure 5.4-8. Geometry relaxation is responsible for the preferred activation of lower vibrational levels of the  $1^3B_u$  state ( $M^*$ ) at an incident energy which lies close to the center of the  $2^2B_g$  resonance ( $M^*$ ). Note that the

increasing population of anti-bonding orbitals, when going from  $M$  over  $M^*$  to  $M^{*-}$ , causes the representative potential wells to be shifted to larger values of the schematic normal coordinate. The larger the shift, the more pronounced the effect.

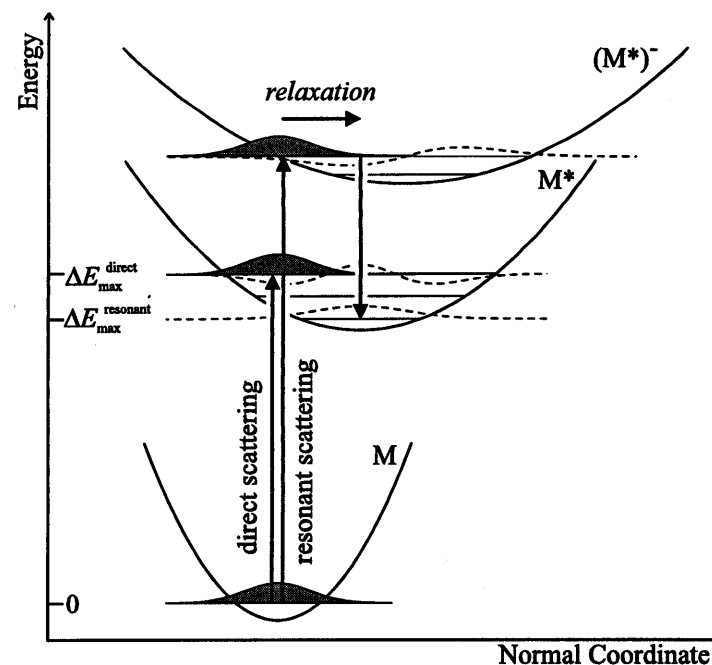


Figure 5.4-9

Illustration of the dependence of the vertical excitation energy on the scattering mechanism.

At very low  $E_{in}$  the  $1^2B_g$  resonance excites preferably higher vibrational levels of the  $1^3B_u$  state (not shown in Figure 5.4-9). The  $1^2B_g$  resonance is a 1p resonance, in contrast to the  $2^2B_g$  resonance, which is of 2p-1h type. Less anti-bonding orbitals are populated and the representative potential well is shifted less. The  $1^2B_g$  resonance lies significantly below the  $2^2B_g$  resonance. Thus higher vibrational levels of the resonance have to be accessed, resulting in higher vibrational levels of the triplet state being excited.

#### Assignment of Resonances

The results of the calculations are summarized and compared to the experimental energies in Table 5.4-5. The assignment of the two lowest 1p resonances as  $1^2A_u$  and  $1^2B_g$  is in accord with the previous studies. The low

intensity of the  $1^2B_g$  resonance in the vibrational excitation functions is not predicted and thus an indication for a shorter resonance lifetime. The observation of signal due to the  $1^2B_g$  resonance in the  $1^3B_u$  excitation function is reproduced well by the calculations. Note, that the appearance of a 1p resonance in the excitation function of an electronically excited state is not a general indicator for extensive 1p / 2p-1h mixing.

The main bands observed in the excitation function of the triplet states are attributed to 2p-1h resonances and are assigned as  $2^2B_g$  and  $2^2A_u$ . We prefer the assignment to two different resonances, because the calculations reproduce the observed selective decay (and the resonance energies) in a satisfactory manner.

Table 5.4-5

Experimental and theoretical energies (in eV) of  $\pi^*$  resonances in butadiene. Experimental energies are determined either from the electron transmission spectrum (ETS) or from excitation functions (EFs). Resonances not observed in a spectrum are indicated by the gray shaded areas. Both theoretical studies (Calc.) employed semi-empirical CI calculations, performed on the anion (present) or the cation (previous).

state	present study			previous studies		
	ETS	EFs	Calc.	ETS <sup>a</sup>	EFs <sup>b</sup>	Calc. <sup>b</sup>
$1^2A_u$	0.80	1.0	0.80	0.62	0.9	0.62
$1^2B_g$	2.87	2.9	2.32	2.82	2.8	3.16
$2^2B_g$		4.9	4.35		5.0	5.69
$2^2A_u$		6.2	5.87		6.7	7.57
$3^2A_u$			7.30		8.1	9.13
					11.0	10.56
					12.5	11.86

<sup>a</sup>Jordan and Burrow 1987. <sup>b</sup>Falcetta and Jordan 1991.

None of the higher-lying resonances observed by Falcetta and Jordan (Figure 5.4-10, Table 5.4-5) could be identified in our spectra. In part, this could be due to different collection efficiencies for forward and backward scattered electrons of the instruments. Furthermore the measurement of excitation functions can be complicated by the appearance of artifacts, referred to as "focusing". If the instrument is not tuned optimally with respect to the suppression of these artifacts, these can convert an otherwise unstructured spectrum into a wavy one.

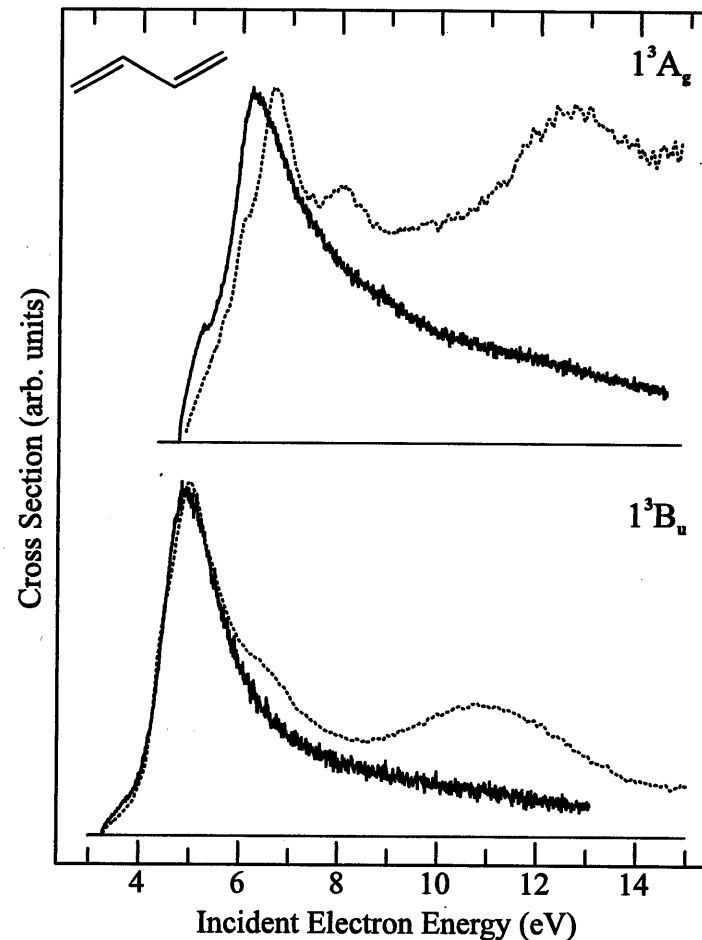


Figure 5.4-10  
Excitation functions of the  $1^3B_u$  and the  $1^3A_g$  triplet states of butadiene measured by Falcetta and Jordan (1991) (broken trace) and from the current study (solid trace).

#### 5.4.4. Summary and Conclusions

Resonances in butadiene have been studied by electron impact spectroscopy. Four  $\pi^*$  resonances have been found in the excitation functions of pure vibrationally and electronically excited states and assigned as  $1^2A_u$  (1.0),  $1^2B_g$  (2.9),  $2^2B_g$  (4.9) and  $2^2A_u$  (6.2 eV). On the basis of INDO/S CI calculations the first two are identified as 1p shape resonances and the second two as 2p-1h shape resonances. Configuration interaction between 1p and 2p-1h configurations is predicted to be weak.

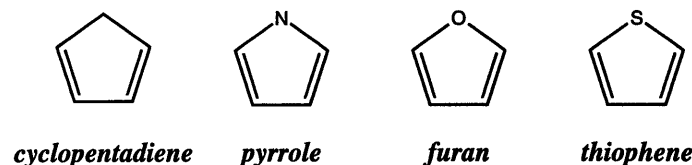
The absence of the  $2^2A_u$  resonance in the excitation function of the  $1^3B_u$  state and the weaker signal enhancement due to the  $2^2B_g$  in the  $1^3A_g$  excitation function is interpreted as a selectivity in the preferred decay channel of the 2p-1h resonances. The branching ratios for the 2p-1h resonances are reproduced well by the CI calculations.

The observation of the  $1^2B_g$  resonance in the  $1^3B_u$  excitation function demonstrates, that a resonance cannot be classified as 1p or 2p-1h type on the basis of whether it is observed in a vibrational or electronic excitation function, neither is it an indication for extensive 1p /2p-1h configuration mixing.

## 5.5. 2p-1h Shape Resonances in Cyclic Conjugated Dienes

### 5.5.1. Introduction

The selective decay of  $\pi^*$  shape resonances observed for butadiene stimulated us to extend the study to related molecules. Pentadiene, pyrrole, furan and thiophene (Scheme 5.5-1) were chosen for this study, because they are all five-membered rings containing the cis-butadiene moiety. Distinct similarities in the electronic structure of these cyclodienes with respect to that of butadiene are known, of which two will be pointed out here. (i) Their ET spectra (Staley *et al.* 1981 and Van Veen 1976) all reveal two  $\pi^*$  1p resonances ( $1^2B_1$  and  $1^2A_2$ ), which are associated with electron capture into the  $\pi_{\alpha s}^*$  and  $\pi_{\alpha a}^*$  orbitals respectively (see Figure 5.5-14 for the labeling of the MOs). (ii) Two low-lying  $\pi, \pi^*$  triplet states ( $1^3B_2$  and  $1^3A_1$ ) have been observed for each of these cyclodienes (Flicker *et al.* 1976, Frueholz *et al.* 1979, Swiderek *et al.* 1993 and Van Veen 1976). This is of special importance to the present study, because the selective decay of 2p-1h resonances, which enhance triplet excitation, can only be studied, if excitation functions of more than one triplet state can be recorded.



Scheme 5.5-1

In the current investigation resonances, with weight on the  $\pi^*$  2p-1h shape resonances, are studied by electron impact spectroscopy. Low energy EEL spectra, ET spectra, as well as vibrational and electronic excitation functions are presented. The observed resonances and their branching ratios are interpreted on the basis of semiempirical CI calculations.

### 5.5.2. Results

#### EEL Spectra

The results of previous experimental and theoretical studies on the electronic excitation energies of cyclopentadiene, pyrrole, furan and thiophene have been summarized by Serrano-Andrés *et al.* (1993b,c), Palmer *et al.* (1995) and the references therein. The following description of the current EEL spectra

will be restricted to the vibrational and valence triplet excitation processes. Exceptions are made, whenever previously unknown features are observed.

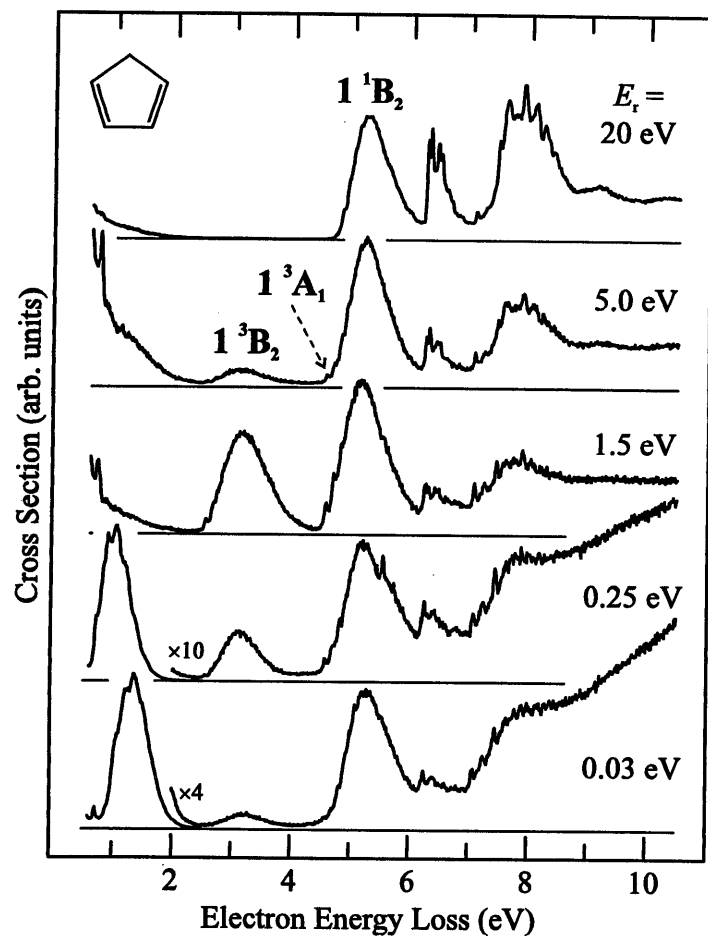


Figure 5.5-1

Survey EEL-spectra of cyclopentadiene recorded at various residual energies.

**Cyclopentadiene.** Survey EEL spectra of cyclopentadiene are shown in Figure 5.5-1. The first band at 5.22 eV in the  $E_r = 20$  eV spectrum is due to the excitation into the  $1^1B_2$  valence state. The sharp peaks above an energy-loss of 6 eV are mainly due to Rydberg excitations. At lower residual energy the spin-forbidden transition into the lowest triplet state ( $1^3B_2$ ) becomes apparent through a partly vibrationally structured band. The peak at 2.55 eV is assigned

to the 0-0 transition. For  $E_r \leq 0.25$  eV the most intense signal stems from resonant vibrational excitation.

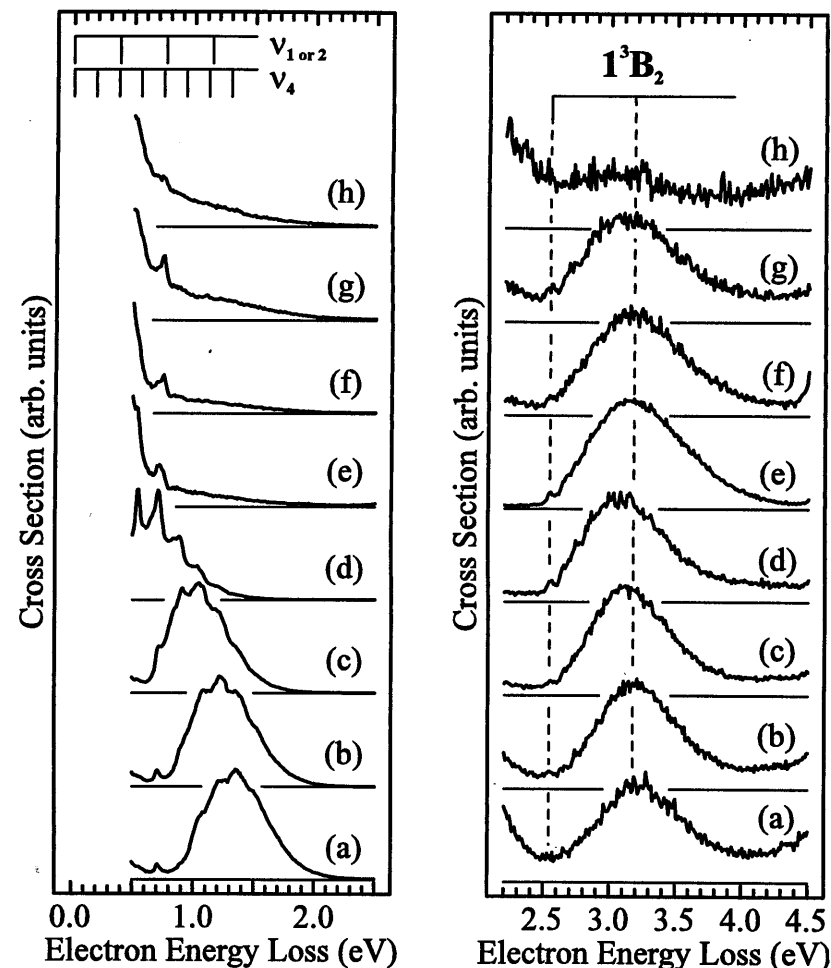


Figure 5.5-2

EEL spectra of cyclopentadiene measured at  $E_r = 0.03$  (a), 0.10 (b), 0.25 (c), 0.50 (d), 1.54 (e), 3.47 (f), 5.00 (g) and 20 eV (h) in the energy-loss region of pure vibrational (left) and triplet (right) excitation.

Vibrational energy-loss spectra are shown in Figure 5.5-2 (left). "Unspecific" and, to a lesser degree, "specific" resonant vibrational excitation by the  $1^2B_1$  resonance is observed at low residual energy. The partly structured



band at 1.35 eV in the  $E_r = 0.03$  eV spectrum is moved to lower energy-loss and gains in structure with increasing  $E_r$ . The observed vibrational structure is complex. In accord with the  $\pi^*$  nature of the  $1^3B_1$  resonance it is interpreted as the preferred excitation of the  $\nu_4$  C=C stretch mode ( $1500\text{ cm}^{-1} \approx 186\text{ meV}$ , Castellucci *et al.* 1975). At higher residual energy ( $E_r \geq 3.47$  eV) "specific" excitation of the totally symmetric  $\nu_1$  ( $3091\text{ cm}^{-1}$ ) or  $\nu_2$  ( $3075\text{ cm}^{-1}$ ) C-H stretch mode is observed. Excitation of C-H modes is generally attributed to  $\sigma^*$  resonances (Allan 1989).

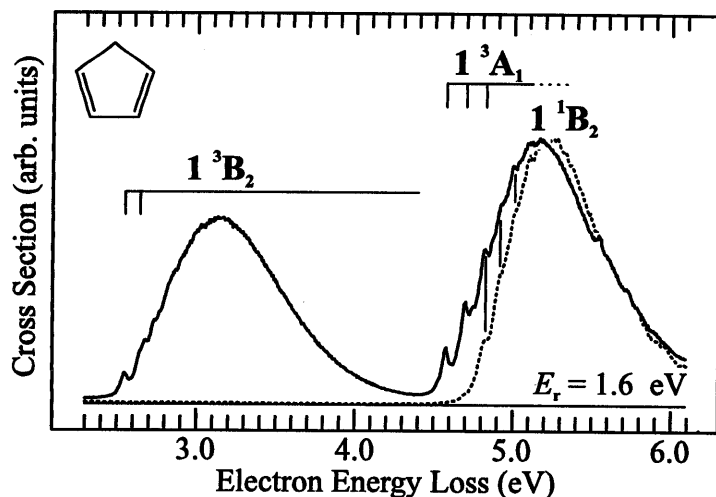


Figure 5.5-3

EEL spectra of cyclopentadiene measured at  $E_r = 1.6$  eV (solid line) and  $E_r = 20$  eV (broken line). The structure observed on the low energy tail of the  $1^1B_2$  band is assigned to the second triplet state  $1^3A_1$ .

EEL spectra measured at residual energies between 0.03 and 20 eV in the region of the lowest triplet transition are depicted in Figure 5.5-2 (right). The  $1^3B_2$  band changes in position and form with changing residual energy. The bands maximum moves between 3.22 ( $E_r = 0.03$  eV) and 3.06 eV ( $E_r = 0.50$  eV), its width at half-height changes from 0.61 ( $E_r = 0.03$  eV) to 0.86 eV ( $E_r = 1.54$  eV).

At low residual energy a vibrationally structured band appears in the EEL spectra just below the optically allowed transition into the  $1^1B_2$  state (Figure 5.5-3). A vibrational progression starting at an energy-loss of 4.58 eV and spaced by 0.12 eV ( $970\text{ cm}^{-1}$ ) is observed and attributed to the second valence triplet state  $1^3A_1$ . The 4.58 eV feature is assigned to the 0-0 transition. The third peak of this series coincides with the 0-0 transition into the  $1^1B_2$  state. At higher

energy-loss the  $1^3A_1$  band is masked by the dipole-allowed transition into the  $1^1B_2$  state.

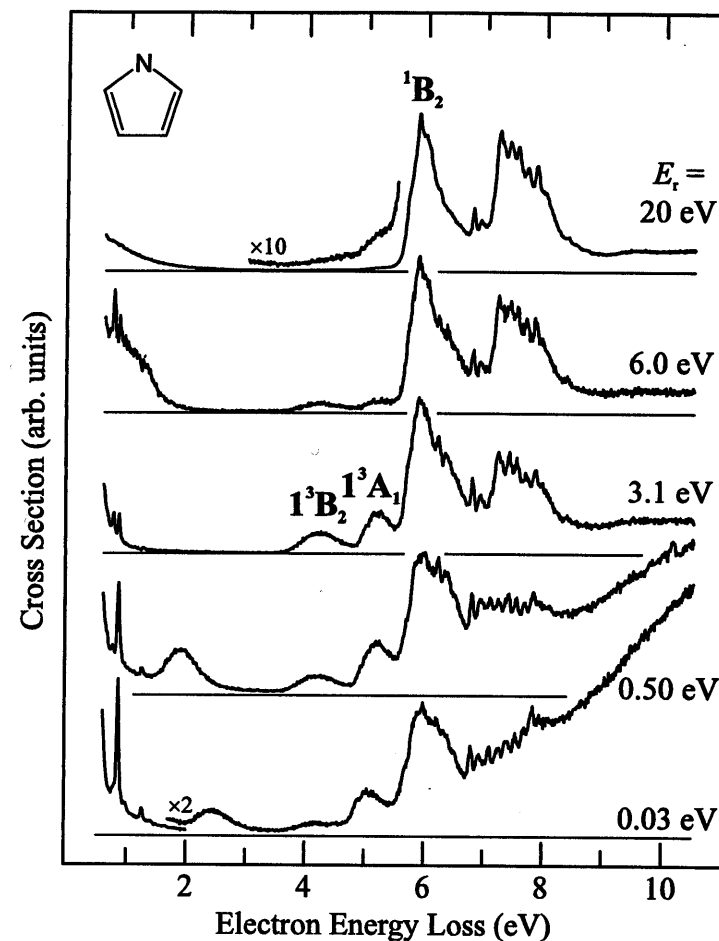
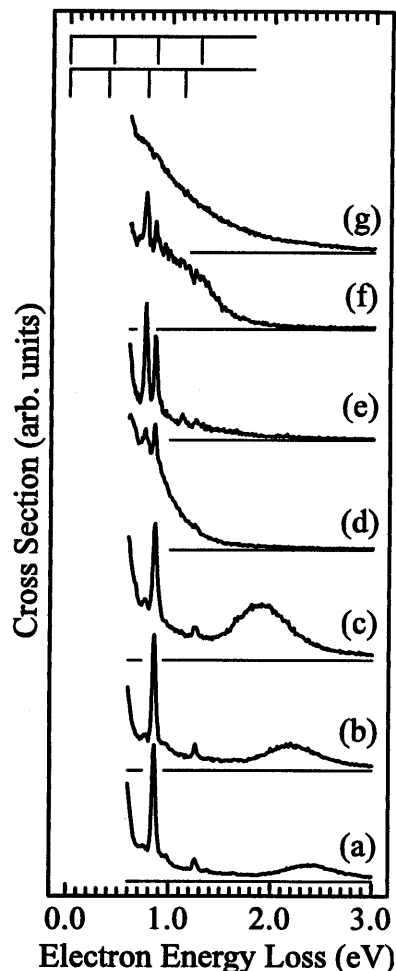


Figure 5.5-4

EEL spectra of pyrrole measured at  $E_r = 0.1, 0.50, 3.1, 6.0$  and  $20$  eV.

**Pyrrole.** Survey EEL-spectra of pyrrole are shown in Figure 5.5-4. At medium and low residual energy ( $E_r \leq 6.0$  eV) two triplet bands at 4.21 and 5.17 eV are observed, previously assigned to the transitions into  $1^3B_2$  and  $1^3A_1$  valence excited triplet states (Van Veen 1976). The shoulder seen between 4.9 and 5.4 eV in the  $E_r = 20$  eV spectrum is not attributed to the  $1^3A_1$  state, but believed to result from a dipole-forbidden spin-allowed transition (Flicker *et al.*

1976). A similar, weak feature is observed in the vapor absorption spectrum and is absent in the crystal spectrum (Bavia *et al.* 1976). It has been assigned to the  $^1(\pi_{SA}, 3s)$  Rydberg state. The intense band extending from 5.4 to 6.7 eV is the result of various optically allowed Rydberg and valence transitions. The largest contribution is expected from the valence  $^1B_2$  excitation (5.98 eV peak,  $E_r = 0.03$  eV). Signal due to  $^1(\pi_{SA}, 3p)$  Rydberg transitions move the maximum of this band to 5.86 eV at  $E_r = 20$  eV.



Vibrational EEL spectra are shown in Figure 5.5-5. Two cases of "unspecific" resonant vibrational excitation are observed. (i) The band at 2.4 eV in the  $E_r = 0.10$  eV spectrum, which is moved to lower energy-loss with increasing  $E_r$ , is attributed to the  $^2B_1$  shape resonance. (ii) The broad feature centered around 1.0 eV in the  $E_r = 6.00$  eV spectrum is an indication for another, possibly a  $\sigma^*$ , resonance.

The  $\nu = 2$  and 3 levels of a C-H and a ring stretch mode are excited specifically throughout all the depicted spectra, except for the one measured at  $E_r = 20$  eV. The ring stretch mode is excited more effectively at low  $E_r$ , while the excitation of a C-H mode is stronger at medium  $E_r$ .

**Figure 5.5-5**  
Vibrational EEL spectra of pyrrole measured at  $E_r = 0.10$  (a), 0.25 (b), 0.50 (c), 1.6 (d), 4.3 (e), 6.0 (f) and 20 eV (g).

**Furan.** Survey EEL spectra of furan are presented in Figure 5.5-6. The two bands, best seen in the  $E_r = 2.4$  eV spectrum, extending from 3.3 to 4.8 and 4.8 to 5.6, centered at 3.95 and 5.22 eV respectively, have been assigned to the

two lowest valence triplet states (Van Veen 1976). The band observed between 5.5 and 7.3 eV is the result of various valence and Rydberg excitations. Its form and position change noticeably with changing  $E_r$ . For  $E_r = 20$  eV the maximum lies at 6.04 eV and has been assigned to the vertical excitation energy of lowest valence excited singlet state  $^1B_2$ , which is believed to contribute predominantly at this residual energy. The weak features observed in the VUV absorption spectrum on the low energy side of the strong  $^1B_2$  band have been attributed to the  $^2A_1$  valence state, which has been determined to lie at 5.80 eV (Roebber *et al.* 1980).

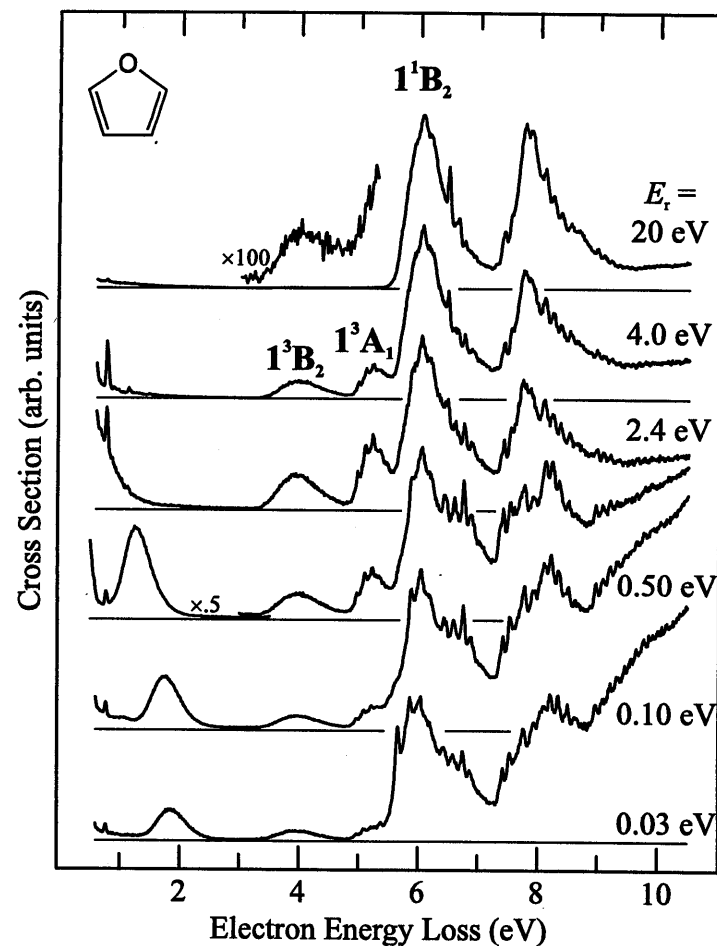


**Figure 5.5-6**  
Survey EEL spectra of furan measured at various constant residual energies.

It is of interest to note, that the two sharp peaks at 5.67 and 5.87 eV observed in the  $E_r = 0.03$  eV spectrum have not been reported before. We assign them to the  ${}^2(\pi_{SA}, 3s^2)$  Feshbach resonance. Its parent state  ${}^1(\pi_{SA}, 3s)$  is known to lie at 5.91 eV (Roebber *et al.* 1980), resulting in a Feshbach decrement of 0.24 eV.

The band centered at 1.84 in the  $E_r = 0.03$  eV is moved to lower energy-loss with increasing  $E_r$ . It is attributed to "unspecific" vibrational excitation, due to the  ${}^2B_1$  resonance. The peak at 0.77 eV appears throughout all spectra and is assigned to the "specific" excitation of the  $v = 2$  level of a C-H stretch mode.

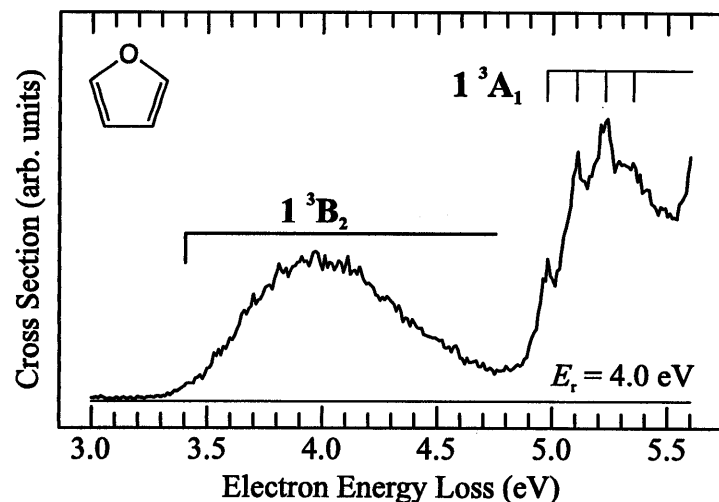


Figure 5.5-7

EEL spectrum of furan recorded in the region of the lowest valence triplet states at a constant residual energy of 4.0 eV.

An EEL spectrum, recorded at  $E_r = 4.0$  eV, is shown in Figure 5.5-7. The first band extends from 3.3 to 4.8 eV and peaks at 3.95 eV. No vibrational structure is discernible. A pronounced vibrational progression is observed in the second triplet band (4.8 to 5.6 eV) with members of this progression peaking at 4.98 (0-0 transition), 5.11 and 5.24 eV. The EEL spectrum of Flicker *et al.* (1976), measured at a constant incident energy of 50 eV and a scattering angle of  $50^\circ$  only partly resolves this structure, not revealing the 0-0 transition.

**Thiophene.** Survey EEL spectra of thiophene measured at constant residual energies between 0.03 and 20 eV are shown in Figure 5.5-8. The two lowest valence triplet states are found at 3.74 and 4.62 eV. The band observed in the region from 4.9 to 6.5 in the  $E_r = 20$  eV has a maximum at 5.43 eV, with weak vibrational structure visible on the band envelope. At  $E_r = 0.03$  eV the

onset of the now structureless band is moved to 5.0 eV and the maximum to 5.61 eV. A magnetic circular dichroism study (Håkansson *et al.* 1977) has reported at least two transitions in this region of the spectrum, at 5.26 and 5.64 eV. The CASPT2 study by Serrano-Andrés *et al.* (1993c) predicts two valence singlet-singlet transitions with similar oscillator strength at 5.33 ( $2^1A_1$ ,  $f = 0.09$ ) and 5.72 eV ( $1^1B_2$ ,  $f = 0.07$ ). Our spectra confirm this assignment, placing the  $2^1A_1$  state at 5.43 and the  $1^1B_2$  state at 5.61 eV.

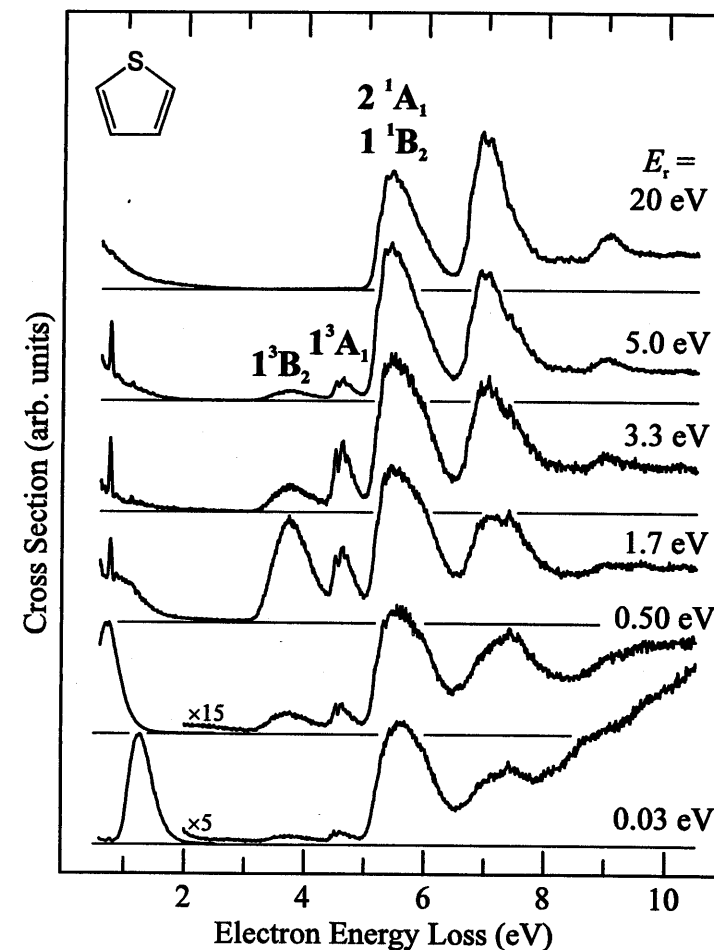


Figure 5.5-8

Survey EEL spectra of thiophene.

Figure 5.5-9 shows an EEL spectrum measured at  $E_r = 3.3$  eV, recorded in the region of the lowest triplet states. The  $1^3B_2$  band peaks at 3.74 eV. In contrast to previous electron impact studies the second triplet band shows vibrational structure starting with a weak shoulder at 4.38 eV, followed by peaks at 4.50 and 4.62 eV. The shoulder is assigned to the 0-0 transition and the observed peaks could be members of a single vibrational progression with a spacing of  $0.12$  eV ( $970$   $\text{cm}^{-1}$ ).

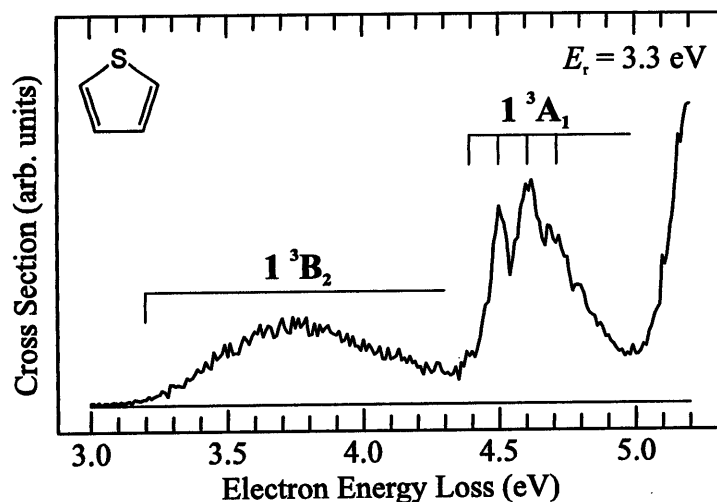


Figure 5.5-9

EEL spectrum of thiophene recorded with a constant residual energy of 3.3 eV.

### ET Spectrum and Excitation Functions

For the assignment of resonance energies the rules are applied, which were introduced in the butadiene chapter. (i) In the case of electronically excited states, resonance energies are determined from the excitation function measured at or closest to the vertical transition energy. (ii) In the case of pure vibrational excitation that excitation function is used, which was measured at the smallest  $\Delta E$ .

With respect to the dependence of the resonance center on the energy-loss, a similar line of argumentation as in the butadiene chapter is applied. It is assumed, that when probing increasingly higher vibrational levels of the same electronic state, the bands associated with resonances are shifted to higher incident energy. When probing different electronic states the bands may be shifted to, but in general less than what one would expect from a linear continuation with respect to the increasing energy-loss. The assignment of

resonances on the basis of these arguments will not always be without some arbitrariness. None the less, tentative assignments will be given in the description of the excitation functions and discussed in more detail in section 5.5.3.

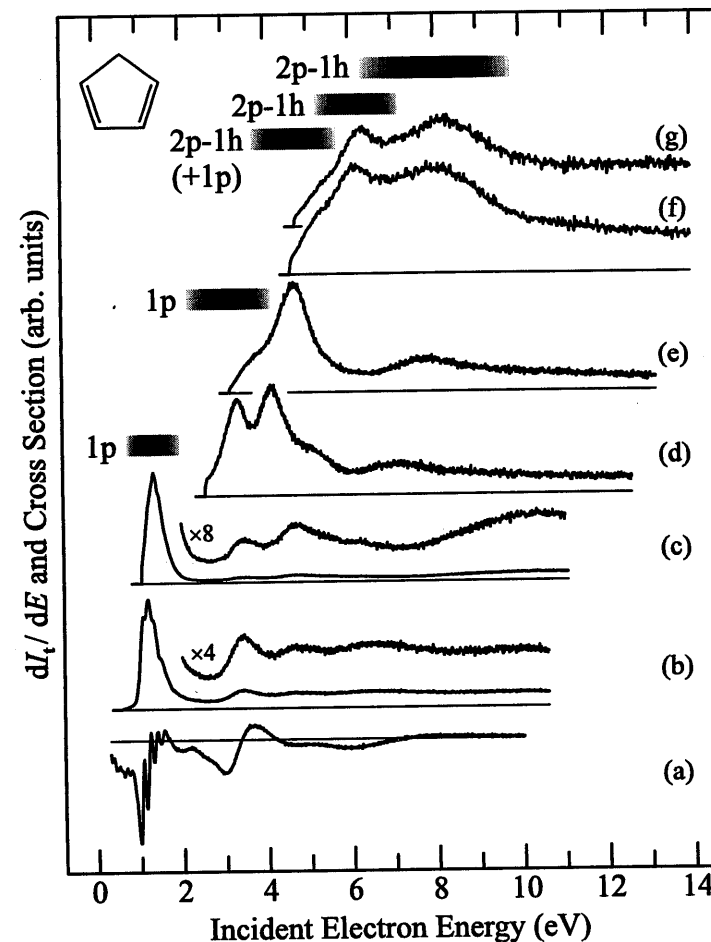


Figure 5.5-10

ET spectrum (a) and excitation functions (b-g) of cyclopentadiene. Pure vibrational (b:  $\Delta E = 0.56$  eV, c:  $\Delta E = 1.03$  eV),  $1^3B_2$  (d:  $\Delta E = 2.55$  eV, e:  $\Delta E = 3.14$  eV) and  $1^3A_1$  (f:  $\Delta E = 4.58$  eV, g:  $\Delta E = 4.70$  eV) excitation functions are shown.

**Cyclopentadiene.** The ET spectrum of cyclopentadiene is compared to various vibrational and electronic excitation functions in Figure 5.5-10. The ET

spectrum reveals two resonances at 1.35 and 3.33 eV, which have been assigned to the  $\pi^*$  1p resonances  $1^2B_1$  and  $1^2A_2$  (Staley *et al.* 1981). The first band shows vibrational structure with a spacing of 0.16 eV ( $1291\text{ cm}^{-1}$ ). In accord with the  $\pi^*$ -nature of the  $1^2B_1$  resonance it is interpreted as excitation of a totally symmetric CC stretch mode. At higher incident energies weaker signal variations are observed, indicating higher lying resonances.

Vibrational excitation functions are shown for the  $v = 3$  level of the  $\nu_4$  C=C stretch mode ( $\Delta E = 0.56\text{ eV}$ ) and for  $\Delta E = 1.03\text{ eV}$ , an energy-loss at which unresolved vibrations contribute predominantly to the signal. Both excitation functions show an intense band at low  $E_{in}$ , followed at higher  $E_{in}$  by much weaker bands. The 1.20 eV band ( $\Delta E = 0.56\text{ eV}$ ) is assigned to the  $1^2B_1$  resonance. This 1p resonance shows vibrational structure spaced by 0.13 eV and appears at 1.66 eV in the  $\Delta E = 1.03\text{ eV}$  spectrum. The second band, centered at 3.45 eV in both spectra, is assigned to the  $1^2A_2$  resonance. The assignment of the third band at 4.70 eV is uncertain. It could either be attributed to the 2p-1h resonance, which dominates the  $\Delta E = 3.14\text{ eV}$  spectrum, or a third 1p resonance, due to electron capture into the pseudo  $\pi^*$  orbital. Further bands are observed at 6.6 ( $\Delta E = 0.56\text{ eV}$ ) and 10.4 eV ( $\Delta E = 1.03\text{ eV}$ ) and are left unassigned.

The excitation functions of the lowest triplet state, measured in the vicinity of the 0-0 ( $\Delta E = 2.55\text{ eV}$ ) and the vertical excitation energy ( $\Delta E = 3.14\text{ eV}$ ), indicate at least four resonances, which enhance  $1^3B_2$  formation. Two bands are observed in the  $\Delta E = 3.14\text{ eV}$  spectrum at 4.69 and 7.80 eV. Both are assigned to 2p-1h resonances and are shifted to lower  $E_{in}$  (4.15 and 7.11 eV respectively) in the 0-0 excitation function. In this spectrum two additional resonances are revealed at 3.34 eV and 5.13 eV. The first is assigned to the  $1^2A_2$  resonance, the latter may possibly be due to the pseudo  $\pi^*$  1p resonance.

Two bands are observed at 6.19 and 8.04 eV in the excitation function of the 0-0 transition into the  $1^3A_1$  state. These are moved to 6.29 and 8.21 eV in the excitation function of the 0-1 transition. The 6.29 eV band is not seen in the excitation functions of the  $1^3B_2$  state and is assigned to a third 2p-1h resonance, which lies in-between the two previously assigned 2p-1h resonances. The 8.21 eV band is tentatively attributed to the 2p-1h resonance, centered at 7.80 eV in the  $\Delta E = 3.14\text{ eV}$  spectrum.

**Pyrrole.** The ET spectrum of pyrrole is compared to various excitation functions in Figure 5.5-11. The resonance energies of the two lowest  $\pi^*$  shape resonances are determined on the basis of the ET spectrum to be 2.41 and 3.51 eV, in good agreement with the previously recorded values of 2.38 and 3.44 eV (Van Veen, 1976). The signal variation between 6 and 8 eV is attributed to a broad  $\sigma^*$  1p resonance. These three resonances are also observed in the vibrational excitation functions at 2.48, 3.50 and 6.9 ( $\Delta E = 0.77\text{ eV}$ ) and 2.50, 3.60 and 7.2 eV ( $\Delta E = 0.86\text{ eV}$ ) respectively. Note that the intensity of the  $\sigma^*$

resonance in the  $\Delta E = 0.77\text{ eV}$  spectrum is comparable to that of the lowest  $\pi^*$  resonance.

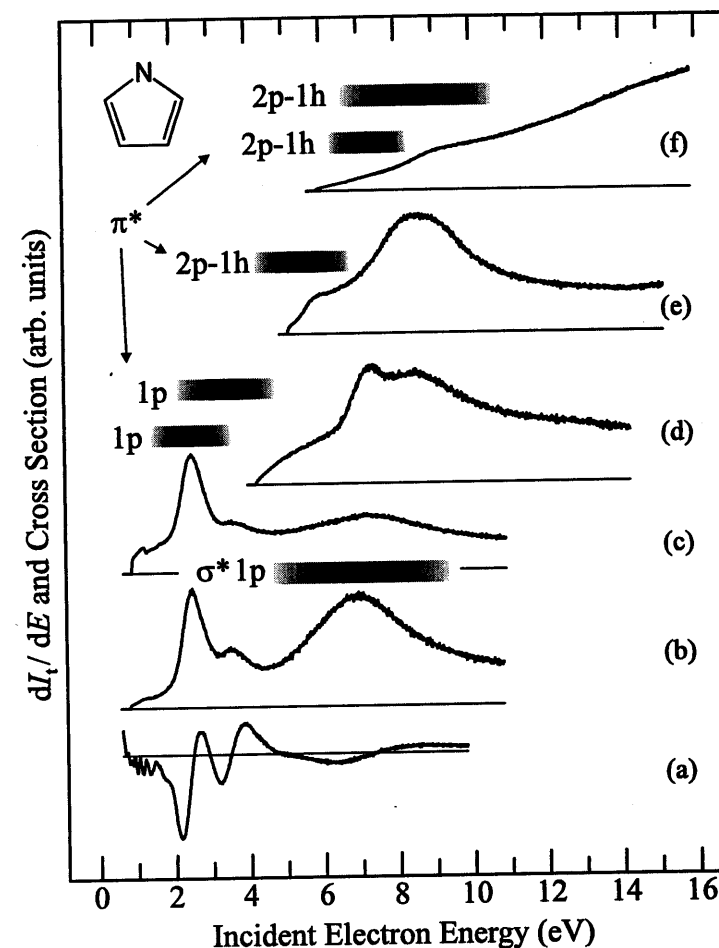


Figure 5.5-11

ET spectrum (a) of pyrrole compared to excitations functions of pure vibrational excitation (b and c:  $\Delta E = 0.77$  and  $0.86\text{ eV}$ ), the lowest triplet state (d:  $\Delta E = 4.20\text{ eV}$ ), the second lowest triplet state (e:  $\Delta E = 5.10\text{ eV}$ ) and the first optically allowed valence transition (f:  $\Delta E = 5.86\text{ eV}$ ).

The  $1^3B_2$  excitation function ( $\Delta E = 4.20\text{ eV}$ ) features a low energy shoulder, centered around 5.5 eV, a relatively narrow peak at 7.33 eV and a broad band at 8.53 eV. Three resonances are associated with these features, of

which the highest one is also detected in the  $1^3A_1$  excitation function ( $\Delta E = 5.10$  eV) at 8.62 eV. The 7.33 peak is not observed in the  $1^3A_1$  spectrum. The shoulder at 6.0 eV may be attributed to a fourth resonance or associated with the resonance, responsible for the 5.5 eV shoulder in the excitation function of the lowest triplet state.

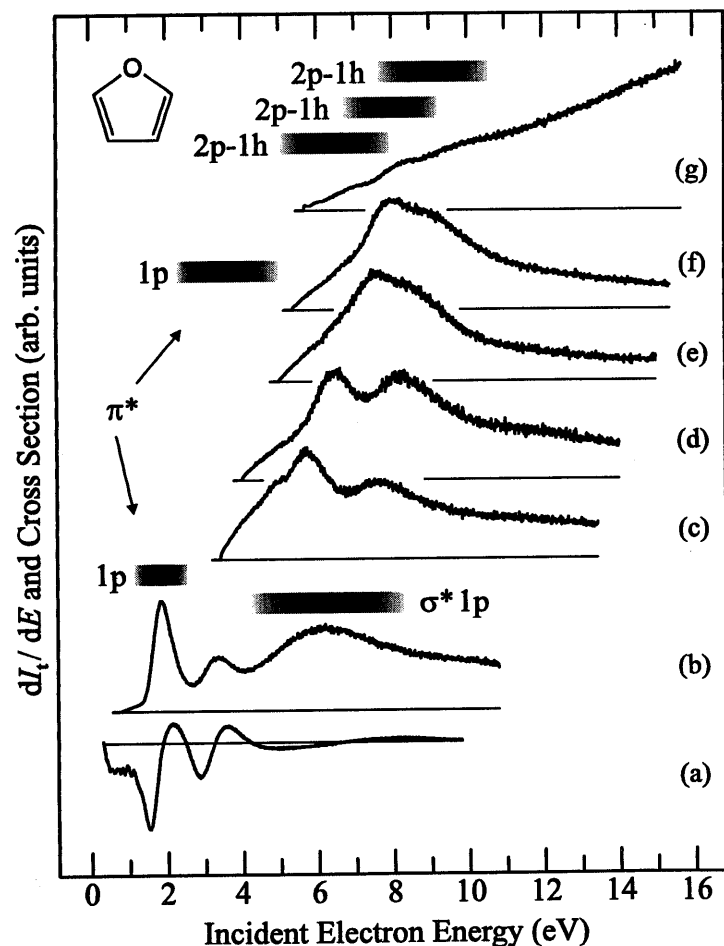


Figure 5.5-12

ET spectrum (a) of furan compared to excitation functions of pure vibrational excitation (b:  $\Delta E = 0.77$  eV), the lowest triplet state (c and d:  $\Delta E = 3.41$  and  $3.99$  eV), the second lowest triplet state (e and f:  $\Delta E = 4.97$  and  $5.34$  eV) and the first dipole-allowed transition (g:  $\Delta E = 5.66$  eV).

The excitation function measured at  $\Delta E = 5.86$  eV and associated predominantly with the optically-allowed transition into the  $1^1B_2$  state is almost structureless and increases monotonically with incident energy, characteristic for a direct scattering mechanism.

**Furan.** The ET spectrum in Figure 5.5-12 is similar to the previously published one, revealing the two lowest resonances  $1^2B_1$  and  $1^2A_2$ , centered at 1.85 and 3.23 eV. Both resonances appear also in the  $\Delta E = 0.77$  eV excitation function at 1.85 and 3.36 eV respectively. At 6.2 eV a broad band is visible in the vibrational excitation, assigned to a  $\sigma^*$  shape resonance.

For each triplet state two excitation functions, one measured at the 0-0 and the other at the vertical transition energy, are shown in Figure 5.5-12. The  $1^3B_2$  excitation functions shows two bands, observed at 6.48 and 8.22 eV in the  $\Delta E = 3.99$  eV spectrum. In the  $\Delta E = 3.41$  eV spectrum these bands are shifted to lower  $E_{in}$  and found at 5.73 and 7.62 eV. These bands are assigned to two 2p-1h resonances. The spectra indicate that slightly above threshold the second  $\pi^*$  1p resonance can also contribute to the excitation of the  $1^3B_2$  state.

The  $1^3A_1$  excitation functions also show two bands. They are centered at 7.65 and 8.41 eV in the  $\Delta E = 4.97$  eV spectrum and at 8.05 and 8.89 eV in the  $\Delta E = 5.34$  eV spectrum, indicating at least one more 2p-1h resonance. The higher lying of the two bands is tentatively assigned to third 2p-1h resonance, while the lower lying is associated with the second 2p-1h resonance, observed in the  $1^3B_2$  excitation functions.

The  $\Delta E = 5.66$  eV excitation function ( $1^1B_2$  state) increases nearly monotonically with increasing  $E_{in}$ , typical of optically-allowed transitions.

**Thiophene.** The ET spectrum, vibrational and electronic excitation functions of thiophene are shown in Figure 5.5-13. Two low lying resonances are detected in the ET spectrum at 1.26 and 2.76 eV. These are known from a previous study and have been assigned to the  $\pi^*$  1p shape resonances  $1^2B_1$  and  $1^2A_2$  (Van Veen 1976). The first feature shows a vibrational progression spaced by 0.085 eV ( $690$   $\text{cm}^{-1}$ ), which was not observed in the previous study. The features centered at 5.3 and 7.9 eV are very weak and could be attributed to two more resonances. The previous study assigned a similar structure to one resonance at 6.77 eV.

Three resonances are detected in the vibrational excitation function ( $\Delta E = 0.78$  eV) at 1.27, 2.83 and 5.5 eV. The first two are assigned to the two  $\pi^*$  1p resonances. The third is tentatively assigned to a  $\sigma^*$  1p resonance, but a possible assignment to the lowest  $\pi^*$  2p-1h resonance cannot be excluded.

The  $1^3B_2$  excitation function ( $\Delta E = 3.72$  eV) reveals two bands, an intense one at 5.38 eV and a weaker one at 7.39 eV. Two bands, of which the second is more intense than the first, are also observed in the  $1^3A_1$  excitation function ( $\Delta E = 4.62$  eV) at 6.22 and 7.93 eV. The  $\pi^*$  1p resonances clearly lie too low in energy to be associated with the described features, therefore we

assign these features to  $\pi^*$  2p-1h resonances. If we are observing four resonances with pronounced selectivity in their excitation preference, or only two resonances with qualitatively opposite branching ratios can not be distinguished at this point. The  $\Delta E = 5.45$  eV excitation function shows no pronounced structure, indicating that predominately nonresonant scattering is responsible for the excitation of the  $2^1A_1$ .

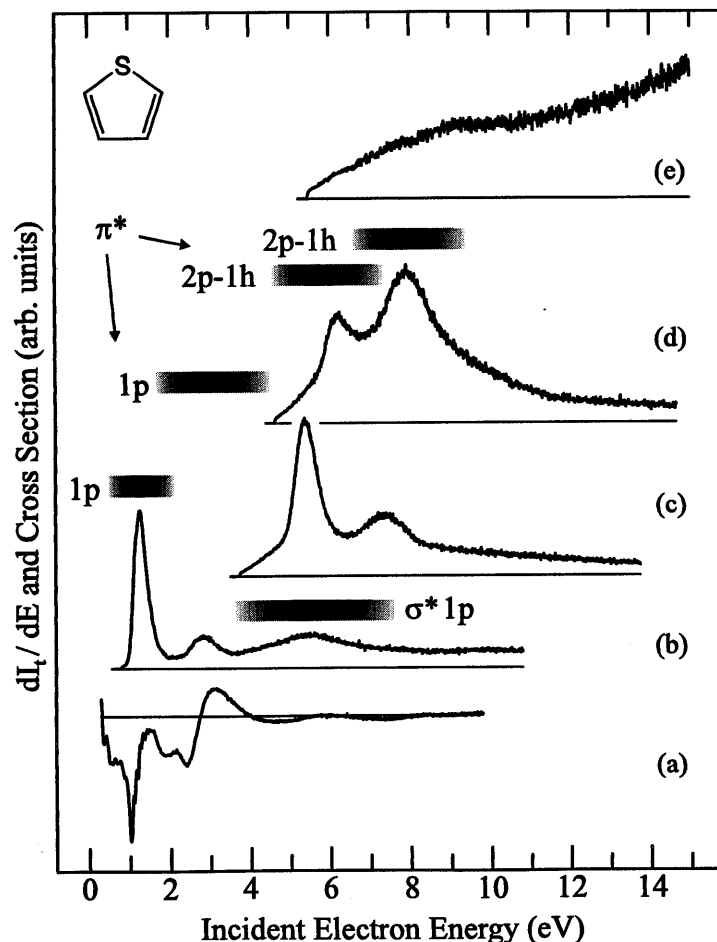


Figure 5.5-13

ET spectrum (a) of thiophene compared to vibrational (b:  $\Delta E = 0.78$  eV) and electronic excitations functions, measured at the vertical excitation energies of the  $1^3B_2$  (c:  $\Delta E = 3.72$  eV),  $1^3A_1$  (d:  $\Delta E = 4.62$  eV) and  $2^1A_1$  (e:  $\Delta E = 5.45$  eV) state.

## Calculations

Electron attachment energies (AEs) for the lowest  $\pi^*$  orbitals (Table 5.5-1) were derived from the HF/6-31G virtual orbital energies, as described by Chen and Gallup (1990). The previously introduced nomenclature for the butadiene-like  $\pi$  orbitals is used (Figure 5.5-14). For cyclopentadiene the AE of the pseudo  $\pi^*$  orbital ( $\pi_{CH_2}^*$ ) has also been estimated. The gap between the  $\pi_{AS}^*$  and  $\pi_{AA}^*$  AEs is the biggest in cyclopentadiene and decreases, when going from cyclopentadiene over thiophene and furan to pyrrole, in agreement with the experimental observations.

Table 5.5-1  
Electron attachment energies (in eV) for the lowest  $\pi^*$  orbitals determined from HF/6-31G orbital energies calculated at the HF/6-31G geometry.

	cyclo- pentadiene	pyrrole	furan	thiophene
$\pi_{CH_2}^*$	5.07			
$\pi_{AA}^*$	3.64	3.64	3.22	3.18
$\pi_{AS}^*$	1.10	2.35	1.58	0.86

Similar to the butadiene study INDO/S CI calculations were carried out for the neutral and anionic states of interest. All singly excited configurations were included in the CI calculation of the triplet states. The INDO/S triplet parametrisation was used, except for thiophene, for which no triplet parameters were available. For the calculation of the anionic states all single and double excitations within the  $\pi^*$  manifold were considered. Decay factors were determined between the anionic and neutral states, aiding the assignment of the observed resonances.

Table 5.5-2  
Calculated INDO/S energies  $E_{calc}$  (in eV) and wave functions for the neutral ground and lowest excited triplet states of cyclopentadiene.

state	$E_{calc}$	$a^2$	$\pi_{CH_2}$	$\pi_{SS}$	$\pi_{SA}$	$\pi_{AS}^*$	$\pi_{AA}^*$	$\pi_{CH_2}^*$
$1^1A_1$	0.0	1.00	$\uparrow\downarrow$	$\uparrow\downarrow$	$\uparrow\downarrow$			
$1^3B_2$	1.94	0.88 0.10	$\uparrow\downarrow$ $\uparrow\downarrow$	$\uparrow\downarrow$ $\uparrow$	$\uparrow$ $\uparrow\downarrow$	$\uparrow$		$\uparrow$
$1^3A_1$	3.44	0.67 0.31	$\uparrow\downarrow$ $\uparrow\downarrow$	$\uparrow\downarrow$ $\uparrow$	$\uparrow$ $\uparrow\downarrow$	$\uparrow$		$\uparrow$

The results are summarized in Table 5.5-2 to Table 5.5-13.  $E_0$  is the experimentally determined energy (from the ET spectrum) of the ground state anion relative to the neutral ground state. All configurations contributing more than 20% ( $a^2 > .20$ ) to anion wave function or more than 10% to the neutral wave function are listed. Higher decay possibilities ( $d \geq .20$ ) are highlighted.

Table 5.5-3

Calculated INDO/S energies  $E_{\text{calc}}$  (in eV) and wave functions for the lowest doublet states of the cyclopentadiene anion.

state	$E_{\text{calc}}$	$E_0 + E_{\text{calc}}$	$a^2$	$\pi_{\text{CH}_2}$	$\pi_{\text{SS}}$	$\pi_{\text{SA}}$	$\pi_{\text{AS}}^*$	$\pi_{\text{AA}}^*$	$\pi_{\text{CH}_2}^*$
$1^2\text{B}_1$	0.00	1.35	0.93	$\uparrow\downarrow$	$\uparrow\downarrow$	$\uparrow\downarrow$	$\uparrow$		
$1^2\text{A}_2$	1.30	2.65	0.81	$\uparrow\downarrow$	$\uparrow\downarrow$	$\uparrow\downarrow$		$\uparrow$	
$2^2\text{A}_2$	3.21	4.56	0.70	$\uparrow\downarrow$	$\uparrow\downarrow$	$\uparrow$	$\uparrow\downarrow$		
$2^2\text{B}_1$	4.66	6.01	0.43	$\uparrow\downarrow$	$\uparrow\downarrow$	$\uparrow$	$\downarrow$	$\uparrow$	
				$\uparrow\downarrow$	$\uparrow\downarrow$	$\uparrow$	$\uparrow$	$\downarrow$	$\uparrow$
$2^2\text{B}_1$	4.66	6.01	0.38	$\uparrow\downarrow$	$\uparrow$	$\uparrow\downarrow$	$\uparrow\downarrow$		
				$\uparrow\downarrow$	$\uparrow$	$\uparrow\downarrow$	$\uparrow\downarrow$		
$3^2\text{B}_1$	5.91	7.26	0.64	$\uparrow\downarrow$	$\uparrow\downarrow$	$\uparrow$	$\downarrow$	$\uparrow$	
				$\uparrow\downarrow$	$\uparrow\downarrow$	$\uparrow$	$\uparrow$	$\downarrow$	$\uparrow$
				$\uparrow\downarrow$	$\uparrow\downarrow$	$\downarrow$	$\uparrow$	$\uparrow$	
$4^2\text{B}_1$	6.39	7.74	0.79	$\uparrow\downarrow$	$\uparrow\downarrow$	$\uparrow\downarrow$		$\uparrow$	
$3^2\text{A}_2$	7.00	8.35	0.47	$\uparrow\downarrow$	$\uparrow\downarrow$	$\uparrow$		$\uparrow\downarrow$	
				$\uparrow\downarrow$	$\uparrow$	$\uparrow\downarrow$	$\downarrow$	$\uparrow$	
				$\uparrow\downarrow$	$\uparrow$	$\uparrow\downarrow$	$\uparrow$	$\downarrow$	$\uparrow$
$3^2\text{A}_2$	7.00	8.35	0.33	$\uparrow\downarrow$	$\uparrow$	$\uparrow\downarrow$	$\uparrow$	$\downarrow$	$\uparrow$
				$\uparrow\downarrow$	$\uparrow$	$\uparrow\downarrow$	$\uparrow$	$\downarrow$	$\uparrow$
				$\uparrow\downarrow$	$\downarrow$	$\uparrow\downarrow$	$\uparrow$	$\uparrow$	$\uparrow$

Table 5.5-4

Calculated INDO/S energies  $E_{\text{calc}}$  (in eV) and wave functions for the neutral ground and lowest excited triplet states of pyrrole.

state	$E_{\text{calc}}$	$a^2$	$\pi_{\text{SS}}$	$\pi_{\text{SA}}$	$\pi_{\text{AS}}^*$	$\pi_{\text{AA}}^*$
$1^1\text{A}_1$	0.00	1.00	$\uparrow\downarrow$	$\uparrow\downarrow$		
$1^3\text{B}_2$	2.47	0.87	$\uparrow\downarrow$	$\uparrow$	$\uparrow$	
$1^3\text{A}_1$	3.76	0.64	$\uparrow\downarrow$	$\uparrow$		$\uparrow$
		0.33	$\uparrow$	$\uparrow\downarrow$	$\uparrow$	

Table 5.5-5

Calculated INDO/S energies  $E_{\text{calc}}$  (in eV) and wave functions for the lowest doublet states of the pyrrole anion.

state	$E_{\text{calc}}$	$E_0 + E_{\text{calc}}$	$a^2$	$\pi_{\text{SS}}$	$\pi_{\text{SA}}$	$\pi_{\text{AS}}^*$	$\pi_{\text{AA}}^*$
$1^2\text{B}_1$	0.00	2.41	0.93	$\uparrow\downarrow$	$\uparrow\downarrow$	$\uparrow$	
$1^2\text{A}_2$	0.88	3.29	0.82	$\uparrow\downarrow$	$\uparrow\downarrow$		$\uparrow$
$2^2\text{A}_2$	3.76	6.17	0.70	$\uparrow\downarrow$	$\uparrow$	$\uparrow\downarrow$	
				$\uparrow\downarrow$	$\uparrow$	$\uparrow\downarrow$	
$2^2\text{B}_1$	4.38	6.79	0.36	$\uparrow$	$\uparrow\downarrow$	$\uparrow\downarrow$	
				$\uparrow\downarrow$	$\uparrow$	$\downarrow$	$\uparrow$
				$\uparrow\downarrow$	$\uparrow$	$\uparrow$	$\downarrow$
$3^2\text{B}_1$	5.49	7.90	0.64	$\uparrow\downarrow$	$\uparrow$	$\downarrow$	$\uparrow$
				$\uparrow\downarrow$	$\uparrow$	$\uparrow$	$\downarrow$
				$\uparrow\downarrow$	$\downarrow$	$\uparrow$	$\uparrow$
$3^2\text{A}_2$	6.39	8.80	0.51	$\uparrow$	$\uparrow\downarrow$	$\downarrow$	$\uparrow$
				$\uparrow$	$\uparrow\downarrow$	$\uparrow$	$\downarrow$
				$\downarrow$	$\uparrow\downarrow$	$\uparrow$	$\uparrow$
$4^2\text{A}_2$	6.73	9.14	0.24	$\uparrow\downarrow$	$\uparrow$		$\uparrow\downarrow$
				$\uparrow$	$\uparrow\downarrow$	$\downarrow$	$\uparrow$
				$\downarrow$	$\uparrow\downarrow$	$\uparrow$	$\uparrow$

Table 5.5-6

Calculated INDO/S energies  $E_{\text{calc}}$  (in eV) and wave functions for the neutral ground and lowest excited triplet states of furan.

state	$E_{\text{calc}}$	$a^2$	$\pi_{\text{SS}}$	$\pi_{\text{SA}}$	$\pi_{\text{AS}}^*$	$\pi_{\text{AA}}^*$
$1^1\text{A}_1$	0.00	1.00	$\uparrow\downarrow$	$\uparrow\downarrow$		
$1^3\text{B}_2$	2.47	0.84	$\uparrow\downarrow$	$\uparrow$	$\uparrow$	
		0.14	$\uparrow$	$\uparrow\downarrow$		$\uparrow$
$1^3\text{A}_1$	4.20	0.80	$\uparrow\downarrow$	$\uparrow$		$\uparrow$
		0.19	$\uparrow$	$\uparrow\downarrow$	$\uparrow$	



Table 5.5-7

Calculated INDO/S energies  $E_{\text{calc}}$  (in eV) and wave functions for the lowest doublet states of the furan anion.

state	$E_{\text{calc}}$	$E_0 + E_{\text{calc}}$	$a^2$	$\pi_{\text{SS}}$	$\pi_{\text{SA}}$	$\pi_{\text{AS}}^*$	$\pi_{\text{AA}}^*$
$1^2B_1$	0.00	1.85	0.92	$\uparrow\downarrow$	$\uparrow\downarrow$	$\uparrow$	
$1^2A_2$	0.57	2.42	0.84	$\uparrow\downarrow$	$\uparrow\downarrow$		$\uparrow$
$2^2A_2$	4.03	5.88	0.63	$\uparrow\downarrow$	$\uparrow$	$\uparrow\downarrow$	
$2^2B_1$	4.61	6.46	0.52	$\uparrow\downarrow$	$\uparrow$	$\downarrow$	$\uparrow$
				$\uparrow\downarrow$	$\uparrow$	$\uparrow$	$\downarrow$
				$\uparrow\downarrow$	$\downarrow$	$\uparrow$	$\uparrow$
$3^2B_1$	5.60	7.45	0.58	$\uparrow\downarrow$	$\uparrow$	$\downarrow$	$\uparrow$
				$\uparrow\downarrow$	$\uparrow$	$\uparrow$	$\downarrow$
				$\uparrow\downarrow$	$\downarrow$	$\uparrow$	$\uparrow$
$3^2A_2$	6.44	8.29	0.40	$\uparrow$	$\uparrow\downarrow$	$\downarrow$	$\uparrow$
				$\uparrow$	$\uparrow\downarrow$	$\uparrow$	$\downarrow$
				$\downarrow$	$\uparrow\downarrow$	$\uparrow$	$\uparrow$
$4^2A_2$	6.93	8.78	0.55	$\uparrow$	$\uparrow\downarrow$	$\downarrow$	$\uparrow$
				$\uparrow$	$\uparrow\downarrow$	$\uparrow$	$\downarrow$
				$\downarrow$	$\uparrow\downarrow$	$\uparrow$	$\uparrow$

Table 5.5-8

Calculated INDO/S energies  $E_{\text{calc}}$  (in eV) and wave functions for the neutral ground and lowest excited triplet states of thiophene.

state	$E_{\text{calc}}$	$a^2$	$\pi_{\text{SS}}$	$\pi_{\text{SA}}$	$\pi_{\text{AS}}^*$	$\pi_{\text{AA}}^*$
$1^1A_1$	0.00	1.00	$\uparrow\downarrow$	$\uparrow\downarrow$		
$1^3B_2$	1.72	0.88	$\uparrow\downarrow$	$\uparrow$	$\uparrow$	
		0.11	$\uparrow$	$\uparrow\downarrow$		$\uparrow$
$1^3A_1$	3.00	0.61	$\uparrow\downarrow$	$\uparrow$		$\uparrow$
		0.29	$\uparrow$	$\uparrow\downarrow$	$\uparrow$	

Table 5.5-9

Calculated INDO/S energies  $E_{\text{calc}}$  (in eV) and wave functions for the lowest doublet states of the thiophene anion.

state	$E_{\text{calc}}$	$E_0 + E_{\text{calc}}$	$a^2$	$\pi_{\text{SS}}$	$\pi_{\text{SA}}$	$\pi_{\text{AS}}^*$	$\pi_{\text{AA}}^*$	$\pi^*$	$\pi^*$
$1^2B_1$	0.00	1.26	0.94	$\uparrow\downarrow$	$\uparrow\downarrow$	$\uparrow$			
$1^2A_2$	1.38	2.64	0.84	$\uparrow\downarrow$	$\uparrow\downarrow$			$\uparrow$	
$2^2A_2$	3.48	4.74	0.73	$\uparrow\downarrow$	$\uparrow$	$\uparrow\downarrow$			
$2^2B_1$	4.63	5.89	0.41	$\uparrow$	$\uparrow\downarrow$	$\uparrow\downarrow$			
				0.34	$\uparrow\downarrow$	$\uparrow$	$\downarrow$	$\uparrow$	
					$\uparrow\downarrow$	$\uparrow$	$\uparrow$	$\downarrow$	$\uparrow$
$3^2B_1$	6.09	7.35	0.65	$\uparrow\downarrow$	$\uparrow$	$\downarrow$	$\uparrow$		
				$\uparrow\downarrow$	$\uparrow$	$\uparrow$	$\downarrow$	$\uparrow$	
				$\uparrow\downarrow$	$\downarrow$	$\uparrow$	$\uparrow$	$\uparrow$	
$4^2B_1$	6.42	7.68	0.64	$\uparrow\downarrow$	$\uparrow\downarrow$			$\uparrow$	
$3^2A_2$	6.44	7.80	0.75	$\uparrow\downarrow$	$\uparrow\downarrow$				$\uparrow$
$4^2A_2$	6.98	8.24	0.51	$\uparrow$	$\uparrow\downarrow$		$\uparrow\downarrow$		
				$\uparrow$	$\uparrow\downarrow$	$\downarrow$	$\uparrow$		
				$\downarrow$	$\uparrow\downarrow$	$\uparrow$	$\downarrow$	$\uparrow$	

Table 5.5-10

Calculated INDO/S decay factors  $d$  determined between the anionic and neutral states of cyclopentadiene.

$d$	$1^2B_1$	$1^2A_2$	$2^2A_2$	$2^2B_1$	$3^2B_1$	$4^2B_1$	$3^2A_2$
$1^1A_1$	<b>0.93</b>	<b>0.81</b>	0.08	0.00	0.12	<b>0.79</b>	0.01
$1^3B_2$	<b>0.83</b>	0.16	<b>0.63</b>	0.12	<b>0.52</b>	0.07	0.10
$1^3A_1$	<b>0.30</b>	<b>0.57</b>	0.11	0.18	<b>0.27</b>	0.03	<b>0.42</b>

Table 5.5-11

Calculated INDO/S decay factors  $d$  determined between anionic and neutral states of pyrrole.

$d$	$1^2B_1$	$1^2A_2$	$2^2A_2$	$2^2B_1$	$3^2B_1$	$3^2A_2$	$4^2A_2$
$1^1A_1$	<b>0.93</b>	<b>0.82</b>	0.04	0.00	0.02	0.01	0.03
$1^3B_2$	<b>0.82</b>	0.13	<b>0.62</b>	<b>0.25</b>	<b>0.45</b>	0.07	0.12
$1^3A_1$	<b>0.32</b>	<b>0.56</b>	0.08	0.12	<b>0.37</b>	<b>0.31</b>	0.04

Table 5.5-12

Calculated INDO/S decay factors  $d$  determined between the anionic and neutral states of furan.

$d$	$1^2B_1$	$1^2A_2$	$2^2A_2$	$2^2B_1$	$3^2B_1$	$3^2A_2$	$4^2A_2$
$1^1A_1$	<b>0.92</b>	<b>0.84</b>	0.03	0.00	0.02	0.01	0.02
$1^3B_2$	<b>0.79</b>	0.16	<b>0.55</b>	<b>0.40</b>	<b>0.29</b>	0.12	0.19
$1^3A_1$	<b>0.20</b>	<b>0.71</b>	0.13	0.04	<b>0.47</b>	<b>0.35</b>	0.04

Table 5.5-13

Calculated INDO/S decay factors  $d$  determined between the anionic and neutral states of thiophene.

$d$	$1^2B_1$	$1^2A_2$	$2^2A_2$	$2^2B_1$	$3^2B_1$	$4^2B_1$	$3^2A_2$	$4^2A_2$
$1^1A_1$	<b>0.94</b>	<b>0.84</b>	0.06	0.00	0.09	<b>0.64</b>	<b>0.75</b>	0.03
$1^3B_2$	<b>0.83</b>	0.15	<b>0.65</b>	0.11	<b>0.51</b>	0.08	0.00	0.07
$1^3A_1$	<b>0.37</b>	<b>0.54</b>	0.08	0.16	<b>0.26</b>	0.03	0.01	<b>0.27</b>

### 5.5.3. Discussion

#### EEL Spectra

Various 0-0 excitation energies of  $\pi \rightarrow \pi^*$  transitions were determined for the first time (in the gas phase). The present results are compared to the results of previous studies in Table 5.5-14. The agreement for the triplet states is within experimental error, wherever previous results are available. In comparison to butadiene the values for cyclopentadiene are the most similar. The lowest triplet state of pyrrole, furan and thiophene all lie at least 0.5 eV

above the  $1^3B_g$  state in butadiene, while the gap between the two lowest triplet states is smaller than in butadiene.

Table 5.5-14

Summary of the excitation energies (in eV) of the current and previous EEL studies on cyclopentadiene, pyrrole, furan and thiophene. The results for butadiene from the previous chapter are included. Numbers in brackets refer to 0-0 transition energies.

molecule	phase	$1^3B_2$	$1^3A_1$	$1^1B_2$	$2^1A_1$
cyclopentadiene	gas <sup>a</sup>	3.15 (2.55)	(4.58)	5.22 (4.82)	
	gas <sup>b</sup>	3.10		5.26	
	solid <sup>c</sup>	3.35 (2.56)		5.1 (4.56)	
pyrrole	gas <sup>a</sup>	4.21	5.17	5.98	
	gas <sup>d</sup>	4.21		5.89	6.80
	gas <sup>e</sup>	4.2	5.1		
furan	gas <sup>a</sup>	3.95	5.22 (4.98)	6.04	
	gas <sup>d</sup>	3.99	5.22	6.06	6.44
	gas <sup>e</sup>	4.0	5.2		
	gas <sup>f</sup>	3.99	5.15	6.04	5.80
thiophene	gas <sup>a</sup>	3.74	4.62 (4.38)	5.61	5.43
	gas <sup>d</sup>	3.75	4.62	5.93	5.48
	gas <sup>e</sup>	3.7	4.6		
		$1^3B_u$	$1^3A_g$	$1^1B_u$	$2^1A_g$
butadiene	gas <sup>a</sup>	3.24 (2.59)	4.92	5.91 (5.75)	

<sup>a</sup>Present study. <sup>b</sup>Frueholz *et al.* (1979). <sup>c</sup>Swiderek *et al.* (1993). <sup>d</sup>Flicker *et al.* (1976). <sup>e</sup>Van Veen (1976). <sup>f</sup>Palmer *et al.* (1995).

These observations can be explained on a MO level (see Figure 5.5-14), if we idealize electronic excitation as the promotion of a single electron and assume that the appropriate configuration energy is proportional to the respective orbital gap. Therefore butadiene and cyclopentadiene have similar excitation energies because the  $\pi$  and  $\pi^*$  orbital energies are quite similar. In contrast to pyrrole, furan and thiophene, where the HOMO-LUMO gap increases and the separation of the occupied  $\pi$  orbital energies as well as the separation of the unoccupied  $\pi^*$  orbitals decreases.

**Cyclopentadiene.** The 0-0 transition energies for  $1^3B_2$  and  $1^3A_1$  states have been determined for the first time in the gas phase. The vertical transition into the  $1^3A_1$  state can be estimated to lie between 4.9 and 5.0 eV, assuming a similar band width as the  $1^3B_2$  band. The CASPT2 calculations of Serrano-

Andrés *et al.* (1993b) predict the second triplet state to lie at 4.90 eV, which agrees well with the estimate. It has been shown that CASPT2 predicts the transitions energies of the lowest valence triplet states in general within 0.2 eV of the experimental value (Roos *et al.* 1994).

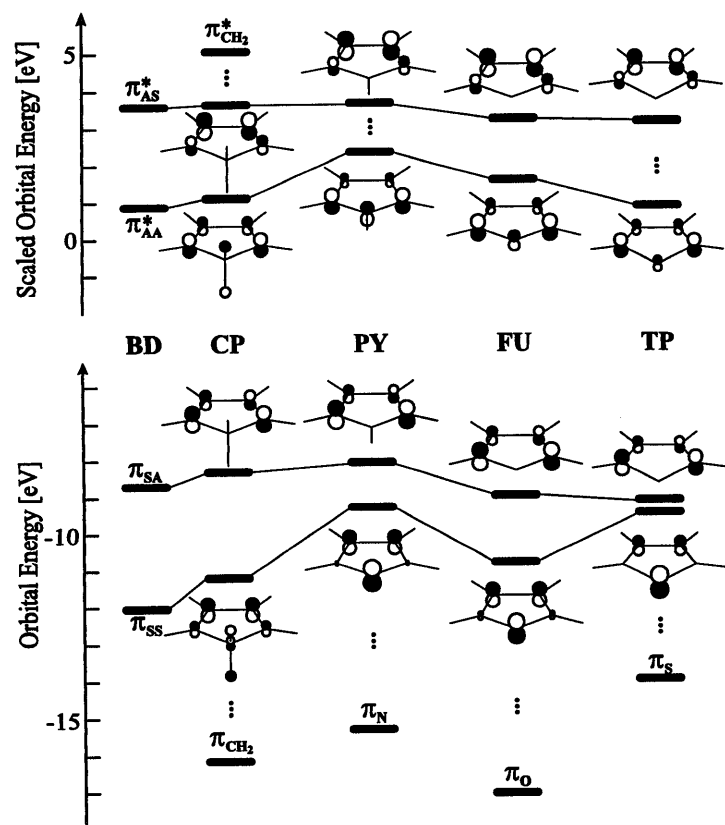


Figure 5.5-14

Comparison of the  $\pi$  and  $\pi^*$  HF-SCF/6-31G orbitals, orbital energies (occupied orbitals) and scaled orbital energies (unoccupied orbitals) of trans-butadiene (BD), cyclopentadiene (CP), pyrrole (PY), furan (FU) and thiophene (TP).

The dependence of the form and position of the lowest triplet band on the residual energy is caused by the fact that more than one resonance is involved in the excitation process. The excitation functions of the  $1^3B_2$  state reveal, that at low  $E_r$  the  $1^2A_2$  1p resonance and at higher  $E_r$  a 2p-1h resonance excites the  $1^3B_2$  state predominately. Consult chapter 5.4.3 for a general explanation of this observation.

The lowest triplet band of cyclopentadiene is compared to the calculated spectrum of Zgierski and Zerbetto (1993) in Figure 5.5-15. The agreement is surprisingly good. The 0-0 peak at 2.55 eV is followed by a shoulder (ca. 700  $\text{cm}^{-1}$ ) and two peaks (1000 and 1500  $\text{cm}^{-1}$ ). The calculations indicate that these features are due to the excitation of at least four different totally symmetric modes with an energy of 717, 1030, 1350 and 1438  $\text{cm}^{-1}$ . The calculated Stokes' shift of 5315  $\text{cm}^{-1}$  is in good agreement with the observed gap of 0.60 eV (ca. 5000  $\text{cm}^{-1}$ ) between 0-0 line and the maximum of the band.

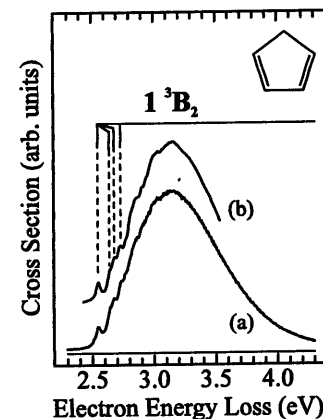


Figure 5.5-15  
EEL spectrum (a) of cyclopentadiene ( $E_r = 1.6$  eV) in the region of the lowest triplet state  $1^3B_2$  compared to calculated spectrum (b) of Zgierski and Zerbetto (1993).

**Pyrrole.** The EEL spectra of pyrrole are the only ones of this study which show no vibrational structure in either triplet bands, an indication for vibronic coupling between the  $\pi^*$  and a low-lying  $\sigma^*$  resonance. The study of Flicker *et al.* (1976) did not detect the second triplet state because they measured under conditions, under which the  $1^3A_1$  band is masked by Rydberg transitions. The assignment by Flicker *et al.* of the band observed at 6.80 eV to the  $2^1A_1$  valence state is controversial. The results of CASPT2 calculations (Serrano-Andrés *et al.* 1993b) predict this state at 5.92 eV, with a small oscillator strength of  $f = 0.020$ .

**Furan.** The  $1^3A_1$  0-0 transition was detected for the first time and determined to lie at 4.98 eV. Although (different) assignments for the  $2^1A_1$  valence state have been proposed by Flicker *et al.* (1976) and Roebber *et al.* (1980), calculations indicate (Serrano-Andrés *et al.* 1993b, and Palmer and *et al.* 1995) the transition into the  $2^1A_1$  valence state to be too weak to be observed in an EEL spectrum. No further evidence for the location of the  $2^1A_1$  state is found in our spectra.

The  $^2(\pi_{SA}, 3s^2)$  Feshbach resonance has been located at 5.67 eV. As is typical for Feshbach resonances, it only appears at very low residual energies.

Its Feshbach decrement of 0.24 eV is somewhat smaller than the generally observed value of 0.5 eV (Robin 1985).

**Thiophene.** Vibrational structure in the second triplet band has previously not been observed. The 0-0 transition is determined to lie at 4.38 eV. In comparison to the previously discussed molecules the high oscillator strength of the  $2^1A_1$  state is surprising. Serrano-Andrés *et al.* (1993c) argue that the higher oscillator strength of the  $2^1A_1$  transition in thiophene is due to the weaker influence of doubly excited configurations in the  $2^1A_1$  wave function.

#### Calculations and Assignment of Shape Resonances

In qualitative agreement with the experiment the two lowest triplet states of each molecule are calculated to be the  $1^3B_2$  followed by the  $1^3A_1$  state, both resulting from  $\pi \rightarrow \pi^*$  excitations. Mixture between  $\pi \rightarrow \pi^*$  and  $\sigma \rightarrow \sigma^*$  configurations in the neutral is predicted to be negligible, confirming the assignment of resonances detected in the triplet excitation functions to be  $\pi^*$  and not  $\sigma^*$  resonances. All triplet states are calculated too low in energy. The largest deviations between calculated and experimental energies are observed for thiophene, where the calculated values are up to 2.0 eV too low. This larger discrepancy is due to the lack of a triplet parametrisation for second row atoms.

For the anion mixture between 1p and 2p-1h configurations is calculated to be weak. As a result, the decay of a 2p-1h resonance into the neutral ground state does not have a high probability. This strengthens the preferred assignment of the features in the vibrational excitation functions to 1p and not 2p-1h resonances. The low lying  $\pi^*$  1p resonances in general have a large decay factor with respect to the  $\pi \rightarrow \pi^*$  excited triplet states. Note, that in this case the probability of the 1p resonance to decay into a triplet state is controlled by the energy of the resonance relative to the triplet state. If the resonance lies notably below the respective triplet state, then the decay probability is small, even though the decay factor may be large.

In accord with the experiment the lowest two resonances of each molecule are predicted to be 1p resonances ( $1^2B_1$  and  $1^2A_2$ ), interpreted as temporary capture of an electron in the antibonding orbitals  $\pi_{AS}^*$  and  $\pi_{AS}^*$  respectively. Cyclopentadiene and thiophene possess additional  $\pi^*$  orbitals and thus additional 1p  $\pi^*$  resonances are calculated. In contrast to the  $1^2B_1$  and  $1^2A_2$  resonances, decay of the higher lying 1p resonances into the  $1^3B_2$  and  $1^3A_1$  states are indicated to be unfavorable.

**Cyclopentadiene.** The results for the cyclopentadiene anion are summarized in Table 5.5-15. Besides the two known 1p resonances  $1^2B_1$  and  $1^2A_2$  a third 1p resonance is identified. The band at 4.70 eV in the  $\Delta E = 1.03$  eV spectrum and the shoulder at 5.13 eV in the  $\Delta E = 2.55$  eV spectrum (Figure 5.5-10) are attributed to the  $\pi_{CH}^*$  1p resonance, in accord with the predicted AE of 5.07 eV.

**Table 5.5-15**  
Summary of the experimentally determined and calculated resonance energies (in eV) for the cyclopentadiene anion.

sym.	type	present				previous		
		$E_{\text{calc}}$		$E_{\text{exp}}$		$E_{\text{exp}}$		
		CI <sup>a</sup>	AE <sup>b</sup>	EF(S <sub>0</sub> ) <sup>c</sup>	EF(T <sub>1</sub> ) <sup>d</sup>	EF(T <sub>2</sub> ) <sup>e</sup>	ETS <sup>f</sup>	ETS <sup>g</sup>
$1^2B_1$	$\pi^*$ 1p	1.35	1.10	1.20			1.35	1.19
$1^2A_2$	$\pi^*$ 1p	2.65	3.64	3.45	3.34		3.33	3.3
$2^2A_2$	$\pi^*$ 2p-1h	4.56			4.69			
$2^2B_1$	$\pi^*$ 1p	7.74	5.07	4.70	5.13			
$2^2B_1$	$\pi^*$ 2p-1h	6.01				6.29		
$2^2B_1$	$\pi^*$ 2p-1h	7.26			7.80	8.21		

<sup>a</sup>INDO/S CI calculation. <sup>b</sup>HF-SCF/6-31G scaled orbital energies. <sup>c</sup>Excitation functions. <sup>d</sup>ET spectrum. <sup>e</sup>ET spectrum (Staley *et al.* 1981).

The three  $\pi^*$  1p shape resonances are determined by the INDO/S method to lie at 1.35 ( $1^2B_1$ ), 2.65 ( $1^2A_2$ ) and 7.74 eV ( $2^2B_1$ ). The INDO/S energies are worse than the predicted AEs, but the decay properties are reproduced in a satisfactory manner. Decay into the neutral ground state is most favorable. The  $1^3B_2$  state is calculated below the higher two 1p resonances. Their decay into the same is none the less predicted to be not very probable ( $d_{T_1} = 0.16$  and  $0.07$ , Table 5.5-10), in accord with the low intensity of the  $\Delta E = 2.55$  eV signal in the respective energy region.

The three lowest  $\pi^*$  2p-1h resonances are calculated at 4.56, 6.01 and 7.26 eV. The decay factors of these three resonances with respect to the  $1^3B_2$  state are 0.63, 0.12 and 0.52. Thus the first triplet state is predicted to be excited predominantly by the first and third resonance, as is observed. The second triplet state is excited strongly by the third resonance, to a lesser degree by the second resonance and weakly by the first resonance. Again the decay factors (0.11, 0.18 and 0.27) between these resonances and the  $1^3A_1$  state reproduce this behavior well.

**Pyrrole.** The results for the pyrrole anion are summarized in Table 5.5-16. The assignment of the broad, intense band around 6.9 eV in the vibrational excitation function ( $\Delta E = 0.77$  eV, Figure 5.5-11) of pyrrole to a  $\sigma^*$  1p resonance and not a  $\pi^*$  2p-1h resonance is indirectly confirmed by the INDO/S calculations. None of the decay factors calculated between the 2p-1h resonances and the neutral ground state (Table 5.5-11) is larger than 0.04, indicating a very small probability for these decay channels.

Table 5.5-16

Summary of the experimental and calculated resonance energies (in eV) for the pyrrole anion.

sym.	type	present						previous
		$E_{\text{calc}}$		$E_{\text{exp}}$				$E_{\text{exp}}$
		CI <sup>a</sup>	AE <sup>b</sup>	EF(S <sub>0</sub> ) <sup>c</sup>	EF(T <sub>1</sub> ) <sup>d</sup>	EF(T <sub>2</sub> ) <sup>e</sup>	ETS <sup>f</sup>	ETS <sup>g</sup>
1 <sup>2</sup> B <sub>1</sub>	π* 1p	2.41	2.35	2.48			2.41	2.38
1 <sup>2</sup> A <sub>2</sub>	π* 1p	3.29	3.64	3.50			3.51	3.44
2 <sup>2</sup> A <sub>2</sub>	π* 2p-1h	6.17			5.5	6.0		
	σ* 1p			6.9			7.2	
2 <sup>2</sup> B <sub>1</sub>	π* 2p-1h	6.79			7.33			
2 <sup>2</sup> B <sub>1</sub>	π* 2p-1h	7.90			8.53	8.62		

<sup>a</sup>INDO/S CI calculation. <sup>b</sup>HF-SCF/6-31G scaled orbital energies. <sup>c-e</sup>Excitation functions. <sup>f</sup>ET spectrum. <sup>g</sup>ET spectrum (Van Veen 1976).

The features observed in the triplet excitation functions are assigned to three resonances. The first only weakly excites either of the triplet states. The second selectively decays into the 1<sup>3</sup>B<sub>2</sub> state, while the third causes stronger excitation of both triplet states. While the second two resonances can be classified with confidence to two 2p-1h resonances, the nature of the first is harder to determine. We assume it to be a (broad) 2p-1h resonance, although the signal could also be attributed to the high energy tail of the second π\* 1p resonance.

Either assignment is only partly reproduced by the calculations. The decay factors between these three resonances and the 1<sup>3</sup>B<sub>2</sub> state are 0.62, 0.25 and 0.45. While the second two are conform with the observations, the first indicates a strong decay of the lowest 2p-1h resonance into the lowest triplet state, which is not observed. The decay factors for the second triplet state are 0.08, 0.12 and 0.37, indicating that the third 2p-1h resonance decays the strongest into the 1<sup>3</sup>B<sub>2</sub> state. Thus the third resonance is predicted to decay strongly into both triplet states, confirming the assignment of the broad band around 8.6 eV to the third 2p-1h resonance.

**Furan.** The results for the furan anion are shown in Table 5.5-17. The π\*<sub>AA</sub> resonance is calculated at a similar energy as the 1<sup>3</sup>B<sub>2</sub> state with a decay factor of  $d = 0.16$  (Table 5.5-12), confirming the accessibility of this decay channel. A weak contribution from the π\*<sub>AA</sub> resonance is observed slightly above threshold in the 1<sup>3</sup>B<sub>2</sub> excitation function.

Table 5.5-17

Summary of the experimental and calculated resonance energies (in eV) for the furan anion.

sym.	type	present							previous
		$E_{\text{calc}}$		$E_{\text{exp}}$				$E_{\text{exp}}$	
		CI <sup>a</sup>	AE <sup>b</sup>	EF(S <sub>0</sub> ) <sup>c</sup>	EF(T <sub>1</sub> ) <sup>d</sup>	EF(T <sub>2</sub> ) <sup>e</sup>	ETS <sup>f</sup>	ELS <sup>g</sup>	ETS <sup>h</sup>
1 <sup>2</sup> B <sub>1</sub>	π* 1p	1.85	1.58	1.85			1.85		1.76
1 <sup>2</sup> A <sub>2</sub>	π* 1p	2.42	3.22	3.36			3.23		3.14
2 <sup>2</sup> A <sub>2</sub>	Feshbach							5.67	
	σ* 1p			6.2					
2 <sup>2</sup> A <sub>2</sub>	π* 2p-1h	5.88			6.48				
2 <sup>2</sup> B <sub>1</sub>	π* 2p-1h	7.45			8.22	8.05			
2 <sup>2</sup> A <sub>2</sub>	π* 2p-1h	8.29				8.89			

<sup>a</sup>INDO/S CI calculation. <sup>b</sup>HF-SCF/6-31G scaled orbital energies. <sup>c-e</sup>Excitation functions. <sup>f</sup>ET spectrum. <sup>g</sup>EEL spectrum. <sup>h</sup>ET spectrum (Van Veen 1976).

The decay ratios of the three observed 2p-1h resonances is reproduced correctly by the INDO/S calculations, if it is assumed that the second lowest calculated 2p-1h resonance is masked by the neighboring resonances. The preferred decays of the lowest 2p-1h resonance into the 1<sup>3</sup>B<sub>2</sub> state ( $d_{T1} / d_{T2} = 0.55 / 0.13$ ) and of the fourth 2p-1h resonance into the 1<sup>3</sup>A<sub>1</sub> state ( $d_{T1} / d_{T2} = 0.07 / 0.31$ ), as well as the strong excitation of both triplet by the third resonance ( $d_{T1} / d_{T2} = 0.45 / 0.37$ ) is predicted correctly.

In addition to the shape resonances the (π<sub>SA</sub>, 3s<sup>2</sup>) Feshbach resonance has been detected at 5.67 eV in the  $E_r = 0.03$  eV EEL spectrum. Its energy cannot be calculated by the INDO/S method, because semiempirical methods use minimal basis sets and are therefore not adequate for the treatment of states involving Rydberg-type orbitals.

**Thiophene.** A summary of the results for the thiophene anion is found in Table 5.5-18. The agreement of the calculated AEs with the experimentally determined resonance energies of the π\*<sub>AS</sub> and π\*<sub>AA</sub> resonances is worse than in the other cases. Note, that thiophene is the only molecule in the present study involving a second row atom. The determination of the scaling parameters of Chen and Gallup (1990) only considered molecules with first row atoms, so that a larger discrepancy is expected.

The INDO/S calculations favor the interpretation of the triplet excitation spectra on the basis of four 2p-1h resonances. The calculated decay factors (Table 5.5-13) for the decay of these four 2p-1h resonances are 0.65, 0.11, 0.51

and 0.07 ( $1^3B_2$  state) and 0.08, 0.16, 0.26 and 0.27 ( $1^3A_1$  state). The first and third 2p-1h resonances are calculated to predominately decay into the  $1^3B_2$  state, while the second and fourth 2p-1h resonance prefer to decay into the  $1^3A_1$  state. The observed bands in the triplet excitation functions are therefore tentatively assigned to four (selectively decaying) 2p-1h resonances.

Table 5.5-18

Summary of the experimental and calculated resonance energies (in eV) for the thiophene anion.

sym.	type	present						previous
		$E_{\text{calc}}$		$E_{\text{exp}}$				$E_{\text{exp}}$
		CI <sup>a</sup>	AE <sup>b</sup>	EF(S <sub>0</sub> ) <sup>c</sup>	EF(T <sub>1</sub> ) <sup>d</sup>	EF(T <sub>2</sub> ) <sup>c</sup>	ETS <sup>f</sup>	ETS <sup>g</sup>
$1^2B_1$	$\pi^*$ 1p	1.26	0.86	1.27			1.26	1.76
$1^2A_2$	$\pi^*$ 1p	2.64	3.18	2.83			2.76	3.14
$2^2A_2$	$\pi^*$ 2p-1h	4.74			5.38			
	$\sigma^*$ 1p			5.5				
$2^2B_1$	$\pi^*$ 2p-1h	5.89				6.22		
$2^2B_1$	$\pi^*$ 2p-1h	7.35			7.39			
$2^2A_2$	$\pi^*$ 2p-1h	8.24				7.93		

<sup>a</sup>INDO/S CI calculation. <sup>b</sup>HF-SCF/6-31G scaled orbital energies. <sup>c-e</sup>Excitation functions.

<sup>f</sup>ET spectrum. <sup>g</sup>ET spectrum (Van Veen 1976).

#### 5.5.4. Conclusions

This study has shown that triplet excitation in cyclopentadiene, pyrrole, furan and thiophene is enhanced if not dominated by  $\pi^*$  2p-1h resonances in the incident energy range up to 10 eV above threshold. These 2p-1h resonances often show a pronounced selectivity in the excitation of either one or the other triplet state.  $\pi^*$  1p resonances can contribute to the excitation of triplet states if these are energetically accessible. Mixture between  $\pi^*$  1p and 2p-1h configurations is predicted to be small. As a result the decay of  $\pi^*$  2p-1h resonances into the neutral ground state is improbable. Consequently pure vibrational excitation is ascribed solely to 1p resonances.  $\pi^*$  1p resonances contribute strongly up to 4 eV above threshold. The contribution from  $\sigma^*$  1p resonances is dominant in the energy range between 4 and 8 eV above threshold.

In comparison to butadiene more  $\pi^*$  2p-1h resonances are detected in the cycloienes. This indicates longer resonance lifetimes and therefore smaller

resonance widths, resulting in more pronounced variations in the DCS of the triplet excitation processes. This is attributed to the high pseudo-symmetry of the  $\pi^*_{As}$  orbital, *i.e.* greater influence of higher  $l$  partial waves in the scattering mechanism. Due to the contribution from the ring closing group or heteroatom the LUMO is given the character of a distorted  $D_{5h}$  orbital, already noted by Staley *et al.* (1981) for the 1p  $\pi^*_{As}$  shape resonance in cyclopentadiene.

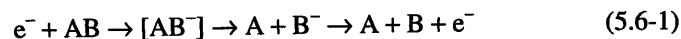
INDO/S calculations, although only of qualitative nature, are helpful in the assignment of 2p-1h resonances and reproduce the observed selective decay in a satisfactory manner. With respect to 1p resonances, the use of scaled orbital energies is the more reliable tool for the prediction of 1p shape resonance energies.

## 5.6. Dissociative Attachment Study of Ozone

### 5.6.1. Introductory Remarks

This Chapter presents two manuscripts on the collisions of low-energy electrons with ozone. The study resulted from a collaboration with the Department of Physics and Astronomy of the University College London (UCL). I contributed the results of the dissociative attachment study of ozone. The later part of the DA study was used to introduce the two newly arrived co-workers D. Popovic and M. Stepanovic to the DA spectrometer.

The publication "Production of vibrationally autodetaching  $O_2^-$  in low-energy electron impact on ozone" (*J. Phys. B.: At. Mol. Opt. Phys.* **29**, 1996, p. 3487) presents experimental evidence for a scattering process which is intermediate between inelastic electron scattering and dissociative attachment.



In this case the intermediate negative ion dissociates into a fragment anion, which subsequently rapidly loses its extra electron by autodetachment, producing two neutral fragments. To the best of our knowledge this study presents the first case of such a process, where an assignment of the detached electron spectrum to individual vibronic transitions in the fragment anion is possible, yielding detailed information of the product anion state distribution.

The manuscript "Resonances in collisions of low-energy electrons with ozone: Experimental elastic and vibrationally inelastic differential cross sections and dissociative attachment spectra" (starting on page 146) is in press at *J. Phys. B*. It complements and extends the existing experimental work on the vibrationally elastic and vibrationally inelastic DCSs and on dissociative attachment.

### 5.6.2. Publications

(see next page)

*J. Phys. B: At. Mol. Opt. Phys.* **29** (1996) 3487-3495. Printed in the UK

## Production of vibrationally autodetaching $O_2^-$ in low-energy electron impact on ozone

Michael Allan†, Knut R Asmis†, Duška B Popović†, Momir Stepanović†, Nigel J Mason‡ and Julia A Davies‡

† Institut de Chimie Physique, Université de Fribourg, Pérolles, CH-1700 Fribourg, Switzerland  
‡ Department of Physics and Astronomy, University College London, London WC1E 6BT, UK

Received 18 March 1996, in final form 24 May 1996

**Abstract.** Attachment of electrons with energies of 1.2 to 2 eV to ozone was found to lead to the production of O and vibrationally excited  $O_2^-$ , the latter subsequently lose electrons by vibrational autodetachment. This type of electron scattering is intermediate between inelastic electron scattering and dissociative attachment. Spectra of the detached electrons have resolved vibrational structure, which can be assigned to the individual  $O_2^-/O_2$  vibronic transitions, providing detailed information on the product state distribution. The absolute integral cross section for the production of  $O_2^-$  in vibrational states  $v' \geq 4$  was found to be substantial, for example at 1.7 eV it is  $0.27 \times 10^{-16} \text{ cm}^2$  (with an error bar of about  $+0.2 \times 10^{-16} \text{ cm}^2$  and  $-0.12 \times 10^{-16} \text{ cm}^2$ ). Measurements of the signal onsets permit an independent determination of the dissociation energy of ozone into O and  $O_2$  with the result  $D_0 = 1.06 \pm 0.04 \text{ eV}$ . Comparison of the peak width of the electrons detached by  $O_2^-$  in this work with the width of peaks of  $O_2^-$  resonances observed in electron- $O_2$  scattering indicates a moderate degree of rotational excitation in the present process.

### 1. Introduction

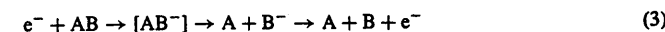
Resonant collisions of slow electrons with molecules generally result either in elastic or inelastic scattering,



leaving behind the undissociated target molecule in its ground or excited state, or they lead to dissociative attachment,



where the intermediate negative ion resonance dissociates, resulting in a neutral and a stable anionic fragment, which can then be detected in a mass spectrometer. An intermediate case is also possible, however, amounting to dissociation into two neutral fragments,



where the intermediate negative ion dissociates into a fragment anion which subsequently rapidly loses its extra electron by autodetachment. In the latter process the departing electron carries information about the final state of the fragment  $B^-$ , providing detailed information about the dissociation mechanism. Furthermore, when the fragment kinetic energy release is small the dissociation energy of AB can be determined directly from the electron-energy-loss spectrum.

Very few examples of process (3) have been reported, possibly because it requires that the lifetime of the fragment  $B^-$  towards autodetachment is sufficiently long that it does not lose its extra electron before the dissociation of the resonance  $[AB^-]$  is completed. The most notable example is the production of the autodetaching atomic anion  $N^-$  in collisions of 10 eV electrons with  $N_2$ , discovered nearly simultaneously by Mazeau *et al* (1978) and by Spence and Burrow (1979). Further examples are found in electron collisions with large polyatomic molecules in which polyatomic anionic fragments detach very slow, nearly thermal electrons, sometimes on very long time scales up to microseconds, permitting their observation in a mass spectrometer (Christophorou 1978). An interesting example is the production of metastable, bent  $CO_2^-$  (Cooper and Compton 1972). Near thermal electrons detached with nanosecond delay by vibrationally excited  $CH_3^-$  ions were reported in electron collisions with acetaldehyde (Dressler and Allan 1986).

In this paper we report the discovery of the production of autodetaching  $O_2^-$  anions in collisions of slow electrons with ozone. This case of process (3) is particularly interesting in comparison with the above-mentioned cases, because (i) the autodetaching fragment is molecular and simultaneously small, with resolvable vibrational structure, and (ii) the spectrum of the detached electrons is not limited to a single peak of near thermal electrons, but covers several tenths of an electronvolt. These two aspects lead to an interesting, structured spectrum of the ejected electrons and to the best of our knowledge it is the first case of process (3), where assignment of the detached electron spectrum to individual vibronic transitions in the fragment anion is possible, yielding detailed information of the product anion state distribution. The present paper is a continuation of a systematic investigation of electron collisions with ozone (Johnstone *et al* 1992, Davies *et al* 1993, Newson *et al* 1995, Gingell *et al* 1995, Mason *et al* 1996 and Walker *et al* 1996).

## 2. Instrumental

Preparation and handling of ozone of substantial purity requires considerable experience. We accomplished this task with the ozone production apparatus designed and constructed at the UCL. The techniques have been described previously by Johnstone *et al* (1992), Davies *et al* (1993) and Newson *et al* (1995).

The spectra were recorded with the electron spectrometer described by Allan (1992, 1995). Ozone was introduced into the collision region from a storage bulb as an effusive beam through a nozzle with 250  $\mu\text{m}$  diameter and about 0.3 mm long, kept at about 45 °C. All spectra were corrected for the instrumental response function, determined on the helium elastic signal and the near threshold ionization continuum of helium. Absolute differential cross sections (DCS) were determined using the relative flow technique (Nickel *et al* 1989). The application of this technique was somewhat complicated by the decomposition of the ozone within the metallic gas handling system and the capacitance manometer used to measure gas flow, and by the limited purity of ozone (although purities of up to 97% in the collision region were ultimately achieved). The details of the procedure used will be described in more detail in a forthcoming publication (Allan *et al* 1996a). The complications result in a larger error of the absolute values, believed to be accurate within  $\pm 50\%$  (or, more appropriately, within a factor of about 1.5). The error may be larger for residual energies below about 0.2 eV. The energy scale was calibrated on the 19.366 eV resonance in helium and on sharp features in the vibrationally inelastic cross sections of  $O_2$  in  $O_2/O_3$  mixtures and is accurate within  $\pm 20$  meV. The resolution was between 20 and 25 meV (FWHM, in energy-loss mode). A Wien filter was used in the analyser to prevent stable fragment anions from reaching the detector.

## Production of vibrationally autodetaching $O_2^-$

The quadrupole mass spectrometer used to record the yield of stable  $O_2^-$  ions was also described previously (Dressler and Allan 1985, Bulliard *et al* 1994).

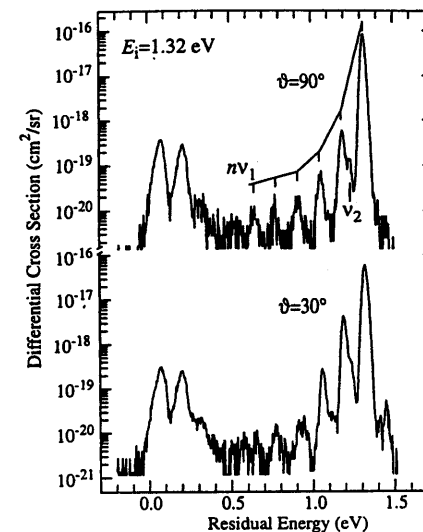


Figure 1. Electron-energy-loss spectra of ozone, recorded with a constant incident energy of 1.32 eV at the two scattering angles indicated. The ordinate is the absolute differential cross section, and is shown logarithmically to accommodate the large variations of the cross section magnitude. The energy of the scattered electrons (and not the customary energy-loss) is indicated as the abscissa. The most intense peak, at  $E_r = 1.32$  eV, is thus the elastic peak, and the progression of peaks to its left, with rapidly decreasing intensity, is due to vibrational excitation of ozone, principally a progression in the  $\nu_1$  symmetric stretch as indicated. The two peaks at low residual energies are due to electrons ejected from vibrationally excited  $O_2^-$ , formed by electron impact on ozone.

## 3. Results and discussion

In the process of an investigation of electron scattering in ozone, the full account of which will be published later, we discovered a peculiar distribution of scattered electrons when the incident electrons had energies between about 1.2 eV and 2 eV. An illustrative example is shown in figure 1. Apart from the expected vibrationally inelastic peaks, the intensity of which diminishes rapidly with increasing vibrational quantum number, an unexpected group of electrons is observed in the low-energy part of the spectra. It is noteworthy that whereas the magnitude of the elastic DCS, and even more the magnitudes of the vibrationally inelastic DCSs of ozone, are different for the two scattering angles, the magnitude of the DCS of the low-energy peaks is (within experimental error bar) the same in both spectra. Note further that the DCS is quite substantial for the low-energy peaks, indeed it is comparable to vibrationally inelastic DCSs at this energy.

Further experiments revealed that the group of low-energy electrons appears for incident



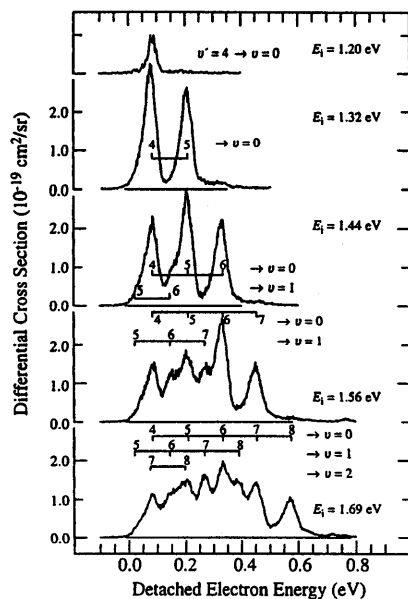


Figure 2. The low-energy group of electrons recorded with different incident electron energies. The individual  $\text{O}_2^-/\text{O}_2$  vibronic transitions are indicated by vertical bars above the spectra. The initial vibrational states  $v'$  of  $\text{O}_2^-$  are indicated by numbers above the bars. Transitions belonging to the same final state  $v$  of  $\text{O}_2$  are then connected by a horizontal line and labelled on the right (the top trace is not on an absolute scale).

electron energies larger than about 1.15 eV and becomes weak and obscured by ozone energy-loss features for incident electron energies above about 2 eV. The spectrum of the low-energy electrons is shown for five different incident energies in figure 2. The shape and width of the spectrum varies dramatically for different incident energies, but distinct peaks can be discerned in the spectra, which always appear at the same residual energy, excluding their assignment to excited states of the target ozone, which would be fixed to a given energy-loss. The group of low-energy electrons can then easily be identified as being ejected by vibrationally excited  $\text{O}_2^-$ , itself produced in electron collisions with ozone. The relevant potential energy curves are shown in figure 3. Figure 4 shows a detailed example of the spectrum obtained with an incident energy of 1.69 eV, when  $\text{O}_2^-$  in vibrational states up to  $v' = 8$  are produced (the threshold energies will be discussed in more detail below). Figure 4 shows that the relatively complex spectrum is entirely accounted for—no peaks are observed which would not correspond to one of the predicted transitions, and conversely a peak is observed for each of the predicted transitions. The weak peaks at 0.71 and 0.76 eV are due to a small  $\text{O}_2$  impurity (excitation of the  $a^1\Delta_g$  state) and the excitation of the (700) vibrational level of ozone. The weak shoulder at about 0.62 eV is probably the (800) vibrational level of ozone. A minor point worth mentioning are the weak bands found to the right of the main low-energy group in figures 1 and 2. Specifically, the  $v' = 6 \rightarrow v = 0$

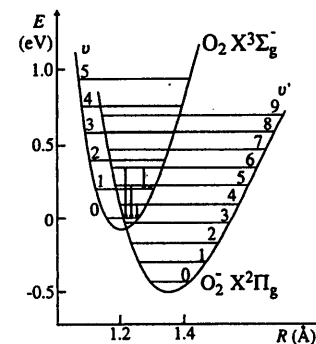
Production of vibrationally autodetaching  $\text{O}_2^-$ 

Figure 3. Schematic potential curves of  $\text{O}_2$  and  $\text{O}_2^-$  based on the curves given by Celotta *et al* (1972). Vertical arrows illustrate the transitions encountered when  $\text{O}_2^-$  in states up to  $v' = 6$  is produced, which is the case with an incident energy of 1.44 eV, shown by the centre trace in figure 2.

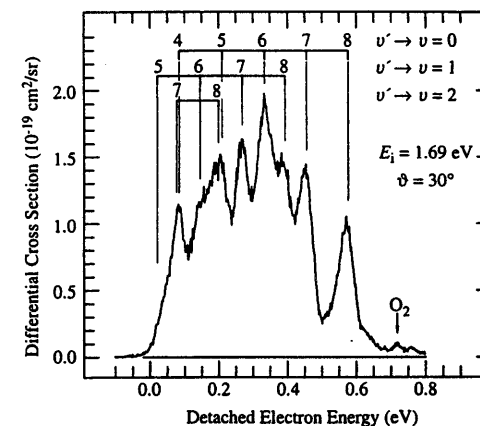


Figure 4. Detailed view of the spectrum of electrons ejected by  $\text{O}_2^-$  generated in collisions of 1.69 eV electrons with ozone. The individual vibronic transitions are labelled as in figure 2. A small peak due to a small  $\text{O}_2$  impurity in the ozone gas is labelled by an arrow.

appears very weakly already with an incident energy of 1.32 eV, below the threshold for the formation of  $\text{O}_2^-$  in  $v' = 6$ , similarly the  $v' = 7 \rightarrow v = 0$  appears very weakly already with an incident energy of 1.44 eV, below the threshold for the formation of  $\text{O}_2^-$  in  $v' = 7$ , etc. Two possible explanations of these weak bands can be proposed. They could be due to thermal population of vibrations in the target ozone, lowering the threshold for the formation of  $\text{O}_2^-$  in a given  $v'$ . The high energy tail of the incident beam, due to final resolution of the instrument, is also likely to contribute to the weak bands.

Summing under the whole width of the spectra in figure 2 (and comparing the resulting

area with the area under the elastic peak) gives the differential cross sections for the sum of all observed  $O_2^-/O_2$  transitions at each incident energy, that is the sum of cross sections for production of  $O_2^-$  in the vibrational states  $v' \geq 4$ . The differential cross sections may then be multiplied by  $4\pi$  to obtain the integral cross sections, under the assumption that the cross sections are isotropic, an assumption which appears justified by the spectra in figure 1, and which is plausible in view of the lifetime of the autodetaching  $O_2^-$  being longer than the rotational period. The results are summarized in table 1. The dominant cause of error of the absolute values is the uncertainty of the instrumental response function at very low energies. The combined error of the absolute values in table 1 is estimated to be a factor of two. The cross section cannot, unfortunately, be obtained for energies higher than those given in the table, because the pertinent spectral region becomes obscured by energy-loss peaks due to electronic excitation of ozone (Allan *et al* 1996b).

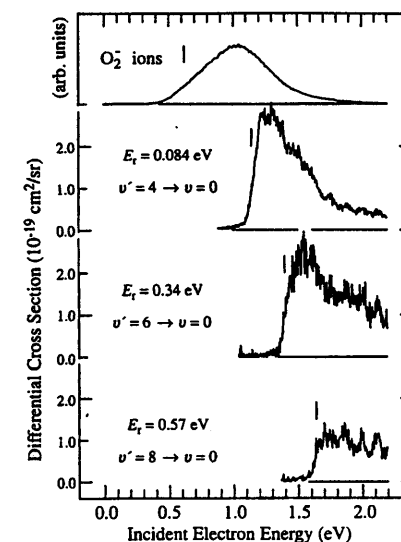
**Table 1.** Integral cross sections  $\sigma_i$  for production of  $O_2^-$  in vibrational states  $v' \geq 4$  in collisions of electrons with ozone.  $E_i$  is the incident electron energy. The error is estimated to be a factor of two (for example the lower and upper limits of  $\sigma_i$  at 1.69 eV are  $0.13 \times 10^{-16}$  and  $0.54 \times 10^{-16}$  cm<sup>2</sup>, respectively).

$E_i$ (eV)	1.32	1.44	1.56	1.69
$\sigma_i (10^{-16}$ cm <sup>2</sup> )	0.15	0.21	0.25	0.27

The individual vibronic peaks in the spectra of figures 2 and 4 are not doublets as would be expected because of the spin-orbit coupling in  $O_2^-$ . The resolution of the present instrument is sufficient to resolve this splitting at room temperature in electron collisions with  $O_2$  (Allan 1995). Runs with ozone/oxygen mixture have shown that the resolution was sufficient even under the conditions used in recording the spectra in figures 2 and 4. We attribute the absence of visible peak doubling in these figures to rotational peak broadening, indicating that  $O_2^-$  is formed rotationally excited in the present experiment, i.e. with rotational temperature higher than ambient. This observation is not surprising in view of the bent geometry of ozone. The degree of rotational excitation of  $O_2^-$  is modest, however, as indicated by the overall width of the vibronic features. This width (FWHM) is 50 meV for the  $v' = 5 \rightarrow v = 0$  peak in the second-from-top trace in figure 2. For comparison, the width of the  $O_2^-$  resonance peaks (i.e. the width of one spin-orbit doublet), recorded previously at a comparable temperature and with comparable resolution, is 38 meV (Allan 1995).

The width of the peaks, could, in principle, also be broadened by perturbation of the autodetaching  $O_2^-$  by the O atom, which could still be in the vicinity at the time of autodetachment. However, we feel that the contribution of this effect is negligible since the rapid increase of the autodetachment rate of  $O_2^-$  with increasing  $v'$  would make it strongly dependent on  $v'$ , contrary to the observation in figure 2.

The assignment in figure 4 allows the dependence of the excitation of individual vibrational levels  $v'$  of  $O_2^-$  to be discussed as a function of the incident electron energy, as shown in figure 5. The cross sections exhibit nearly vertical onsets. Yield of stable  $O_2^-$  ions recorded with a quadrupole mass spectrometer, that is  $O_2^-$  ions in  $v' = 0, 1, 2$  and 3, is also shown for comparison in figure 5. The fact that the onset of the  $O_2^-$  yield is not vertical is probably due to the fact that four thresholds for the individual  $v'$  levels 0 to 3 are involved, combined with the inferior resolution of the dissociative attachment spectrometer (about 0.1 eV). Both bound and vibrationally autodetaching states of  $O_2^-$  appear to be due to the dissociation of the same resonance, extending from about 0.5 eV to about 2 eV. It

Production of vibrationally autodetaching  $O_2^-$ 

**Figure 5.** Cross sections for the yield of the designated  $O_2^-/O_2$  transitions in electron collisions with ozone, shown as a function of the incident energy. Vertical bars mark thresholds calculated with  $D_0 = 1.06$  eV. No attempt has been made to deconvolute band overlap, which occurs (only) at energies which are significantly above threshold (cf figure 4). The vibrational structure, seen in particular in the lowest trace, is caused by overlapping energy-loss bands due to excitation of low-lying electronic states of ozone. The top trace shows the yield of bound, stable  $O_2^-$  ions.

is probably a core excited Feshbach resonance with one of the low-lying valence excited states of ozone, in the 1–2 eV range, as parent. There are four potential parent states and more than one resonance may well be involved in the dissociation.

The energy balance of equation (3) above indicates that the overall electron-energy-loss is equal to the dissociation energy  $D_0$  of ozone into ground state  $O_2$  and O, under the assumption that a negligible amount of kinetic energy is imparted to the heavy fragments at the signal onset. Figure 6 shows the pertinent energy-loss spectra, recorded at constant residual energies corresponding to distinct  $O_2^-/O_2$  vibronic transitions. The signal onset is at  $\Delta E = 1.06 \pm 0.04$  eV, the error bar being the combined uncertainty of identifying the onset on the steep sloping part of the spectra in figure 6, and of the energy-scale contribution. This number is, strictly speaking, only the upper limit for the dissociation energy because of possible kinetic energy of the products  $O_2$  and O. Note, however, that it is highly unlikely that kinetic energy is imparted to the heavy particles at the signal onsets in figure 6, in view of the fact that the signal onsets occur at the same energy-loss for the four traces. The dissociation step in the present process, the dissociation of the negative ion resonance  $O_3^-$  into O and  $O_2^-$ , occurs with excess energy and this excess energy is different for the four traces in figure 6. If non-zero kinetic energy were imparted to the products O and  $O_2^-$  at the signal onsets in figure 6, then the amount of this kinetic energy would almost certainly depend on the amount of excess energy in the dissociation step, and the onsets of the four

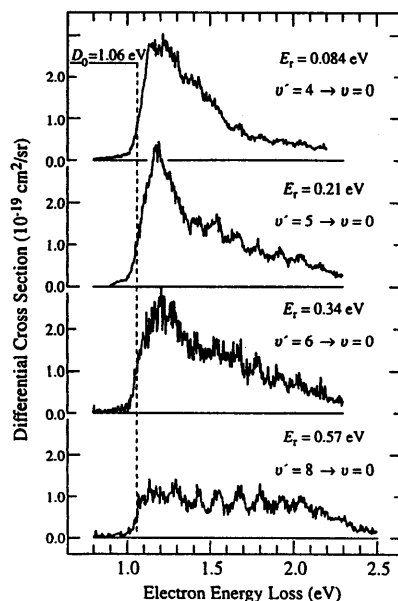


Figure 6. Electron-energy-loss spectra of ozone, recorded at constant residual energies corresponding to the designated  $O_3^-/O_2^-$  transitions. The broken vertical line indicates the dissociation energy of ozone. The vibrational structure is due to overlapping electronic transitions of ozone.

traces in figure 6 would occur at different energy losses.

The present value  $D_0 = 1.06 \pm 0.04$  eV is in excellent agreement with the accepted thermochemical value of  $1.05 \pm 0.02$  eV (as quoted by Cole and Zare 1972), as opposed to other values found in the literature (a list of the various values was given by Hiller and Vestal 1981).

#### Acknowledgments

We wish to express our sincere appreciation to Professor E Haselbach for his continuing support and encouragement in the present work. The spectrometers could not have been constructed without the exceptional enthusiasm and ingenuity of E Brosi of the mechanical laboratory and P-H Chassot of the electronics laboratory. This work is part of project 2028-040398.94/1 of the Swiss National Science Foundation (SNSF). Travel support from the SNSF-British Research Council exchange program (SNSF projects 83BC-041085 and 83BC-042816) is gratefully acknowledged. NJM is grateful for the continued support of the Royal Society during the course of this work; JAD acknowledges the support of the Gassiot committee of the Meteorological Office for provision of a studentship.

#### References

- Allan M 1992 *J. Phys. B: At. Mol. Opt. Phys.* **25** 1559-75  
 —1995 *J. Phys. B: At. Mol. Opt. Phys.* **28** 5163-75  
 Allan M, Asmis K R, Popovic D B, Stepanovic M, Mason N J and Davies J A 1996a *J. Phys. B: At. Mol. Opt. Phys.* **29** in press  
 Allan M, Mason N J and Davies J A 1996b *J. Chem. Phys.* in press  
 Bulliard C, Allan M and Haselbach E 1994 *J. Phys. Chem.* **98** 11040-5  
 Celotta R J, Bennett R A, Hall J L, Siegel M W and Levine J 1972 *Phys. Rev. A* **6** 631  
 Christophorou L G 1978 *Adv. in Electronics and Electron Physics* **46** 55-129  
 Cole J L and Zare R N 1972 *J. Chem. Phys.* **57** 5331-5  
 Cooper C D and Compton R N 1972 *Chem. Phys. Lett.* **14** 29-32  
 Davies J A, Johnstone W M, Mason N J, Biggs P and Wayne R P 1993 *J. Phys. B: At. Mol. Opt. Phys.* **26** L767  
 Dressler R and Allan M 1985 *J. Chem. Phys.* **92** 449-55  
 —1986 *J. Electron. Spectrosc.* **41** 275-87  
 Gingell J M, Davies J A and Mason N J 1995 *Physica* **17** 113-28  
 Hiller J F and Vestal M L 1981 *J. Chem. Phys.* **74** 6096-105  
 Johnstone W M, Mason N J, Newell W R, Biggs P, Marston G and Wayne R P 1992 *J. Phys. B: At. Mol. Opt. Phys.* **25** 3873-83  
 Mason N J, Gingell J M, Davies J A, Zhao H, Walker I C and Siggel M 1996 *J. Phys. B: At. Mol. Opt. Phys.* **29** in press  
 Mazeau J, Gresteau F, Hall R I and Huetz A 1978 *J. Phys. B: At. Mol. Phys.* **11** L557  
 Newson K A, Luc S D, Price S D and Mason N J 1995 *Int. J. Mass Spec. Ion Proc.* **148** 203  
 Nickel J C, Zetner P W, Shen G and Trajmar S 1989 *J. Phys. E: Sci. Instrum.* **22** 730-8  
 Spence D and Burrow P D 1979 *J. Phys. B: At. Mol. Phys.* **12** L179  
 Walker I C, Mason N J, Gingell J M, Davies J A, Zhao H and Marston G 1996 *J. Phys. B: At. Mol. Opt. Phys.* **29** in press

## Resonances in Collisions of Low-Energy Electrons with Ozone: Experimental Elastic and Vibrationally Inelastic Differential Cross Sections and Dissociative Attachment Spectra

Michael Allan, Knut R. Asmis, Duska B. Popovic, and Momir Stepanovic

Institut de Chimie Physique, Université de Fribourg, Pérolles, CH-1700 Fribourg, Switzerland

Nigel J. Mason and Julia A. Davies

Department of Physics and Astronomy, University College London, London WC1E 6BT, England

### Abstract.

A comprehensive study of the elastic and vibrationally inelastic scattering of low-energy electrons on ozone, as well as of the dissociative electron attachment has been carried out. Absolute differential cross sections (DCSs) for the elastic and vibrationally inelastic scattering are presented as a function of electron energy and of scattering angle. The elastic data is compared to existing experimental and theoretical work. Two shape resonances are observed in the vibrational DCSs, peaking at 4.2 and 6.6 eV. We used the Koopmans' theorem to assign them as  $A_1$  and  $B_2$ , with temporary capture of the incident electron into  $\sigma^*$  orbitals which are very strongly antibonding with respect to the O-O bond length. Both resonances excite not only the totally symmetric vibrations  $\nu_1$  and  $\nu_2$ , but also the antisymmetric ( $B_2$ ) stretch vibration  $\nu_3$ , and we assign the excitation of the latter to vibronic coupling between the resonances. Dissociative electron attachment below 5 eV yields  $O^-$  and  $O_2^-$  with considerable intensity.  $O_3^-$  formation through three-body attachment or ion-molecule reactions is also observed. Four resonant peaks are observed in the dissociative attachment spectra, at 0.4 eV, 1.3 eV, 3.2 eV, and 7.5 eV. The ions are formed with moderate kinetic energies for the first, nearly zero kinetic energy for the second, and with large kinetic energies for the third resonance. The resonances in the dissociative attachment spectra are assigned as the 'high energy tail' of the  $B_1$  ground state of  $O_3^-$ , a core excited resonance, the  $A_1$  shape resonance, and a Feshbach resonance, respectively. The  $A_1$  shape resonance appears at a lower energy in the dissociative attachment channel than in the vibrational excitation channel because of kinetic shift. Angular distribution and approximate absolute values are given for the  $O^-$  formation at 3.2 eV.

### Introduction

Ozone is a particularly interesting target for the study of low energy electron scattering, both because of its environmental and technological relevance, and its exceptional electronic structure (small separation of the highest occupied (HOMO) and the lowest unoccupied (LUMO) molecular orbitals, low-lying electronically excited states) and chemical properties (for example very low dissociation energy). Only few electron collision studies of ozone have been reported, perhaps because of the difficult preparation and handling of high purity ozone, and because of its corrosive nature. Electron-energy-loss spectra (EELS) of ozone have been reported by Celotta *et al.* (1974) and by Swanson and Celotta (1975). Energy-loss spectrum and absolute differential elastic cross sections were reported at six different energies between 3 and 20 eV and angles between  $12^\circ$  and  $168^\circ$  by Shyn and Sweeney (1993). Johnstone *et al.* (1992) and Davies *et al.* (1993) reported vibrational energy-loss spectra at a series of energies between 3.5 - 7 eV and scattering angles in the range of  $40^\circ$  -  $120^\circ$ , Mason *et al.* (1996) reported low-energy EELS using an electron trap.

Dissociative attachment of electrons to ozone was studied at low energies by swarm techniques and these results were reviewed by Phelps (1969) and by Massey (1976). Early beam studies of dissociative attachment were performed by Curran (1961). Recent dissociative attachment results, over a large energy range, were obtained by Walker *et al.* (1996). In the final stages of the preparation of this manuscript we learned about a concurrent cross-beam study of dissociative attachment to ozone by Skalny *et al.* (1996).

Very little theoretical work has been performed. Okamoto and Itikawa (1993) reported effective potential (local exchange) calculations of the differential elastic cross sections as a function of scattering angle at four energies between 5-20 eV, Sarpal *et al.* (1994) used the R-matrix method to calculate integral elastic cross sections.

In this communication we wish to complement and extend the existing experimental work on the elastic and vibrationally inelastic DCSs (summed over all rotational transitions) and on dissociative attachment.

### Instrumental

Preparation and handling of ozone of high purity requires considerable experience. We accomplished this task with the mobile ozone production apparatus designed and constructed at the UCL. The techniques have been described previously by Johnstone *et al.* (1992), Davies *et al.* (1993) and Newson *et al.* (1995).

The spectra were recorded with an electron-energy-loss (EEL) spectrometer described by Allan (1992, 1995a, b). Ozone was introduced into the collision region from a storage bulb as an effusive beam through a nozzle

with 250  $\mu\text{m}$  diameter and 0.3 mm long, kept at 45°C. The spectra were, except where otherwise noted, corrected for the instrumental response function, determined on the helium elastic signal and the helium near threshold ionization continuum. Absolute DCSs were determined using the relative flow technique (Nickel *et al.* 1989). The application of this technique was complicated by the decomposition of ozone in the metallic part of the gas handling system, including the capacitance manometer used to measure gas flow, and by the limited purity of ozone (although up to 97% ozone in the collision region was achieved). The details of the procedure used to circumvent these problems are described in Section 5, Appendix. These complications result in an error of the absolute values larger than in the previous investigation of  $\text{O}_2$  (Allan 1995a, b), the present values are accurate within  $\pm 30\%$  for the elastic cross sections and  $\pm 40\%$  for the vibrationally inelastic cross sections (more precisely, the upper limit is obtained by multiplying, the lower limit by dividing by a factor of 1.3 respectively 1.4 for elastic and inelastic DCS). The error is larger for residual energies below about 0.2 eV. A more detailed discussion of the errors is given in the Appendix. The energy scale was calibrated on the 19.366 eV resonance in helium and on sharp features in the vibrationally inelastic cross sections of  $\text{O}_2$  in  $\text{O}_2/\text{O}_3$  mixtures and is accurate to within  $\pm 20$  meV. The resolution was between 20 and 25 meV (fwhm, in energy-loss mode). A Wien filter was used in the analyzer to separate stable fragment anions and scattered electrons.

The dissociative attachment spectrometer used to measure the yield of mass-selected stable anions as a function of electron energy was also described previously by Dressler and Allan (1985) and Bulliard *et al.* (1994). It employs a magnetically focused trochoidal electron monochromator to prepare a beam of quasi-monoenergetic electrons. Fragment anions are collected at 90° and detected with a quadrupole mass spectrometer.

## Results and Discussion

**Elastic cross sections.** We first used the relative flow method to measure the elastic DCS at 30° and at an incident energy of 10 eV and obtained the value of  $2.04 \pm 0.6 \times 10^{-16} \text{ cm}^2/\text{sr}$ . This value was then used to normalize a spectrum of the elastic DCS recorded as a function of the electron energy at 30°, with the result shown in the top trace of Figure 1. The angular distributions of the elastic signal were then recorded at 2, 5, 10, and 15 eV and corrected for the instrumental response function determined on elastic scattering in helium. These spectra were subsequently normalized at 30° to the absolute values at the respective energies, taken from the top trace in Figure 1. The normalized angular distributions are shown in Figure 2. Finally, the elastic signal was recorded at 90° as a function of electron energy, corrected for the instrumental response function, and normalized to the values determined at 90° from the angular distributions in Figure 2. The resulting DCS is shown in the bottom curve of Figure 1. Note that this curve can not be made to fit exactly the angular

distributions (Figure 2) at all four energies simultaneously, because of the finite precision of the correction for the instrumental response function. A compromise fit was therefore made, giving reasonably small deviations at the four energies. (Less weight was given to the points at low energies, where the calibration of the instrumental response function is less reliable. The deviations are indicative of the reliability of the response calibration procedure over wide ranges of scattering angles and electron energies. In the present case they are +5%, -6%, -14%, and +21% at 15 eV, 10 eV, 5 eV, and 2 eV, respectively.)

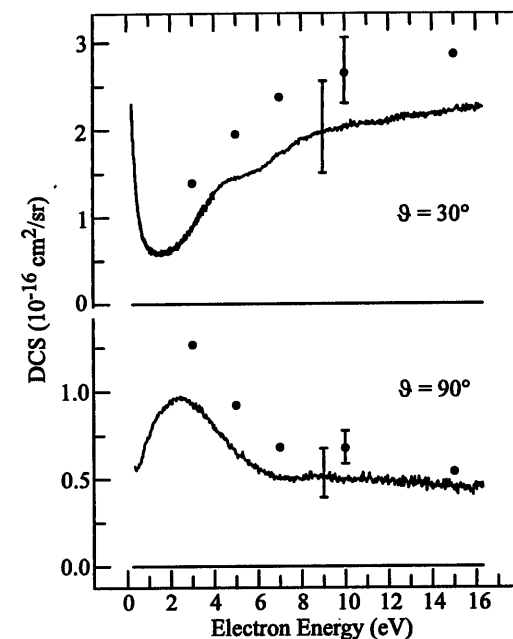


**Figure 1**

Elastic DCSs as a function of electron energy. Dots indicate the experimental results of Shyn and Sweeney (1993). Representative error bars ( $\pm 15\%$  for the data of Shyn and Sweeney (1993) and a factor of 1.3 for the present work) are indicated.

The shapes of the curves, both energy-dependence and angular distributions, are found to agree quite well with the data of Shyn and Sweeney (1993), in particular in terms of the shape of the curves, although the present absolute values are consistently smaller, by amounts varying in most cases between 20% and 25%. This is within the combined error bars of the two experiments (Shyn and Sweeney have an error limit of  $\pm 15\%$ ), and may be considered as satisfactory in view of the corrosive nature of ozone and the problems stemming from its rapid decomposition in the inlet manifold.

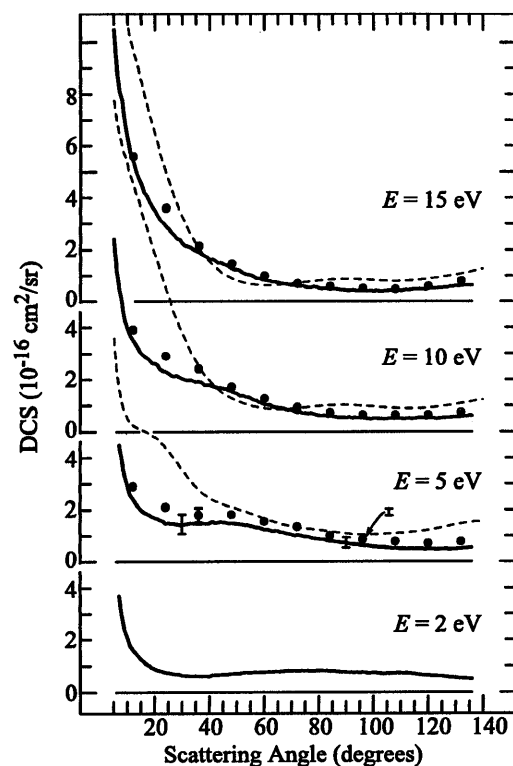


Figure 2

Angular distributions of elastic cross sections. Present results are shown as heavy line, the experimental results of Shyn and Sweeney (1993) as dots, theoretical results of Okamoto and Itikawa (1993) as dashed line. Representative error bars are indicated as in Figure 1.

The theoretical results of Okamoto and Itikawa (1993) reproduce well the main features of the experiment, in particular the steep rise of the cross sections at low scattering angles, a broad flat region around  $90^\circ$ , and a slow rise at large scattering angles.

**Vibrational excitation.** Two examples of vibrational energy-loss spectra are shown in Figure 3. Long progressions and numerous combination vibrations are observed for all three vibrational modes, indicating efficient resonant excitation. (Vibrational frequencies are taken from the review article of Steinfeld *et al.* 1987.) The two stretch vibrations  $\nu_1$  and  $\nu_3$  can not be resolved at low quanta, because the energy-difference is too small, but are resolved at higher quanta: for example the peaks (400) and (004) are well separated.

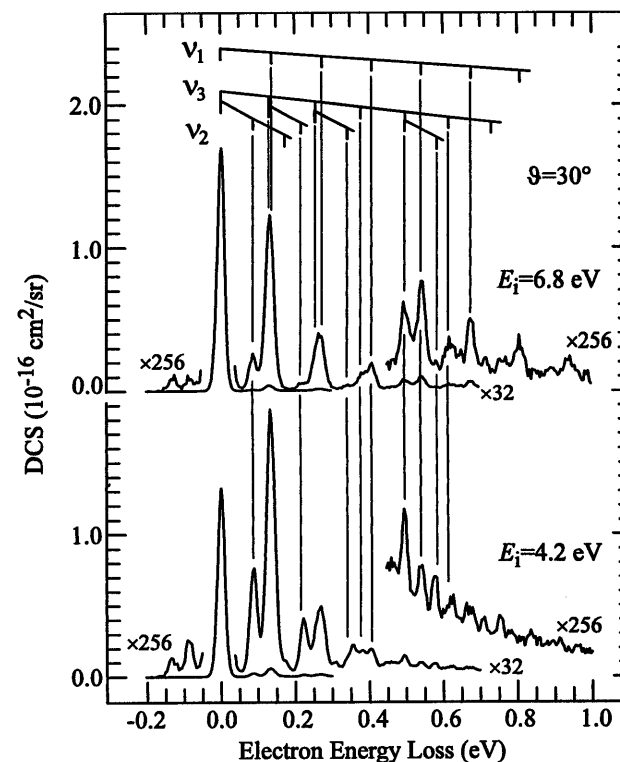


Figure 3

Vibrational electron energy-loss spectra.

Figures 4-6 show the vibrationally inelastic DCSs in function of the incident electron energy. The absolute values of the DCSs were determined by recording energy-loss spectra at suitable incident energies, such as those in Figure 3, correcting them for the instrumental response function, and integrating under the elastic and the vibrationally inelastic peaks. The ratios of the integrals were then normalized to the value of the absolute elastic DCSs taken from the curves in Figure 1, yielding absolute values of the vibrationally inelastic DCSs at single incident energies. These values were then used to normalize the excitation functions (corrected for the instrumental response function) of the individual vibrations.

The rise of the cross sections with decreasing energy near threshold is assigned to direct excitation of the IR-active vibrations. This mechanism is indicated by the fact that the cross section peaks at threshold are larger at  $30^\circ$  than at  $90^\circ$ , and that they are nearly absent in the overtone excitations, which have little IR activity. Two shape resonances can be discerned in the spectra,

peaking at 4.2 eV (confirming the conclusion of Davies *et al.* 1993), and at 6.6 eV. The 4.2 eV resonance appears in all excitation functions, but the excitation caused by the 6.6 eV resonance is selective. This resonance is nearly absent in the excitation functions of the (010) and (110) vibrations in Figures 4 and 5, where bending is excited.

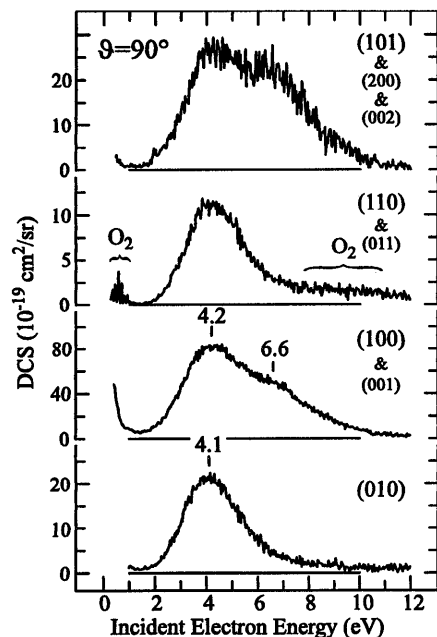


**Figure 4**

Vibrationally inelastic DCSs at 90° in function of electron energy. The stretch vibrations  $\nu_1$  and  $\nu_2$  can not be resolved (see Figure 3). The absolute DCSs were determined from the area under the bands in energy-loss spectra and refer to the sum of the individual overlapping transitions.

The large vibrational cross sections identify the resonances as 'one particle' resonances (generally called 'shape resonances') with the incident electron being temporarily captured in an unoccupied orbital of the ozone molecule in its ground state. We attempt to assign the shape resonances by applying the Koopmans' theorem (Koopmans, 1934), together with an empirical scaling relation  $AE = (\epsilon - 2.33)/1.31$  (Chen and Gallup 1990), relating Hartree-

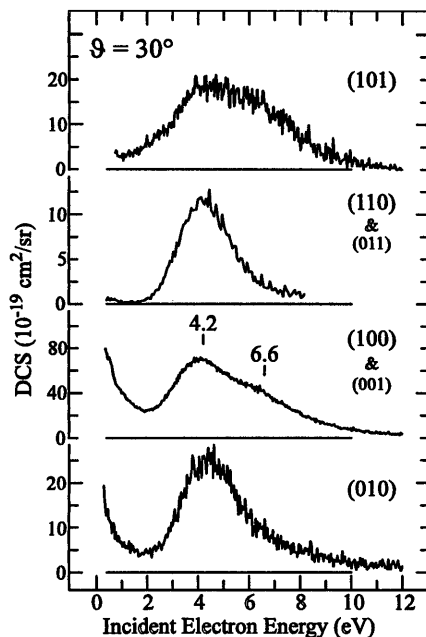


**Figure 5**

Vibrationally inelastic DCSs at 30°. The stretch vibrations overlap as noted in caption of Figure 4.

Fock (HF) virtual orbital energies  $\epsilon$  to an estimated attachment energy  $AE$  (both in eV).

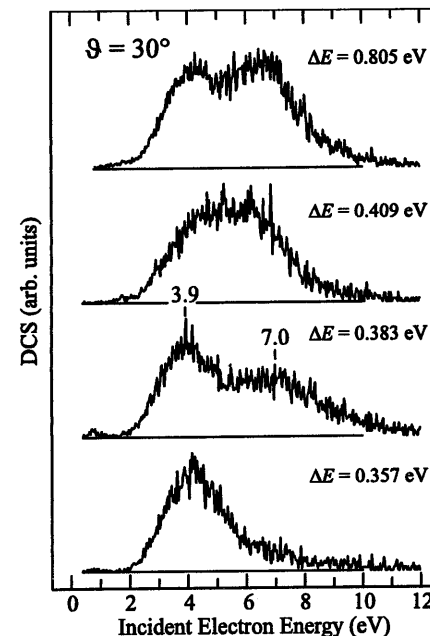


**Figure 6**

Vibrationally inelastic DCSs at 30° and at larger energy-losses. The energy-loss bands (Figure 4) overlap more heavily than in the foregoing Figures. The DCSs are therefore given only in relative units and the transitions are not assigned in the Figure.

$\Delta E = 0.357$  eV corresponds nominally to the (111) state,  $\Delta E = 0.383$  eV to (003),  $\Delta E = 0.409$  eV to (300), and  $\Delta E = 0.805$  eV to (600), all with a large contribution of the underlying vibrational quasicontinuum.

This crude but transparent method generally yields useful estimates of vertical electron attachment energies for one particle resonances, when used with the 6-31G or the 6-31G\* basis sets. The application of the Koopmans' theorem to ozone is less justified than for many other molecules because the small energy-difference between the highest occupied and the lowest unoccupied MOs (HOMO-LUMO gap) necessitates a substantial admixture of a doubly excited configuration for an adequate description of its ground state, making the present single determinant RHF treatment only a crude approximation. In spite of this limitation Koopmans' theorem provides a useful insight into the resonant structure of ozone and we show the results in Figure 7. The smaller basis set (6-31G) was chosen because it (accidentally) yields an optimized geometry which is close to the experiment, and rapid variation of the orbital energies with the O-O distance make correct geometry important. The LUMO of ozone,  $B_1$ , is also included in Figure 7 for completeness, its energy with the above scaling relation results in a qualitatively correct prediction of the vertical electron affinity.

The simple model appears to be sufficient to identify the observed shape resonances as  $A_1$  and  $B_2$ , both with temporary occupation of  $\sigma^*$  orbitals, even though the very high degree of agreement of the calculated data in Figure 7 with experiment is, of course, fortuitous. This assignment and the relative order of the shape resonances is in accord with the R-matrix calculations of Sarpal *et al.*

(1994), who predicted  $A_1$  and  $B_2$  resonances at 8.2 and 11.1 eV, but add that the true resonance energies may be up to 3 eV lower, in qualitative agreement with the present observations.

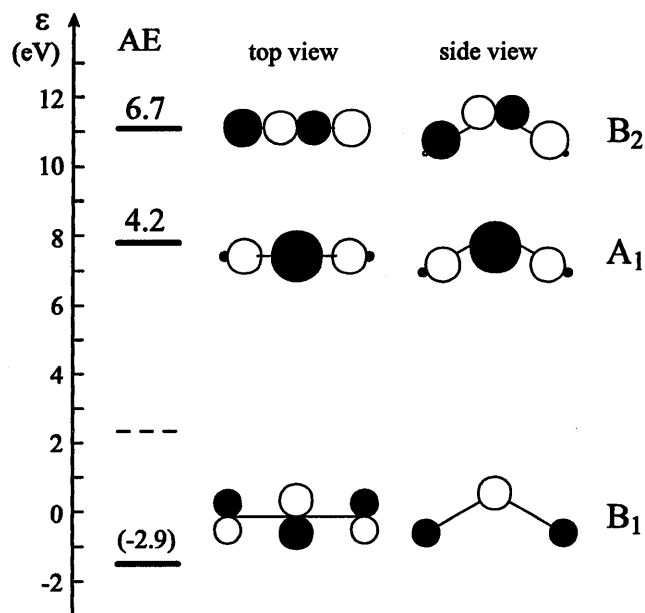


Figure 7

Energies of RHF/6-31G virtual orbitals obtained with the program Gaussian (Frisch *et al.* 1992) (scale on the left; at the HF/6-31G optimized geometry) and vertical attachment energies, estimated from the orbital energies using Koopmans' theorem and an empirical scaling relation as explained in the text. Temporary occupation of the  $A_1$  and  $B_2$  orbitals gives shape resonances, occupation of the lowest orbital  $B_1$  leads to stable  $O_3^-$  ground state (experimental adiabatic electron affinity of ozone is  $2.1028 \pm 0.0025$  eV, Novick *et al.* 1979). Schematic diagrams of the orbitals were drawn with the program MOPLLOT (Schmelzer and Haselbach 1971).

The intense excitation of stretch vibrations by both resonances is well rationalized by the antibonding character of both virtual orbitals with respect to the O-O bond length, evident in the orbital diagrams in Figure 7. The preferred excitation of the bending vibration by the 4.2 eV resonance is more difficult to explain on qualitative arguments and a calculation of a potential surface would be desirable.

Symmetry arguments indicate that resonances will excite vibrations belonging to the same irreducible representation as the force field acting on the nuclei, that is vibrations with the symmetry species equal to the direct product

of the symmetry species of the MO with itself (Wong and Schulz 1975, Gallup 1993). In the present case of nondegenerate orbitals this rule amounts to the prediction that only totally symmetrical vibrations will be excited. On the other hand excitation of additional vibrations, not predicted by this rule, is observed in nearly all polyatomic molecules and has been rationalized in two different ways. The first assumes that the electron may leave in a partial wave other than that in which it entered, in particular in the s-wave, thus modifying the force field and exciting vibrations with the symmetry species equal to the symmetry species of the MO (Wong and Schulz 1975, Gallup 1993). The second invokes vibronic coupling of two resonances, which may lead to the excitation of vibrations with the symmetry species equal to the direct product of the symmetry species of the coupled resonances (Estrada *et al.* 1986).

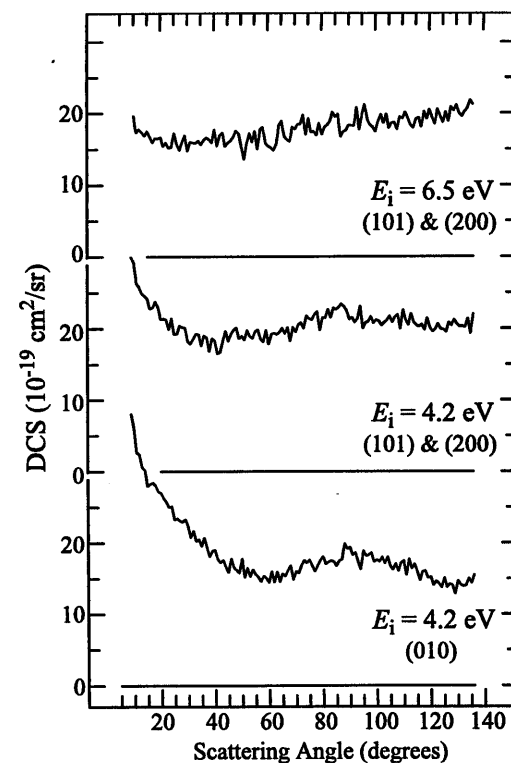


Figure 8

Angular distributions of electrons having excited the vibrations indicated.

The first two vibrations in ozone,  $\nu_1$  and  $\nu_2$ , are totally symmetric, the antisymmetric stretch vibration  $\nu_3$  belongs to  $B_2$ . As noted above, and illustrated



in Figures 3-6, all three vibrations are excited by both shape resonances. Excitation of the totally symmetric vibrations  $\nu_1$  and  $\nu_2$  is rationalized by the first rule described above and does not require further comment. The excitation of  $\nu_3$  is more interesting and we point out that the explanation in terms of vibronic coupling of the  $A_1$  and  $B_2$  resonances is particularly attractive. The direct product of  $A_1$  and  $B_2$  is  $B_2$ , explaining why *both* resonances excite  $\nu_3$ . The two resonances overlap, and the close proximity in energy enhances their coupling.

Figure 8 shows the angular distributions of the vibrationally inelastically scattered electrons. Only the lowest trace shows a distinct behavior, reminiscent of a d-wave. The tables given by Read (1968) specify the lowest partial wave for the  $A_1$  resonance as  $l=0$ ,  $m=0$ , that is s-wave, with isotropic angular distribution, the next higher wave is  $l=1$ ,  $m=0$ , that is p-wave. The experimental angular distribution in the lowest trace of Figure 8 is thus not dominated by the lowest partial waves, but contribution of higher partial waves is significant. The lowest partial wave for the  $B_2$  resonance is  $l=1$ ,  $m=1$ , that is p-wave, and, as in the case of the  $A_1$  resonance this partial wave is not sufficient to rationalize the top trace in Figure 8. The lowest trace in Figure 8 is, however, in accord with the conclusion of Sarpal *et al.* (1994) who predict both  $A_1$  and  $B_2$  resonances to be predominantly of d and f wave in character.

**Dissociative electron attachment.** Dissociative attachment spectra obtained with the present quadrupole mass spectrometer are shown in Figure 9. These spectra were recorded with the  $127^\circ$  cylindrical ion kinetic energy analyser and the ion extraction optics tuned to enhance the detection of ions with low kinetic energies. The threshold for  $O^-$  production, calculated from the dissociation energy  $D_0=1.05\pm 0.02$  eV (Gole and Zare 1972) and the electron affinity of the oxygen atom  $EA=1.46$  eV, is  $-0.41$  eV, and the observed  $O^-$  signal onset at 0 eV is thus not surprising. There is some fine structure superimposed on the  $O^-$  band, a weak feature at 0.50 eV and a double peak at 1.18 and 1.35 eV. These structures could be due to opening of dissociation channels with vibrationally excited  $O_2$  fragment, as will be discussed in more detail below, or it could be due to structure of the core excited resonances which are intermediates of the dissociation. Note that evidence for structured dissociative excited states of  $O_3^-$  in this energy range has been obtained in laser photodissociation studies of Hiller and Vestal (1981).

In addition to the fragment ion signals shown in Figure 9, we also observed a weaker band in the  $O^-$  yield at an incident energy of 7.5 eV. The ions have relatively large kinetic energies, 1-2 eV. This confirms the corresponding observation of Walker *et al.* (1996).

The electron affinity of  $O_2$  is 0.440 eV (Celotta *et al.*, 1972) and the threshold for  $O_2^-$  ( $\nu'=0$ ) production is at 0.61 eV. Accordingly, the observed onset of the  $O_2^-$  signal is clearly above 0 eV and the fact that it is slightly below the energetical threshold could be due to thermal vibrational excitation of the

target and the finite resolution of the instrument (about 0.1 eV). Formation of autodetaching  $O_2^-$  ( $\nu' \geq 4$ ) has been reported in a previous publication (Allan *et al.* 1996a). Substantial yield of  $O_3^-$  ions was also found with the mass spectrometer at pressures in the collision chamber higher than about  $5 \times 10^{-5}$  mbar (this value being a rough estimate from the penning gauge reading of the background pressure and the expected collision-chamber/main-chamber pressure ratio). The  $O_3^-$  signal increases with pressure faster than the  $O^-$  signal, indicating that it is formed by a three body process, which could be three body attachment, an ion-molecule reaction, or a charge transfer. (We recorded the  $O^-$  and  $O_2^-$  yields in Figure 9 at different pressures to ascertain that they are not pressure dependent. Note also that with exception of Figure 9 all data presented in this publication has been recorded with a crossed beam instrument and is not affected by three body reactions.)

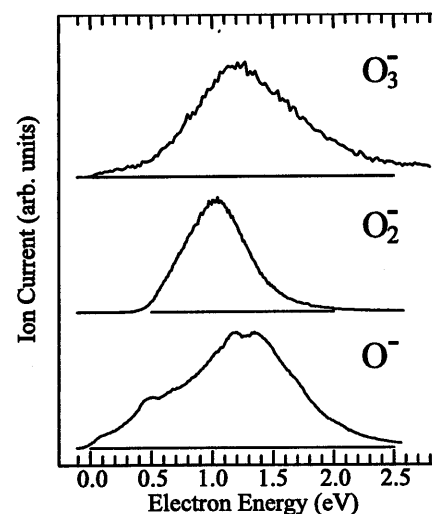


**Figure 9**  
Yields of  $O^-$  and  $O_2^-$  fragment ions from dissociative attachment to  $O_3$ . Yield of  $O_3^-$ , resulting at higher sample pressures from three-body processes, is shown in the top curve.

The present electron-energy-loss spectrometer is equipped with a Wien filter and can also be used to record dissociative attachment spectra, albeit without mass resolution and with lower sensitivity. It has the advantage of a much higher resolution with respect to the kinetic energy of the fragment ions, in part because of higher resolution of the charged particle analyzers, but primarily because of the cross-beam arrangement which greatly reduces the thermal Doppler broadening.

Figure 10 shows the spectra of the fragment ion energies for three incident electron energies, recorded with the EEL-spectrometer. The measured distribution at the incident energy of  $E_i=1.3$  eV (the bottom trace in Figure 10) shows very little kinetic energy release, the majority of the ions have kinetic

energies of less than 0.2 eV. The signal intensities obtained with the quadrupole mass spectrometer (Figure 9) indicate that  $1/2 - 2/3$  of the signal is due to  $O^-$  at this incident energy. The maximum energetically possible kinetic energy of  $O^-$  is 1.13 eV at this incident energy and the measurement thus indicates that the major part of the available energy appears as internal energy of the  $O_2$  fragment. (The maximum kinetic energy of an  $O_2^-$  fragment at  $E_i=1.3$  eV is 0.23 eV.) The maximum kinetic energy of  $O^-$  is 0.6 eV at the incident electron energy of 0.5 eV. The data at the incident energy of 0.5 eV (although noisy) permits the conclusion that the proportion of ions with kinetic energies of about 0.3 eV (as compared to the number of ions with nearly 0 eV) is larger at  $E_i=0.5$  eV than it is at  $E_i=1.3$  eV, that is the fraction of the available energy converted to kinetic energy is larger at  $E_i=0.5$  eV than it is at  $E_i=1.3$  eV. Finally, the maximum kinetic energy of  $O^-$  is 2.4 eV at the incident electron energy of 3.2 eV, and the spectrum indicates that a large percentage of the available energy is released as kinetic energy. The peak of the distribution is at 2.1 eV, corresponding to 58% of the available energy ( $2/3$ , or 66.6% being the kinetic maximum).

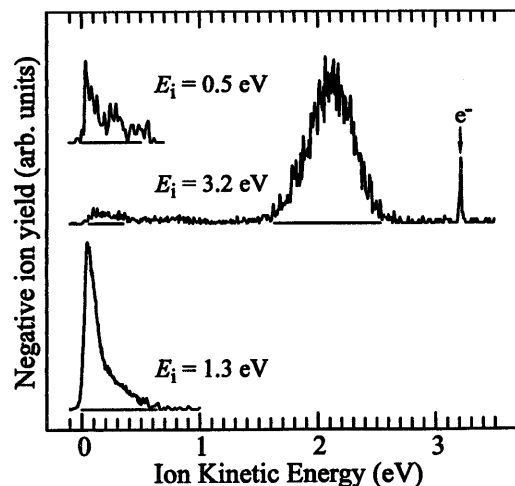


Figure 10

Spectra of ion kinetic energies at three incident electron energies (top and bottom spectra were recorded at  $90^\circ$ , center at  $30^\circ$ ). The narrow peak at 3.2 eV in the center trace is due to elastically scattered electrons which were not entirely rejected by the Wien filter. The intensity of this residual peak (1.9 c/s) and the intensity of the elastic peak under otherwise identical conditions but with the Wien filter tuned for electrons (24'000 c/s) indicate a rejection factor of the Wien filter of more than 104.

The upper trace in Figure 11 shows the yield of the 'slow' ions in function of the incident electron energy. One resonance, peaking at 1.3 eV, appears in the low-energy ion yield. There is an indication of a weak vibrational structure on this band which could be due to openings of new thresholds for the formation of  $O_2$  molecules in successively higher vibrational states, an observation similar to that made in  $CO_2$  (Dressler and Allan 1985). The weak signal did not permit a recording with less statistical noise, but note that the structures appear at all the expected positions indicated by the grid above the band in Figure 11, justifying reasonable confidence that the observation is 'real' and not just accidental variations.

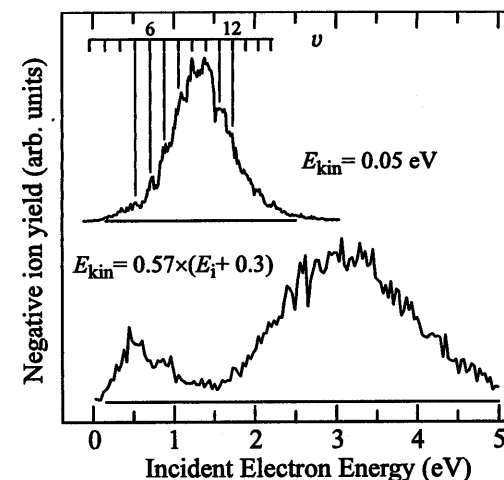


Figure 11

Yield of ions with nearly zero kinetic energies (top trace) and yield of  $O^-$  ions with kinetic energies equal to a substantial fraction of the available energy (bottom trace). Both  $O^-$  and  $O_2^-$  contribute to the upper spectrum, the lower spectrum is due to  $O^-$  alone since the available energy is insufficient for the formation of  $O_2^-$  with the required kinetic energy. Grid above the top spectrum indicates thresholds for the formation of  $O^-$  and  $O_2$  in the excited vibrational states  $v$ . These spectra are not corrected for the instrumental response function.

The lower trace in Figure 11 shows the yield of the 'fast' ions (on grounds of kinetic energy, they must be  $O^-$  ions). It was recorded by varying the analyzer energy synchronously with the incident electron energy in such a way as to measure the yield of ions with a kinetic energy (in eV)  $E_{kin} = 0.57 \times (E_i - E_{thr})$ . The spectrum thus shows the yield of  $O^-$  ions with kinetic energy equal to about 57% of the available energy (that is 86% of their maximum energy), staying approximately on the peak of the kinetic energy distribution of the middle curve in Figure 10. (We used a value of -0.3 eV in the

above expression instead of the correct threshold value of  $E_{\text{thr}} = 0.41$  eV because we were misled (by a typing error in a publication quoting  $D_0$ ) into believing that the dissociation energy of ozone is  $D_0 = 1.13$  eV (instead of the correct value  $D_0 = 1.05$  eV) at the time of recording the spectrum. The difference is, fortunately, not significant for the present purpose, it is absorbed in the width of the  $\text{O}^-$  kinetic energy distribution.)

**Table 1**  
Summary of the resonances observed in this work.

Energy (eV)	Assignment	channels of observation
0.4	tail of the $\text{B}_1$ ground state of $\text{O}_3^-$	$\text{O}^-$ formation
1.3	valence core excited resonance(s)	$\text{O}_2^-$ and $\text{O}^-$ formation (low $E_{\text{kin}}$ )
3.2	$\text{A}_1$ shape resonance <sup>a)</sup>	$\text{O}^-$ formation (high $E_{\text{kin}}$ )
4.2	$\text{A}_1$ shape resonance <sup>a)</sup>	vibrational excitation
6.6	$\text{B}_2$ shape resonance	vibrational excitation
7.5	Feshbach resonance	$\text{O}^-$ formation

a) The same resonance peaks at lower energy in the dissociative attachment channel of observation than in the vibrational DCS because of the kinetic shift.

The dissociative attachment results below 5 eV may be summarized (see also Table 1) by saying that two resonant bands, at 0.4 and at 3.2 eV are observed with substantial kinetic energy release, and one band, at 1.3 eV, with small kinetic energy release. We propose that the 0.4 eV band is due to the  $\text{B}_1$  ground state of  $\text{O}_3^-$ . This state is located at -2.1 eV, but its 'high energy tail' is likely to be responsible for the 0.4 eV peak. Low-lying core excited resonances are an alternative assignment, however. We then assign the 1.3 eV peak to valence core excited resonance (or resonances), which have one or several of the valence excited state(s) in the 1.3 eV region (see, for example, Arnold *et al.*, 1994, or Allan *et al.*, 1996b) as parents. This proposition is based on the observation that dissociative attachment bands (with negligible release of kinetic energy) were found at approximately the energy of low-lying excited states in many molecules, where they have been assigned to core excited resonances with the excited states (generally singlets) as parents. Examples are  $\text{CS}_2$  (Dressler *et al.* 1987), *o*-chloro-bromomethyl-benzene (Bulliard *et al.* 1994), and other compounds (Bulliard 1994, Khvostenko 1990). Ozone is an additional example of a molecule with this type of a resonance. Finally, we assign the 3.2 eV dissociative attachment band to the  $\text{A}_1$  shape resonance already discussed above in connection with vibrational excitation. Reference to

the orbital diagram in Figure 7 indicates that efficient dissociation may be expected for this resonance because of the pronounced antibonding character of the temporary occupied MO with respect to the O-O distance. Vibronic coupling with the  $\text{B}_2$  resonance is likely to play an important role in the dissociation, by providing a distortion along the  $\text{B}_2$  coordinate. The fact that this resonance gives rise to a dissociative attachment band at 3.2 eV and to a band in the DCS for vibrational excitation at 4.2 eV is a manifestation of the common 'kinetic shift' whereby an attachment into a 'low-energy tail' of a resonance leads to larger probability of dissociation because of larger 'survival probability' of the temporary negative ion on the parts of potential surface with larger internuclear separations, where the autodetachment rate is smaller.

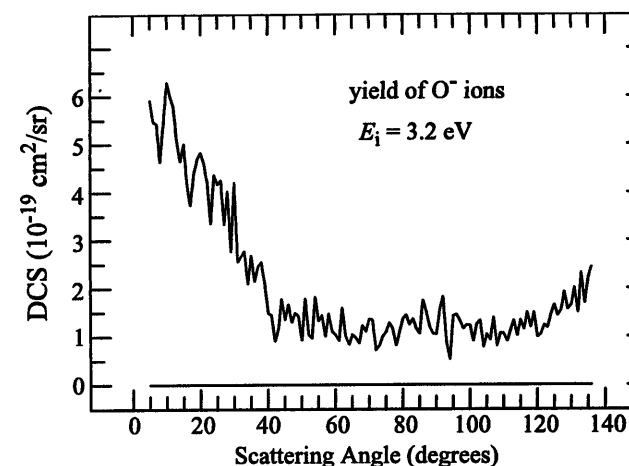


**Figure 12.**

Yield of fragment ions as a function of scattering angle. The spectrum was recorded with the energy-loss spectrometer, which does not provide mass resolution beyond distinguishing between electrons and ions, but the ions in this spectrum must be  $\text{O}^-$  because of their high kinetic energies.

Finally, the electron-energy-loss instrument allows measurement of the angular distribution of the fragment ions. Difficulty of controlling the collection efficiency of the instrument for very slow ions limits the measurement to cases where the ion energy is larger than about 1 eV. This permits the measurement of the angular distribution at the 3.2 eV band, and the result is shown in Figure 12. The distribution is qualitatively well compatible with the assignment of the 3.2 eV dissociative attachment band to the  $\text{A}_1$  shape resonance as proposed above. This is particularly clear when regarding the top view of the temporarily occupied  $\text{A}_1$  MO in Figure 7. Best overlap with the incident planar wave is obtained for a molecule oriented 'colinearly' (in the top view projection) with

the incident beam direction. Subsequent dissociation of the temporary negative ion (faster than molecular rotation) leads to angular distribution of the fragments centered around the forward and the backward directions, with a minimum at  $90^\circ$ .

Approximate absolute values of the DCS have been provided in Figure 12, with an error bar of about a factor of two. It has been obtained by normalizing to the intensity of the elastic peak, under the assumption that the response of the instrument is equal for electrons and for ions, and by summation of  $O^-$  ions with all kinetic energies, achieved by integrating under the kinetic energy distribution band in the center trace of Figure 10.

The present dissociative attachment results are in very good agreement with previous or concurrent studies in other laboratories. The properties of the various instruments, in particular their sensitivities as functions of ion kinetic energy, and the angle at which the fragment ions are collected, must be taken in consideration when making the comparison, however. The present results agree very well with the early results of Curran (1961) at electron energies below 2 eV in all respects, that is his ion yield curves agree with those shown in Figure 9 and his finding of low kinetic energy release agree with the present results in Figure 10. The 3.2 eV  $O^-/O_3$  band can not be discerned in the spectra of Curran (and the present spectra in Figure 9) because of reduced sensitivity of a typical ion extraction optics for ions with substantial kinetic energy, and because the ions were extracted at  $90^\circ$ , where the cross section has a minimum (Figure 12). The same statements can be made when comparing the present results with the findings of Skalny *et al.* (1996).

The present results are in excellent agreement with the work of Walker *et al.* (1996). In particular, the 3.2 eV  $O^-/O_3$  band was observed by Walker *et al.* (1996) both in their total ion collection tube, which collects fragment ions in a wide range of scattering angles and without discriminating ions with high kinetic energy, and in their mass spectrometer, which collects ions approximately in the forward direction, and where signal was integrated over all ion kinetic energies.

## Conclusions

The present results significantly extend the existing work on low-energy electron-ozone collisions. Five resonant features, summarized in Table 1, were identified and assigned and their decay channels characterized. Substantial cross sections for vibrational excitation and dissociative attachment were measured, likely to affect both natural and man-made ozone-containing plasmas in a significant way. Indications of an important role played by vibronic coupling between  $A_1$  and  $B_2$  shape resonances in vibrational excitation and dissociation were found. We point out the need for more theoretical work on the resonances, in particular work including nuclear dynamics.

## Acknowledgments

We wish to express our sincere appreciation to Professor E. Haselbach for his continuing support and encouragement in the present work. The spectrometers could not have been constructed without the exceptional enthusiasm and ingenuity of E. Brosi of the mechanical laboratory and P.-H. Chassot of the electrical laboratory. This work is part of project 2028-040398.94/1 of the Swiss National Science Foundation. Travel support from the SNSF-British Research Council exchange program (projects 83BC-041085 and 83BC-042816) is gratefully acknowledged. NJM is grateful for the continued support of the Royal Society during the course of this work; JAD acknowledges the support of the Gassiot committee of the Meteorological office for provision of a studentship.

## References

- Allan M 1992 *J. Phys. B: At. Mol. Opt. Phys.* **25** 1559-75  
 ——— 1995a *J. Phys. B: At. Mol. Opt. Phys.* **28** 4329-4345  
 ——— 1995b *J. Phys. B: At. Mol. Opt. Phys.* **28** 5163-5175
- Allan M, Asmis K R, Popovic D B, Stepanovic M, Mason N J and Davies J A 1996a *J. Phys. B: At. Mol. Opt. Phys.* **29**, in print
- Allan M, Mason N J and Davies J A 1996b *J. Chem. Phys.*, submitted
- Arnold D W, Xu C, Kim, E H and Neumark D M 1994 *J. Chem. Phys.* **101** 912-22
- Bulliard C 1994 Ph. D. Thesis, unpublished
- Bulliard C, Allan M and Haselbach E 1994 *J. Phys. Chem.* **98** 11040-5
- Celotta R J, Bennett R A, Hall J L, Siegel M W and Levine J 1972 *Phys. Rev. A* **6** 631
- Celotta R J, Mielczarek S R and Kuyatt C E 1974 *Chem. Phys. Lett.* **24** 428-430
- Chen D and Gallup G A 1990 *J. Chem. Phys.* **93**, 8893
- Curran R K 1961 *J. Chem. Phys.* **35**, 1849-51
- Davies J A, Johnstone W M, Mason N J, Biggs P and Wayne R P 1993 *J. Phys. B: At. Mol. Opt. Phys.* **26** L767
- Dressler R and Allan M 1985 *Chem. Phys.* **92** 449-455
- Dressler R, Allan M and Tronc M 1987 *J. Phys. B: At. Mol. Phys.* **20** 393-401
- Estrada H, Cederbaum L S, and Domcke W 1986, *J. Chem. Phys.* **84** 152
- Frisch M J, Trucks G W, Head-Gordon M, Gill P M W, Wong M W, Foresman J B, Johnson B G, Schlegel H B, Robb M A, Replogle E S, Gomperts R, Andres J L, Raghavachari K, Binkley J S, Gonzalez C, Martin R L, Fox D J, Defrees D J, Baker J, Stewart J J P, and Pople J A, Gaussian 92, Gaussian, Inc., Pittsburgh, PA, 1992
- Gallup G A 1993 *J. Chem. Phys.* **99** 827
- Gole J L and Zare R N 1972 *J. Chem. Phys.* **57** 5331-5
- Hiller J F and Vestal M L 1981 *J. Chem. Phys.* **74** 6096-6105

- Johnstone W M, Mason N J, Newell W R, Biggs P, Marston G and Wayne R P 1992 *J. Phys. B: At. Mol. Opt. Phys.* **25** 3873-3883
- Khvostenko V I, Vorob'yov A S and Khvostenko O G 1990 *J. Phys. B: At. Mol. Phys.* **23** 1975-77
- Koopmans T 1934 *Physica* **104**, 1
- Massey H 1976 *Negative Ions*, Cambridge University Press, Cambridge
- Mason N J, Gingell J M, Davies J A, Zhao H, Walker I C, Siggel M 1996 *J. Phys. B: At. Mol. Opt. Phys.* **29** submitted for publication
- Newson K A, Luc S M, Price S D and Mason N J 1995 *Int. J. Mass Spectr. Ion Proc.* **148** 203-13
- Nesbet R K 1979 *Phys. Rev. A* **20** 58-70
- Nickel J C, Zetner P W, Shen G and Trajmar S 1989 *J. Phys. E: Sci Instrum.* **22** 730-738
- Novick S E, Engelking P C, Jones P L, Futrell J H and Lineberger W C 1979 *J. Chem. Phys.* **70** 2652
- Okamoto Y and Itikawa Y 1993 *Chem. Phys. Lett.* **203** 61-4
- Phelps A V 1969 *Can. J. Chem.* **47** 1783-91
- Read F H 1968 *J. Phys. B* **2** 893-908
- Sarpal B K, Pflingst K, Nestmann B M and Peyerimhoff S D 1994 *Chem. Phys. Lett.* **230** 231-6
- Schmelzer A, Haselbach E 1971 *Helv. Chim. Acta* **54** 1299 (the present improved and modernized version of the program has been written by T. Bally, S. Matzinger, and B. Albrecht)
- Shyn T W 1980 *Phys. Rev. A* **47** 2919-2
- Shyn T W and Sweeney C J 1993 *Phys. Rev. A* **22** 916-929
- Skalny J D, Matejcik S, Kiendler A, Stamatovic A and Märk T D 1996 *Chem. Phys. Lett.* in print
- Steinfeld J I, Adler-Golden, S M and Gallagher J W 1987 *J. Phys. Chem. Ref. Data* **16** 911-951
- Swanson N and Celotta R J 1975 *Phys. Rev. Lett.* **35** 783-5
- Walker I C, Gingell J M, Mason N J and Marston G 1996 *J. Phys. B: At. Mol. Opt. Phys.* **29** submitted for publication
- Wong S F and Schulz G J 1975 *Phys. Rev. Lett.* **35**, 1429

## 5.7. Resolution Enhancement of the Photoelectron Spectrometer

In this chapter an article, published in the *Journal of Physical Chemistry* (1995, **99**, p. 17844), is presented to which I contributed the photoelectron (PE) spectra of cyclopentadiene and fully deuterated cyclopentadiene. The quality of the spectra profited from instrumental improvements on the institute's PE spectrometer, performed in the course of the present thesis.

### 5.7.1. Introductory Remarks

Several improvements were undertaken on the (already modified) Perkin-Elmer PE spectrometer in the course of this thesis, with the goal of enhancing its performance, resolution and signal-to-background ratio. Prior to these improvements an instrumental resolution, *i.e.* full-width at half-height of routinely 30 meV and 20 meV at the very best was achieved when measuring organic molecules. At the present stage the PE spectrometer is capable of sustaining a resolution of 12 meV, with reasonable signal intensity and over extended acquisition periods. This improvement of the resolution is very significant because it reveals the vibrational structure, of primary interest in the present work, in much more detail.

### Resolution Limiting Factors

The factors limiting the resolution of gas-phase electron spectra have been discussed in detail by Baltzer *et al.* (1993) and references therein. With respect to PE spectroscopy six factors are mentioned:

- (a) Spectrometer resolving power
- (b) Plasma potentials
- (c) Time-dependent surface contact potentials
- (d) Linewidth of the excitation radiation
- (e) Lifetime broadening
- (f) Doppler broadening

Of these factors only the first three have been considered explicitly in the present modification of the instrument. The current setup can still be improved with respect to the first three factors, but the crucial factor for achieving sub-10 meV resolution with adequate signal intensity is surely the improvement of the UV excitation source.

A new type of microwave excited discharge source (Baltzer and Karlsson 1989), meeting the demands of high photon flux and narrow lines, is commercially available. The measured line width is 1.2 meV for the He I $\alpha$  line at 21.22 eV at an vacuum ultraviolet radiation flux of about  $3 \times 10^{14}$  photons per

second in a cone of  $11^\circ$  opening angle. This width is believed to be almost an order of magnitude smaller than the width encountered in classical photoionization sources. On the other hand these sources cost around 100'000 SFr, too expensive for the current project.

### Instrumental Modifications

A major improvement in performance of the PE spectrometer resulted from the replacement of the manually controlled analog electronics with computer-controlled digital electronics. Details of the new circuitry are described in the manual of the PE spectrometer (Asmis 1996). An important consequence of the replacement was the possibility to fully automate the calibration procedure.

Due to modification of the electrode surfaces caused by the gas load, the internal potentials (external plus contact potentials) change successively with time, giving rise to a drift of the photoelectron lines. The shift will eventually reach a limit for the substance studied, but the time to reach equilibrium is typically several hours. Furthermore, there is a temperature and pressure dependence of the contact potentials. The drift velocity can be considerable and is often the resolution limiting factor, if it is not corrected appropriately.

A "drift control" procedure was programmed, which adjusts the reference level of the voltage used to sweep the spectrum after a predefined number of sweeps. This is done by recording a reference line or structure with good intensity in-between successive sweeps, determining the absolute drift and correcting the reference voltage appropriately for the next sweep. The argon  $3P_{3/2}$  line at 15.759 eV was generally used for this procedure. As an example of how much better the resolution in practice has become, predominantly as a result of the "drift control", two PE spectra of the same substance are shown in Figure 5.7-1. The spectra were measured at the optimal settings before and after these improvements.

Baltzer *et al.* (1993) have shown that a further source for the deterioration of the resolution is caused by a potential gradient along the ionizing beam. The photoionization of a sample gas produces electrons, which normally have considerable kinetic energy, and residual ions. Due to the small electronic mass, the velocity difference between the electrons and the residual ions is very large, resulting in an excess of positive ions in the ionization region. These ions build up a space charge creating a plasma potential distribution. In order to correct the potential gradient Baltzer *et al.* propose to incorporate two properly shaped electrodes in the gas cell, one at the entrance and one at the exit hole of the photon beam.

Due to mechanical constraints present in our instrument, we were limited to incorporate one cylindrical, vertically displaceable, "correction" electrode, which was generally positioned slightly above the exit slit for the photoelectrons. By applying an adjustable voltage in the order of 70 mV to the

"correction" electrode, the resolution could be improved from about 13 meV (optimized settings without "correction" electrode) to below 11 meV. The dimensions of the "correction" electrode are described in the manual of the PE spectrometer.

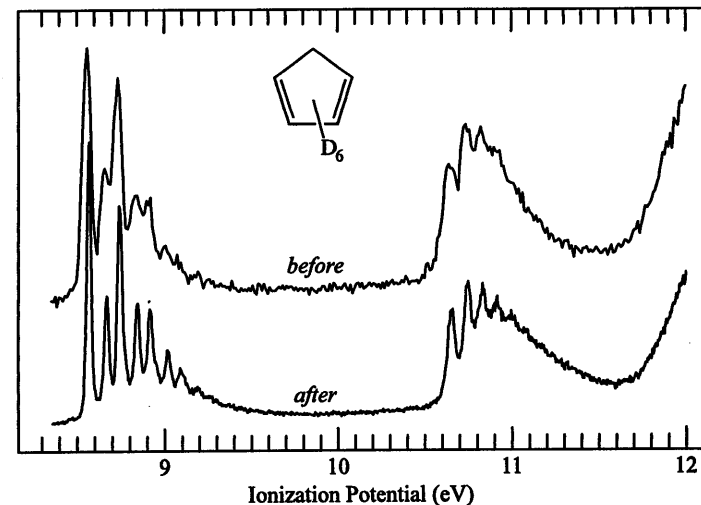


Figure 5.7-1

Comparison of two PE spectra of cyclopentadiene. The top spectrum was recorded at the optimal settings before the modifications, the bottom spectrum was recorded with the improved PE spectrometer, but without the "correction" electrode.

### 5.7.2. Publication

(see next page)

17844

Reprinted from The Journal of Physical Chemistry, 1995, 99.

## Electronic and Vibrational Structure and Scaled Density Functional Force Field of Cyclopentadiene and Its Radical Cation

Leo Truttmann, Knut R. Asmis, and Thomas Bally\*

Institute of Physical Chemistry, University of Fribourg, Pérolles, CH-1700 Fribourg, Switzerland

Received: July 12, 1995; In Final Form: September 14, 1995<sup>o</sup>

The photoelectron (PE) spectra of cyclopentadiene (CP) and its perdeuterated isotopomer (CP-d<sub>6</sub>) and the electronic absorption (EA) and infrared (IR) spectra of the corresponding radical cations are presented. The electronic structure of CP<sup>•+</sup> is discussed on the basis of CASSCF/CASPT2 calculations which reproduce the excited-state energies as derived from the PE and EA spectra very well. Density functional force fields are scaled to fit the observed bands in the IR spectra and vibrational progressions in the first PE bands. The changes in valence force constants upon ionization of CP are discussed on the basis of qualitative expectations and compared to those found earlier for butadiene.

### 1. Introduction

The molecular,<sup>1</sup> electronic,<sup>2,3</sup> and vibrational structure<sup>4</sup> of cyclopentadiene (CP), the prototypical cyclic diene, has been studied thoroughly by both experimental<sup>1,2,4</sup> and theoretical methods.<sup>3</sup> Conversely, less is known about its radical cation (CP<sup>•+</sup>): in 1971 Derrick et al. published a well-resolved photoelectron (PE) spectrum of CP<sup>•+</sup> which was also used to discuss selected features of vibrational structure. Electron spin resonance (ESR) and electronic absorption (EA) spectra of CP<sup>•+</sup> were recorded by Shida et al. in the early 1980s.<sup>5</sup> We are aware of no attempt to compare the EA and PE spectra, both of which show pronounced vibrational structure in the first and second bands, and the full vibrational structure of CP<sup>•+</sup> remains unexplored to date.

The recent literature shows many reports on vibrational structures of small radical cations (up to four atoms) which have been investigated in condensed or gas-phase experiments.<sup>7</sup> However, the study of the vibrational structure of medium-sized organic radical cations has only recently been taken up systematically by several groups using infrared (IR),<sup>8-10</sup> resonance Raman,<sup>11</sup> or different flavors of zero kinetic energy (ZEKE) PE spectroscopy.<sup>12</sup>

Our own activities in this field focus on the changes in the properties of chemical bonds upon ionization which we probe as changes in valence force constants.<sup>10</sup> To this end we try to get a maximum of information about the vibrational structure of a given radical cation and its parent neutral and use this to scale the force fields obtained by some quantum chemical procedure (the so-called SQM method<sup>13</sup>). This approach has gained in attractiveness as it is now possible to calculate force fields at levels of theory that take the effects of electron correlation into account and thus eliminate some of the artifacts introduced at the Hartree-Fock level.

As our initial investigations centered on *trans*-butadiene<sup>10</sup> (BD) and vinylacetylene,<sup>14</sup> it was logical to extend our study to include the cis-configured cyclic diene, CP, especially since the force field of the neutral parent is well documented.<sup>4</sup> Thus, we present the results of our efforts to elucidate the electronic and vibrational structure of CP<sup>•+</sup> by means of PE, EA, and IR spectroscopy as well as different quantum chemical calculations. For the purpose of comparison we reoptimized the valence force field of neutral CP and found some interesting discrepancies

with that determined previously on the basis of the same experimental data but from an empirical rather than a quantum mechanical force field.

### 2. Experimental Section

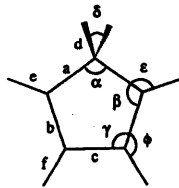
**Syntheses.** CP was obtained by fractional distillation from the dimer, and its purity was checked by analytical GC. CP-d<sub>6</sub> was made by repeated H/D exchange in HMPT containing D<sub>2</sub>O/NaOD. After seven cycles the content of CP-d<sub>6</sub> was ≈95% by NMR.

**Ion Preparation and Spectroscopy.** The techniques and apparatus used for EA and IR matrix isolation spectroscopy have been described previously<sup>10</sup> and were used without modification. All experiments were carried out pairwise, once with CH<sub>2</sub>Cl<sub>2</sub> and once with CD<sub>2</sub>Cl<sub>2</sub> as electron scavenger to eliminate spectroscopic features due to these (only bands that show identical behavior in both experiments are associated with CP). The region above 500 cm<sup>-1</sup> was studied with a Bomem DA3 interferometer, below 500 cm<sup>-1</sup> a dispersive instrument was used where necessary (ν<sub>18</sub> of CP-d<sub>6</sub><sup>•+</sup>). The PE spectra were recorded on a modified Perkin-Elmer instrument operated in preretardation (and hence constant resolution) mode<sup>15</sup> under computer control. Calibration was effected with a Xe/Ar mixture, and the spectral resolution was 12 meV (digital resolution 2 meV).

**Calculations.** Following the earlier related example of butadiene, Hessians of CP and CP<sup>•+</sup> were initially calculated by the (U)MP2/6-31G<sup>+</sup> procedure at geometries optimized at the same level using the Gaussian92 program package.<sup>16</sup> Later we found that force fields obtained with hybrid Hartree-Fock/density functional methods yielded surprisingly good agreement with the observed spectra. In particular, Beckes hybrid gradient corrected exchange functionals<sup>17a,b</sup> in combination with the correlation functional by Lee Yang and Parr<sup>17c</sup> (BLYP/B3LYP)<sup>17d</sup> gave optimized geometries in close agreement with experiment (in the case of CP) and/or with those calculated at highly correlated levels (QCISD, cf. Table 1). More importantly, the corresponding force fields allowed an unambiguous assignment of most fundamentals with no scaling and gave gratifyingly small deviations between observed and calculated frequencies after scaling, except for the strongly anharmonic C-H/C-D stretching vibrations. Due to the importance of configurational mixing, structures of electronically excited CP<sup>•+</sup> were optimized by a CASSCF procedure with an active space comprising four π-MO's containing three π-electrons.

Force Field of Cyclopentadiene

J. Phys. Chem., Vol. 99, No. 51, 1995 17845

TABLE 1: Geometries of CP and CP<sup>•+</sup> by Different Methods<sup>a</sup>


	CP				CP <sup>•+</sup>				
	exp <sup>1c</sup>	QCISD	B3LYP	CAS(1 <sup>2</sup> A <sub>1</sub> )	UQCISD	UB3LYP	CAS(1 <sup>2</sup> A <sub>2</sub> )	CAS(1 <sup>2</sup> B <sub>1</sub> )	CAS(2 <sup>2</sup> B <sub>1</sub> )
a	150.1	150.9	150.7	151.1	149.6	149.6	149.7	148.7	148.6
b	135.4	135.0	134.9	134.8	140.2	140.1	139.4	140.5	145.8
c	146.5	147.7	147.0	147.7	140.9	141.1	140.1	148.3	142.7
d	109.9	110.1	110.1	108.8	110.2	110.2	108.7	109.4	109.9
e	108.1	108.7	108.4	107.3	108.8	108.6	107.3	107.0	107.3
f	108.2	108.7	108.5	107.3	108.7	108.4	107.3	107.3	106.9
α	102.8	102.9	103.2	102.4	102.0	102.1	101.5	106.4	101.3
β	109.3	109.4	109.1	109.8	109.9	109.8	110.0	108.2	112.0
γ	109.3	109.1	109.3	109.0	109.0	109.1	109.2	108.6	107.4
δ	106.3	106.5	105.8	106.9	105.8	105.1	106.9	104.6	103.5
ε	123.6	123.8	123.9	123.7	124.6	124.5	124.6	125.8	123.9
φ	126.0	126.4	126.3	126.4	125.3	125.4	125.3	127.0	125.0

<sup>a</sup> The 6-31G<sup>+</sup> basis set was used in all calculations. For a description of methods, see text. All bond lengths a-f in picometers; angles α-φ in degrees.

The geometries of the different states obtained by different procedures are summarized in Table 1, which also lists the experimental numbers for neutral CP. For the scaling of the force field, a nonredundant set of internal coordinates R<sub>i</sub> was defined following the standards proposed by Pulay et al.<sup>18</sup> These were grouped into symmetry-adapted linear combinations S<sub>i</sub>, which were used in an SQM force field fitting procedure as described by Pulay et al.<sup>13</sup> With a B3LYP Hessian, near coincidence between calculated and observed IR frequencies of CP<sup>•+</sup> could be obtained within a scaling model involving only six independently varied factors. In the case of neutral CP, where the full vibrational structure of both isotopomers is available, a more refined model was used that involved 12 different factors to scale the diagonal force constants and one to scale two off-diagonal elements separately.<sup>19</sup>

Coordinate and force field transformations were effected using parts of the Umat and Bmat modules in the McIntosh/Peterson vibrational analysis package<sup>20</sup> which were incorporated into a program for fitting calculated to observed spectra by a Simplex procedure.<sup>21</sup> Excited state calculations were done with the CASSCF/CASPT2 model<sup>22</sup> using ANO type basis sets,<sup>23</sup> a combination that has recently proven to be very reliable for polyene radical cations.<sup>24</sup> The active space for the full CI comprised five electrons in the three occupied and the lowest three virtual MOs of π-symmetry. This (5,6) active space includes the pseudo-π<sup>(\*)</sup> MOs of the CH<sub>2</sub> groups, and it described the final CASPT2 wave function to >80% for all states considered. The MO basis was reoptimized for every state, but the CASSCF wave functions (which served also to calculate the transition moments) were still roughly orthogonal. These calculations were carried out with the Molcas/2 suite of programs.<sup>25</sup>

### 3. Results and Discussion

**3.1. PE and EA Spectra: Electronic Structure.** Figure 1a shows the EA spectrum of matrix-isolated CP after X irradiation. Next to the two band systems of CP<sup>•+</sup> at 450–650 and 300–370 nm<sup>26</sup> is an absorption that rises around 430 nm

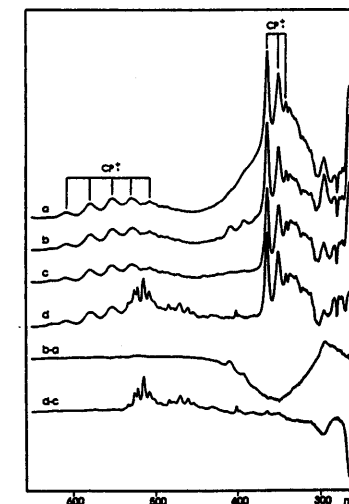


Figure 1. (a) Spectrum of cyclopentadiene after (minus before) X irradiation in argon. Features denoted by CP<sup>•+</sup> are ascribed to the radical cation. (b) Same after photolysis at >630 nm. Note the disappearance of the broad band underlying the second CP<sup>•+</sup> band system, highlighted in difference spectrum b-a below. (c) After short irradiation at 365 nm. (d) After photolysis at 313 nm. Note that the bands of CP<sup>•+</sup> are not affected by any photolyses.

and underlies the sharp peaks of the second CP<sup>•+</sup> band. Photolysis of this sample at >630 nm (Figure 1b) leads to the disappearance of a broad band peaking at 355 nm (cf. difference spectrum b-a) while a pair of small bands rise around 400 nm. However, these disappear again upon short irradiation at 365 nm (Figure 1c). Finally, photolysis at 313 nm leads to a marked

<sup>o</sup> Abstract published in *Advance ACS Abstracts*, December 1, 1995.



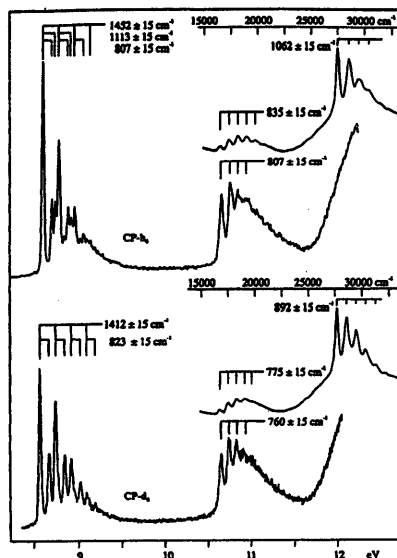


Figure 2. Photoelectron spectra of CP and CP- $d_6$  and EA spectra of the corresponding radical cations superposed on the same energy scale (origin placed in  $\nu = 0$  component of the first PE band).

decrease of the UV bands at 300 and 260 nm (Figure 1d) while a series of new sharp peaks arise between 530 and 450 nm (cf. spectrum d-c).

Apparently, ionization of CP is accompanied by the formation of at least two side products (cf. the downward pointing features in the difference spectra b-a and d-c) which can be bleached at different wavelengths. As the concomitant changes in the IR spectra were too small to permit an identification of these species or their photoproducts, we will not speculate about their identity at this point.<sup>26</sup> However, we wish to retain that *no photoinduced changes in the intensity of the optical bands of CP<sup>•+</sup> could be observed*. Hence CP<sup>•+</sup> appears to be entirely photostable under the conditions of photoconversion of the side products, a feature which will permit a distinction of the IR bands of CP<sup>•+</sup> from those of the latter.

Figure 2 shows the PE spectra of CP and CP- $d_6$  and, superimposed on the same energy scale, the EA spectra of the corresponding radical cations. The vertical transition energies observed at the neutral (experimental)<sup>16</sup> and the radical cation geometries of CP (calculated) are juxtaposed to those calculated by the CASPT2 procedure in Figure 3 and Table 2. The former serves also to illustrate the pronounced changes in the configuration energies between the two geometries and to show how these changes are attenuated by going to the CASSCF and finally to the CASPT2 level, as it appears to be typical for polyene radical cations.<sup>24</sup>

As expected and confirmed through the calculations, the second PE band of CP and the first EA band of CP<sup>•+</sup> are due to the same state ( $1^2B_1$ ). As in the case of linear polyene cations,<sup>27</sup> the energy of this state appears to be little affected by going from the neutral to the cation geometry despite the strong changes in geometry (cf. Table 1) and the corresponding shifts of the configuration energies. Experimentally, the shift is not easy to determine precisely due to Franck-Condon

effects: if we assume that the first PE peak represents the true origin of the energy scale for the radical cation, the band maximum corresponding to the  $1^2B_1$  state shifts by 1 or 2 quanta of the dominant vibrational progression which corresponds to about 0.1 or 0.2 eV, respectively. The calculated shift of 0.33 eV is still higher, but this represents a difference between potential energies and does not take into account effects due to overlap of vibrational wave functions.

The second excited state of CP<sup>•+</sup> at its equilibrium geometry is also predicted in reasonable accord with experiment (0.25 eV too high). In contrast, the second EA band of CP<sup>•+</sup> is clearly not due to the same state as the third PE band of CP (which is not fully shown in Figure 2). Whereas the latter may be ascribed to ionizations of  $\sigma$ -electrons,<sup>5</sup> the former must be due to excitations within the  $\pi$ -manifold of electrons. Indeed, the CASPT2 model predicts a second  $^2B_1$  state close to  $\nu_{\max}$  of the second EA band and gives an oscillator strength of 0.14, in agreement with the observed intensity (transitions into  $\sigma$  excited states have much smaller transition moments and are normally not observed in the EA spectra of planar unsaturated radical ions).

The calculations predict furthermore that the  $2^2B_1$  state undergoes a pronounced red shift of 0.63 eV upon relaxation of the cation from the neutral geometry. Unfortunately, this prediction cannot be verified because this state, which would in any event appear only very weakly in the PE spectrum due to the lack of Koopmans character,<sup>27</sup> lies in a region which is masked by  $\sigma$ -ionizations.

**Comparison with BD<sup>•+</sup>:** Not unexpectedly, the different states of CP<sup>•+</sup> observed in the above experiments are shifted relative to its open-chain analogue, BD<sup>•+</sup> (for a comparison of  $I_{\nu}$  and  $\nu_{\max}$  cf. Table 2), but these shifts are not uniform. An explanation for these features can be derived from the MOs depicted in Figure 3: Due to the node of the CP HOMO at the position of the bridging CH<sub>2</sub> group, the 0.46 eV shift of  $I_{\nu,1}$  (and, via Koopmans' theorem, the energy of the  $\pi_2$ -MO) relative to BD is mainly due to the *inductive* influence of the CH<sub>2</sub> group (a small additional destabilization may arise from the antibonding cis-1,4 interaction which is absent in BD). Conversely,  $I_{\nu,2}$  ( $\rightarrow \epsilon(\pi_1)$ ) is shifted by 0.74 eV, although inductive destabilization should be less than in the HOMO due to the smaller terminal coefficients in  $\pi_1$ . However, hyperconjugation with the CH<sub>2</sub> pseudo- $\pi$  MO, which is now possible due to the absence of a node at this site, causes additional destabilization. The 0.31 eV shift in  $I_{\nu,2} - I_{\nu,1}$  between BD and CP at the neutral geometry and reflects exactly this effect. At the cation geometry the shift is slightly smaller, i.e., the difference is attenuated.

The displacement of the second excited state of CP<sup>•+</sup> relative to BD<sup>•+</sup>, as seen in the EA spectrum, is much more pronounced (0.8 eV). If we assume that this state arises essentially by HOMO - LUMO excitation (as suggested by the CASSCF calculations), we can understand why this is so: Whereas the inductive influence of the CH<sub>2</sub> group destabilizes both MOs by similar amounts, the LUMO is selectively stabilized by hyperconjugation via the pseudo- $\pi^*$  MOs of CH<sub>2</sub>, which leads to a narrowing of the HOMO-LUMO gap. Interestingly, the red shift of this transition is quite similar to that found in the neutral parent compounds (0.66 eV<sup>23</sup>). Of course, in actual fact the situation is more complicated due to effects of configuration interaction, but it appears that a qualitative understanding of the differences in electronic structure between the two compounds is possible on the basis of a simple MO model.

In contrast to BD<sup>•+</sup> the spectra of CP<sup>•+</sup> show pronounced vibrational structure. We will exploit this fact in the following attempt to establish a force field for CP<sup>•+</sup>.

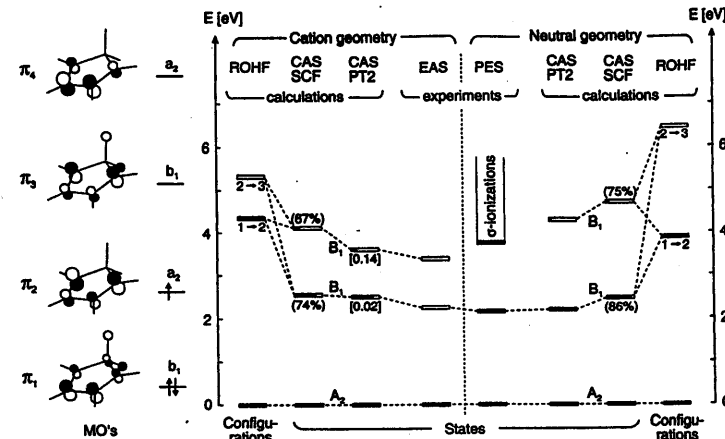


Figure 3. Excited configurations and states of CP<sup>•+</sup> at the neutral and the cation equilibrium geometries. Numbers in parentheses denote percent Koopmans configuration (black bars), numbers in brackets are oscillator strengths for excitation from cation ground state. Discussion see text.

TABLE 2: Excited-State Energies of CP<sup>•+</sup> from Experiment and Calculations and Comparison with Butadiene Radical Cation

	neutral (experimental) geometry			cation (B3LYP/6-31G*) geometry			butadiene radical cation		
	CASSCF	CASPT2	PES <sup>a</sup>	CASSCF	CASPT2	EAS <sup>b</sup>	PES <sup>c</sup>	EAS <sup>d</sup>	
$1^1A_2'$	-192.569 89	-193.124 64	8.56 eV	-192.577 63	-193.135 00	(0)	9.05 eV	(0)	
$1^1B_1$	+2.46 eV	+2.21 eV	+2.12 eV	+2.61 eV	+2.54 eV	+2.25 eV	+2.43 eV	+2.40 eV	
$2^1B_1$	+4.77 eV	+4.30 eV	?	+4.20 eV	+3.67 eV	+3.40 eV	?	+4.20 eV	

<sup>a</sup> From photoelectron spectrum in Figure 2. <sup>b</sup> From  $\nu_{\max}$  in electronic absorption spectrum in argon (Figure 2). <sup>c</sup> From photoelectron spectrum.<sup>27a</sup> <sup>d</sup> From electronic absorption spectrum in argon.<sup>27a</sup> Absolute energies of ground state in hartrees,  $I_{\nu,1}$  for PES-entries.

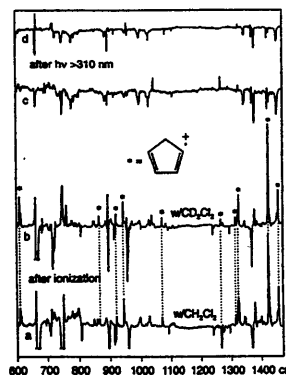


Figure 4. IR spectra of CP after (minus before) ionization (a/b) and after (minus before) photolysis at 313 nm (c/d). Bands that rise on ionization and do not change upon photolysis are ascribed to CP<sup>•+</sup>, provided they appear likewise in experiments with CH<sub>2</sub>Cl<sub>2</sub> (a/c) and CD<sub>2</sub>Cl<sub>2</sub> (b/d), respectively, as electron scavenger. They are labeled with asterisks.

**3.2. IR (and PE) Spectra: Vibrational Structure.** In Figure 4 the changes in the IR spectra upon X irradiation and subsequent photolysis at  $\lambda > 310$  nm of samples containing CP and CH<sub>2</sub>Cl<sub>2</sub> or CD<sub>2</sub>Cl<sub>2</sub>, respectively, as electron scavenger are shown, whereas the same is done for CP- $d_6$  in Figure 5. As mentioned above, CP<sup>•+</sup> was found to be practically photostable

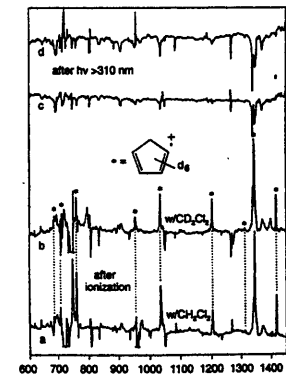


Figure 5. Same as Figure 4 for CP- $d_6$ . See caption of Figure 4. to irradiation at the wavelength of its intense, second absorption band ( $\lambda \approx 310$ -370 nm) with different lamps. Therefore, in contrast to the previous case of BD<sup>•+</sup>, where the *bleaching* of peaks which had formed newly upon X irradiation was used to identify those belonging to the parent cation,<sup>10</sup> the *photostability* of the CP<sup>•+</sup> peaks was used as a distinguishing criterion.

Thus, peaks which rise in concert upon X irradiation, are independent of the type of electron scavenger and are photostable were taken into consideration as fundamentals of CP or CP- $d_6$ , respectively. The assignment of the more intense bands became already evident by comparison with the unscaled



TABLE 3: Definition of Internal and Symmetry Coordinates for CP

internal coordinate	description <sup>a</sup>	composition	symmetry coordinate <sup>b</sup>				scaling factors	
			a <sub>1</sub>	a <sub>2</sub>	b <sub>1</sub>	b <sub>2</sub>	f(CP)	f(CP <sup>2+</sup> )
R <sub>1</sub>	r(C-C)	r(C <sub>1</sub> -C <sub>2</sub> )	S <sub>1</sub>			S <sub>20</sub>	0.981	0.964
R <sub>2</sub>	r(C-C)	r(C <sub>1</sub> -C <sub>3</sub> )						
R <sub>3</sub>	r(C-C)	r(C <sub>2</sub> -C <sub>3</sub> )	S <sub>2</sub>			S <sub>21</sub>	0.899	
R <sub>4</sub>	r(C-C)	r(C <sub>3</sub> -C <sub>4</sub> )						
R <sub>5</sub>	r(C-C)	r(C <sub>4</sub> -C <sub>5</sub> )	S <sub>3</sub>			S <sub>22</sub>	0.916	
R <sub>6</sub>	r(C-H)	r(C <sub>2</sub> -H <sub>6</sub> )						
R <sub>7</sub>	r(C-H)	r(C <sub>3</sub> -H <sub>7</sub> )	S <sub>4</sub>			S <sub>23</sub>	0.915	
R <sub>8</sub>	r(C-H)	r(C <sub>4</sub> -H <sub>8</sub> )						
R <sub>9</sub>	r(C-H)	r(C <sub>5</sub> -H <sub>9</sub> )	S <sub>5</sub>			S <sub>15</sub>	0.915	
R <sub>10</sub>	r(C-H)	r(C <sub>1</sub> -H <sub>10</sub> )						
R <sub>11</sub>	r(C-H)	r(C <sub>2</sub> -H <sub>11</sub> )	S <sub>6</sub>			S <sub>16</sub>	0.900	
R <sub>12</sub>	φ(C-H)	β <sub>2</sub> - γ <sub>2</sub>						
R <sub>13</sub>	φ(C-H)	β <sub>3</sub> - γ <sub>3</sub>	S <sub>7</sub>			S <sub>24</sub>	0.938	
R <sub>14</sub>	φ(C-H)	β <sub>4</sub> - γ <sub>4</sub>						
R <sub>15</sub>	φ(C-H)	β <sub>5</sub> - γ <sub>5</sub>	S <sub>8</sub>			S <sub>25</sub>	0.947	
R <sub>16</sub>	σ(CH <sub>2</sub> )	δ						
R <sub>17</sub>	ω(CH <sub>2</sub> )	ε <sub>10</sub> - ε <sub>11</sub> + φ <sub>10</sub> - φ <sub>11</sub>	S <sub>9</sub>			S <sub>16</sub>	0.900	
R <sub>18</sub>	ω(CH <sub>2</sub> )	ε <sub>10</sub> + ε <sub>11</sub> - φ <sub>10</sub> - φ <sub>11</sub>						
R <sub>19</sub>	τ(CH <sub>2</sub> )	ε <sub>10</sub> - ε <sub>11</sub> - φ <sub>10</sub> + φ <sub>11</sub>	S <sub>10</sub>			S <sub>11</sub>	0.953	
R <sub>20</sub>	δ(ring)	a <sub>1</sub> + a <sub>2</sub> (α <sub>2</sub> + α <sub>3</sub> ) + b <sub>1</sub> (α <sub>4</sub> + α <sub>5</sub> ) <sup>c</sup>						
R <sub>21</sub>	δ(ring)	(a - b)(α <sub>2</sub> - α <sub>3</sub> ) + (1 - a)(α <sub>4</sub> - α <sub>5</sub> ) <sup>d</sup>	S <sub>11</sub>			S <sub>11</sub>	0.988	
R <sub>22</sub>	ω(C-H)	α <sub>6</sub>						
R <sub>23</sub>	ω(C-H)	α <sub>7</sub>	S <sub>12</sub>			S <sub>17</sub>	1.067	
R <sub>24</sub>	ω(C-H)	α <sub>8</sub>						
R <sub>25</sub>	ω(C-H)	α <sub>9</sub>	S <sub>13</sub>			S <sub>18</sub>	1.025	
R <sub>26</sub>	τ(ring)	b(τ <sub>1</sub> + τ <sub>2</sub> ) + a(τ <sub>3</sub> + τ <sub>4</sub> ) + τ <sub>5</sub> <sup>e</sup>						
R <sub>27</sub>	τ(ring)	(a - b)(τ <sub>3</sub> - τ <sub>4</sub> ) + (1 - a)(τ <sub>1</sub> + τ <sub>2</sub> ) <sup>e</sup>	S <sub>14</sub>			S <sub>19</sub>	1.086	

<sup>a</sup> v, stretch; φ, rock; ω, wag; σ, scissor; δ, deformation; τ, torsion. <sup>b</sup> When symmetry coordinates are composed from pairs of internal coordinates, those of a<sub>1</sub> and a<sub>2</sub> symmetry represent positive, those of b<sub>1</sub> and b<sub>2</sub> symmetry negative combinations, respectively, each normalized by 0.707; a<sub>1</sub> and b<sub>2</sub> are in-plane, a<sub>2</sub> and b<sub>1</sub> out-of-plane deformations. <sup>c</sup> Scaled on the basis of only one frequency (lack of experimental data). <sup>d</sup> The factors a and b are equal to cos 144° and cos 72°, respectively.

B3LYP/6-31G\* force field (cf. section 2) and was confirmed after scaling it as described in section 3.3. Finally, some of the smaller bands were incorporated into the fitting procedure and retained if they did not lead to any significant deterioration of the difference between observed and calculated frequencies and intensities.

In this way, 12 out of 23 IR-active fundamentals of CP-h<sub>6</sub><sup>2+</sup> and 10 IR bands of CP-d<sub>6</sub><sup>2+</sup> could be assigned. In addition, the force fields predicted two additional totally symmetric normal vibrations in close agreement with the progressions at 1110 and 805 cm<sup>-1</sup> in the first PE band of CP-h<sub>6</sub> (the one at 1452 ± 15 cm<sup>-1</sup> coinciding with a strong IR band at 1456 cm<sup>-1</sup>) and one near the progression of 823 cm<sup>-1</sup> in the first PE band of CP-d<sub>6</sub>. Hence these numbers were incorporated in the fitting procedure and were reproduced within experimental uncertainty by the final force field.

3.3. Force Field of CP Revisited. Table 3 shows the internal valence coordinates of CP according to the recommendations of Pulay et al.<sup>13</sup> and the symmetry coordinates derived therefrom. The latter were assembled into groups of similar types for the purpose of scaling. In the case of CP where all 54 fundamentals of the h<sub>6</sub> and d<sub>6</sub> isotopomer have been assigned,<sup>4</sup> a model with 12 independent scaling factors was used (in addition, three off-diagonal elements were scaled separately, see below). On the basis of this model and the B3LYP/6-31G\* Hessian, the root mean square (rms) difference between observed and calculated frequencies was minimized as a function

of the above scaling factors as described previously.<sup>10,21,29</sup> The resulting optimized scaling factors are listed in the second to last column of Table 3.

This fitting was done on the basis of the experimental data provided some time ago by Castellucci et al.<sup>4</sup> Initially we found it impossible to attain any satisfactory agreement between calculated and observed frequencies and intensities for the a<sub>1</sub> and b<sub>2</sub> C-C and CH<sub>2</sub> deformations. After some exploratory calculations it turned out that the problem was clearly due to ν<sub>23</sub> of CP-d<sub>6</sub> which had been assigned to weak IR and Raman bands around 1230 cm<sup>-1</sup> in the crystal spectra. When this frequency was left out of the fitting procedure, the rms difference quickly fell below 5 cm<sup>-1</sup> for the frequencies under 2000 cm<sup>-1</sup> and ν<sub>23</sub> of CP-d<sub>6</sub> was predicted at ≈1190 cm<sup>-1</sup>. In search of a suitable experimental counterpart, we found a weak band at 1174 cm<sup>-1</sup> which had actually been assigned to ν<sub>23</sub> in an earlier paper by the same authors<sup>30</sup> but had eventually been abandoned in favor of the 1231 cm<sup>-1</sup> peak and relegated to the status of a combination band.<sup>4,30</sup> However, we hesitate to confirm this reassignment because the difference between predicted and observed ν<sub>23</sub> could be improved only at the cost of other agreements.

Thus we suppressed ν<sub>23</sub> in the final refinement of the CP force field which required in addition that the S<sub>16,17</sub>/S<sub>19</sub> off-diagonal elements of the force constant matrix be scaled separately to attain optimal agreement (optimized scaling factor: f = 0.847). Eventually, the scaled B3LYP/6-31G\* force

## Force Field of Cyclopentadiene

TABLE 4: Comparison of Diagonal and Some Important Off-Diagonal Valence Force Constants of CP and CP<sup>2+</sup><sup>34</sup>

force constant <sup>a</sup>	description <sup>b</sup>	CP <sup>c</sup>	CP <sup>d</sup>	CP <sup>2+</sup> <sup>e</sup>
k <sub>1</sub> = k <sub>2</sub>	r(C-C)	4.76	4.46	4.40
k <sub>3</sub> = k <sub>4</sub>	r(C=C)	8.07	8.08	6.45
k <sub>5</sub>	r(C-C)	4.37	4.84	6.45
k <sub>6</sub> = k <sub>7</sub>	r(C-H)	5.15	5.25	(5.21) <sup>f</sup>
k <sub>8</sub> = k <sub>9</sub>	r(C-H)	5.15	5.21	(5.23) <sup>f</sup>
k <sub>10</sub> = k <sub>11</sub>	r(C-H)	4.57	4.67	4.62
k <sub>12</sub> = k <sub>13</sub>	φ(C-H)	4.57	0.43	0.45
k <sub>14</sub> = k <sub>15</sub>	φ(C-H)	4.57	0.45	0.46
k <sub>16</sub>	σ(CH <sub>2</sub> )	0.39	0.64	0.62
k <sub>17</sub>	ω(CH <sub>2</sub> )		0.38	0.37
k <sub>18</sub>	ω(CH <sub>2</sub> )		0.56	0.55
k <sub>19</sub>	τ(CH <sub>2</sub> )		0.54	0.53
k <sub>20</sub>	δ(ring)		1.61	1.62
k <sub>21</sub>	δ(ring)		1.48	1.45
k <sub>22</sub> = k <sub>23</sub>	α(C-H)	0.30	0.27	0.34
k <sub>24</sub> = k <sub>25</sub>	α(C-H)	0.44	0.61	0.51
k <sub>26</sub>	τ(ring)		0.47	(0.27)
k <sub>27</sub>	τ(ring)		2.10	(1.01)
k <sub>1,2</sub>		0.63	0.14	0.36
k <sub>1,3</sub> = k <sub>2,4</sub>		0.23	0.30	0.39
k <sub>3,4</sub>		-0.15	-0.15	0.33
k <sub>3,5</sub> = k <sub>4,5</sub>		0.23	0.42	0.52
k <sub>10,11</sub>		0.09	0.06	0.06
k <sub>24,25</sub>		-0.23	-0.14	(0.05) <sup>f</sup>
k <sub>24,26</sub> = k <sub>25,26</sub>			0.14	(0.05) <sup>f</sup>
k <sub>24,26</sub> = k <sub>25,26</sub>			0.14	(0.05) <sup>f</sup>
k <sub>24,27</sub> = -k <sub>25,27</sub>			0.72	(0.37) <sup>f</sup>

<sup>a</sup> In internal coordinates R<sub>1</sub> - R<sub>27</sub> (cf. Table 1). <sup>b</sup> Cf. footnote a in Table 1. <sup>c</sup> Castellucci et al.<sup>4</sup> <sup>d</sup> Present work. <sup>e</sup> Unoptimized scaling factor set to 0.95 (lack of experimental data).

field reproduced the experimental frequencies of CP and CP-d<sub>6</sub> with an rms difference of 3.5 cm<sup>-1</sup> below 2000 cm<sup>-1</sup> (the largest deviation of 9.6 cm<sup>-1</sup> being found for ν<sub>24</sub>(b<sub>2</sub>) of CP-h<sub>6</sub>), 18.2 cm<sup>-1</sup> for the highly anharmonic C-H stretches, and 9.15 cm<sup>-1</sup> overall.<sup>31</sup> This result can be considered as very satisfactory indeed, and the present force field of CP may certainly be regarded as reliable. The small scattering of the optimized scaling factors (0.95 ± 0.06)<sup>31</sup> shows that the B3LYP density functional scheme appears to be capable of very reliable predictions of force fields, in accord with similar recent experiences.<sup>32</sup>

The present force field generally shows reasonable agreement with the purely empirical one derived previously<sup>4</sup> (cf. Table 4, third column). The largest differences among the comparable force constants<sup>33</sup> are in the C-C stretches and the off diagonal elements involving those and the C=C stretches. Also, the force constant for the CH<sub>2</sub> scissoring motion is significantly higher in our force field. All attempts to fit a force field starting from the corresponding values as proposed by Castellucci et al.<sup>4</sup> failed to give satisfactory agreement with experiment.

The diagonal and some important off-diagonal force constants of CP are listed in Table 4 next to those of the radical cation (see next section). The full force field as well as a table with the resulting frequencies, intensities, and potential energy distributions (PED) is available as supporting information or in digital ASCII form from the correspondence author upon request. The PED show that extensive mode mixing prevails among the in-plane deformations such that no single bands can be attributed to group vibrations.

3.4. Force Field of CP<sup>2+</sup>. Using the same approach as outlined above, but with a simpler scaling model (6 instead of 12 independent scaling factors, no separate scaling of off-diagonal elements), we fitted the B3LYP/6-31G\* force field of CP<sup>2+</sup> to the 25 pieces of spectroscopic information available to us. Due to lack of experimental data, the force constants for C(sp<sup>2</sup>)-H stretches and the ring torsions were left unscaled.

We encountered no major difficulties in the fitting procedure and the optimized scaling factors (0.94 ± 0.04) and rms deviations (5.5 cm<sup>-1</sup>) indicates that the B3LYP scheme appears to work equally well for open-shell systems, in accord with recent findings for the notoriously difficult phenoxy radical.<sup>34,35</sup>

The optimized scaling factors and scaled force constants of CP<sup>2+</sup> are listed in the last columns of Table 3 and 4, respectively, while the observed frequencies of IR-active normal modes are compared to the calculated values and the potential energy distribution (PED) in symmetry coordinates in Table 5. These latter values can be used "in reverse" to add up the contributions of the observed fundamentals to the definition of different symmetry coordinates. In this way we find that the important valence force constants for C-C and C=C stretches are all defined to >66% by the available experimental data. The same is true for the CH rocking and the CH<sub>2</sub> scissoring modes whereas the out-of-plane force field is generally less well defined, and the C(sp<sup>2</sup>)-H stretches are entirely undefined.<sup>36</sup>

With the above in mind we can proceed to compare the force constants of CP<sup>2+</sup> to those of the parent neutral. As in the previous case of butadiene<sup>10</sup> we find that the double bonds (k<sub>3,4</sub>) are weakened by ≈20% upon ionization. The concomitant strengthening of the essential single bond between them (k<sub>5</sub>) is more pronounced in CP (+33%) than in BD (+22%), a discrepancy that arises mainly from differences in the corresponding force constants of the neutrals (4.84 vs 5.2 aJ/Å), the final values in the cations being again quite similar (6.45 vs 6.37 aJ/Å).

As expected from the nodal properties of the HOMO, the force constants of the C-C single bonds to the CH<sub>2</sub> group (k<sub>1,2</sub>) and those of the C-H deformations within the latter (k<sub>16-19</sub>) are barely affected by ionization. Similarly, the in-plane deformations of the ring (k<sub>20,21</sub>) and the hydrogen atoms attached to it (k<sub>12-15</sub>) do not change significantly, whereas the corresponding out-of-plane deformations (k<sub>22-25</sub>) are more strongly influenced by the changes in the π-system. In particular, the ring twisting coordinates (k<sub>26,27</sub>) appear to be very strongly affected, but unfortunately, the corresponding force constants are not sufficiently well defined to draw any meaningful conclusions, also because some off-diagonal elements in the out-of-plane part of the force fields undergo pronounced changes upon ionization.

3.5. Vibrational Structure in Excited States of CP<sup>2+</sup>. We had noted above that the vibrational structure in the first PE bands of CP and CP-d<sub>6</sub> could be easily assigned by means of the above force field and was in fact helpful for the determination of some totally symmetric fundamentals. However, we also pointed out the slight discrepancy between the vibrational intervals in the first EA band of CP<sup>2+</sup> and in the second PE band of CP, which was just on the borderline of falling within the experimental uncertainty (±0.02 eV in the PE spectra, ±15 cm<sup>-1</sup> in the EA spectra). Thus we wanted to examine the possibility if in fact two different totally symmetric fundamentals may be activated in the two different processes of excitation (from the neutral ground state in the PE spectrum, from the ionic ground state in the EA spectrum). For this purpose we determined the geometry changes in the course of the two excitations at the CAS(3,4) SCF level (cf. Table 1 above).

In Figure 6 we plot these geometry changes as displacements in a center-of-mass coordinate system. Indeed, we find that lengthening of the double bonds (by 5.7 pm) is the dominant feature on excitation from the neutral ground state whereas the essential single bond is hardly affected (+0.6 pm).<sup>37</sup> Conversely, upon excitation from the ionic ground state (1<sup>2</sup>A<sub>2</sub>), the dominant feature is the lengthening of the essential single bond

TABLE 5: Comparison of Observed<sup>a</sup> and Calculated<sup>b</sup> IR Frequencies of CP<sup>++</sup>

		CP <sup>++-h<sub>g</sub></sup>			CP <sup>++-d<sub>g</sub></sup>		
		obs	calc	%F	obs	calc	%F
A <sub>1</sub>	ν <sub>1</sub>	3103.6	5	5 <sup>90</sup> , 4 <sup>19</sup>	2314.2	2	5 <sup>70</sup> , 4 <sup>23</sup>
	ν <sub>2</sub>	2885	20	4 <sup>90</sup> , 5 <sup>19</sup>	2286.3	4	4 <sup>70</sup> , 5 <sup>23</sup>
	ν <sub>3</sub>	1456	20	3 <sup>65</sup> , 2 <sup>14</sup> , 10 <sup>6</sup>	2102.6	21	6 <sup>90</sup>
	ν <sub>4</sub>	1435.7	1	9 <sup>85</sup> , 7 <sup>90</sup> , 1 <sup>12</sup>	1420.0	31	22 <sup>65</sup> , 3 <sup>37</sup> , 8 <sup>10</sup> , 10 <sup>4</sup>
	ν <sub>5</sub>	1325	47	8 <sup>95</sup>	1314.5	1	7 <sup>74</sup> , 3 <sup>25</sup> , 2 <sup>21</sup> , 1 <sup>21</sup>
	ν <sub>6</sub>	1107.5	2	8 <sup>77</sup> , 7 <sup>25</sup> , 2 <sup>25</sup>	1029.7	24	9 <sup>84</sup> , 1 <sup>31</sup> , 3 <sup>4</sup> , 2 <sup>1</sup>
	ν <sub>7</sub>	1088.3	≈0	3 <sup>90</sup> , 8 <sup>90</sup> , 2 <sup>10</sup> , 1 <sup>7</sup>	946.6	12	9 <sup>90</sup> , (1-3) <sup>10</sup> , (10/7) <sup>6</sup>
	ν <sub>8</sub>	944	14	1 <sup>91</sup> , 7 <sup>15</sup>	827.3	1	8 <sup>90</sup> , 10 <sup>35</sup> , 7 <sup>13</sup> , 2 <sup>4</sup>
	ν <sub>9</sub>	804.2	≈0	10 <sup>90</sup> , 6 <sup>5</sup>	760	8	7 <sup>71</sup> , 1 <sup>90</sup> , 8 <sup>70</sup> , (3/10) <sup>5</sup>
	ν <sub>10</sub>	1103.1	1	11 <sup>90</sup> , 12 <sup>13</sup>	727.3	1	10 <sup>70</sup> , 8 <sup>25</sup> , 7 <sup>25</sup>
	ν <sub>11</sub>	991.1	1	13 <sup>90</sup> , 14 <sup>24</sup> , 12 <sup>4</sup>	792.1	1	13 <sup>90</sup> , 11 <sup>24</sup> , 14 <sup>12</sup>
B <sub>1</sub>	ν <sub>12</sub>	775.8	1	12 <sup>77</sup> , 11 <sup>14</sup>	580.2	1	12 <sup>67</sup> , 11 <sup>24</sup>
	ν <sub>13</sub>	418.1	1	14 <sup>84</sup> , 13 <sup>37</sup> , 11 <sup>7</sup>	349.7	1	14 <sup>90</sup> , 11 <sup>7</sup>
	ν <sub>14</sub>	2901	9	15 <sup>90</sup>	2146.2	7	15 <sup>90</sup>
	ν <sub>15</sub>	963.3	≈0	17 <sup>90</sup> , 18 <sup>23</sup> , 16 <sup>10</sup>	842.5	≈0	17 <sup>90</sup> , 16 <sup>20</sup> , 18 <sup>14</sup> , 19 <sup>14</sup>
	ν <sub>16</sub>	866.2	10	18 <sup>70</sup> , 16 <sup>27</sup> , 19 <sup>9</sup>	680.2	6	18 <sup>90</sup> , 16 <sup>13</sup> , 19 <sup>7</sup>
B <sub>2</sub>	ν <sub>17</sub>	612	44	(16-19) <sup>25</sup>	458	32	(17,18) <sup>90</sup> , 19 <sup>90</sup> , 16 <sup>17</sup>
	ν <sub>18</sub>	270.1	2	19 <sup>70</sup> , 16 <sup>24</sup>	210.7	1	19 <sup>90</sup> , 16 <sup>29</sup>
	ν <sub>19</sub>	3095.3	11	23 <sup>60</sup> , 22 <sup>39</sup>	2295.9	1	23 <sup>60</sup> , 22 <sup>31</sup>
	ν <sub>20</sub>	3082.5	3	22 <sup>60</sup> , 23 <sup>39</sup>	2276.8	2	22 <sup>60</sup> , 23 <sup>31</sup>
	ν <sub>21</sub>	1423	100	21 <sup>21</sup> , 23 <sup>23</sup> , 24 <sup>8</sup>	1345	100	21 <sup>60</sup> , 25 <sup>10</sup> , (20,27) <sup>4</sup>
	ν <sub>22</sub>	1313	4	20 <sup>29</sup> , 24 <sup>24</sup> , 25 <sup>24</sup>	1204	26	20 <sup>25</sup> , 26 <sup>22</sup> , (25/27) <sup>9</sup>
	ν <sub>23</sub>	1266	12	26 <sup>21</sup> , 24 <sup>23</sup> , 20 <sup>13</sup>	1008.1	2	24 <sup>29</sup> , 25 <sup>24</sup> , 26 <sup>22</sup>
	ν <sub>24</sub>	1071	8	24 <sup>30</sup> , 21 <sup>13</sup> , 25 <sup>22</sup>	812.7	1	27 <sup>21</sup> , 25 <sup>24</sup> , (21/24) <sup>21</sup>
	ν <sub>25</sub>	920	5	20 <sup>20</sup> , 26 <sup>29</sup> , 21 <sup>4</sup>	744.9	3	27 <sup>24</sup> , (24/25) <sup>19</sup> , 20 <sup>13</sup>
	ν <sub>26</sub>	915.0	1	27 <sup>29</sup> , 20 <sup>11</sup> , 24 <sup>8</sup>	707	8	26 <sup>27</sup> , 24 <sup>17</sup> , (20/27) <sup>18</sup>
	ν <sub>27</sub>	4.96	1		5.52	3	

<sup>a</sup> From IR spectra in Figure 2, except where noted. <sup>b</sup> From scaled BLYP/6-31G\* force field (six-parameter model, see text). <sup>c</sup> Relative IR intensity, normalized to most intense peak. <sup>d</sup> Potential energy distribution of normal modes in terms of symmetry coordinates; superscripts denote percentage contribution. <sup>e</sup> From vibrational progression in first PE band (Figure 2). <sup>f</sup> Root-mean-square deviation between observed and calculated frequencies.

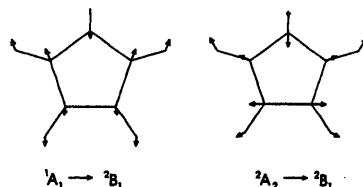


Figure 6. Geometry changes upon excitation into the  $1^2B_1$  state of CP<sup>++</sup> from the neutral ground state ( $1^1A_1$ ) and from the cation ground state ( $1^2A_2$ ), respectively, depicted as deformations in a center-of-mass coordinate systems.

(+8.2 pm) with the double bonds being much less affected (+1.1 pm).<sup>37b</sup> It would therefore be surprising if these two disparate geometry changes would lead to activation of the same fundamental in the  $1^2B_1$  state.

However, the  $a_1$  modes resulting from a CASSCF frequency calculation of the first excited state of CP<sup>++</sup> calculation were too widely spaced to allow an assignment of the vibrational progression in the two spectra in terms of different fundamentals. Thus we conclude that the vibrational progression in the second PE and the first EA bands are caused by the same totally symmetric normal vibration which must be essentially a ring-breathing mode such that it can accommodate increases in the lengths of the double bonds and the essential single bond simultaneously. Ultimately, a proper answer to this question will require a Franck-Condon analysis as it has been done for neutral CP.<sup>38</sup>

Turning to the second excited state of CP<sup>++</sup>, we note from Table 1 that the main geometry change is again in the formal double bonds which are lengthened by 6.4 pm from the cation ground state. However, the significant dependence of the vibrational progression of the second EA band on deuteration

(cf. Figure 2) indicates that some C-H/D wagging motion must be involved in the normal mode which is mainly activated in this excitation. Unfortunately, an attempt to calculate the force constant matrix for the second  $2B_1$  state resulted in a large negative frequency and hence no conclusions could be drawn from that.

#### 4. Conclusions

The electronic and vibrational structure of the radical cation of cyclopentadiene (CP<sup>++</sup>) was investigated by PE, EA, and IR spectroscopy. The results were interpreted on the basis of different ab initio quantum mechanical methods. Thereby the nature of the ionic states of CP<sup>++</sup> was elucidated and compared to that of related butadiene radical cation. Furthermore, a valence force field was obtained by scaling a density functional force field with 25 observed fundamental frequencies of CP<sup>++-h<sub>g</sub></sup> and CP<sup>++-d<sub>g</sub></sup>. On a similar basis, the force field of neutral CP was refined whereby an earlier misassignment was revealed.

A comparison of the diagonal force constants for C-C stretches of CP and CP<sup>++</sup> shows a weakening of the double bonds and the strengthening of the essential single bond, whereas the bonds to the CH<sub>2</sub> group as well as the latter itself are hardly affected. These findings are in accord with the nodal structure of the HOMO from which ionization occurs and complement those observed earlier for related butadiene radical cation.

The vibrational structure in the excited  $1^2B_1$  states of CP<sup>++</sup> is discussed on the basis of CASSCF force fields. Despite the disparate geometry changes upon  $1^1A_1 \rightarrow 1^2B_1$  and  $1^2A_2 \rightarrow 1^2B_1$  excitation, respectively, the same fundamental appears to be active in shaping the Franck-Condon envelope in both cases.

**Acknowledgment.** This work is part of project No. 2028-040398.94 of the Swiss National Science Foundation. We would like to thank Prof. M. Allan for his help with the PE spectra and Prof. E. Haselbach for his support and encouragement.

**Supporting Information Available:** The full force field as well as a table with the resulting frequencies, intensities, and potential energy distributions (PED) (12 pages). Ordering information is given on any current masthead page.

#### References and Notes

- (1) (a) Schomaker, V.; Pauling, L. *J. Am. Chem. Soc.* 1939, 61, 1769. (b) Liebigh, G.; Marsh, R. E. *Acta Crystallogr.* 1965, 19, 202. (c) Damiani, D.; Ferreri, L.; Gallinella, E. *Chem. Phys. Lett.* 1976, 37, 265.
- (2) (a) Scheibe, G.; Grienschen, H. Z. *Phys. Chem.* 1934, 825, 52. (b) Price, W. C.; Walsh, A. D. *Proc. R. Soc. London, Ser. A* 1941, 179, 201. (c) Fickert, W. C.; Paddock, E.; Sackter, E. *J. Am. Chem. Soc.* 1941, 63, 1073. (d) Evans, D. F. *J. Chem. Soc.* 1960, 1735. (e) Frueholz, R. D.; Flicker, W. M.; Mosher, O. A.; Kupperman, A. *J. Chem. Phys.* 1979, 70, 2003. (f) McDiarmid, R.; Sabljic, A.; Doehring, J. P. *Ibid.* 1985, 83, 2147. (g) Sabljic, A.; McDiarmid, R. *Ibid.* 1990, 93, 3850. (h) McDiarmid, R.; Sabljic, A. *J. Phys. Chem.* 1991, 95, 6455. (i) Shang, O.; Hudson, B. S. *Chem. Phys. Lett.* 1991, 183, 63. (j) Sabljic, A.; McDiarmid, R.; Gedanken, A. *Ibid.* 1990, 96, 2442.
- (3) (a) Allinger, N. L.; Miller, M. A. *J. Am. Chem. Soc.* 1964, 86, 2811. (b) Barfield, M. *J. Chem. Phys.* 1967, 47, 3831. (c) Del Bene, J.; Jaffé, H. H. *Ibid.* 1968, 48, 4050. (d) Hayashi, T.; Nakajima, T. *Bull. Soc. Chem. Jpn.* 1975, 48, 980. (e) Nakatsuji, H.; Kitao, O.; Yonezawa, T. *J. Chem. Phys.* 1985, 83, 723. (f) Galasso, V. *Chem. Phys.* 1991, 153, 13. (g) Zgierski, M. Z.; Zerbetto, F. *Chem. Phys. Lett.* 1991, 179, 131. (h) Serrano-Andrés, L.; Merchán, M.; Nebot-Gil, I.; Roos, B. O.; Fülcher, M. *J. Am. Chem. Soc.* 1993, 115, 6184.
- (4) (a) Castellucci, E.; Manzelli, P.; Fortunato, B.; Gallinella, E.; Mirono, F. *Spectrochim. Acta* 1975, 31A, 451 and earlier papers cited therein. (b) Cuff, L.; Kertesz, M. *J. Phys. Chem.* 1994, 98, 12223.
- (5) (a) Derrick, P. J.; Asbrink, L.; Edqvist, O.; Jonsson, B.-O.; Lindholm, E. *Int. J. Mass Spectrom. Ion Phys.* 1971, 6, 203. (b) Derrick, P. J.; Asbrink, O.; Edqvist, O.; Lindholm, E. *Spectrochim. Acta* 1971, 27A, 2525.
- (6) (a) ESR: Shida, T.; Egawa, Y.; Kubodera, H.; Kato, T. *J. Chem. Phys.* 1980, 73, 5963 (see also: Barnabas, M. V.; Trifunac, A. D. *J. Chem. Soc., Chem. Commun.* 1993, 813). (b) EA: Shida, T.; Momoze, T.; Ono, N. *J. Phys. Chem.* 1985, 89, 815 (see also: Shida, T. *Electronic Absorption Spectra of Radical Ions*; Elsevier: Amsterdam, 1988; p 36).
- (7) For a compilation, see: Jacox, M. E. *J. Chem. Ref. Data* 1990, 19, 1387; 1988, 17, 269; 1984, 13, 945.
- (8) (a) Vala, M.; Szczepanski, J.; Pauzat, F.; Parisel, O.; Talbi, D.; Ellinger, Y. *J. Phys. Chem.* 1994, 98, 9187 and earlier papers by the same authors cited therein. (b) Hudgins, D. M.; Allamandola, L. J. *J. Phys. Chem.* 1995, 99, 3033 and earlier papers from the NASA Ames group cited therein. (9) Forney, D.; Jacox, M. E.; Thompson, W. E. *J. Mol. Spectrosc.* 1992, 153, 680.
- (10) Tang, W.; Zhang, X.-L.; Bally, T. *J. Phys. Chem.* 1993, 97, 4373.
- (11) (a) Sun, Q.; Tripathi, G. N. R.; Schuler, R. H. *J. Phys. Chem.* 1990, 94, 6273 and earlier papers from the same group. (b) Kamizuki, T.; Dudev, T.; Hirose, C. *J. Phys. Chem.* 1991, 95, 5845. (c) Buntix, G. Poizat, O. *Laser Chem.* 1990, 10, 333. (d) Oiyama, M.; Okazaki, S. *J. Electroanal. Chem. Interfacial Electrochem.* 1991, 297, 557. (e) Kawashima, H.; Kato, T.; Shida, T. *J. Raman Spectrosc.* 1991, 22, 187; *Chem. Phys. Lett.* 1990, 163, 59. (f) Danzer, G. D.; Golas, J. A.; Strommen, D. P.; Kincald, J. R. *J. Raman Spectrosc.* 1991, 22, 3. (g) Brouwer, A. M.; Langkilde, F. W.; Bsjöer, E.; Wilbrandt, R. *Chem. Phys. Lett.* 1994, 225, 386. Kesztzwey, T.; Wilbrandt, R.; Cave, R. J.; Johnson, J. E. *J. Phys. Chem.* 1994, 98, 5632.
- (12) (a) Müller-Dethlefs, K.; Schlag, E. W. *Annu. Rev. Phys. Chem.* 1991, 42, 109. (b) Takahashi, M.; Kimura, K. *J. Chem. Phys.* 1992, 97, 2920. (c) Lu, K.-T.; Weisshaar, J. C. *J. Chem. Phys.* 1993, 99, 4247 and references therein.
- (13) Pulay, P.; Fogarasi, G.; Pongor, G.; Boggs, J. E.; Vargha, A. *J. Am. Chem. Soc.* 1983, 105, 7073.
- (14) Scherrer, D.; Bally, T., unpublished results (see: Scherrer, D. Ph.D. Dissertation No. 1066, University of Fribourg, Switzerland, 1993).
- (15) Dressler, R.; Neuhäus, L.; Allan, M. *J. Electron Spectrosc. Relat. Phenom.* 1983, 31, 181.
- (16) Frisch, M. J.; Trucks, G. W.; Head-Gordon, M.; Gill, P. M. W.; Wong, M. W.; Foresman, B. B.; Johnson, B. G.; Schlegel, H. B.; Robb, M. A.; Replogle, E. S.; Gomperts, R.; Andres, J. L.; Raghavachari, K.; Binkley, J. S.; Gonzalez, C.; Martin, R. L.; Fox, D. J.; DeFrees, D. J.; Baker, J.; Stewart, J. J. P.; Pople, J. A. Gaussian, Inc.: Pittsburgh, PA, 1992.
- (17) (a) Becke, A. D. *Phys. Rev. A* 1988, 38, 3098. (b) Becke, A. D. *J. Chem. Phys.* 1993, 98, 5648. (c) Lee, C.; Yang, W.; Parr, R. G. *Phys. Rev. B* 1988, 37, 785. (d) For a description of the density functionals as implemented in Gaussian 92, see: Johnson, B. G.; Gill, P. M. W.; Pople, J. A. *J. Chem. Phys.* 1993, 98, 5612.
- (18) Pulay, P.; Fogarasi, G.; Pang, F.; Boggs, J. E. *J. Am. Chem. Soc.* 1979, 101, 2550.
- (19) Note that in the standard SQM force field procedure, off-diagonal elements are scaled by the geometric mean of the constants used for the corresponding diagonal elements, respectively.

## 5.8. INDO/S Study of 2,2-Dimethylisoidene and all-trans-1,3,5,7-Octatetraen

### 5.8.1. Introductory Remarks

In this chapter the paper "Triplet Energy of 2,2-Dimethylisoidene from Electron-Energy-Loss Spectroscopy and Photoinduced Triplet Energy Transfer", published in *Helvetica Chimica Acta* (p. 1541, Vol. 77, 1994), is presented. The paper resulted from a collaboration with the group of Prof. J. Wirz (University of Basel), who studied the lowest triplet state by flash photolysis. The theoretical section of this project was part of the diploma work of S. El houar (1993), which I supervised.

Our contribution concentrated on the theoretical characterization of the lowest excited triplet and singlet state of 2,2-dimethylisoidene. Excitation energies of lowest valence-excited states of 2,2-dimethylisoidene and all-trans-1,3,5,7-octatetraen, which served as a reference compound, were calculated with the INDO/S method. All single excitations were included in the CI space and the triplet parametrisation was used for the triplet states. The results were compared to the previously measured EEL spectra and analyzed, especially with respect to the biradicaloid character of 2,2-dimethylisoidene and the applicability and limitations of the "SDT-rule" (Forster *et al.* 1980).

### 5.8.2. Publication

(see next page)

Separatum

HELVETICA CHIMICA ACTA - Vol. 77 (1994)

1541

### 138. Triplet Energy of 2,2-Dimethylisoidene from Electron-Energy-Loss Spectroscopy and Photoinduced Triplet Energy Transfer

by Michael Allan\*, Knut R. Asmis, Sarah El houar, and Edwin Haselbach

Institut de Chimie Physique de l'Université de Fribourg, Pérolles, CH-1700 Fribourg

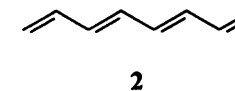
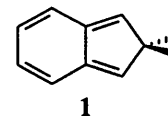
and Marco Capponi, Bernhard Urwyler, and Jakob Wirz\*

Institut für Physikalische Chemie der Universität Basel, Klingelbergstrasse 80, CH-4056 Basel

(8.VI.94)

The excited electronic states of 2,2-dimethylisoidene (**1**) have been studied by electron-energy-loss spectroscopy. Its vertical gas-phase triplet ( $1^3B_2$ ) and singlet ( $1^1B_2$ ) excitation energies are 1.61 and 3.19 eV, respectively. The excited states are thus lowered by 0.49 eV and 1.21 eV, respectively, when compared to the corresponding states of (all-*E*)-octatetraene, which serves as a reference compound. These shifts are partially reproduced by ZINDO calculations. The spectra give no evidence for a  $2^1A_g$  state below the  $1^1B_2$  state, but this lack of observation does not exclude its existence. The lowest triplet state  $T_1(1)$  was further characterized by flash photolysis.  $T_1(1)$  was observed as a transient intermediate,  $\lambda \leq 350$  nm, with a lifetime of 8  $\mu$ s in degassed hexane. The adiabatic excitation energy of  $T_1(1)$  was bracketed to the range of  $1.1 \pm 0.1$  eV by energy-transfer experiments. Relationships between the energies of the lowest excited singlet and triplet states of **1** and the lowest excited doublet state of its radical cation  $1^{\cdot+}$  - essentially a non-Koopmans' state - are discussed.

**Introduction.** - The title compound 2,2-dimethylisoidene (**1**) contains, from a spectroscopic point of view, a nearly unperturbed *o*-xylylene chromophore, but is much more stable than the parent compound because of steric hindrance towards dimerization [1]. It thus permits a convenient study of the electronic structure of this chromophore and its comparison with (all-*E*)-octatetraene (**2**). The  $\pi$ -system of both compounds consists of four conjugated C=C bonds, but already the HMO model indicates that the additional link in **1** results in a reduced HOMO-LUMO gap ( $0.59\beta$  for **1**,  $0.69\beta$  for **2**). Thus, **1** is an example of a molecule having relatively small, unconventional chromophore with low-lying excited states [2].



In accordance with expectation, the absorption spectrum of **1** in 3-methylpentane glass at 77 K revealed a comparatively low-lying transition with origin at *ca.* 2.9 eV [1], corresponding essentially to a HOMO→LUMO excitation from SCF-CI calculations, and giving **1** its canary yellow color. The origin of the first absorption band of the radical cation  $1^{\cdot+}$  (in 3-methylpentane glass at 77 K) lies at 1.60 eV [3]. The lack of a corresponding transition in the photoelectron spectrum of **1** and comparison with the results of

calculations revealed the unusual fact that already the *first* excited doublet state of  $D_1(1^+)$  is of non-Koopmans' nature, i.e., that this state is not well described by one of the electron configurations obtained by removing an electron from the closed-shell ground configuration of **1** [3] [4].

The present work complements existing data on the electronic states of **1**. We report triplet and singlet excitation energies in the gas phase, determined by electron-energy-loss (EEL) spectroscopy, as well as the energy, lifetime, and the absorption of the lowest triplet state of **1** in solution, determined by flash photolysis.

**Experimental.** - The trochoidal electron spectrometer used in the present work has been described in detail in [5]. It uses magnetically focussed trochoidal monochromators as electron-energy filters, instead of the more conventional cylindrical or hemispherical condensers, and a collision chamber with only small apertures for the incident and scattered electron beams instead of a gas nozzle. This construction results in high sensitivity and small sample consumption, an imperative prerequisite for recording a spectrum with a small amount of sample (ca. 20 mg). The experiment involves bombarding the sample vapor at low pressure (ca.  $10^{-4}$  mbar) with a beam of electrons of varying incident energy  $E_i$  and detecting electrons scattered at a fixed residual energy  $E_r$ . The incident electrons can collisionally excite the target molecules, thereby losing an amount of kinetic energy  $\Delta E = E_i - E_r$  equal to the excitation energy. A spectrum of excited states is obtained by plotting the scattered electron  $I_s$  current against the electron loss  $\Delta E$ . The collision chamber was kept at ca.  $100^\circ$  during the measurement, the resolution was ca. 0.045 eV, and the energy scale is accurate to within 0.03 eV.

Flash photolysis was accomplished by excitation with either an electric discharge flashlamp (1000-J electric energy, 20- $\mu$ s pulse width at half height) or frequency-doubled (20 ns, 530 nm, 200 mJ) or triplet (20 ns, 353 nm, 50 mJ) pulses from a Nd glass laser. The spectrographic and kinetic detection systems and the software for transient kinetic analysis have been described in [6].

2,2-Dimethylisoidene (**1**) was synthesized by debromination of 1,3-dibromo-2,2-dimethylindane (**3**) with lithium amalgam as described by *Dolhier et al.* [1]. The following procedural details were found to be important to achieve satisfactory results. Li (0.1 g) was cut and rolled under dry pentane and added to 20 g of Hg under Ar. The supernatant solvent was then evaporated and the reaction vessel evacuated. All subsequent operations were done under vacuum ( $< 1$  Pa). Formation of the amalgam from the heterogeneous mixture was accelerated by ultrasonic treatment. After 40 min, a degassed soln. of **3** (0.5 g) in 5 ml of dry pentane was slowly added to the amalgam, and the mixture was stirred at r.t. After 15 min, the solvent and the yellow product were evaporated at r.t. and recondensed. Markedly improved yields were obtained, when the dark grey residue was then extracted repeatedly by addition of degassed pentane (10 ml), ultrasonic treatment for 10 min, and evaporation until the supernatant solvent remained colorless (5-10 extractions). The combined extracts were slowly freed from the solvent at  $-55^\circ$ . The residue contained, in addition to yellow **1**, an unknown volatile grey material, possibly Hg. Separation of **1** from this material was achieved by repeated sublimation at  $-20^\circ$ . The purified solid product **1** (71 mg, 30% yield) could be stored indefinitely under vacuum at  $-70^\circ$ . Solid **1** should be handled at temperatures below  $0^\circ$  to avoid decomposition.

Isoidene **1** reacts instantly with 4-phenyl-3H-1,2,4-triazoline-3,5-dione (NPTD) to give the expected *Diels-Alder* adduct. M.p.: 163-164°.  $^1\text{H-NMR}$  ( $\text{CDCl}_3$ , TMS): 0.90 (s, 3 H); 1.60 (s, 3 H); 4.90 (s, 2 H); 6.75-6.85 (m, 2 H); 7.2-7.5 (m, 7 H). MS: 319 ( $M^+$ ). This reaction was used to determine the extinction coefficient of **1** in benzene soln. The extinction coefficient of a fresh sample of NPTD (*Fluka, purum*,  $> 98\%$ ) in dry benzene was determined as  $\epsilon(\lambda_{\text{max}} = 540 \text{ nm}) = 222 \pm 5 \text{ M}^{-1} \text{ cm}^{-1}$ . A weighted, ca. twofold excess of NPTD was added to a soln. of **1** (ca.  $10^{-3} \text{ M}$ ) in benzene (10 ml) the extinction of which at 400 nm had been measured with a 1-mm cell. The yellow color of **1** was rapidly quenched upon dissolution of NPTD, and subsequently the red color of NPTD developed. The extinction of excess NPTD was then measured at 540 nm and used to calculate the amount of reacted NPTD. Three such determinations gave  $\epsilon(1, 400 \text{ nm}) = 3060 \pm 200 \text{ M}^{-1} \text{ cm}^{-1}$ . As a test of this procedure, known amounts of tetracene were 'titrated' in the same way. Single measurements were accurate to within  $\pm 10\%$ .

**Results.** - *EEL Spectroscopy.* Energy-loss spectra were recorded at several residual energies and a representative spectrum is shown in Fig. 1. It was recorded at low residual energy and thus shows both triplet and singlet electronically excited states [5]. The more intense band, peaking at 3.19 eV, persists even at higher residual energies and must correspond to the singlet excited state  $1^1\text{B}_2$ . The lowest vibrational level appears at

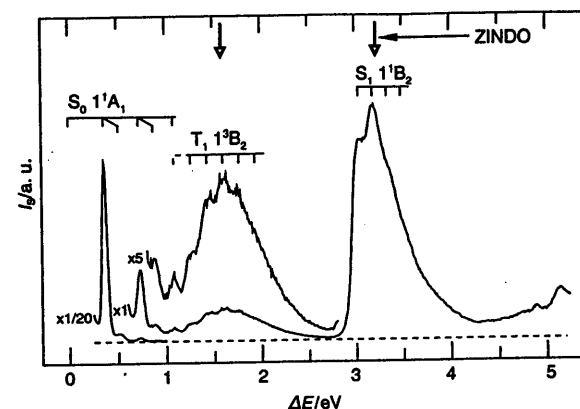


Fig. 1. Electron-energy-loss spectrum of 2,2-dimethylisoidene (**1**), that is plot of the scattered electron current  $I_s$  (in arbitrary units) vs. the electron-energy loss  $\Delta E$ , recorded with a residual energy of 3.5 eV. Results of ZINDO calculations are indicated by vertical arrows.

3.04 eV, in agreement with the matrix absorption value of 2.85 eV [1], if allowance is made for a bathochromic shift of 0.19 eV in the matrix. The spectra show no evidence for another singlet excited state below the  $1^1\text{B}_2$  state, although a  $2^1\text{A}_1$  state could be the lowest excited singlet state of **1**, analogous to the  $2^1\text{A}_1$  state of (all-*E*)-octatetraene reported in [7]. Our earlier EEL measurements of **2** failed to disclose this state [8], and we, therefore, cannot exclude a similar failure in the case of **1**. Nevertheless, we shall henceforth use the symbol  $S_1$  to denote the  $1^1\text{B}_2$  state at 3.19 eV.

The broader band, peaking at 1.61 eV, becomes less intense at higher residual energies, indicating that it corresponds to the lowest triplet state  $1^3\text{B}_2$  of **1**. Its vibrational structure with a spacing of ca. 0.15 eV ( $1200 \pm 150 \text{ cm}^{-1}$ ) is consistent with the excitation of a C=C stretching vibration, as would be expected for a  $\pi-\pi^*$  excitation. The observed transition energies are given in Table 1.

Table 1. Experimental (band maxima in eV  $\pm 0.03$  eV) and Calculated (ZINDO) Energies for the Lowest Triplet  $T_1$  ( $1^3\text{B}_2$  and  $1^3\text{B}_1$ ) and the Singlet  $S_1$  ( $1^1\text{B}_2$  and  $1^1\text{B}_1$ ) States of **1** (this work) and **2** ([8])

Compound	$E(T_1)$		$E(S_1)$		$E(S_1) - E(T_1)$	
	exp.	calc.	exp.	calc.	exp.	calc.
(all- <i>E</i> )-Octatetraene ( <b>2</b> )	2.10	2.15	4.40	3.91	2.30	1.76
2,2-Dimethylisoidene ( <b>1</b> )	1.61	1.59	3.19	3.23	1.58	1.62

The signal below 1 eV is due to excitation of high vibrational levels of the electronic ground state of **1**, with C-H and C=C stretching vibrations being active. Unfortunately, these peaks partially overlap with the triplet band, making it impossible to localize with certainty its origin, i.e., the adiabatic triplet energy. Either 1.08 eV or 1.26 eV are possible values.

**Flash Photolysis.** Flash photolysis of a  $5 \times 10^{-4}$  M solution of **1** in degassed hexane with a 20-ns laser pulse at 353 nm (3.51 eV) gave rise to transient bleaching of the absorption of **1** in the range of 360–440 nm (2.82–3.44 eV), and transient absorption at shorter wavelengths,  $\lambda \leq 350$  nm ( $\geq 3.87$  eV). No absorption changes were detected above 440 nm ( $\leq 2.82$  eV). Part of the transient bleaching and all of the transient absorption decayed by first-order kinetics with a rate of  $1.3 \times 10^5$  s $^{-1}$ . The energy-transfer experiments described below clearly identify this transient intermediate as the lowest triplet state of **1**.

Flash photolysis of polycyclic aromatic hydrocarbons produces well-known, characteristic triplet-triplet absorptions in the visible region [9]. The decay rate of these transient absorptions was accelerated in the presence of **1**, indicating triplet-energy transfer to occur from the aromatic hydrocarbons to **1**. For reasons of solubility, benzene was used as a solvent in all experiments. The energy transfer rate,  $k_{et}$ , was calculated by comparison of the observed decay rates of the aromatic hydrocarbon triplets in the presence,  $k_{obs}^0$ , and absence,  $k_{obs}^q$ , of quencher **1**:  $k_{et}[Q] = k_{obs}^q - k_{obs}^0$ .

Decay kinetics of the transient aromatic triplets in the absence of quencher **1** usually contained a second-order contribution due to triplet-triplet annihilation. To avoid this complication, a sufficient amount of **1** was always added such that the observed decay was cleanly-first-order due to dominant decay by the energy-transfer process. Under these circumstances the ill-defined contribution  $k_{obs}^0$  was negligible, i.e.,  $k_{et}[Q] \approx k_{obs}^q$ . The reactivity of **1** did not allow determination of its amount by weighing. The quencher was thus added from a stock solution of known extinction, and the concentration [Q] was calculated using the extinction coefficient  $\epsilon(1, 400 \text{ nm}) = 3060 \pm 200 \text{ M}^{-1}\text{cm}^{-1}$  (see *Experimental*). This value is in agreement with previous estimates for the extinction coefficient of *o*-xylylene [10].

The energy-transfer rate constants thus determined were in the range expected [11] for exothermic triplet-energy transfer,  $\log(k_{et}/\text{s}^{-1}) = 9.5 \pm 0.2$ , except for the sensitizers with the lowest triplet energy (Table 2). The triplet energies of the top five aromatic hydrocar-

Table 2. Rate Constants for Triplet-Energy Transfer between Various Benzenoid Aromatic Hydrocarbon Donors and **1** in Degassed Benzene at Ambient Temperature ( $23 \pm 2^\circ$ )

Sensitizer	$\log(k_{et}/\text{s}^{-1})^a$	$E(T_1)/\text{eV}^b$	$\lambda_{obs}/\text{nm}^c$	$\lambda_{exc}/\text{nm}^d$
Dibenz[ <i>a,h</i> ]anthracene	9.5	2.27	580	conv.
Benz[ <i>a</i> ]anthracene	9.3	2.05	485	conv.
Anthracene	9.5	1.85	420	conv.
Dibenzo[ <i>a,l</i> ]pyrene	9.7	1.75	490	conv./353
Tetracene	9.4	1.28	485	conv.
Violanthrene	9.4	1.20	550	conv.
Isoviolanthrene	9.1	1.10	625	530
Dibenzo[ <i>a,l</i> ]pentacene	9.1	1.06	545	530
Benzo[ <i>a</i> ]pentacene	6.8	0.95	520	530
Pentacene	< 6.5	0.86	500	530

<sup>a</sup>) Average energy-transfer rate constants from ca. 10 individual measurements. In most cases, 2–3 different solutions were prepared independently. Standard error  $\pm 0.1$  log units.

<sup>b</sup>) Triplet energies; sources are given in the text.

<sup>c</sup>) Wavelengths of maximum triplet-triplet absorption used for observation of triplet decay rates.

<sup>d</sup>) Excitation source: 'conv.' indicates conventional electric discharge, numbers indicate laser wavelengths.

bons [12] listed in Table 2 and of pentacene [13] are known accurately. The triplet energies of violanthrene, isoviolanthrene, dibenzo[*a,l*]pentacene, and benzo[*a*]pentacene were estimated by empirical correlation with the energies of the  $^1L_a$  band (0–0 transition) in benzene solution (Fig. 2). Such an interpolation should yield values accurate to  $\pm 0.04$  eV due to the structural similarity of all compounds considered. As predicted by the correlation, the triplet-state energies of isoviolanthrene and dibenzo[*a,l*]pentacene are very similar: both triplet states co-exist in equilibrium in solutions containing both compounds at similar concentrations, and energy transfer can be observed directions by flash photolysis. The relative ordering of the triplet energies of the last three entries in Table 2 was verified by the observation of 'irreversible' energy between neighboring pairs.

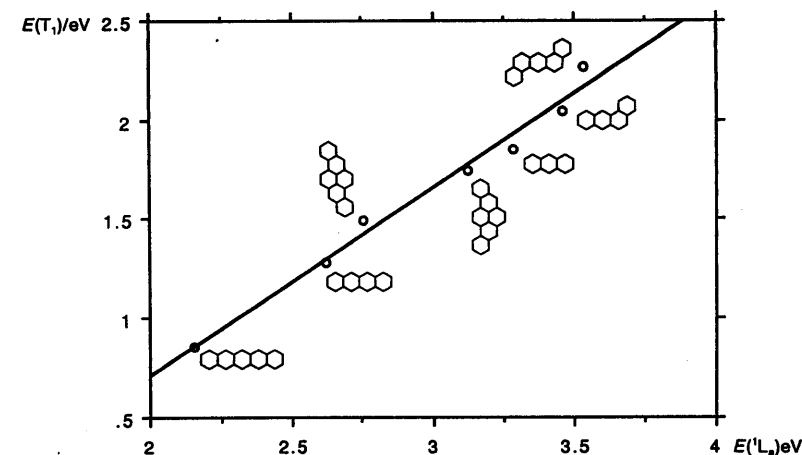


Fig. 2. Correlation between 0–0 energies of the  $^1L_a$  bands ( $E(^1L_a)$ ) of polycyclic aromatic hydrocarbons in benzene solution and the energies of their lowest triplet state,  $E(T_1)$ . The slope and intercept of the linear regression line are  $0.95 \pm 0.06$  and  $(-1.18 \pm 0.18)$  eV, respectively. This linear relation was used to calculate the triplet energies of violanthrene, isoviolanthrene, dibenzo[*a,l*]pentacene, and benzo[*a*]pentacene given in Table 2.

Balzani *et al.* have developed a simple model function for the dependence of energy-transfer rates in fluid solution on the spectroscopic energy difference between donor and acceptor [11]. Balzani's function (Eqn. 29 in [11]) was adjusted to the measured values of  $k_{et}$  (Table 2, excluding pentacene) by nonlinear least-squares fitting. The solid line drawn in Fig. 3 is the best fit obtained with the following values for the two adjustable parameters: Energy of  $T_1(1)$  equal to  $1.10 \pm 0.01$  eV,  $k_{et}^0 = (0.91 \pm 0.24) \times 10^{10}$  s $^{-1}$ . The parameters  $k_d = 1 \times 10^{10}$  M $^{-1}$  s $^{-1}$  and  $k_{-d} = 1.2 \times 10^{10}$  s $^{-1}$  (benzene), and  $\Delta G^*(0) = 0.062$  eV for polycyclic arenes were taken from [11] and held constant. (The reader is referred to [11] for the definition of these parameters.)

The last entry of Table 2 shows that energy transfer from triplet pentacene to **1** is immeasurably slow, indicating that this process is endothermic. We, therefore, sought evidence for the reverse process, i.e., energy transfer from triplet **1** to pentacene. To this

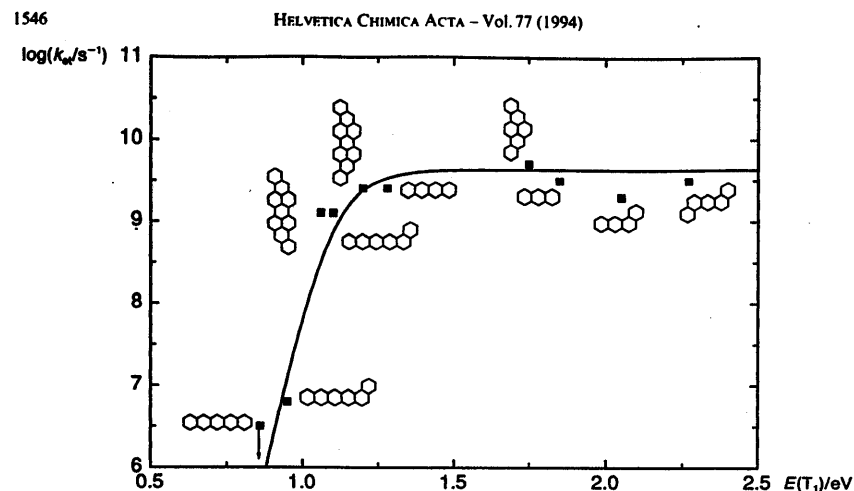


Fig. 3. Correlation of triplet energies,  $E(T_1)$ , of polycyclic aromatic hydrocarbon sensitizers with observed rate constants,  $k_{et}$ , of triplet-energy transfer to isoidene. The solid line is the best fit of Balzani's function (Eqn. 29 in [11]) to the experimental data. Fitting parameters are given in the text. The point shown for pentacene is an upper limit and was not included in the fitting procedure.

end, we used a degassed benzene solution containing benzophenone ( $5 \times 10^{-3} \text{ M}$ ), **1** ( $7 \times 10^{-4} \text{ M}$ ), and pentacene ( $1.6 \times 10^{-5} \text{ M}$ ). Under these conditions, most of the exciting light at 353 nm was absorbed by benzophenone. The transient absorbance waveform at 500 nm showed a rapid rise during the laser pulse. The initial absorbance then decayed to about half of its intensity with a rate of  $ca. 3 \times 10^6 \text{ s}^{-1}$  but subsequently rose again to nearly its original intensity with a rate of  $ca. 1.5 \times 10^5 \text{ s}^{-1}$ , before it finally decayed on a much longer time scale. In the absence of **1**, the intermediate rise was not observed, and the slow decay was much weaker. In the absence of pentacene, the initial absorbance decayed completely with a first-order rate of  $3 \times 10^6 \text{ s}^{-1}$ . The latter solution, when monitored at 320 nm, showed a biexponential decay curve with rates of  $3 \times 10^6 \text{ s}^{-1}$  and  $1.1 \times 10^5 \text{ s}^{-1}$ . These experiments clearly show that **1** serves as a triplet-energy relay between benzophenone and pentacene: The initial rise in absorbance is due to the immediate formation of triplet benzophenone ( $\lambda_{\text{max}} = 530 \text{ nm}$ ) and a small amount of triplet pentacene through direct excitation. Triplet benzophenone is quenched predominantly by **1** whose concentration exceeds that of pentacene by a factor of forty. Hence, the time-resolved rise in absorbance observed between 1 and 5  $\mu\text{s}$  after the laser pulse may be attributed to energy transfer from triplet **1** (which does not absorb at the observation wavelength of 500 nm) to pentacene. The rate of this rise is close to the decay rate of triplet **1** in the absence of pentacene, since the concentration of pentacene ( $1.6 \times 10^{-5} \text{ M}$ ) was too low to reduce the lifetime of **1** substantially. Despite its low efficiency, energy transfer from triplet **1** to pentacene is easily detected by the intermediate rise in absorbance at 500 nm thanks to the extremely high extinction coefficient of triplet pentacene. The final slow decay corresponds to the decay of triplet pentacene. Similar results were obtained with a mixture containing fluorenone, **1**, and pentacene.

**Discussion.** – The data compiled in Table 1 illustrate the effect of the additional link in the *o*-xylylene chromophore (in comparison with a linear tetraene) by comparing the energies of triplet and singlet states originating from HOMO-LUMO excitation in **1** and **2**. A lowering of the excited state energies as well as a reduction of the triplet/singlet ( $T_1/S_1$ ) splitting are observed experimentally. ZINDO calculation [14] including all singly excited configurations in the CI expansion were performed for the  $S_1$  and  $T_1$  states of **1** and **2**. (The energies of the  $T_1$  states were taken as the difference of the  $S_0$  and  $T_1$  total energies.) We note from Table 1 a satisfactory agreement between theory and experiment except for  $S_1(2)$ , the energy of which is considerably underestimated.

Molecules with very small HOMO-LUMO gaps have triplet ground states and are diradicals. Molecules with somewhat larger HOMO-LUMO gaps have the normal excited state ordering, that is a singlet ground state, but some of the diradical-like properties remain conserved and they may, therefore, be called diradicaloids (*cf. e.g.* [2] for a discussion of this topic). The question arises whether the reduced HOMO-LUMO gap makes **1** a diradicaloid. It has been proposed that this term should be applied to molecules with a lowest triplet state of less than 100 kJ/mol (*ca.* 1 eV) above  $S_0$  [15], hence **1** approaches, but does not quite reach this limit.

The first intense triplet absorption band observed in the flash photolysis experiment of **1** lies to the blue of the first ground-state absorption band, like those of the extended linear acenes. This finding agrees well with predictions for the triplet-triplet absorption spectrum of *o*-xylylene calculated by a semiempirical PPP SCF CI model [16]. The parity-forbidden  $T_1(1^3B_2) \rightarrow T_2(2^3B_2)$  transition is calculated to lie at 2.4 eV (515 nm). This energy would cause the  $T_2$  state to be hidden under the high-energy tail of the  $S_1$  band in the spectrum of Fig. 1, where it cannot be identified as a separate peak. The first transition of oscillator strength ( $f = 0.25$ ) is  $T_1(1^3B_2) \rightarrow T_3(3^3B_2)$  at 4.2 eV (293 nm), in agreement with the experimental absorption observed for **1** ( $\lambda \leq 350 \text{ nm}$ ).

The rates of triplet energy transfer from various sensitizers to **1** given in Table 2, and the observation of triplet energy transfer from **1** to pentacene prove that the adiabatic triplet energy of **1** is lower than that of violanthrene (1.2 eV), higher than that of pentacene (0.86 eV), and very close to those of isoviolanthrene and dibenzo[*a,l*]pentacene (both 1.1 eV). In view of the uncertainty in the triplet energies of the reference compounds, we propose an energy of  $T_1(1)$  to be  $1.1 \pm 0.1 \text{ eV}$ . Although the energy-transfer experiments were done with benzene solutions, the triplet energies of the reference compounds were determined in apolar rigid glassy matrices at 77 K. Therefore, the above value refers to these conditions. The solvent shift is thus expected to be small, allowing comparison with the gas phase EEL value of 1.08 eV.

Ten years ago, Kumar *et al.* have proposed the value of  $1.0 \pm 0.1 \text{ eV}$  as an estimate of the triplet energy of non-bridged *o*-xylylenes and of the enols of 2-methylbenzaldehyde and 2-methylacetophenone, based on the observation of triplet energy transfer from the enol triplets to  $\beta$ -carotene [17]. We have previously shown [18] that these triplets decay to a mixture of (*Z*)- and (*E*)-isomers of the ground-state enols, although they must have been generated initially as the (*Z*)-isomers. Calculations had suggested that the relaxed geometries of these enol triplets were essentially coplanar, but experimental evidence was put forward that equilibrium between the (*Z*)- and (*E*)-conformers was reached within 100 ns in the triplet state [18]. The fact that the triplet energy of the bridged compound **1**

1548

HELVETICA CHIMICA ACTA - Vol. 77 (1994)

is quite similar to those of the non-bridged enols indicates that rotation of one of the two methylene groups *does not* substantially stabilize the triplet state of *o*-xylylenes.

A simple approximate relation has been proposed for the singlet and triplet energies ( $E(S_1)$  and  $E(T_1)$ ) of a neutral molecule and the doublet energy  $E(D_1)$  of its radical cation, provided all three transitions correspond to the HOMO-LUMO promotion, and that further conditions are met (the 'SDT rule' [3]). The relation states that  $D_1$  should lie between  $T_1$  and  $S_1$  or, quantitatively,  $E(D_1) = [E(T_1) \times E(S_1)]^{1/2}$ . While this relation has been remarkably well satisfied in the case of stilbene systems [19] a systematic study of benzenoid hydrocarbons indicated that predictions of  $D_1$  are on the average too low by ca. 0.35 eV [20]. Applying the above relation yields  $E(D_1) = 2.26$  eV for isolated  $1^+$  using the energies of  $T_1(1)$  and  $S_1(1)$  from Table 1. The experimental vertical value in the gas phase can be estimated as  $E(D_1) = 1.9$  eV from the center of gravity of the double-peaked band in the matrix spectrum of  $1^+$  at ca. 1.7 eV [3] and allowing for a matrix shift of ca. 0.2 eV. Hence,  $E(T_1) < E(D_1) < E(S_1)$  is satisfied, but there is a quantitative disagreement with theory by about the amount established in [20], indicating that a deviation of this magnitude may generally be expected as a consequence of the assumptions underlying the 'SDT-rule' [3].

This work is part of projects 20-34071.92 (M.A. and E.H.) and 20-34094.92 (J.W.) of the Schweizerischer Nationalfonds zur Förderung der wissenschaftlichen Forschung.

## REFERENCES

- [1] W. R. Dolbier, Jr., K. Matsui, H. J. Dewey, D. V. Horák, J. Michl, *J. Am. Chem. Soc.* **1979**, *101*, 2136.
- [2] J. Fabian, R. Zahradnik, *Angew. Chem.* **1989**, *101*, 693.
- [3] P. Forster, R. Gschwind, E. Haselbach, U. Klemm, J. Wirz, *Nouv. J. Chim.* **1980**, *4*, 365.
- [4] R. Schulz, A. Schweig, W. Zittlau, *J. Am. Chem. Soc.* **1983**, *105*, 2980.
- [5] M. Allan, *J. Electron Spectrosc. Relat. Phenom.* **1989**, *48*, 219.
- [6] E. Hasler, A. Hörmann, G. Persy, H. Platsch, J. Wirz, *J. Am. Chem. Soc.* **1993**, *115*, 5400. S. Gerber, J. Wirz, *EPA Newslett.* **1989**, *36*, 19.
- [7] H. Petek, A. J. Bell, Y. S. Choi, K. Yoshihara, B. A. Tounge, R. L. Christensen, *J. Chem. Phys.* **1993**, *98*, 3777.
- [8] M. Allan, L. Neuhaus, E. Haselbach, *Helv. Chim. Acta* **1984**, *67*, 1776.
- [9] H. Labhart, H. Heinzelmann, in 'Organic Molecular Photophysics', Ed. J. B. Birks, Wiley, New York, 1973, Vol. 1.
- [10] J. Michl, C. R. Flynn, *J. Am. Chem. Soc.* **1973**, *95*, 5802; W. S. Trahanovsky, J. R. Macias, *ibid.* **1986**, *108*, 6820.
- [11] V. Balzani, F. Bolletta, F. Scandola, *J. Am. Chem. Soc.* **1980**, *102*, 2152.
- [12] J. B. Birks, 'Photophysics of Aromatic Molecules', Wiley, New York, 1970; S. P. McGlynn, T. Azumi, H. Kinoshita, 'Molecular Spectroscopy of the Triplet State', Prentice-Hall, Englewood Cliffs, 1969.
- [13] J. Burgos, M. Pope, Ch. E. Swenberg, R. R. Alfano, *Phys. Status Solid. B* **1977**, *83*, 249.
- [14] A. D. Bacon, M. C. Zerner, *Theor. Chim. Acta* **1979**, *53*, 21; W. D. Edward, M. C. Zerner, *ibid.* **1987**, *72*, 347.
- [15] J. Wirz, *Pure Appl. Chem.* **1984**, *56*, 1289.
- [16] M. Gisin, J. Wirz, *Helv. Chim. Acta* **1983**, *66*, 1556.
- [17] C. V. Kumar, S. K. Chattopadhyay, P. K. Das, *J. Am. Chem. Soc.* **1983**, *105*, 5143.
- [18] R. Haag, J. Wirz, P. J. Wagner, *Helv. Chim. Acta* **1977**, *60*, 2595.
- [19] E. Haselbach, U. Klemm, R. Gschwind, T. Bally, L. Chassot, S. Nitsche, *Helv. Chim. Acta* **1982**, *65*, 2464.
- [20] Z. H. Khan, M. M. Hussain, E. Haselbach, *Appl. Spectrosc.* **1993**, *47*, 2140.

## 6. SUMMARY

The construction and development of an instrument to measure electrons scattered inelastically into an angle of  $0^\circ$  and  $180^\circ$  is described. The instrument enables us to measure differential cross section (DCS) ratios for  $0^\circ$  and  $180^\circ$  as well as excitation functions at either  $0^\circ$  or  $180^\circ$ . In combination with the electrostatic instrument available in Fribourg we can thus measure absolute inelastic differential cross sections at  $180^\circ$ . The performance of the instrument was tested on the resonant vibrational excitation of  $N_2$ , after which it was applied to the studies of helium, ethylene and fulvene.

In helium the  $0^\circ$  and  $180^\circ$  DCSs for near-threshold excitation and ionization were measured. In the case of the absolute DCSs discrepancies between experiment and theory exceeding the error limits are found only for the triplet states at  $180^\circ$  and to a lesser degree at  $0^\circ$ . Furthermore, we found that the near-threshold ionization continuum of helium does not provide a suitable standard for the determination of the instrumental response at either small or large scattering angles, by showing that the distribution of the secondary electrons is then no longer uniform. This result will provide important input for further theoretical developments of the currently much studied problem of two simultaneously departing electrons.

In ethylene the excitation of the lowest triplet state was studied. The novel instrument yielded DCS at  $0^\circ$  and  $180^\circ$  which permitted, for the first time, a comprehensive test of the pioneering Schwinger-Multichannel calculations of McKoy and Winstead (1993) on a relatively large molecule. The calculation is found to reproduce correctly important qualitative features, for example the strongly backward-peaked behavior of the DCS at higher incident energies, but the calculated resonance energies are up to 3 eV too high and the DCSs are calculated too large by a factor of two. This indicates the need for further development of the theory of electron scattering on polyatomic molecules.

Triplet and singlet excited states of fulvene and 6,6'-dimethylfulvene were studied in the gas phase by electron energy-loss spectroscopy. With the aid of  $0^\circ$  and  $180^\circ$  EEL spectra two valence triplet states were observed for each molecule. To support the assignments multi-configurational second-order perturbation calculations (CASSCF/CASPT2) were performed. The calculated energies of the first two valence triplet and singlet transitions are within 0.19 eV of the experiment.

Evidence for a selective decay of two-particle-one-hole resonances in butadiene, cyclopentadiene, pyrrole, furan and thiophene was found in the excitation functions of the two lowest triplet states of each of these molecules and interpreted on the basis of semiempirical configuration interaction calculations.



Dissociative attachment spectra of ozone were measured. The study presents experimental evidence for a scattering process which is intermediate between inelastic electron scattering and dissociative attachment, yielding detailed information of the product anion state distribution.

Other projects comprised the resolution and performance improvement of the photoelectron spectrometer and a semiempirical study of the lowest excited states of indene.

## 7. APPENDIX

### 7.1. True-Spin States for The Three-Electron Systems

Quantum chemical programs in general make use of a spin-free formulation, which can cause some confusion to the inexperienced user. In contrast to the two-electron system, the total electronic wave functions of the three-electron system cannot be factored into a spatial part and a spin part. In such a case it is necessary to take the spin functions into account in setting up the total wave function in order to obtain a spatial function of the correct symmetry. Once this is done, it is always possible to set up an expression for any spin-free operator, which does not involve the spin functions (Matsen 1964).

This issue can be formulated as follows: How many spectroscopic states, *i.e.* true-spin states, are generated, when three electrons are distributed in all permissible ways among three non-degenerate space orbitals? A summary of a general solution pathway will be given here. The interested reader is referred to the detailed discussion by Pilar (1968).

The number of unique electron configurations  $C$  generated by distributing  $N$  electrons in  $L$  spinorbitals is given by

$$C = \frac{L!}{N!(L-N)!} \quad (7-1)$$

Each configuration can be written mathematically as an antisymmetrized wave function (Slater determinant)  $\Phi$ .

$$\Phi = \frac{1}{\sqrt{N!}} \begin{vmatrix} S_1(1) & S_2(1) & \cdots & S_N(1) \\ S_1(2) & S_2(2) & \cdots & S_N(2) \\ \vdots & \vdots & \ddots & \vdots \\ S_1(N) & S_2(N) & \cdots & S_N(N) \end{vmatrix} = |S_1 S_2 \cdots S_N| \quad (7-2)$$

The shorthand notation on the right is generally used and corresponds to the antisymmetrized (and normalized) form of an electron configuration of  $N$  electrons, in which the first electron occupies the spinorbital  $S_1$ , the second spinorbital  $S_2$ , *etc.*. The spinorbital  $S(i)$  of the  $i^{\text{th}}$  electron is given by the product of a space orbital  $\varphi(i)$  and a spin function  $\alpha(i)$  or  $\beta(i)$ , abbreviated either by  $\lambda(i)$  or  $\bar{\lambda}(i)$ :



$$S(i) = \begin{cases} \lambda(i) = \varphi(i)\alpha(i) \\ \bar{\lambda}(i) = \varphi(i)\beta(i) \end{cases} \quad (7-3)$$

Since we are concerned with true-spin states, *i.e.* states which are characterized by a definite relative alignment of the electron spins, the appropriate wave functions are chosen such that they are eigenfunctions of the  $S^2$  and  $S_z$  operator.

$$S^2\Psi = \left[ \sum_P \mathbf{P}_{\alpha\beta} + \frac{1}{4} \left[ (n_\alpha - n_\beta)^2 + 2n_\alpha + 2n_\beta \right] \right] \Psi = S(S+1)\Psi \quad (7-4)$$

$$S_z\Psi = \frac{1}{2}(n_\alpha - n_\beta)\Psi = S_z\Psi \quad (7-5)$$

Here  $n$  gives the total number of electrons with  $\alpha$  or  $\beta$  spin respectively.  $\mathbf{P}_{\alpha\beta}$  is an operator which exchanges  $\alpha$  and  $\beta$  functions in the original wave function, with the sum taken over all possible interchanges.

Slater determinants are automatically eigenfunctions of the  $S_z$  operator, but *not necessarily* eigenfunctions of the  $S^2$  operator. In order to obtain  $S^2$  eigenfunctions, an appropriate spin-projection operator  $\mathbf{O}_k$  is applied to those Slater determinants, which are not eigenfunctions of  $S^2$ .

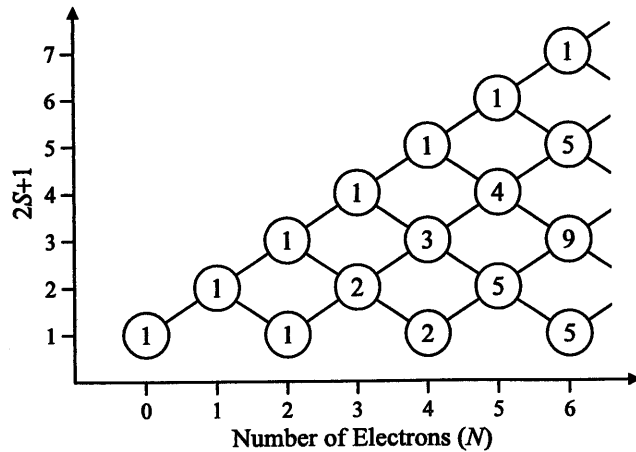


Figure 7-1

Branching diagram showing the number of states of a given multiplicity ( $2S+1$ ) obtainable from  $N$  independent electrons.

Table 7-1  
Orthonormal configuration state functions (CSFs) describing the true-spin states of the three electron problem.

true spin state	$2S+1$	$M_s$	configuration state function (CSF)
${}^2\Psi_1$	2	+1/2	${}^2\Psi_1^{+1/2} =  \lambda_1\bar{\lambda}_1\lambda_2 $
		-1/2	${}^2\Psi_1^{-1/2} =  \lambda_1\bar{\lambda}_1\bar{\lambda}_2 $
${}^2\Psi_2$	2	+1/2	${}^2\Psi_2^{+1/2} =  \lambda_1\bar{\lambda}_1\lambda_3 $
		-1/2	${}^2\Psi_2^{-1/2} =  \lambda_1\bar{\lambda}_1\bar{\lambda}_3 $
${}^2\Psi_3$	2	+1/2	${}^2\Psi_3^{+1/2} =  \lambda_1\lambda_2\bar{\lambda}_2 $
		-1/2	${}^2\Psi_3^{-1/2} =  \bar{\lambda}_1\lambda_2\bar{\lambda}_2 $
${}^2\Psi_4$	2	+1/2	${}^2\Psi_4^{+1/2} =  \lambda_2\bar{\lambda}_2\lambda_3 $
		-1/2	${}^2\Psi_4^{-1/2} =  \lambda_2\bar{\lambda}_2\bar{\lambda}_3 $
${}^2\Psi_5$	2	+1/2	${}^2\Psi_5^{+1/2} =  \lambda_1\lambda_3\bar{\lambda}_3 $
		-1/2	${}^2\Psi_5^{-1/2} =  \bar{\lambda}_1\lambda_3\bar{\lambda}_3 $
${}^2\Psi_6$	2	+1/2	${}^2\Psi_6^{+1/2} =  \lambda_2\lambda_3\bar{\lambda}_3 $
		-1/2	${}^2\Psi_6^{-1/2} =  \bar{\lambda}_2\lambda_3\bar{\lambda}_3 $
${}^4\Psi_1$	4	+3/2	${}^4\Psi_1^{+3/2} =  \lambda_1\lambda_2\lambda_3 $
		+1/2	${}^4\Psi_1^{+1/2} = \frac{1}{\sqrt{3}} ( \lambda_1\lambda_2\bar{\lambda}_3  +  \lambda_1\bar{\lambda}_2\lambda_3  +  \bar{\lambda}_1\lambda_2\lambda_3 )$
		-1/2	${}^4\Psi_1^{-1/2} = \frac{1}{\sqrt{3}} ( \bar{\lambda}_1\bar{\lambda}_2\lambda_3  +  \bar{\lambda}_1\lambda_2\bar{\lambda}_3  +  \lambda_1\bar{\lambda}_2\bar{\lambda}_3 )$
		-3/2	${}^4\Psi_1^{-3/2} =  \bar{\lambda}_1\bar{\lambda}_2\bar{\lambda}_3 $
${}^2\Psi_7$	2	+1/2	${}^2\Psi_7^{+1/2} = \frac{1}{\sqrt{6}} (2 \lambda_1\lambda_2\bar{\lambda}_3  -  \lambda_1\bar{\lambda}_2\lambda_3  -  \bar{\lambda}_1\lambda_2\lambda_3 )$
		-1/2	${}^2\Psi_7^{-1/2} = \frac{1}{\sqrt{6}} (2 \bar{\lambda}_1\bar{\lambda}_2\lambda_3  -  \bar{\lambda}_1\lambda_2\bar{\lambda}_3  -  \lambda_1\bar{\lambda}_2\bar{\lambda}_3 )$
${}^2\Psi_8$	2	+1/2	${}^2\Psi_8^{+1/2} = \frac{1}{\sqrt{2}} ( \lambda_1\bar{\lambda}_2\lambda_3  -  \bar{\lambda}_1\lambda_2\lambda_3 )$
		-1/2	${}^2\Psi_8^{-1/2} = \frac{1}{\sqrt{2}} ( \bar{\lambda}_1\lambda_2\bar{\lambda}_3  -  \lambda_1\bar{\lambda}_2\bar{\lambda}_3 )$

$$\mathbf{O}_k = \prod_{i \neq k} \frac{S^2 - S_i}{S_k - S_i} \quad (7-6)$$

The product is taken over all eigenvalues of  $S^2$  for the system of interest, except the eigenvalue  $S_k$ .  $\mathbf{O}_k$  then projects an eigenfunction of  $S^2$  with an eigenvalue  $S_k$ . In this case it is helpful to know the number of states of a given

multiplicity obtainable from  $N$  independent electrons. This can be deduced from the branching diagram in Figure 7-1.

The advantage of the above described procedure is, that by determining the eigenfunctions of the  $S_z$  and  $S^2$  operator, we automatically also attain the eigenfunctions of the spin-free Hamiltonian  $H$ , because it commutes with both of these operators.

$$[H, S^2] = [H, S_z] = 0 \quad (7-7)$$

In the case of a three-electron system with  $N = 3$  and  $L = 6$  twenty unique electron configurations are possible (eq. 7-1). Of these twenty configurations twelve include only one unpaired electron and eight include three unpaired electrons. From the branching diagram in Figure 7-1 we deduce, that the first twelve configurations lead to six doublet states  ${}^2\Psi_{1..6}$  and the second eight configurations to one quartet  ${}^4\Psi_1$  and another two doublet states  ${}^2\Psi_{7..8}$ . One possible set of wave functions representing these twenty microstates, also known as configuration state functions (CSFs), are listed in Table 7-1. Note, that not all microstates are described by a single Slater determinants, but rather by a linear combination of Slater determinants. This is due to the fact that those Slater determinants, which represent three electrons in three different spaceorbitals and have an  $S_z$  eigenvalue of  $+1/2$  or  $-1/2$ , are not eigenfunctions of the  $S^2$  operator.

## 7.2. Characteristics of the ZINDO Output

The "three electron problem" manifests itself in configuration interaction (CI) calculations on doublet states. In this context two important characteristics of the CI-routine of the ZINDO program (Bacon and Zerner 1979, Edward and Zerner 1987) shall be discussed here. (i) A CI coefficient is not necessarily related to a single Slater determinant, but rather to a CSF, *i.e.* a linear combinations of Slater determinants. (ii) A non-orthogonal CI space may be used.

The ZINDO output refers to CSFs by a numbering scheme. For example the numbering scheme on the left of eq. 7-8 refers to the CSF on the right,

$$\begin{array}{cccc} a & b & \dots & i & j \\ a & b & \dots & i & j \end{array} \triangleq |\lambda_a \bar{\lambda}_a \lambda_b \bar{\lambda}_b \dots \lambda_i \bar{\lambda}_i \lambda_j| \quad (7-8)$$

which corresponds to the electron configuration in which the spaceorbitals  $\phi_a$  to  $\phi_i$  are double occupied and  $\phi_j$  is occupied by an electron with  $\alpha$  spin. In the case of three unpaired electrons three Slater determinants with  $M_S = +1/2$  can be generated. Formation of the appropriate  $S^2$  eigenfunctions leads to three CSFs, two with  $S = 1/2$  (doublet) and one with  $S = 3/2$  (quartet). Thus in the

calculation of doublet states only two CSFs are related to the three Slater determinants with  $M_S = +1/2$ . In the ZINDO output these two CSFs are referred to as follows (doubly occupied orbitals are omitted for reasons of simplicity):

$$\begin{array}{c} a \\ b \end{array} \begin{array}{c} c \\ c \end{array} \triangleq \frac{1}{\sqrt{2}} (|\lambda_a \bar{\lambda}_b \lambda_c| - |\bar{\lambda}_a \lambda_b \lambda_c|) \quad \begin{array}{c} b \\ c \end{array} \begin{array}{c} a \\ c \end{array} \triangleq \frac{1}{\sqrt{2}} (|\lambda_a \lambda_b \bar{\lambda}_c| - |\lambda_a \bar{\lambda}_b \lambda_c|) \quad (7-9,10)$$

The ZINDO CI wave function is then given by

$${}^2\Psi_{\text{ZINDO}} = \dots + a_i \frac{1}{\sqrt{2}} (|\lambda_a \bar{\lambda}_b \lambda_c| - |\bar{\lambda}_a \lambda_b \lambda_c|) + a_j \frac{1}{\sqrt{2}} (|\lambda_a \lambda_b \bar{\lambda}_c| - |\lambda_a \bar{\lambda}_b \lambda_c|) + \dots \quad (7-11)$$

where the  $a$ 's refers to the respective CI coefficients. The CSFs in eqs. 7-9,10 are not orthogonal to each other, *i.e.*

$$\left\langle \frac{1}{\sqrt{2}} (|\lambda_a \bar{\lambda}_b \lambda_c| - |\bar{\lambda}_a \lambda_b \lambda_c|) \middle| \frac{1}{\sqrt{2}} (|\lambda_a \lambda_b \bar{\lambda}_c| - |\lambda_a \bar{\lambda}_b \lambda_c|) \right\rangle = -\frac{1}{2} \quad (7-12)$$

In such cases only the combined contribution of both linear combinations to the CI wave functions can be given and is

$$\langle {}^2\Psi_{\text{ZINDO}} | {}^2\Psi_{\text{ZINDO}} \rangle = \dots + (a_i^2 - a_i a_j + a_j^2) + \dots \quad (7-13)$$

The non-orthogonal CSFs in eqs. 7-9,10 can be transformed into CSFs, which are orthogonal to each other:

$$a'_i = \frac{\sqrt{3}}{2} a_j \quad a'_j = a_i - \frac{1}{2} a_j \quad (7-14,15)$$

$$\begin{aligned} {}^2\Psi_{\text{ZINDO}} = \dots &+ a'_i \frac{1}{\sqrt{6}} (2|\lambda_a \lambda_b \bar{\lambda}_c| - |\lambda_a \bar{\lambda}_b \lambda_c| - |\bar{\lambda}_a \lambda_b \lambda_c|) \\ &+ a'_j \frac{1}{\sqrt{2}} (|\lambda_a \bar{\lambda}_b \lambda_c| - |\bar{\lambda}_a \lambda_b \lambda_c|) + \dots \end{aligned} \quad (7-16)$$

As a result the contribution from each CSF is now given by the square of its CI coefficient.

$$\langle {}^2\Psi_{\text{ZINDO}} | {}^2\Psi_{\text{ZINDO}} \rangle = \dots + a_i'^2 + a_j'^2 + \dots \quad (7-17)$$

Another interesting feature of eq. 7-16 is that in the first CSF the first two electrons are said to be "triplet coupled", while in the second CSF they are said to be "singlet coupled". This will be of importance in the characterization of the possible decay channels of resonances.

There is an arbitrariness in the orthogonalization and we could have just as well applied the following relations:

$$a_i'' = \frac{\sqrt{3}}{2}(a_i - a_j) \quad a_j'' = \frac{1}{2}(a_i + a_j) \quad (7-18,19)$$

$${}^2\Psi_{\text{ZINDO}} = \dots + a_i'' \frac{1}{\sqrt{6}} (2|\lambda_a \bar{\lambda}_b \lambda_c| - |\lambda_a \lambda_b \bar{\lambda}_c| - |\bar{\lambda}_a \lambda_b \lambda_c|) \\ + a_j'' \frac{1}{\sqrt{2}} (|\lambda_a \lambda_b \bar{\lambda}_c| - |\bar{\lambda}_a \lambda_b \lambda_c|) + \dots \quad (7-20)$$

or

$$a_i''' = -\frac{\sqrt{3}}{2}a_i \quad a_j''' = a_j - \frac{1}{2}a_i \quad (7-21,22)$$

$${}^2\Psi_{\text{ZINDO}} = \dots + a_i''' \frac{1}{\sqrt{6}} (2|\bar{\lambda}_a \lambda_b \lambda_c| - |\lambda_a \lambda_b \bar{\lambda}_c| - |\lambda_a \bar{\lambda}_b \lambda_c|) \\ + a_j''' \frac{1}{\sqrt{2}} (|\lambda_a \lambda_b \bar{\lambda}_c| - |\bar{\lambda}_a \bar{\lambda}_b \lambda_c|) + \dots \quad (7-23)$$

Note that in eq. 7-20 the first and third electron are now triplet and singlet coupled, while in eq. 7-23 the second and third electron are triplet and singlet coupled.

## REFERENCES

- Abouaf R., Benoit C. (1990). *Chem. Phys.* **144**, 407.
- Allan M. (1989). *J. Electron Spectrosc. Relat. Phenom.* **48**, 219-351.
- Allan M. (1992). *J. Phys. B.: At. Mol. Opt. Phys.* **25**, 1559.
- Allan M. (1994). *Chem. Phys. Lett.* **225**, 156.
- Allan M. (1994b). Unpublished results.
- Allan M. (1995). *J. Phys. B: At. Mol. Opt. Phys.* **28**, 5163.
- Allan M. (1996). Unpublished results.
- Andersson K., Roos B.O. (1994). In *Modern Electron Structure Theory, Volume I*, World Scientific Publishing, New York.
- Antic D., David D.E., Michl J. (1994). Contributions to the XVth IUPAC Symposium on Photochemistry, Prague, July 1994.
- Asmis K.R., Allan M. (1995). Contributions to the International Symposium on Electron- and Photon-Molecule Collisions and Swarms, Berkeley, July 1995.
- Asmis K.R. (1996). Manuals describing the trochoidal and the photoelectron instrument, in particular the acquisition/control program(s).
- Azria R., LeCoat Y., Ziesel J.-P., Guillotin J.-P., Mharzi B., Tronc M. (1994). *Chem. Phys. Lett.* **220**, 417.
- Bacon A.D., Zerner M.C. (1979). *Theor. Chim. Acta.* **53**, 21.
- Baltzer P., Karlsson L., Lundqvist M., Wannberg B. (1993). *Rev. Sci. Instrum.* **64**, 2179.
- Baltzer P., Karlsson L. (1989). Uppsala University Institute of Physics Report UIIP-1211.
- Bardsley N., Mandl F. (1968). *Rept. Progr. Phys.* **31**, 471.
- Bavia M., Bertinelli F., Taliani C., Zauli C. (1976). *Mol. Phys.* **31**, 479.
- Bulliard C. (1994). Thesis, University of Fribourg (CH).
- Burrow P.D., Jordan K.D. (1975). *Chem. Phys. Lett.* **36**, 5941.
- Burrow P.D., Sanche L. (1972). *Phys. Rev. Lett.* **28**, 333.
- Castellucci E., Manzelli P., Gallinella E., Minore P. (1975). *Spectrochim. Acta* **31A**, 451.
- Chadwick R.R., Zgierski M.Z., Hudson B.S. (1991). *J. Chem. Phys.* **95**, 7204.
- Chen D., Gallup G.A. (1990). *J. Chem. Phys.* **93**, 8893.
- Christophorou L.G., ed. (1984). *Electron-Molecule Interactions and their Applications*, Vols. 1 and 2, Academic Press.
- Cloutier P., Sanche L. (1989). *Rev. Sci. Instrum.* **60**, 1054.
- Collins L.A., Schneider B.I. (1988). In *Electron Molecule Scattering and Photoionization*, P.G. Burke, J.B. West, eds., Plenum, New York.
- Derrick P.J., Åsbrink L., Edqvist O., Jonsson B.-Ö., Lindholm E. (1971). *Int. J. Mass Spectrom. Ion Phys.* **6**, 203.

- Doering J.P. (1979). *J. Chem. Phys.* **70**, 3902.
- Doering J.P., McDiarmid R. (1980). *J. Chem. Phys.* **73**, 3617.
- Doering J.P., McDiarmid R. (1981). *J. Chem. Phys.* **75**, 2477.
- Dressler R., Neuhaus L., Allan M. (1983). *J. Electron Spectrosc. Relat. Phenom.* **31**, 181.
- Dressler R.A. (1985). Thesis, University of Fribourg (CH).
- Edward W.D., Zerner M.C. (1987). *Theor. Chim. Acta.* **72**, 347.
- El houar S. (1993). Diploma work, University of Fribourg (CH).
- Falcetta M.F., Jordan K.D. (1991). *J. Am. Chem. Soc.* **113**, 7455.
- Flicker W.M., Mosher O.A., Kuppermann A. (1976). *J. Chem. Phys.* **64**, 1315. *Chem. Phys. Lett.* **38**, 489.
- Forster P., Gschwind R., Haselbach E., Klemm U., Wirz J. (1980). *Nouv. J. Chim.* **4**, 365.
- Franck J., Hertz G. (1914). *Verhandl. Phys. Ges.* **16**, 457.
- Frisch M.J., Trucks G.W., Schlegel H.B., Gill P.M.W., Johnson B.G., Robb M.A., Cheeseman J.R., Keith T.A., Petersson G.A., Montgomery J.A., Raghavachari K., Al-Laham M.A., Zakrzewski V.G., Ortiz J.V., Foresman J.B., Cioslowski J., Stefanov B.B., Nanayakkara A., Challacombe M., Peng C.Y., Ayala P.Y., Chen W., Wong M.W., Andres J.L., Replogle E.S., Gomperts R., Martin R.L., Fox D.J., Binkley J.S., Defrees D.J., Baker J., Stewart J.P., Head-Gordon M., Gonzalez C., Pople J.A. Gaussian 94 (Revision B.3), Gaussian, Inc.: Pittsburgh, PA, 1995.
- Frueholz R.P., Flicker W.M., Mosher O.A., Kuppermann A. (1979). *J. Chem. Phys.* **70**, 2003.
- Gallup G.A. (1986). *Phys. Rev. A* **34**, 2746.
- Gianturco F.A., Jain A. (1986). *Phys. Reports* **143**, 347-425.
- Grimm-Bosbach T., Thümmel H.T., Nesbet R.K., Pyerimhoff S.D. (1995). *J. Phys. B: At. Mol. Opt. Phys.* **29**, L105.
- Håkansson R., Nordén B., Thulstrup E.N. (1977). *Chem. Phys. Lett.* **50**, 305.
- Hall R.J., Read F.H. (1984). *Molecular Spectroscopy by Electron Scattering*, In: Electron-Molecule Collisions, I. Shimamura, K. Takayanagi, eds., Plenum Press, Chapter 5.
- Herz H.J., Feder R., Meister G., Bauer E.G. (1981). *Solid State Commun.* **38**, 973.
- Hoffmann R. (1971). *Acc. Chem. Res.* **4**, 1.
- Hughes A.L., Rojansky V. (1929). *Phys. Rev.* **34**, 284-90.
- Hudson B.S., Kohler B.E., Schulten K. (1982). *Excited States*, E.C. Lim, ed., Vol.6, 1.
- Ibach H. (1993). *J. Electron Spectrosc. Relat. Phenom.* **64/65**, 819.
- Illenberger E., Momigny J. (1992). *Gaseous Molecular Ions*, Steinkopff Verlag Darmstadt, Springer-Verlag New York, p. 45.
- Jordan K.D., Burrow P.D. (1987). *Chem. Rev.* **87**, 557-88.
- Juang C.-Y., Chao J. S.-Y. (1994). *J. Phys. Chem.* **98**, 13506-12.
- Koopmans T. (1934). *Physica* **1**, 104.
- Kutzelnigg W. (1975). *Einführung in die Theoretische Chemie*, Verlag Chemie, Weinheim.

- Kupperman A., Flicker W.M., Mosher O.A. (1979). *Chem. Rev.* **79**, 77.
- Lane N.F. (1980). *Rev. Mod. Phys.* **52**, 29.
- Lowe J.P. (1978). *Quantum Chemistry*, Academic Press, San Diego.
- Malmqvist P.-Å., Roos B.O. (1989). *Chem. Phys. Lett.* **155**, 189.
- Matsen F.A. (1964). *J. Phys. Chem.* **68**, 3284-96.
- McDaniel E.W. (1989). *Atomic Collisions*, Wiley Interscience.
- McDiarmid R., Doering J.P. (1980). *J. Chem. Phys.* **73**, 4192.
- McKoy V., Winstead C. (1993). Private communication.
- Meinke M., Illenberger E. (1994). *J. Chem. Phys.* **98**, 6601.
- Morrison (1994). Unpublished results.???
- Mosher O.A., Flicker W.M., Kuppermann A. (1973). *J. Chem. Phys.* **59**, 6502; *Chem. Phys. Lett.* **19**, 332.
- Nestmann B.M., Peyerimhoff (1985). *J. Phys. B: At. Mol. Phys.* **18**, 615. *J. Phys. B: At. Mol. Phys.* **18**, 4309.
- Palmer M.H., Walker I.C., Ballard C.C., Guest M.F. (1995). *Chem. Phys.* **192**, 111.
- Pichou F., Huetz A., Joyez G., Landau M., Mazeau J. (1976). *J. Phys. B: Atom. Mol. Phys.* **9**, 933.
- Pilar F.L. (1968). *Elementary Quantum Chemistry*, Chapter 11, McGraw-Hill, Inc..
- Pople J.A., Segal G.A. (1965). *J. Chem. Phys.* **43**, S136.
- Pople J.A., Beveridge D.L., Dobosh P. A. (1967). *J. Chem. Phys.* **47**, 2026.
- Purcell E.M. (1938). *Phys. Rev.* **54**, 818-26.
- Read F.H., Channing J.M. (1996). *Rev. Sci Instrum.* **67**, 2372.
- Reddish T., Wallbank B., Comer J. (1986). *Chem. Phys.* **108**, 159.
- Rescigno T.N., Schneider B.I. (1992). *Phys. Rev. A* **45**, 2894.
- Robin M.B. (1985). *Higher Excited States of Polyatomic Molecules*, Volume III, Academic Press.
- Roebber J.L., Gerrity D.P., Hemley R., Vaida V. (1980). *Chem. Phys. Lett.* **75**, 104.
- Roos B.O. (1987). In *Ab Initio Methods in Quantum Chemistry II*, K.P. Lawley, ed., J. Wiley & Sons Ltd., p. 399.
- Roos B.O., Fülischer M.P., Malmqvist P.A., Merchán M., Serrano-Andrés (1994). In *Quantum Mechanical Electronic Structure Calculations with Chemical Accuracy*, S.R. Langhoff, ed., Kluwer, Dordrecht.
- Roothaan C.C.J. (1951). *Rev. Mod. Phys.* **23**, 69.
- Salem L. (1966). *The Molecular Orbital Theory of Conjugated Systems*, Benjamin: New York.
- Schafer O. (1992). Thesis, University of Fribourg (CH).
- Schimamura I., Takayanagi K., eds. (1984). *Electron-Molecule Collisions*, Plenum Press.

- Schmelzer A., Haselbach E. (1971). *Helv. Chim. Acta* **54**, 1299. (The present improved and modernized version of the program has been written by T. Bally, S. Matzinger, and B. Albrecht.)
- Schulz G.J. (1973). *Rev. Mod. Phys.* **45**, 423.
- Serrano-Andrés L., Merchán M., Nebot-Gil I., Lindh R., Roos B.O., (1993a). *J. Chem. Phys.* **98**, 3151.
- Serrano-Andrés L., Merchán M., Nebot-Gil I., Roos B.O., Fülischer M. (1993b). *J. Am. Chem. Soc.* **115**, 6184.
- Serrano-Andrés L., Merchán M., Fülischer M., Roos B.O. (1993c). *Chem. Phys. Lett.* **211**, 125.
- Shang O., Hudson B.S. (1991). *Chem. Phys. Lett.* **183**, 63.
- Shida T., Hamill W.H. (1966). *J. Am. Chem. Soc.* **88**, 5371.
- Staley S.W., Strnad J.T. (1994). *J. Phys. Chem.* **98**, 116.
- Staley S.W., Bjorke M.D., Giordan J.C., McMillan M.R., Moore J.H. (1981). *J. Am. Chem. Soc.* **103**, 7057.
- Stamatovic A., Schulz G.J. (1968). *Rev. Sci. Instr.* **39**, 1752.
- Stamatovic A., Schulz G.J. (1970)., *Rev. Sci. Instr.* **41**, 423.
- Strahan G.D., Hudson B.S. (1993). *J. Chem. Phys.* **99**, 5780.
- Swiderek P., Michaud M., Hohlneicher G., Sanche L. (1991). *Chem. Phys. Lett.* **178**, 289; *Chem. Phys. Lett.* **187**, 583.
- Swiderek P., Michaud M., Sanche L. (1993). *J. Chem. Phys.* **98**, 8397.
- Swiderek P., Fraser M.-J., Michaud M., Sanche L. (1994). *J. Chem. Phys.* **100**, 70.
- Szabo A., Ostlund N.S. (1989). *Modern Quantum Chemistry, Introduction to Advanced Electronic Structure Theory*, McGraw-Hill.
- Takayanagi K. (1984). *Introduction to Electron-Molecule Collisions*, In: Electron-Molecule Collisions, I. Shimamura, K. Takayanagi, eds., Plenum Press, Chapter 1.
- Trajmar S., Cartwright D.C. (1984). *Excitation of Molecules by Electron Impact*, In: Electron Molecule Interactions and their Applications, L.G. Christophorou, ed., Academic Press, Chapter 2.
- Turner D.W. (1968). *Proc. Roy. Soc. A* **307**, 15.
- Van Veen E.H. (1976). *Chem. Phys. Lett.* **41**, 535.
- Wiberg K.B., Hada C.M., Ellison G.B., Foresman J.B. (1993). *J. Phys. Chem.* **97**, 13586.
- Wong S.F., Schulz G.J. (1975). *Phys. Rev. Lett.* **35**, 1429.
- Yarkony D.R. ed. (1995). *Modern Electronic Structure Theory*, Part I & II, World Scientific Publishing Co., Singapore.
- Zerbetto F., Zgierski M.Z. (1991). *Chem. Phys. Lett.* **176**, 7.
- Zgierski M.Z., Zerbetto F. (1991). *Chem. Phys. Lett.* **179**, 131.
- Zgierski M.Z., Zerbetto F. (1993). *J. Phys. Chem.* **99**, 3721.
- Zubek M., Gulley N., King G.C., Read F.H. (1996). *J. Phys. B.: At.Mol.Opt.Phys.* **29**, L239.

## ACKNOWLEDGEMENTS

I wish to express my sincere gratitude to Paul-Hervé Chassot, Olivier Graber and Raphael Weber of the electronics workshop for the design and assembly of the electronic components. I am equally indebted to Emile Brosi and his co-workers for the fabrication and design of the mechanical components.

I thank Jean-Luc Roulin, Christina Verdeja and Alexandre Robatel for the synthesis of various chemical substances and their help in the chemical laboratory.

My special thanks goes to Dr. Christophe Bulliard, Dr. Stephan Matzinger, Dr. Duska Popovic, Momir Stepanovic and Gabi Wirtz for their companionship during my doctoral work. Our social and scientific exchanges made the past four years most memorable.

I thank Prof. Dr. Werner Hug for introducing me to the exciting research field of Quantum Chemistry.

I thank Dr. Urs Meier and Dr. Markus von Raumer for their assistance, advice and companionship throughout the eight years of my study in Fribourg.

I thank the diploma students Dunja Frey, Sarah El houar and Vroni Huber for their contribution to this thesis and their companionship.

I thank our secretary Verena Schwalm for her assistance and guiding hand.

I further thank my colleagues and co-workers at the Institute Prof. Dr. Thomas Bally, Dr. Nagwa Ghoneim, Jean-Claude Gumy, Dr. Arthur Henseler, Claudia Högemann, Dr. Vojtech Hrouda, Krzysztof Huben, Beat Müller, Dr. Yvan Pariat, Dr. Denis Pilloud, Alexandre Sarbach, Dr. Daniel Scherrer, Dr. Olivier Schafer, Prof. Dr. Paul Suppan, Dr. Leo Truttman, Dr. Eric Vauthey and Zhendong Zhu for interesting discussions and their contribution to the pleasant atmosphere within the Institute.

I wish to thank the Swiss National Science Foundation and the State of Fribourg for their financial support.

My warmest thanks to my love Nathalie for her support during the past years.

## CURRICULUM VITAE

### Personal:

**Name:** ASMIS, Knut Roger  
**Birth:** June 25, 1968 in Berlin (West), Federal Republic of Germany  
**Nationality:** Swiss  
**Marital Status:** Not Married  
**Languages:** German, English and French

### Education:

1987 Mechanical Engineering Traineeship, Siemens AG Berlin  
 1988-1989 Free University Berlin (Germany), Study of Chemistry  
 1989-1992 University of Fribourg (Switzerland), Study of Chemistry  
 Diploma in Chemistry (Major : Physical Chemistry)  
 1993-1996 Institute for Physical Chemistry, University of Fribourg  
 Research Assistant (Study towards Ph.D.), supported by the  
 Swiss National Science Foundation and the State of Fribourg,  
 Supervisor: Prof. M. Allan  
 1995 4th European Summerschool of Quantum Chemistry, Lund  
 (Sweden). Topic: Modern Ab Initio Methods.

### Teaching:

1993-1996 - Teaching Assistant: Physical Chemistry Laboratory Course  
 - Course on "Chemistry and Environment" (with others)

### Publications:

"Triplet-State Energy of the Photostabilizer Tinuvin P", M. Allan, K. Asmis, C. Bulliard, E. Haselbach, P. Suppan, *Helv. Chim. Acta* **76** 993 (1993).  
 "Synthesis and Spectroscopy of Tricyclo[3.3.3.0<sup>3,7</sup>]undec-3(7)-ene : Confirmation of Computational Predictions Regarding the Effects of Pyramidalization on Alkene Ionization Energies and Electron Affinities", J.M. Smith, D.A. Hrovat, W.T. Borden, M. Allan, K.R. Asmis, C. Bulliard, E. Haselbach, U.C. Meier, *J. Am. Chem. Soc.* **115** 3816 (1993).

"Triplet Energy of 2,2-Dimethylisobutene from Electron Energy-Loss Spectroscopy and Photoinduced Triplet Energy Transfer", M.Allan, K.R. Asmis, S.El houar, E. Haselbach, M.Capponi, B. Urwyler, J. Wirz, *Helv. Chim. Acta* **77** 1541 (1994).  
 "Electronic and Vibrational Structure and Scaled Density Functional Force Field of Cyclopentadiene and Its Radical Cation", L.Truttman, K.R. Asmis, T. Bally, *J. Phys. Chem.* **99** 17844 (1995).  
 "Production of Vibrationally Autodetaching O<sub>2</sub><sup>-</sup> Produced in Low-Energy Electron Impact on Ozone", M. Allan, K.R. Asmis, D.B. Popovic, M. Stepanovic, N.J. Mason, J.A. Davies, *J. Phys. B: At. Mol. Opt. Phys.* **29** 3487 (1996).  
 "Resonances in Collisions of Low-Energy Electrons to Ozone: Experimental Elastic and Vibrationally Inelastic Differential Cross Sections and Dissociative Attachment Spectra", M. Allan, K.R. Asmis, D.B. Popovic, M. Stepanovic, N.J. Mason, J.A. Davies, submitted for publication.  
 "Electron Energy-Loss Spectroscopy and Theoretical Study of Triplet and Singlet Excited States of Fulvene", K.R. Asmis, M. Allan, M. Fülischer, submitted for publication.  
 "Measurement of Absolute Differential Cross Sections for the Excitation of the  $n = 2$  States of Helium at 0° and 180°", K.R. Asmis and M. Allan, submitted for publication.  
 "Excess Energy Partition between Electrons Departing at 0° and 180° in the Ionization of Helium near Threshold", K.R. Asmis and M. Allan, to be submitted for publication.  
 "Measurement of Absolute Differential Cross Sections for the Excitation of the  $\pi,\pi^*$  Triplet State of Ethene by Electron Impact at 0° and 180°", K.R. Asmis and M. Allan, to be submitted for publication.

### Talks:

"Selective Formation of Triplet States in the Decay of Radical Anions with Two Excited Electrons", Fall Meeting of the Swiss Society for Photochemistry and Photophysics, 13-14 October 1994, Fribourg (Switzerland).  
 "Measurement of Absolute Differential Cross Sections at 180 Degrees", International Symposium on Electron- and Photon-Molecule Collisions and Swarms, 22-25 July 1995, Berkeley (USA).

During my studies in Fribourg I attended courses given by M. Allan, T. Bally, P. Belser, C. Daul, F. Emmenegger, G. Galetti, A. Gossauer, E. Haselbach, W. Hug, R. Ingold, T. Jenny, M. Maggetti, R. Neier, J. Portmann, L. Schellenberg, W. Schläpfer, P. Suppan and A. von Zelewsky.